LABORATORI NAZIONALI DI FRASCATI
SIS – Pubblicazioni

LNF-95/024 (IR)
18 Maggio 1995

FINUDA TECHNICAL REPORT

The FINUDA Collaboration

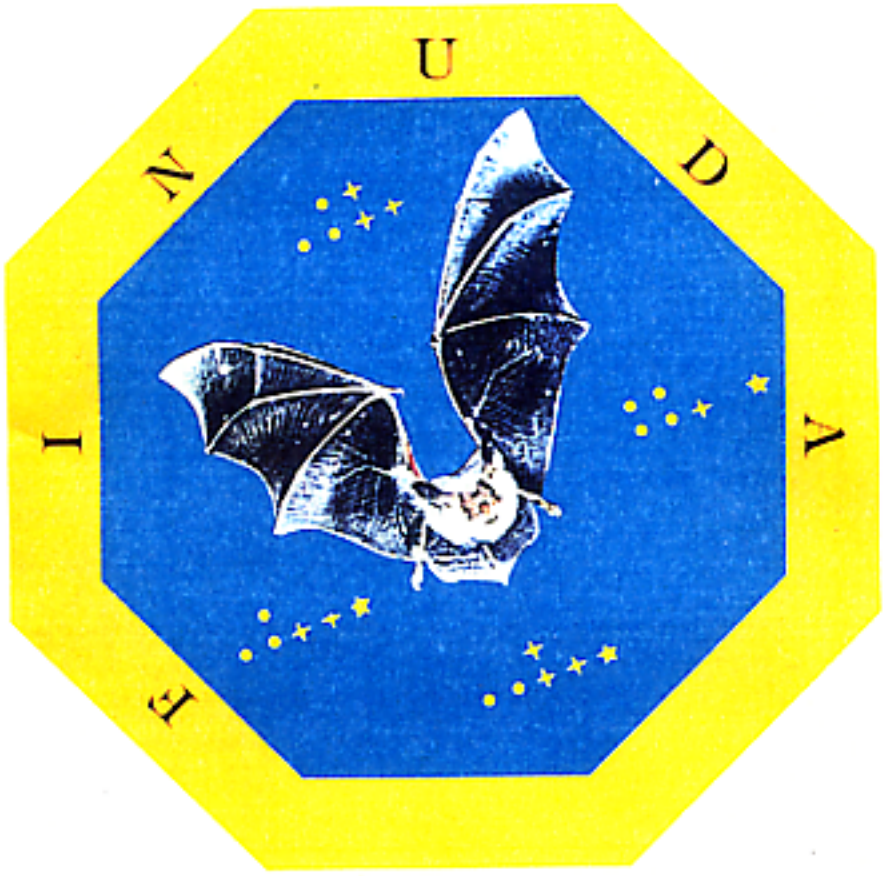

PACS.: 21.80.+a ; 25.80.Nv ; 13.30.Eg

SIS – Pubblicazioni
dei Laboratori Nazionali di Frascati
P.O. Box 13, I-00044 Frascati (Italy)

FINUDA TECHNICAL REPORT

October 1994

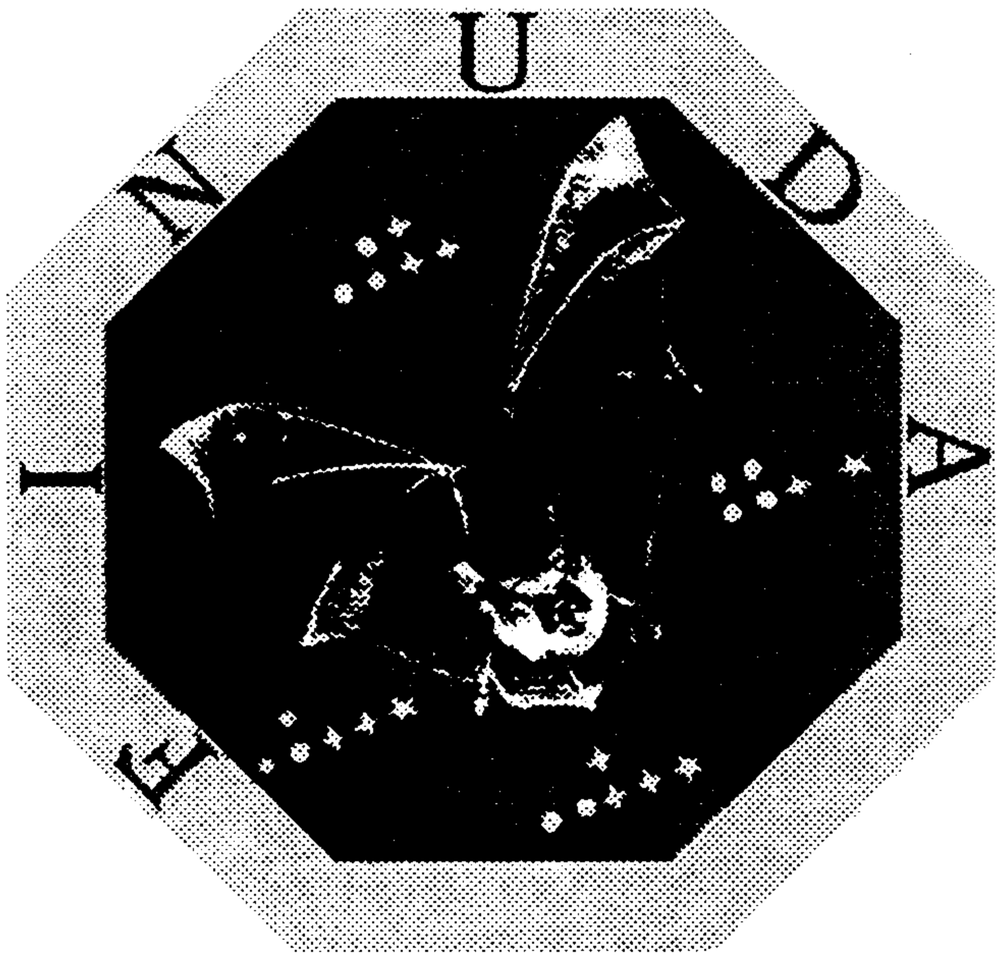

INFN – Laboratori Nazionali di Frascati
SIS – Pubblicazioni

LNF–95/024 (IR)
18 Maggio 1995

FINUDA TECHNICAL REPORT

The FINUDA Collaboration

Researchers: M. Agnello, P. Amaudruz[b], G. Beer[b], M. Bertani[c], S. Bianco[c], E. Botta[d], T. Bressani[d], L. Busso[e], D. Calvo[d], P. Camerini[f], C. Cattaneo[g], L. Celano[h], N. Colonna[h], M. Corradini[i], G.O. Delle Monache[c], G. D'Erasmo[h], A. Donzella[i], F.L. Fabbri[c], A. Feliciello[d], A. Filippi[l], V. Filippini[g], E.M. Fiore[h], L. Fiore[h], P. Gianotti[c], M. Giardoni[c], D.R. Gill[b], N. Grion[f], C. Guaraldo[c], F. Iazzi[a], A. Lanaro[c], L. Lee[l], E. Lodi Rizzini[i], V. Lucherini[c], S. Marcello[d], G. Marciano[g], G.M. Marshall[b], B. Minetti[a], N. Mirfakhrai[n], P. Montagna[g], O. Morra[e], A. A. Nozdrin[b], A. Olin[b], A. Pantaleo[h], V. Paticchio[h], E. Rossetto[d], A. Rotondi[g], R. Rui[f], P. Salvini[g], S. Sarwar[c], A. Sharma[d], G. Smith[b], L. Venturelli[i], S. Yen[b], and A. Zenoni[m]

Students and technicians: G. Antuofermo[h], R. Bacconi[f], C. Becciani[f], L. Benussi[c], D. Bertagni[d], A.G. Iacobelli[h], V. Lunardi[e], A. Mecozzi[c], L. Passamonti[c], D. Quarta[e], V. Russo[b], M. Sacchetti[h], P. Vasta[h]

INFN Technical Services: B. Casavecchia[o], A. Cecchetti[c], A. De Paolis[c], B. Dulach[c], G. Ferretti[c], F. Impavido[a], D. Orecchini[c], D. Pierluigi[c], L. Simonetti[o], S. Valeri[c]

[a]Dipartimento di Fisica del Politecnico di Torino and INFN, Sezione di Torino, I–10125 Torino, Italy
[b]TRIUMF, 4004 Wesbrok Mall, Vancouver, BC, V6T 2A3, Canada
[c]INFN, Laboratori Nazionali di Frascati, I–00044 Frascati, Italy
[d]Dipartimento di Fisica Sperimentale, Università di Torino and INFN, Sezione di Torino, I–10125 Torino, Italy
[e]Istituto di Fisica Generale, Università di Torino and INFN, Sezione di Torino, I–10125 Torino, Italy
[f]Dipartimento di Fisica, Università di Trieste and INFN, Sezione di Trieste, I–34127 Trieste, Italy
[g]Dipartimento di Fisica Nucleare e Teorica, Università di Pavia and INFN, Sezione di Pavia, I–27100 Pavia, Italy
[h]Dipartimento di Fisica, Università di Bari and INFN, Sezione di Bari, I–70126 Bari, Italy
[i]Dipartimento di Elettronica per l'Automazione, Università di Brescia and INFN, Sezione di Torino, I–25060 Brescia, Italy
[l]Dipartimento di Fisica Nucleare e Teorica, Universtà di Pavia and INFN, Sezione di Torino, I–27100 Pavia, Italy
[m]Dipartimento di Elettronica per l'Automazione, Università di Brescia and INFN, Sezione di Pavia, I–25060 Brescia, Italy
[n]Shahid Beheshty University, Dept. of Phys, 19834 Tehran, Iran
[o]INFN, Sezione di Torino – Laboratorio Tecnologico, I–10125 Torino, Italy

Abstract

The present document contains an up-to-date overview of the status of the FINUDA detector. The basic design and the main physics issues remain those of the Proposal. However, a considerable deal of improvements and adaptation to the machine needs was performed and the detector design is, at present, nearly frozen. Also the tests on prototypes are practically completed, and all sub-detectors are passing to the phase of tendering and mass productions, with the objective of having the detector components ready for mid '96.

Contents

1 HYPERNUCLEAR PHYSICS WITH FINUDA 1

1.1 Introduction 1

1.2 Hypernuclear physics 2

1.3 Counting rates and needed resolution 5

1.4 Milestones of the hypernuclear physics program 7

1.5 Expected running sequence for the first year 8

2 THE FINUDA DETECTOR DESIGN 10

2.1 Introduction 10

2.2 The interaction/target region 12

2.3 The outer tracking system 14

2.4 Scintillator arrays 15

3 THE FINUDA MAGNET AND DETECTOR MECHANICS 18

3.1 The iron yoke 18

3.2 Coil and field shape 24

3.3 The cryogenic parameters 25

3.4 The opening and moving mechanical system 30

3.4.1 The precision of alignment and the reproducibility of movements 31

3.5 The internal mechanics 31

3.5.1 Introduction 31

3.5.2 The general supporting structure 31

3.5.3 The mechanical structure supporting targets, ISIM and OSIM 36

3.5.4 The mechanical structure for the drift chambers 39

3.5.5 The mechanical structure for the straw tubes 41

3.5.6 The support for the outer scintillator array (TOFONE) 42

3.5.7 Hints about the way of extracting targets, ISIM and OSIM out of the magnet 42

3.5.8 Hints about the way of inserting the whole structure inside of the magnet 45

4 THE TRACKING SYSTEM **47**

4.1 The silicon vertex detector 47

4.1.1 The ISIM and OSIM detectors 47

4.1.2 Results of tests on prototypes 52

4.1.3 The electronics of ISIM and OSIM 55

4.2 The low-mass high resolution drift chambers 57

4.2.1 General description 57

4.2.2 Cell and gas choice 58

4.2.3 Drift Chamber prototype 68

4.2.4 First results obtained with the drift chamber prototype 77

4.2.5 Final choice of the FINUDA drift chamber 81

4.2.6 Front-end electronics for the drift chambers 89

4.3 The straw tubes array 92

4.3.1 Topology of the array and mechanical structure 93

4.3.2 Design overview 96

4.3.3 Straw tube prototype 97

4.3.4 Results of tests on the prototype with a pion beam 104

4.3.5 Proposed solutions for the components of the design 119

4.3.6 Assembly procedure and monitoring 125

4.4 Tracking system calibrations 127

5 TOFINO and TOFONE **135**

5.1 Internal scintillator barrel (TOFINO) 135

5.1.1 General description 135

5.1.2 TOFINO tests 135

5.2 TOFONE mechanical arrangement 139

5.3 TOFONE prototype performance. 139

5.4 High voltage and electronics read-out of TOFONE 144

5.5 High voltage and controls 144

5.5.1 Scintillator control: the laser system 145

6 TRIGGER **147**

6.1 Trigger Source System: basic triggers 147

6.2 The Global Trigger Supervisor and the Local Trigger Supervisor . . . 151

7 DAQ SYSTEM AND COMPUTER REQUIREMENTS **154**
7.1 Data acquisition (DAQ) architecture 154
7.2 Off-line computing resources 158

8 PHYSICS PERFORMANCES **160**
8.1 Apparatus simulation 160
8.2 Detector resolutions and spectrometer momentum resolution and acceptance 162
8.3 Trigger efficiency and background rejection 166
8.4 Pattern recognition and event reconstruction 169
8.5 K^+ K^- "beam" identification in the interaction region 171
8.6 Track identification inside the spectrometer 173
8.7 Track fitting and momentum reconstruction 175
8.8 Hypernuclear spectroscopy resolution 177

9 INSTALLATION OF THE EXPERIMENT **181**
9.1 Gas distribution control system 181
9.1.1 Drift chambers gas system 183
9.1.2 Straw tube gas system 184
9.2 Detector assembly procedure 185
9.2.1 The Assembly and ASTRA Halls at LNF 185
9.2.2 The transport of the solenoid to LNF and the final assembling 186
9.2.3 Transport and installation of the magnet into the pit 189
9.2.4 Installation of the detector frame inside the magnet 190
9.3 Magnetic measurements 190
9.4 Mechanical alignment 194
9.5 Experimental pit and counting room 197
9.6 Operation 200

10 RESPONSIBILITIES AND TIME SCHEDULE **207**
10.1 Construction schedule 208

Chapter 1

HYPERNUCLEAR PHYSICS WITH FINUDA

1.1 Introduction

A first remark that was never done before is that with FINUDA, for the first time, an experiment of nuclear physics, which is traditionally a fixed target physics, is carried-out at a collider. This approach looks very sound, when expected counting rates and energy resolutions which are the basic performances of the experiment, are compared with those obtained, or foreseen, at fixed target machines. However, working at a collider is very much less flexible than at a fixed target machine, in terms of maintenance, nuclear targets handling, variation of the magnetic field in the solenoid.

The second remarks is that the FINUDA initiative was considered very favorably in the community of hypernuclear physics. It is worthwhile to remind that in the major conferences on the field this year (*5th Conference on Intersection of Particle and Nuclear Physics*, held in St. Petersburg (Fl., USA) from May 31*st* to June 6*th* and HYP 94, the *International Conference on Hypernuclear and Strange Particle Physics*, held in Vancouver (Canada) from July 4*th* to July 8*th*), the leading items were considered the fine spectroscopy of hypernuclear excited states and, even more, the decay of hypernuclear states and the possible implications with a violation of $\Delta I=1/2$ empirical rule. Moreover, the new initiative on hypernuclear physics that will be proposed at the AGS, and that was discussed rather at length, was a new facility for (K^-,π^0) reaction with $\underline{K^-\text{ at rest}}$. The foreseen energy resolution is less than 1 MeV (FWHM) on hypernuclear final states, with a counting rate of $\sim$ 60 hypernuclear states/hour, produced at a capture rate of 10^{-3}/stopped K^-. It is interesting to note that these are not far from the numbers given by FINUDA for the (K^-,π^-) reaction at $\underline{\mathcal{L} = 10^{32}\ \text{cm}^{-2}\ \text{s}^{-1}}$ i.e. 75 hypernuclear states/hour (already at 10^{-3} production rate). However, FINUDA rates result from opposite experimental situations: for the AGS case the flux of stopped K^- is $2 \times 10^4\ \text{s}^{-1}$ and the solid angle of the spectrometer $\sim$ 20 msr, for FINUDA the flux is two orders of magnitude lower

but the spectrometer's solid angle is two orders of magnitude higher. The reason for which the colleagues of AGS chose to concentrate on the (K^-_{stop},π^0) reaction instead of the (K^-_{stop},π^-) apparently more simple, is that they are able to obtain a high K^- stopping rate by using a very thick target, which worsens badly the resolution for outgoing charged particles, but obviously not that for out going $\pi^0 s$.

The nice conclusion is that the two experiments are fully complementary, and FINUDA has the advantage of profiting hopefully of an increase of luminosity up to a factor 10, which is not the case of AGS.

1.2 Hypernuclear physics

In the FINUDA Proposal several physics topics were presented and discussed in terms of interest and feasibility. In the following we will give a list of priorities, basing our judgment on physics ground, shared by the community of hypernuclear physics.

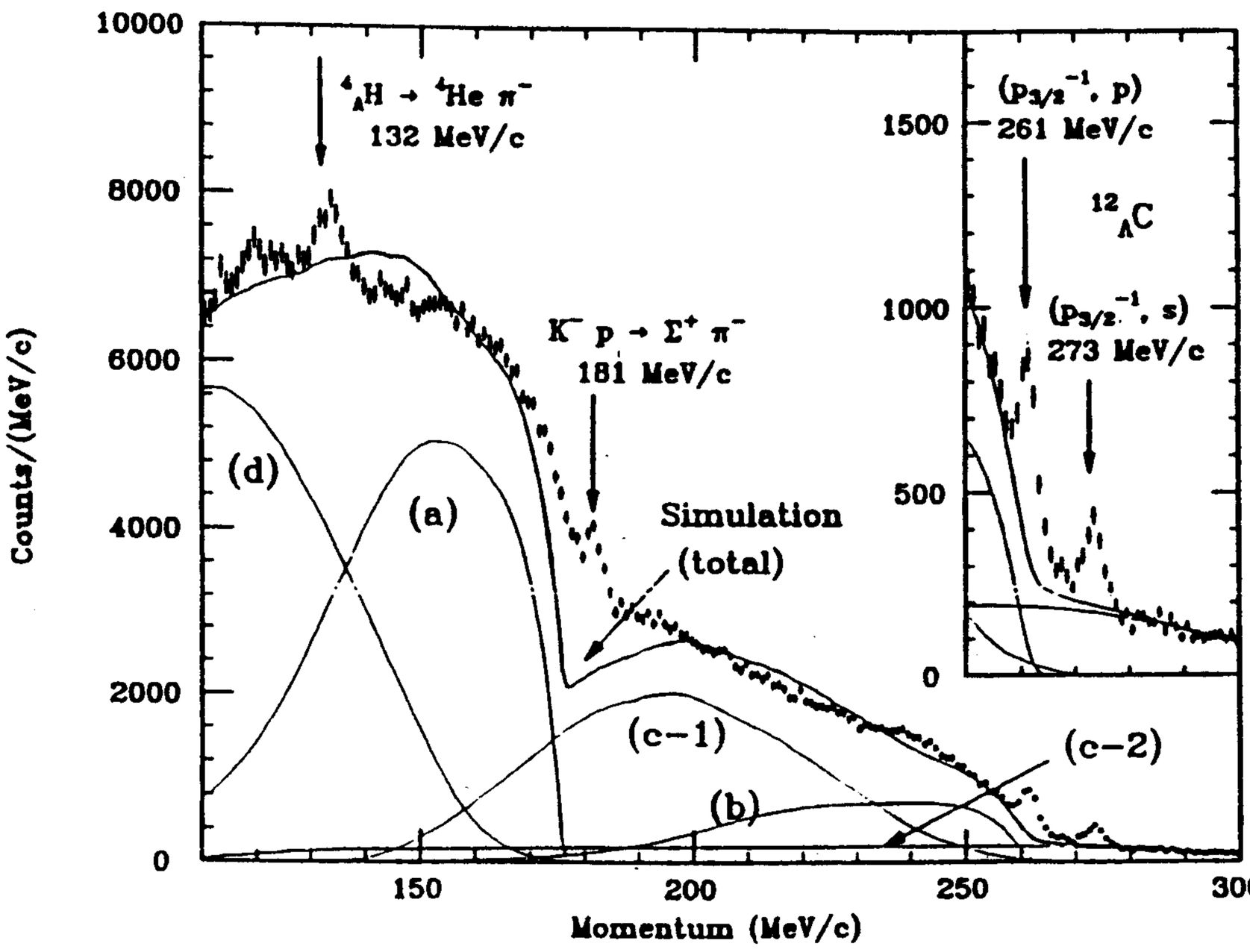

Figure 1.1: π^- spectrum from (stopped K^-, π^-) in $(CH)_n$ reaction measured at KEK.

The spectroscopy of Λ-hypernuclei, with fair energy resolution(< 1 MeV (FWHM) on the hypernuclear final states) extended over the full nuclear mass range, plays

a top priority. Besides the interest for nuclear physics purposes, the intrinsic narrow width of the Λ-hypernuclei bound states affords promising opportunities for the investigation of the hyperon-nucleon interaction. Recently, the hyperon-nucleon interaction has been theoretically investigated with meson-exchange and quark models. The spectroscopic data of hypernuclei can be used to impose strong constraints on the framework of the $\Lambda - \mathcal{N}$ interaction. In this regard, high-quality spectroscopy with good energy resolution is greatly needed. Fig. 1.1 presents the π^- spectrum from (stopped K^-,π^-) reaction in $(CH)_n$ measured at KEK [1], with an energy resolution of $\sim$ 3 MeV (FWHM). Fig.1.2 shows a very recent excitation spectrum of the ${}^{12}_{\Lambda}C$ hypernucleus observed with the (π^+,K^+) reaction in flight [2] with an energy resolution of 2 MeV (FWHM). Two small peaks at $\sim$ 2.6 MeV and 6.8 MeV excitation energy appear. The machine time necessary to produce such a spectrum is not declared, but in some way it can be evaluated from the experimental information given in the preprint. We can argue that it was obtained in at least one week of data taking. With FINUDA we would obtain a spectrum of the same statistical quality in a day at $\mathcal{L} = 10^{32}$ cm^{-2} s^{-1}, in a few hours at $\mathcal{L} = 10^{33}$ cm^{-2} s^{-1}, with a resolution of less than 1 MeV.

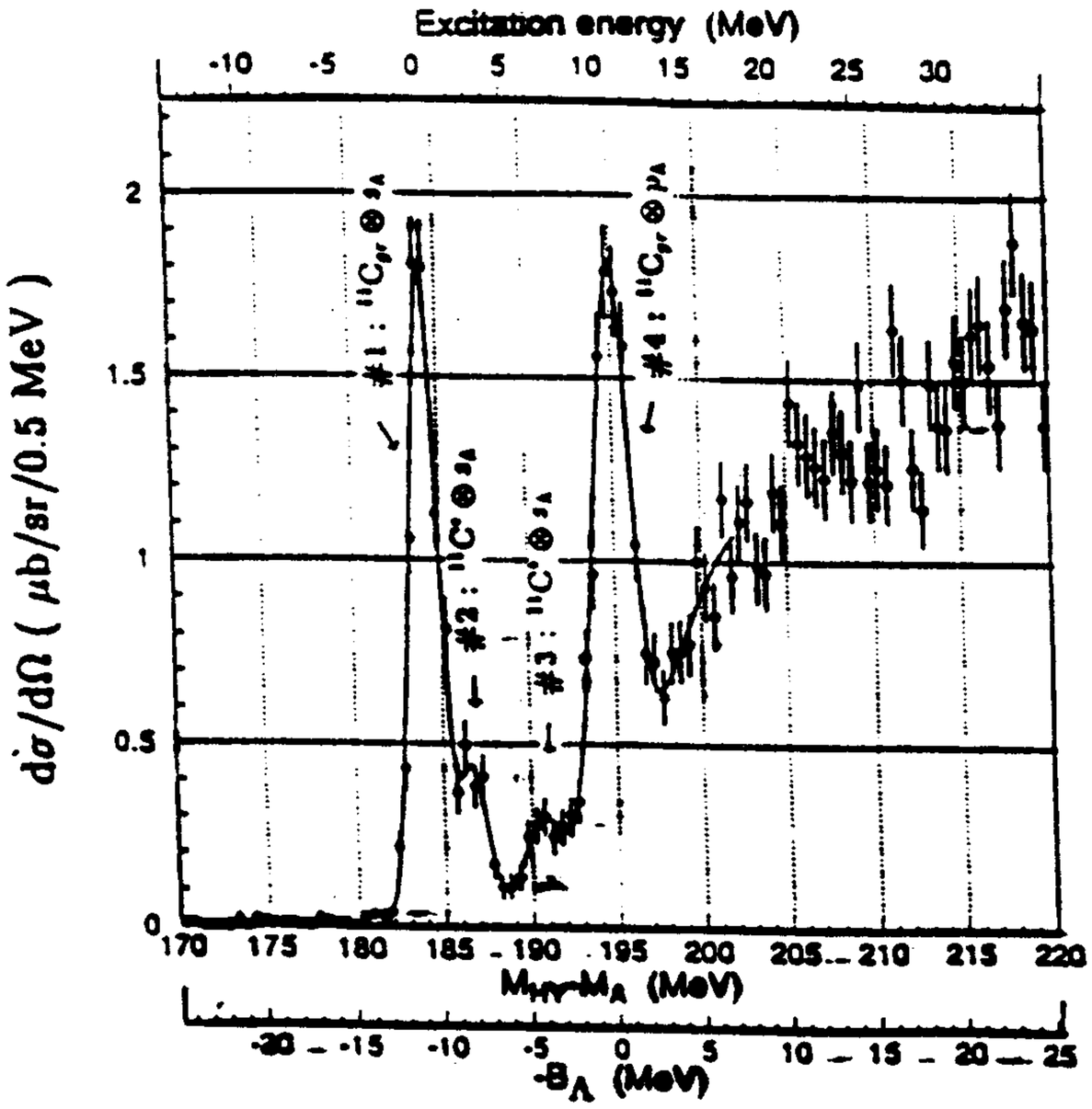

Figure 1.2: Excitation spectrum of ${}^{12}_{\Lambda}C$

The decay of hypernuclei, in particular the study of the non-mesonic ones, leading to (n,n) and (n,p) correlated pairs in the final state, is certainly the "battle horse" of FINUDA, both by physics interest and experimental feasibility. The in-

teresting possibility [3] that the well-known ΔI=1/2 rule might be strongly violated in non-mesonic decay, suggested by the analysis of some decay channels of *s*-shell hypernuclei ($^{4}_{\Lambda}$H, $^{4}_{\Lambda}$He and $^{5}_{\Lambda}$He), spurred a great deal of theoretical interest. Unfortunately no new experimental information was produced in the meantime, due to the extreme difficulty of the measurement. Even the (K^{-}_{stop}, π^{0}) facility at AGS, if approved, could hardly be competitive with FINUDA. Since a massive stopping target will be used, inevitably the measurement of $\sim$ 80 MeV protons would be badly affected by multiple scattering and absorption effects. On the contrary, the very transparent structure of FINUDA is ideal for the study of non-mesonic decay.

Relationship with a possible violation of the $\Delta I = 1/2$ rule may be inferred in two ways, by inclusive or exclusive measurements. In inclusive measurements the relative number of correlated (n,p) and (n,n) pairs will be measured in coincidence with the ground state of a given hypernucleus. It is worthwhile to remind that the decay of an hypernucleus occurs always from the ground state, due to the different lifetimes for weak decays and electromagnetic ones (a part a few cases of metastable states). However, it is known that some excited states of an hypernucleus $^{A}_{\Lambda}X_{Z}$ are essentially due to a configuration of $[^{A-1}_{\Lambda}X_{Z(-1)} + \mathcal{N}]$. In this case we would observe non-mesonic decays which, experimentally, are attributed to an "excited" state of the hypernucleus $^{A}_{\Lambda}X_{Z}$, but in reality belong to an hypernucleus of lower mass. Incidentally, it is a good method to measure with one nuclear target the decay properties of two or sometimes more hypernuclei. The feasibility of this approach, with a very low statistics, was already demonstrated a few years ago [4].

The comparison of inclusive measurement with different theoretical models needs an averaging of the initial states of the $\Lambda\mathcal{N} \rightarrow \mathcal{N}\mathcal{N}$ interaction, and is significative when applied to several hypernuclei of different A. For an exclusive measurement, in which also the final state of the nucleus resulting from the decay is measured, the result may be compared directly with the prediction of the $\Delta I = 1/2$ rule.

Such a task could be performed only if a very precise measurement of the energy of neutrons ($\sim$ 1 MeV) would be possible. Unfortunately this is out of the technical possibilities of a realistic apparatus. However, in the case of one nuclear target we could perform an exclusive measurement. If we consider the following chains of production and decay processes for a ^{6}Li target (the squares indicate the decaying hypernucleus):

$$K^{-} + {}^{6}Li \rightarrow \pi^{-} + \boxed{{}^{6}_{\Lambda}\mathrm{Li}} \rightarrow p + \boxed{{}^{5}_{\Lambda}\mathrm{He}} \rightarrow {}^{3}H + n + p \qquad (1.1)$$

$$K^{-} + {}^{6}Li \rightarrow \pi^{-} + \boxed{{}^{6}_{\Lambda}Li} \rightarrow p + \boxed{{}^{5}_{\Lambda}He} \rightarrow {}^{3}He + n + n \qquad (1.2)$$

$$K^{-} + {}^{6}Li \rightarrow \pi^{0} + \boxed{{}^{6}_{\Lambda}He} \longrightarrow {}^{4}H + n + p \qquad (1.3)$$

$$K^{-} + {}^{6}Li \rightarrow \pi^{0} + \boxed{{}^{6}_{\Lambda}He} \longrightarrow {}^{4}He + n + n \qquad (1.4)$$

we can see that process (1.4) leaves ^{4}He as residual nucleus, and we can profit from its large particle emission threshold (19.8 MeV) to isolate the exclusive processes. π^{0}

is not detected, but we have to take into account the circumstance that a weak decay of an hypernucleus always occurs from the ground state, and that the slowing down time of ${}^{6}_{\Lambda}$He following its formation is much lower than its lifetime. In processes (1.1) and (1.2) the hypernucleus decaying non–mesonically is ${}^{5}_{\Lambda}$He, from the fast decay ${}^{6}_{\Lambda}$Li (particle instable) $\rightarrow p+{}^{5}_{\Lambda}$He. The instrumental resolution for neutrons (10 MeV) is not enough to fully isolate the last exclusive decay. However, with a good statistics, folding techniques may allow a rather sound determination also of this exclusive process. Taking into account that the wave functions of ${}^{3}H$ and ${}^{4}H$ are quite well known from nuclear physics, the radio of the two exclusive processes (1.1) and (1.4) could be related by a simple relationship to the isospin amplitude of the weak interaction.

Continuing in the list of physics items, the existence of Σ–hypernuclei in terms of narrow discrete states seems more and more questioned. Following first claims, all the recent measurements did not find evidence for such states, the only surviving being ${}^{4}_{\Sigma}$He. However, even for this case, experimentally observed as a bump in the π^- spectrum following K^- capture at rest, alternative explanations due to a cusp effect at threshold for $K^-\mathcal{N} \rightarrow \Sigma\pi$ were put forward. It seems then not very fruitful to devote a strong dedicated effort to this subject, but perhaps try to obtain as more information as possible in a subsidiary way to the main two physics issues.

Also the indirect production of hypernuclei from compound processes, signalled in particular by mono-kinetic pions coming from specific two-body decays, like ${}^{4}_{\Lambda}\mathrm{H} \rightarrow {}^{4}\mathrm{He} + \pi^-$, seems to be an argument of minor importance, welcome if obtained in a subsidiary way, but not such to justify a dedicated effort.

1.3 Counting rates and needed resolution

We discuss here only the counting rates relevant to the hypernuclei production and decay, postponing the trigger efficiencies and background rejection to the dedicated paragraph 9.3. The unambiguous detection of a pion peak corresponding to the formation of an hypernuclear states at a given rate depends obviously on:

1) the final energy resolution
2) the background beneath the peak
3) the statistics

Obviously, the statistics is related to the capture rate and the machine luminosity, and decision on it can be taken only following physics considerations, whereas points 1) and 2) can be discussed in a general way. As previously said, Fig.1.1 shows the best experimental example, up to now, of a momentum spectrum of π^- emitted following the stopping of K^- in a (CH)n target. There is a large continuum, due to physical processes, like Λ and Σ formation on quasi-free nucleons, rather well described with known elementary cross-sections and by the broadening due to the Fermi momentum of the nucleons in a nucleus. Superimposed on it we expect peaks:

from $\sim$ 250 to $\sim$ 290 MeV/c (depending on the mass of the target nucleus), due to prompt pions coming from formation of bound hypernuclear states; from $\sim$ 160 to 200 MeV/c due, perhaps, to possible bound, narrow, Σ-hypernuclei formation and around 120-130 MeV/c due to mesonic two-body decays of light Λ-hypernuclei (indirect production).

The maximum resolution is certainly needed around 250-290 MeV/c, and all the tracking and triggering strategy of the FINUDA apparatus has been optimized to this purpose, that represents the main physical goal of the experiment.

Anticipating the results of Chap. 8, we may expect an energy resolution for final hypernuclear states of $\sim$ 0.7 MeV (FWHM), that is a factor $\sim$ 4 better than the KEK experiment. We expect $\sim$ 75 ev./hour for an hypernuclear state produced at a rate of $10^{-3}/K^-_{stop}$ at $\mathcal{L} = 10^{32}$ cm^{-2} s^{-1}. The spectrum of Fig.1.1 has a signal/background ratio of $\sim$ 1:1. Due to our better energy resolution we expect a ratio of 4:1.

Let us calculate in this situation, i.e. with a signal/background ratio of 4:1 at $10^{-3}/K^-_{stop}$, the machine time, at $\mathcal{L} = 10^{32}$ cm^{-2} s^{-1}, necessary in order to get a statistical precision of 10%, for different production rates of hypernuclear states. It is shown in the first row of Tab. 1.1. It appears that detection of states produced with rates up to 10^{-4} is rather easy, but becomes unrealistic at 10^{-5}.

Table 1.1: Machine time (in hours) for production of hypernuclear states at the given % statistical precision

Production rate	*10^{-3} 10% st.*	*10^{-4} 10% st.*	*10^{-5} 10% st.*	*10^{-5} 20% st.*
S/B=4/1 at 10^{-3}	2.45	96	8000	2000
S/B=8/1 at 10^{-3}	1.8	56	4000	1000
S/B=12/1 at 10^{-3}	1.5	40	2300	575

But the assumption of a signal/background ratio of 4:1 for a state produced at 10^{-3} is pessimistic. We see from Fig.1.1 that there is a flat background extending beyond the kinematical limit for prompt π^- emission from hypernuclei production. It is due to the Σ^- decay. Since the π^- momentum of the Σ^- decay at rest ($\Sigma^- \rightarrow n\pi^-$) is only 193 MeV/c, the background around 260 MeV/c is due to the in-flight decay of high energy $\Sigma^- s$. Such $\Sigma^- s$ are produced in K^- absorption by two nucleons without emission of a pion, $K^- + (pn) \rightarrow p\ \Sigma^-$, where high energy ($>$ 50 MeV) protons are emitted. As shown by Tamura et al. [5], the high energy proton is emitted in the opposite direction of that of the background π^-. Then, by requiring an angular correlation among π^- and p, it is possible to eliminate a considerable part of the flat continuum background. This technique was not applied to the KEK experiment, probably due to the necessary use of thick stopping targets that inevitably stopped even the correlated protons.

Due again to our use of thin targets at DAΦNE we may expect to take advantage quite efficiently of this technique. A numerical estimation of the reduction of the background by this technique is not easy, in lack of any experimental information

about the physical quantities involved (skewness of the angular correlation, etc.) but we guess that a reduction factor of at least 2 in the background is realistic. In this case the necessary machine time for different capture rates is reported in row 2 of Tab. 1.1. It appears that detection of states produced at 10^{-5} becomes possible with a statistical precision of 20 %.

If we inject some optimism in our experimental and technical capabilities, and we suppose to have a signal/background ratio of 12:1 at 10^{-3}, the capture rate of 10^{-5} will be easily accessible to the experiment.

The conclusion of this discussion is that in any case, the hypernuclear information obtained by DAΦNE, even from the simple spectroscopic aspect, would be superior to that from any existing or approved facility.

No problems of background are expected for the study of non-mesonic decays. For this case the requirement of a correlated (n,p) or (n,n) pair emitted in coincidence with a well defined peak eliminates all the physical backgrounds (a part the instrumental ones, quite negligible). Rates of (n,p) pairs will be ~ 6/hour and those of (n,n) pairs ~ 1/hour, by assuming a neutron detection efficiency of $\sim 15\%$.

As it will be seen in the following, the optimization of the apparatus for the realization of the above discussed physics items, as well as the necessity of operating with a constant field of 1.1 T, introduces a cut on the momentum spectrum of π^-, just is the region of the possible production of Σ hypernuclei.

However, we may get some information even in the region of low-momentum pions by the following technique. The K^+ is also always stopping in the nuclear target. The $K_{\mu 2}$ decay (63.5%) and $K_{\pi 2}$ decay (21.1%) produce monochromatic lines at 236 and 205 MeV/c, respectively, very useful for the general, on-line, continuous calibration of the spectrometer (see Chap. 4). The rate of these calibration events written on tape with respect to that due to the true events can be adjusted in order to not saturate the DAQ system by eventually pre-scaling them. These calibration events are related to a K^- stopping in the target, that produces the "standard" π^- spectrum of Fig.1.1. Negative pions of momenta lower than $\sim$ 180 MeV/c at 1.1 T spiralize in the spectrometer and do not produce tracks of very good quality for reconstruction and pattern recognition. However we may guess that the momentum resolution for these low-momenta π^- will be less than 1% (FWHM). By assuming that we obtain $\sim$ 50 calibration events/s and assuming that the probability of detecting a π^- of less than 180 MeV/c associated to a calibration event is 10^{-2}, we would collect $\sim 4 \times 10^4$ ev/day in the full inclusive spectrum from $\sim$ 80 to $\sim$ 180 MeV/c. A reasonable statistics of these minimum bias events could then be collected in a fully parasitic way and indicate whether some unexpected structure appears. In this hypothesis, a dedicated second level trigger could be envisaged at a second stage.

1.4 Milestones of the hypernuclear physics program

They can be summarized as follows:

1) Reproduction of the ${}^{12}_{\Lambda}$C excitation spectrum with energy resolution < 1 MeV; detection of states produced at 10^{-4} with a statistical precision of 10%; detection of (n,p) and (n,n) correlated events; measurement of the lifetime. This experiment can be considered as a more accurate and statistically rich re-measurement of the properties of ${}^{12}_{\Lambda}$C , the hypernucleus which was the most extensively studied with counter techniques.

2) High statistics study of the ${}^{6}_{\Lambda}$Li production, decay and lifetime, and possibly the same for ${}^{6}_{\Lambda}$He, with the same ^{6}Li nuclear target, with the aim of obtaining a first answer on the possible violation of the ΔI=1/2 rule in an exclusive measurement.

3) High statistics study of the production, decay and lifetime of the p-shell hypernuclei ${}^{7}_{\Lambda}Li$, ${}^{9}_{\Lambda}Be$, ${}^{10}_{\Lambda}B$.

4) High statistics survey of the production of hypernuclei of higher mass. Targets of ^{27}Al, ^{51}V, ^{59}Co, ^{89}Y, ^{133}Cs, ^{165}Ho, ^{181}Ta and ^{209}Bi could be used in a first round measurement.

5) Following results from 4), more statistics in those cases that will appear of particular interest, and extension to other nuclear targets included in the list of the Proposal.

For all the targets, survey of the low-momenta π^- spectra will be obtained in the parasitic way described above. For high statistics we mean the achievement of $\sim 5 \times 10^2$ events in the (n,n) decay channel.

1.5 Expected running sequence for the first year

We plan to start with the two targets of ^{6}Li and ^{12}C and to run for about three months at the initial luminosity of DAΦNE. Setting-up and commissioning of the apparatus is comprised in this time.

The second block of targets will be ^{7}Li, ^{9}Be and ^{10}B, again for a running time of about three months.

For the remaining 8 targets of heavier mass, we may choose or a single long run of 4-5 months with the 8 different targets in place or two runs of half duration with 4 targets each time. Detailed decision will depend on the running conditions of the machine and of KLOE.

All these measurements will be performed with a constant field of 1.1 T in the solenoid.

Bibliography

[1] R.S. Mayano and T. Yamazaki, in Perspectives of Meson Science (eds. T. Yamazaki, K. Nakoi and K. Nagamine), North-Holland (Amsterdam, 1992) p. 493.

[2] T. Hasegava et al. Preprint INS-Rep.1037 (Institute for Nuclear Study, Tokyo), July 1994.

[3] R.A. Schumacher, Nucl. Phys. **A 547** (1992) 143c.

[4] J.J. Szymansky et al. Phys. Rev. **C 43** (1991) 849.

[5] H. Tamura et al., Phys. Lett. **B 160** (1985) 32.

Chapter 2

THE FINUDA DETECTOR DESIGN

2.1 Introduction

FINUDA is a non focusing magnetic spectrometer with cylindrical geometry. We based our design criteria on reasonable extrapolations of performances of present technology, optimized in order to have a large solid angle, the best momentum resolution and good trigger capabilities.

Fig. 2.1 gives a general view of the proposed detector, which consists of the following parts:

1) an interaction/target region;

2) an external tracking system;

3) an outer scintillator array.

The full apparatus is immersed into a solenoidal field, rather homogeneous over the volume used for the tracking of the charged particles. In the following, we will assume a coordinate frame with the z-axis oriented along the (e^+, e^-) colliding beams direction, and oriented towards the e^+ beam, and the y-axis oriented perpendicularly to the floor. However, we will often refer to cylindrical (ρ, ϕ, z) coordinates. The (K^+, K^-) pairs used for physics are emitted from the interaction region, whose dimensions are assumed to be $\sigma_x = 2$ mm in the x direction and $\sigma_y = 0.02$ mm in the y one; along z, we assume a bunch-crossing region having a σ of 3 cm. We assume, furthermore, at the maximum design luminosity $\mathcal{L} = 10^{33}$ cm^{-2} s^{-1}, a bunch crossing frequency of 380 MHz, with an inter-bunch time of 2.6 ns. The (K^+, K^-) from ϕ decay follow a $sin^2\vartheta$ law, ϑ being the angle relative to the z-axis.

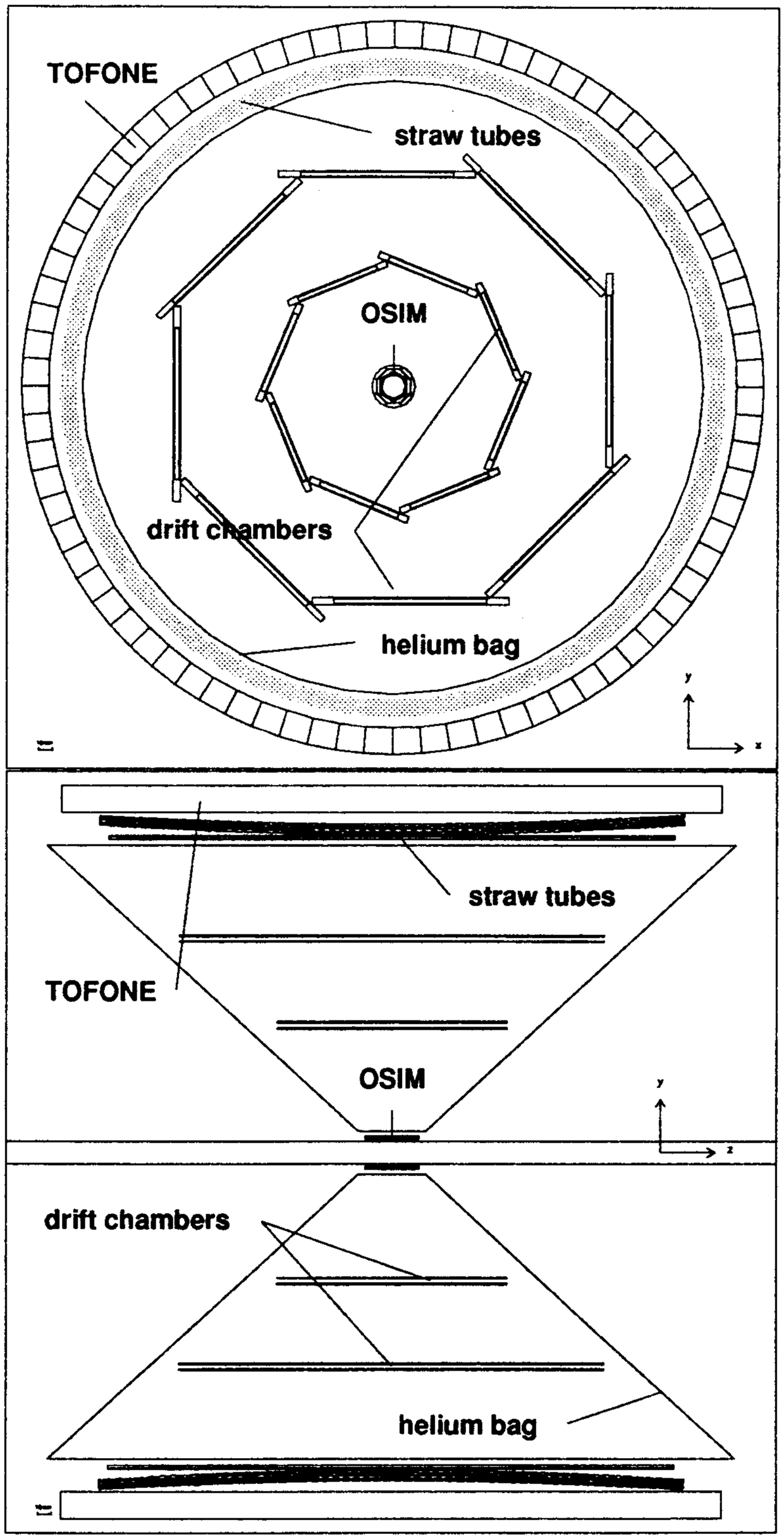

Figure 2.1: General view of the FINUDA detector.

2.2 The interaction/target region

The cylindrical interaction/target region of FINUDA consists of the beam pipe, a scintillator barrel (TOFINO), an internal octagonal Si microstrip array (ISIM) and the internal nuclear stopping target. Fig. 2.2 shows the two views of the proposed arrangement. For completeness we have also indicated the external (outer) decagonal Si microstrip array (OSIM) that, however, is a part of the external tracking system. The above arrangement must accomplish the following tasks:

1) the (K^+, K^-) pairs from ϕ decay have to be identified in a time fast enough to contribute to first level trigger;
2) the (K^+, K^-) coordinates before the nuclear target have to be measured;
3) the monochromatic K^- has to be stopped as near as possible to the external surface of the target.

Since the K^- from ϕ decay have an energy of 16.1 MeV, they cross, before stopping, a very reduced amount of material (e.g. 0.5 g cm^{-2} of ^{12}C). This fact represents the unique feature of DAΦNE, that will allow hypernuclear spectroscopy with unprecedented resolution, but it requires the design of very thin detectors before the nuclear target.

The fast scintillators are used for first level trigger allowing a topology selection of back to back events (K^+, K^- from ϕ decay at rest), a multiplicity information and ΔE/Δx measurement.

The position information from ISIM obtained with a σ of a few tens of microns will allow the reconstruction of the (K^+, K^-) trajectories (we will refer to the rms deviation for the accuracy on the localization, whereas for energy and momentum spectra we will quote the FWHM.) This information, together with the measurement, in the external tracking system, of the trajectory of π^- emitted in the hypernuclear formation reaction, will allow the determination of the position of the stopping point of the K^- inside the thin target. The thicknesses needed for the inner detectors are determined by the requirement of stopping the K^- inside a target of thickness as close as possible to the diffuseness for the range due to its energy straggling, taking into account also the K^- angular distribution.

The proposed thicknesses are the following: 400 μm of Beryllium for the beam pipe, 2.0 mm for the scintillators of TOFINO, 300 μm for ISIM and finally about 1.5 mm for a Carbon stopping target. In these conditions K^- emitted from 45° to 135° stop in the target volume.

The length of the interaction/target region is determined by the requirement of accepting all the (K^+, K^-) pairs emitted from 45° to 135° along z coordinate from -3.5 cm to $+3.5$ cm, which corresponds to the FWHM of the (e^+, e^-) interaction region. The resulting length of the stopping target will be 17 cm and will allow an acceptance for (K^+, K^-) of more than 90%.

The ISIM will provide information on the trajectory of the (K^+, K^-), and the intersection of this trajectory with that of the π^- measured by the external tracking

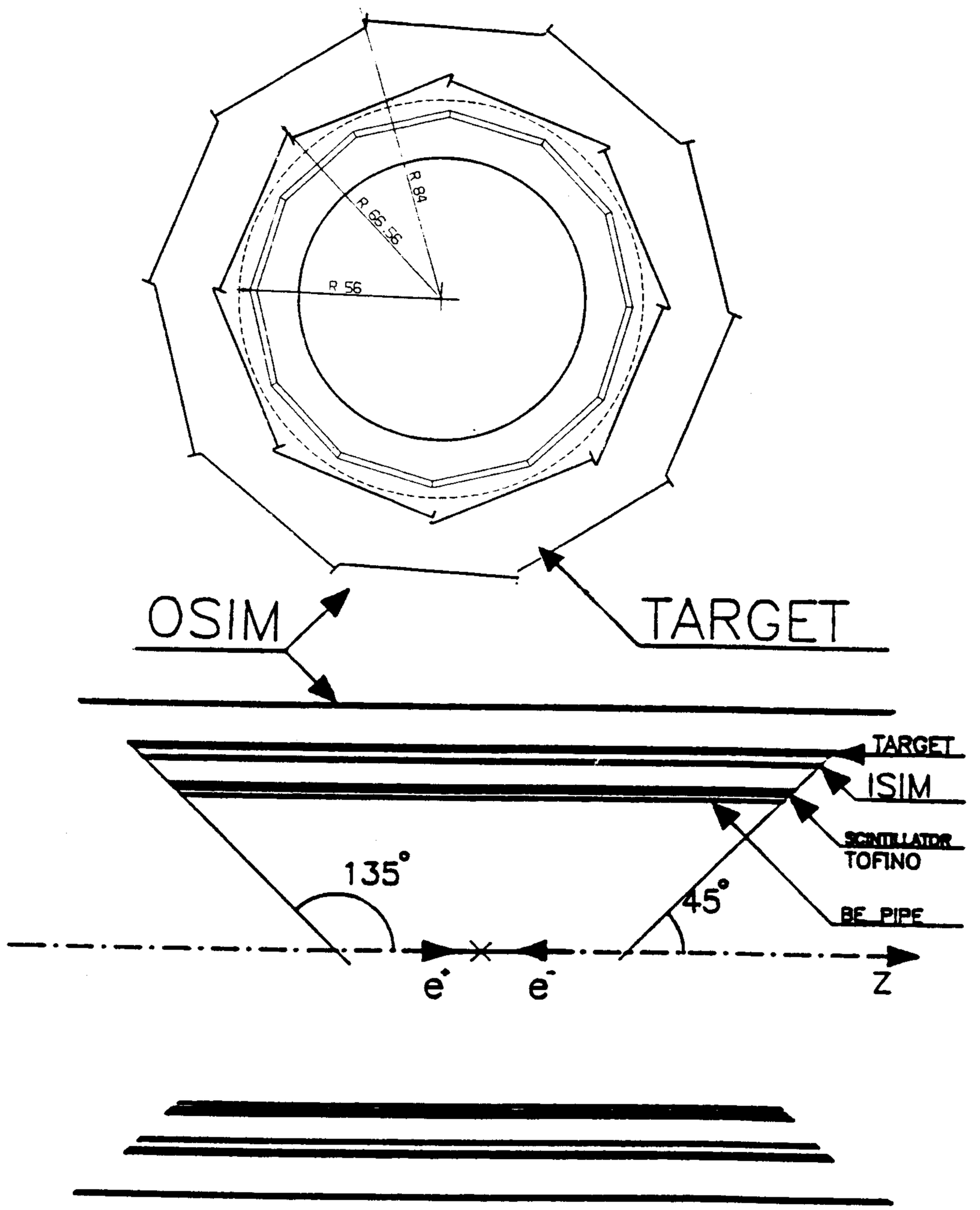

Figure 2.2: The two views of the proposed target/interaction region.

system will give a reliable estimation of the point of formation of the hypernucleus inside the target thickness. The measured momenta of the emitted charged particles could then be corrected also for the energy lost in the already thin target obtaining a further improvement in the momentum resolution.

2.3 The outer tracking system

The performance of the external tracking system is the most crucial since it will allow the measurement of the momenta of π^- emitted from the formation reaction:

$$K^-_{stop} + {}^{A}X_Z \rightarrow {}^{A}_{\Lambda}X_Z + \pi^- \tag{2.1}$$

The momentum resolution enters directly into the determination of the hypernuclear energy levels. It is straightforward to see that, with M_H, M_A, M_π, M_K denoting the masses of the hypernucleus, target nucleus, π^- and K^-, the hypernuclear mass is given by:

$$M_H = M_A + M_K - M_\pi - T_\pi \tag{2.2}$$

neglecting the hypernucleus recoil energy. Then $\Delta M_H = \Delta T_\pi$ and

$$\frac{\Delta T_\pi}{T_\pi} = \frac{\sqrt{p_\pi^2 + m_\pi^2} + m_\pi}{\sqrt{p_\pi^2 + m_\pi^2}} \frac{\Delta p_\pi}{p_\pi} = f(p_\pi) \frac{\Delta p_\pi}{p_\pi} \tag{2.3}$$

The function $f(p_\pi)$ depends obviously on the hypernuclear final state, but in a rather smooth way. Taking as typical ${}^{12}_{\Lambda}C$ in the ground state from a target of ${}^{12}C$, we obtain for (2.1) $p_\pi = 272$ MeV/c, $T_\pi = 166.2$ MeV, and then, for this state $f(p_\pi)$ is 1.4. We may assume this value of $f(p_\pi)$ as a typical one. From (2.3) it is clear that each 10^{-3} in $\Delta p/p$ corresponds to 236 KeV in the energy resolution for the hypernuclear levels.

The minimum information required for the reconstruction of a charged particle trajectory in an almost uniform magnetic field is represented by three points along its path. Factors affecting the momentum resolution are the multiple scattering due to materials along the particle path and the spatial resolution in the determination of the measured points.

The solution we have chosen is that of high spatial resolution low mass detectors immersed in a helium atmosphere to minimize multiple scattering.

The requirement of low mass is particularly stringent on the detectors located along the particle trajectory and can be partially released for the detectors measuring the initial and final point of the tracks

To better face the pattern recognition problem we decided furthermore to measure four points for each track.

The first point on the track is given with accuracies of the order of less than 30 μm by the OSIM array, which is the first track localizing device that the particle

encounters. The last point is given with an accuracy of $\sim$ 100 μm in the (ρ, φ) plane and better than 500 μm in zeta coordinate by an array of straw tubes (ST). The substantial advantage of using ST for the measurement of the last point is that the spatial resolution is independent of the incidence angle of the track.

Two internal points are measured by low mass drift chambers (LMDC) providing a resolution of 100 μm in the (ρ, φ) plane and a much more coarse resolution (1% of the wire length) in the zeta coordinate, obtained by charge division.

Taking into account the minimum amount of materials for these chambers, as described in Chap. 4 and the quoted spatial resolutions, Monte Carlo simulations give a momentum resolution of about 0.25% FWHM for pions of 270 MeV/c.

2.4 Scintillator arrays

The internal scintillator array (TOFINO) has been fixed as being composed of 12 strips, 2.0 mm thick, 14 cm long, 2.5 cm wide each, sub-tending a $\Delta\varphi$ of 30°. The strips will be arranged following a circumference of radius 4.5 cm. We remind that the radius of the Beryllium beam pipe in the interaction region has been agreed with the machine to be 4.3 cm (internal radius), with a thickness of 400 μm. We left further 1 cm from the pipe to TOFINO for mechanical alignement of the beam pipe, cooling or other unforeseen needs of the machine.

In the proposal we intended to use P.M.s to collect the light from the scintillators though $\sim$ 2 m long light guides. Preliminary tests have shown that this arrangement was acceptable concerning the requirement of light collection and timing. However, in the design of the mechanical arrangement of the interaction region, we noticed that the presence of these long light guides caused severe problems of matching with the other detectors. For this reason we decided to discard the solution of the P.M.s outside the field and take instead advantage of the very new development of Hybrid Photo Multiplier Tubes (HPMT), that may operate inside the 1.1 T magnetic field, are of very reduced dimensions and simplify considerably the mechanical problems. More details are given in the dedicated Chap. 5. The outer scintillator array (TOFONE) has been fixed as being composed of 72 slabs of plastic scintillator having a cross section shaped as an isosceles trapezium with 11.6 and 10.7 cm bases and 10 cm height. This shape evolves at each end of the slab to a rectangular cross section with a 9.7 cm base and a 10 cm height, to couple in a simpler way with the lucite light guides and to allow for almost 1 cm free space between each couple of slabs near their ends, in the final mounting where they are adjoining along most of their length.

The smaller number of slabs with respect to 80, as assumed in the original proposal, is a useful compromise between angle definition and z-coordinate overall resolution at the different impinging angles of the detected particles. It furthermore allows a 10% reduction of the connected electronics and H.V. channels.

The internal radius of the cylindrical array of scintillator slabs has been fixed at

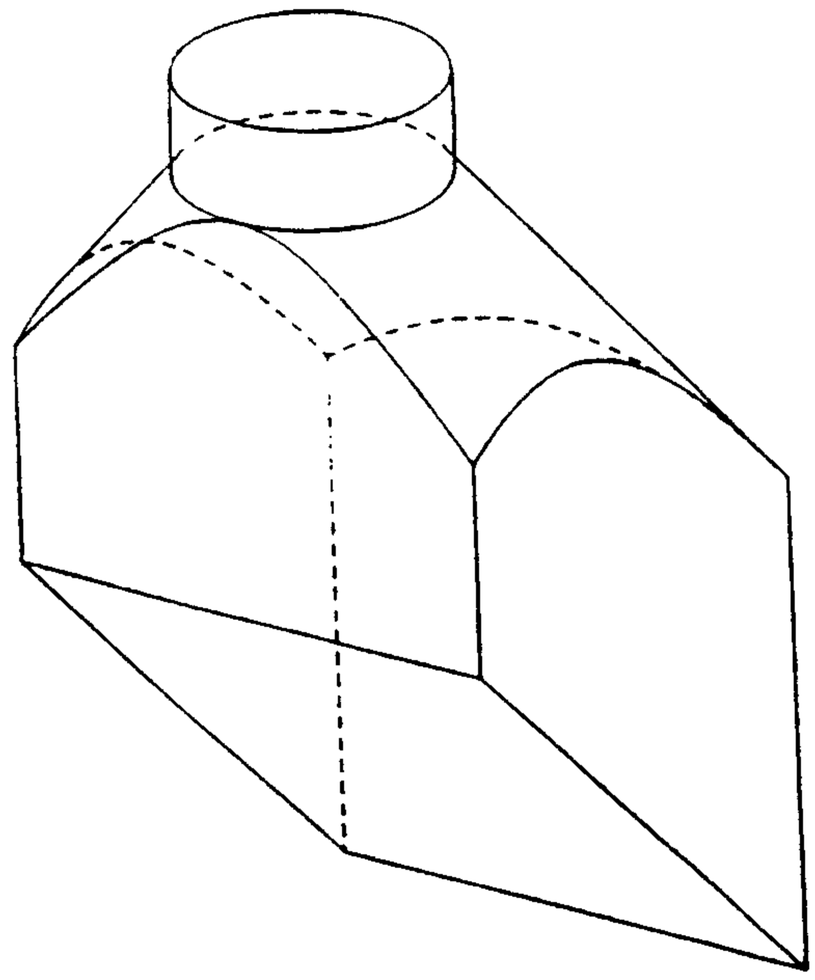

Figure 2.3: Mechanical drawing of a single lucite block with a 90^0 deflector prism and a conical connector to a straight cylindrical light guide.

127 cm, so providing considerably larger space, with respect to the previous value of 109 cm, for locating the straw tubes.

The slab length has been increased to the present value of 255 cm, 25% longer than the initial guess, to reach the edge of the cryostat and take advantage of prismatic light reflectors towards radial directions. The increased solid angle will allow a higher neutron detection efficiency, a goal which is to be pursued also by the neutron detecting scintillators possibly mounted on the inner sides of the solenoid end caps, for which a final decision will be taken only following the executive mechanical plan.

In the center of the 11.6 cm wide face of the scintillators a 2 mm diameter optical fiber will be glued, with the aid of a very small lucite deflector prism, to convey into the scintillator the laser light pulses for timing and the amplitude calibrated light pulses to be used for amplitude response calibration of the photomultipliers.

The scintillation light will be directed out of the magnet with light guides passing through slots, in order to employ phototubes suitable for low magnetic field environments (less than 100 Gauss, as foreseen by the calculations for the regions out of the slots). This choice will prevent any field dependence of the tube gain, minimizing the setting up time required.

The scintillation light bending through 90^0 from axial to radial directions will be accomplished by lucite deflector prisms, which have proved to transmit an optimum amount of the collected light. The prisms will be surmounted by lucite conical connections to the straight cylindrical bars directed out of the magnet. Prisms and conical connections will be manufactured all together as in fig. 2.3. An overall view of one of the TOFONE slabs with complete light guides and phototube housings is obtained from fig. 2.4.

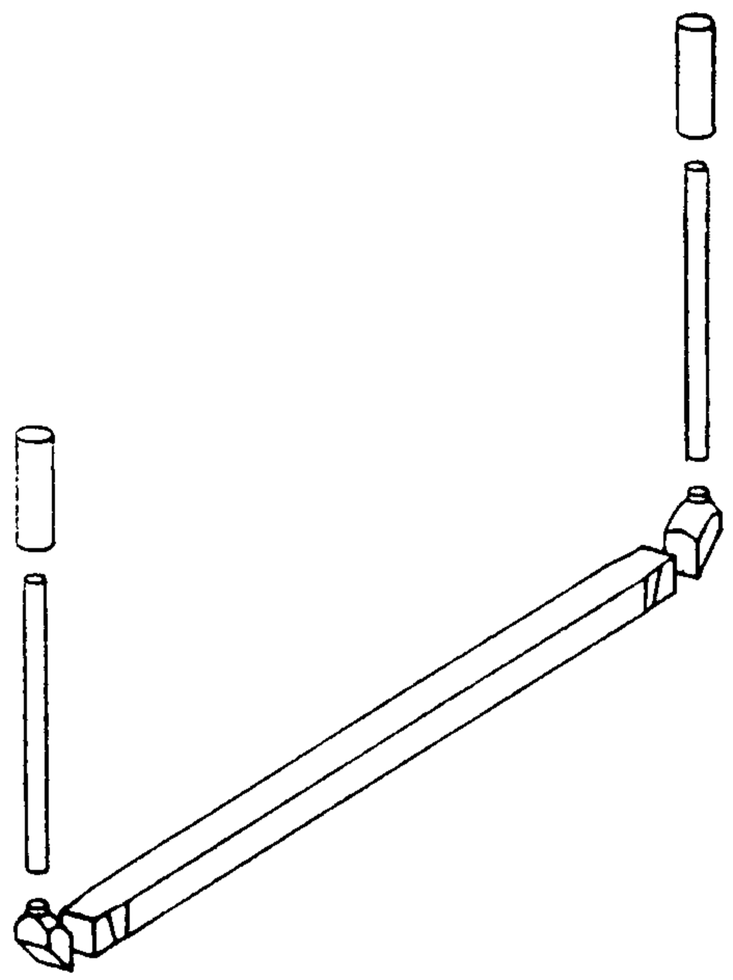

Figure 2.4: Overall view of the constituent parts of one of the 72 elements of TOFONE. It is possible to see the scintillator slab, two assemblies of 90^0 deflector prisms plus conical connectors, two straight cylindrical light guides and two photomultiplier housings.

The scintillation light transmitted out of the magnet will be collected by Philips XP2020 phototubes or similar ones for optimum timing resolution. For the best timing performance these tubes will be driven at high voltages compatible with anode current pulse saturation for almost all detected particle, while the linear pulses for amplitude spectroscopy will be picked up from the last dynode.

Chapter 3

THE FINUDA MAGNET AND DETECTOR MECHANICS

The FINUDA spectrometer has to provide a momentum resolution on the negative pions emitted during hypernuclei formation of the order of 0.2% FWHM. Extensive simulation work performed using Monte Carlo programs has shown that a magnetic field of value higher that 1 Tesla is needed. The foreseen dimensions of the spectrometer, on the other side, are: length $\sim 2m$, radius $\sim 1m$. A conventional warm magnet achieving such a magnetic field in the mentioned volume would lead to an electrical power consumption ($> 2MW$) clearly unmanageable. For this reason, a superconducting solenoid has been considered, and its project is illustrated in the following paragraphs. It will be supplied by ANSALDO, Genova.

3.1 The iron yoke

The FINUDA magnet is a superconducting solenoid with an internal magnetic field of $B_{max} = 1.1$ T, whose magnetic axis coincides with the beam direction (z axis). In the inner volume of the solenoid is contained the so called "tracking volume", which corresponds to the volume generated by the rotation of an isosceles trapezium, with bases of ~ 20 cm and ~ 180 cm and height of ~ 120 cm.

In Table 3.1, the basic parameters of the solenoid are given.

[f], L. Celano

In figure 3.1 the two views (front and side) of the iron yoke are shown.

As it can be seen, the yoke has an octagonal prism shape, and is made of iron; it completely surrounds the tracking volume and provides the flux return path for the solenoid magnetic field. At both extremities of the octagonal yoke, symmetrically around the magnetic axis, 72 slots, of rectangular shape, with dimensions 60 x 120 mm^2 (the longest side along the beam axis), will be made, to allow the passage of the light guides of the external scintillator barrel and of the cables and gas tubes of

Table 3.1: Basic parameters of the FINUDA magnet.

Parameter	value
Field value	1.1 Tesla
Total physical length	380 cm
Total height	420 cm
Cryostat inner radius	1385 mm
Cryostat outside radius	1700 mm
Total N. of turns	764
Operating current	2796 A
Current rise time	19 min
Inductance with iron	1.997 H
Inductance without iron	1.419 H
NI	$2.124 \cdot 10^6$ Ampereturns
Field integral	2.67 Tesla· meter
Weight of iron yoke	230 ton
Weight of cryostat and coil	7.7 ton

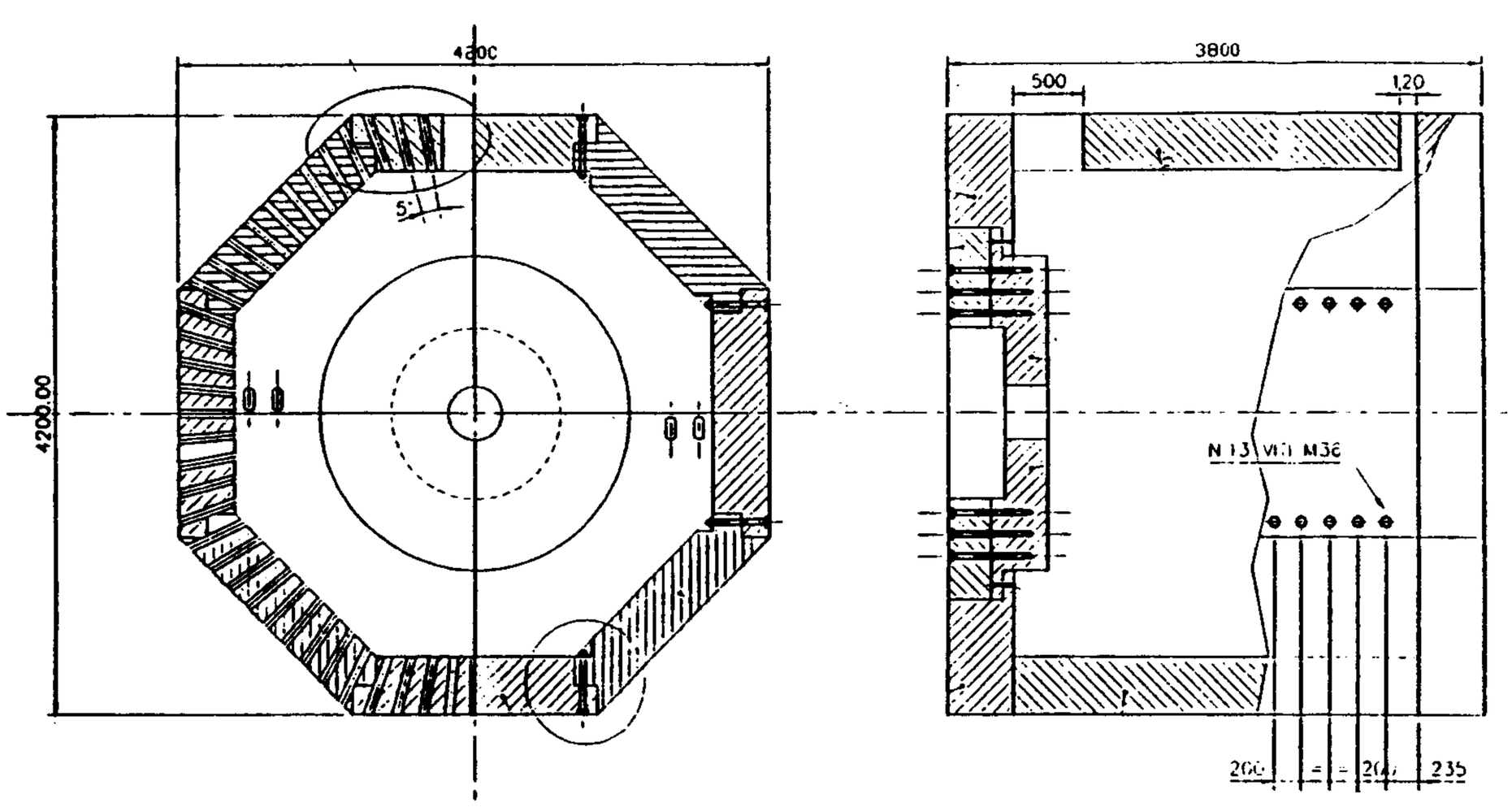

Figure 3.1: Front and side view of the FINUDA iron yoke. In the front view the slots foreseen for light guides, cables and gas tubes are shown

the other detectors. The position of the these slots is shown in figure 3.1. A slot of bigger dimensions (400 x 450 mm^2) will be used for the chimney of the cryostat.

Between the iron yoke and the tracking volume, inside which the FINUDA detectors are mounted, is inserted the cylindrical cryostat, containing the coils.

The cryostat with the coils is shown in figure 3.2, front view and 3.3, side view.

The iron yoke will be constructed by modules of forged soft iron each of thickness 60-80 mm, bolted together to compose a rectangular prism with octagonal basis. The octagonal iron shape gives a great advantage for the assembly and the transportation, while the influence on the field homogeneity is negligible and within the requested tolerances.The iron magnetic excitation curve is shown in figure 3.4.

At the two extremities of the octagonal iron prism, the internal volume is closed by two end-caps. Their shape is octagonal towards the outside, to fit with the shape of the octagonal prism yoke, and have in the middle a hole with a diameter of 38 cm to allow the crossing of the beam pipe and of the focusing magnetic elements of $DA\Phi NE$ with their supports and alignment tools. The thickness of the octagonal iron yoke and the thickness and shape of the two end-caps in the direction along the beam axis have been optimized to minimize the stray field outside the volume enclosed by the iron yoke. This for two reasons: 1) to have a zero field along the axis of $DA\Phi NE$ outside the iron yoke so that the orbits of the circulating electrons/positrons of only 510 MeV are not perturbed; 2) to have a field of not more than 50 Gauss along the border of the octagonal prism, in the position in which the phototubes of the external scintillator barrel will be positioned. The forged pieces (the eight end-caps quadrants and the eight longitudinal straight bars) will be machined at the coupling surface. The yoke will be pre-assembled by bolting the modules to each other and to their support carriages at ANSALDO, to check if machining is in accordance with the design specifications and to allow a test of the final assembly procedure. In figure 3.5 the project for the coupling of the 8 modules forming the octagonal prism is shown.

The weight of the iron yoke is almost equally distributed between the octagonal prism and the two end-caps (113.5 and 116.5 tons, respectively), so that the total weight of the solenoid (iron yoke and cryostat plus coils) will not exceed 240 tons. Moreover, each of the two end-caps will be formed by two independent and symmetric pieces (joined along the symmetry vertical plane containing the beam axis) to allow, with an appropriate opening procedure (see par. 3.4), the access to the detectors without breaking the vacuum in the beam line.

For the iron yoke, as for all other parts of the solenoid, a program of inspection and tests is foreseen. Its steps are the following:

- Analysis control
- Heat treatment control (during forging)
- Measurement of the magnetic permeability
- Plate dimensions control after machining
- Check of the position of the end-caps.

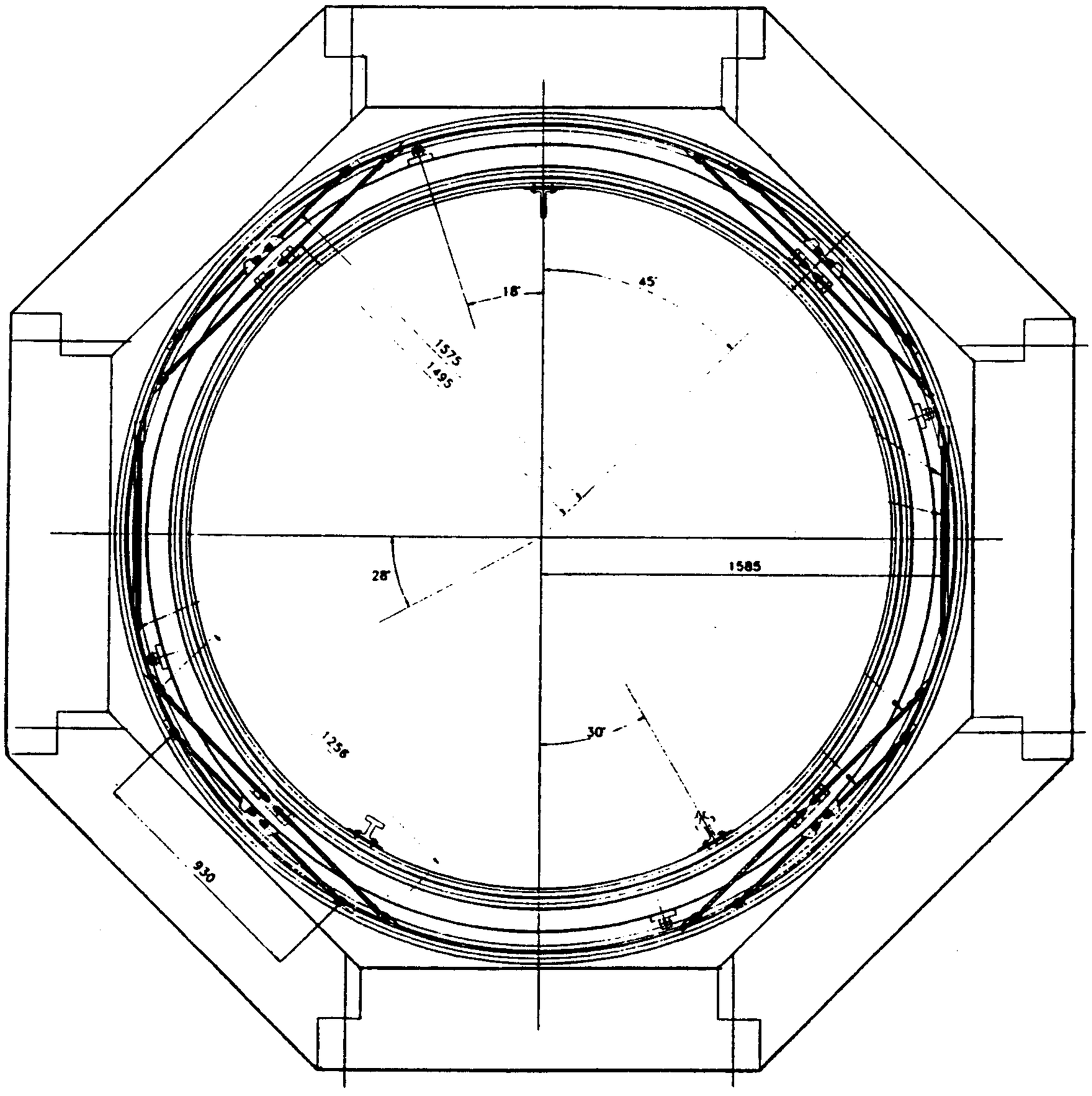

Figure 3.2: Front view of the FINUDA solenoid showing the cryostat and the coil inside the iron yoke.

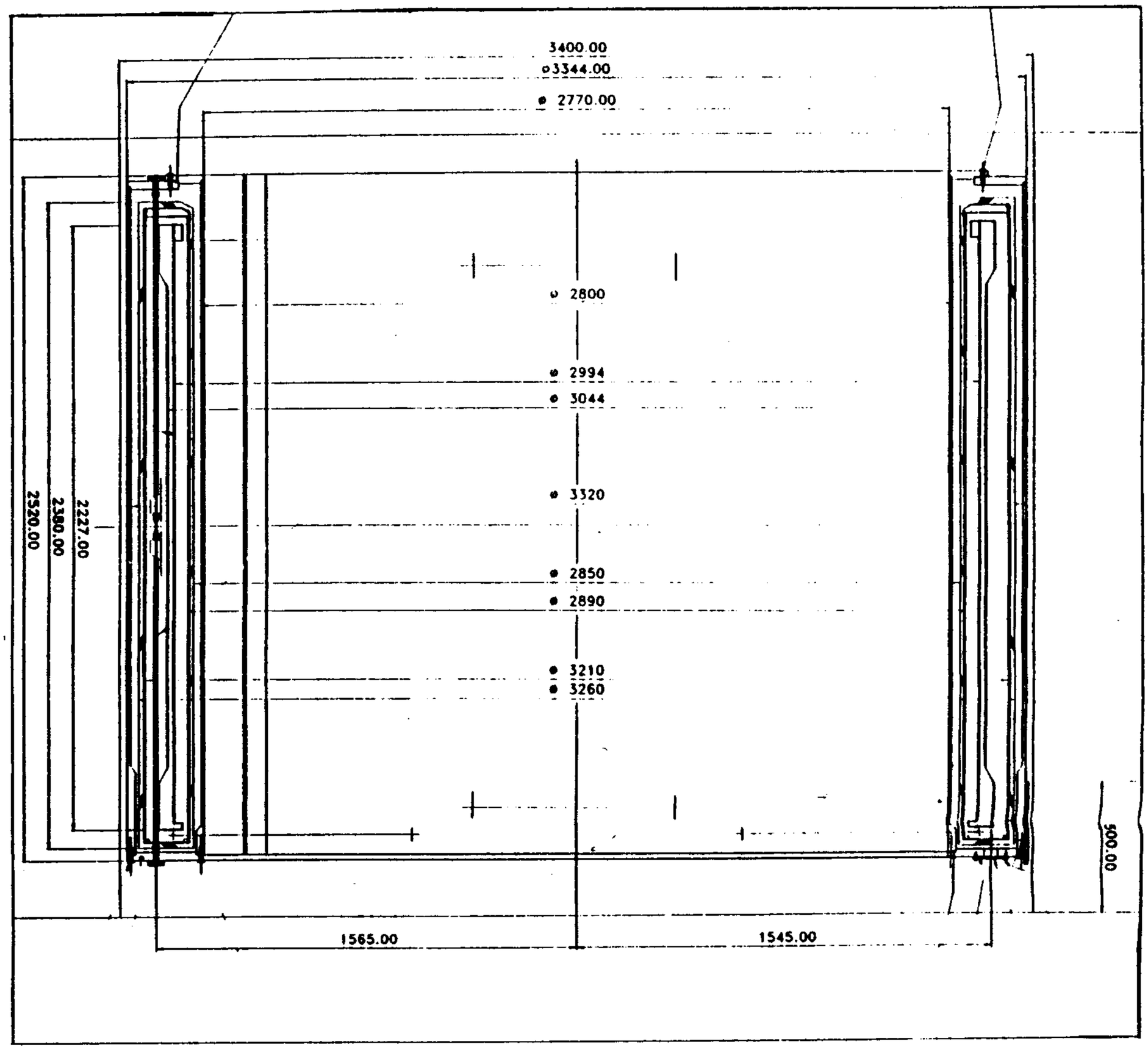

Figure 3.3: Side view of the FINUDA solenoid showing the cryostat and the coil inside the iron yoke.

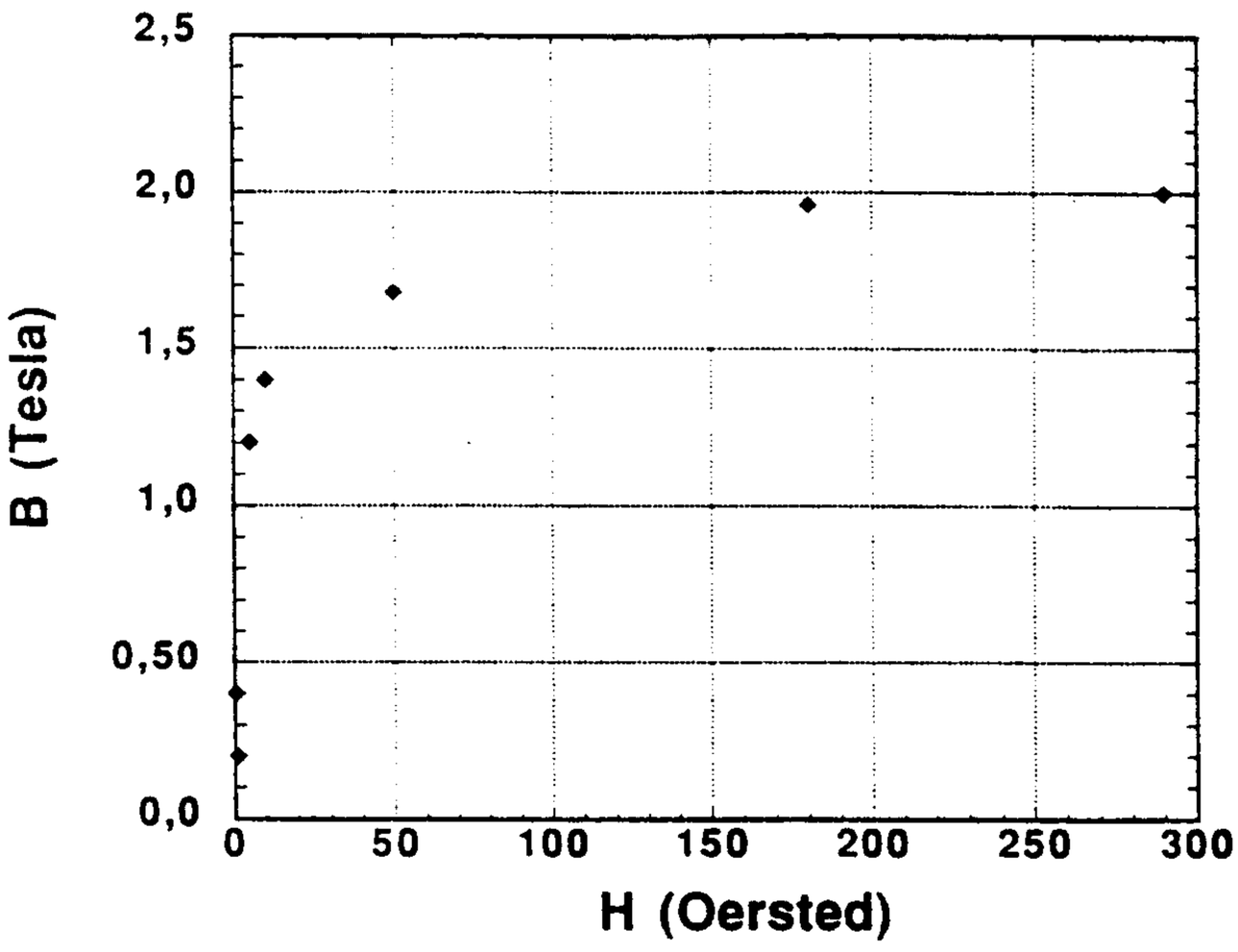

Figure 3.4: Excitation curve of the FINUDA solenoid.

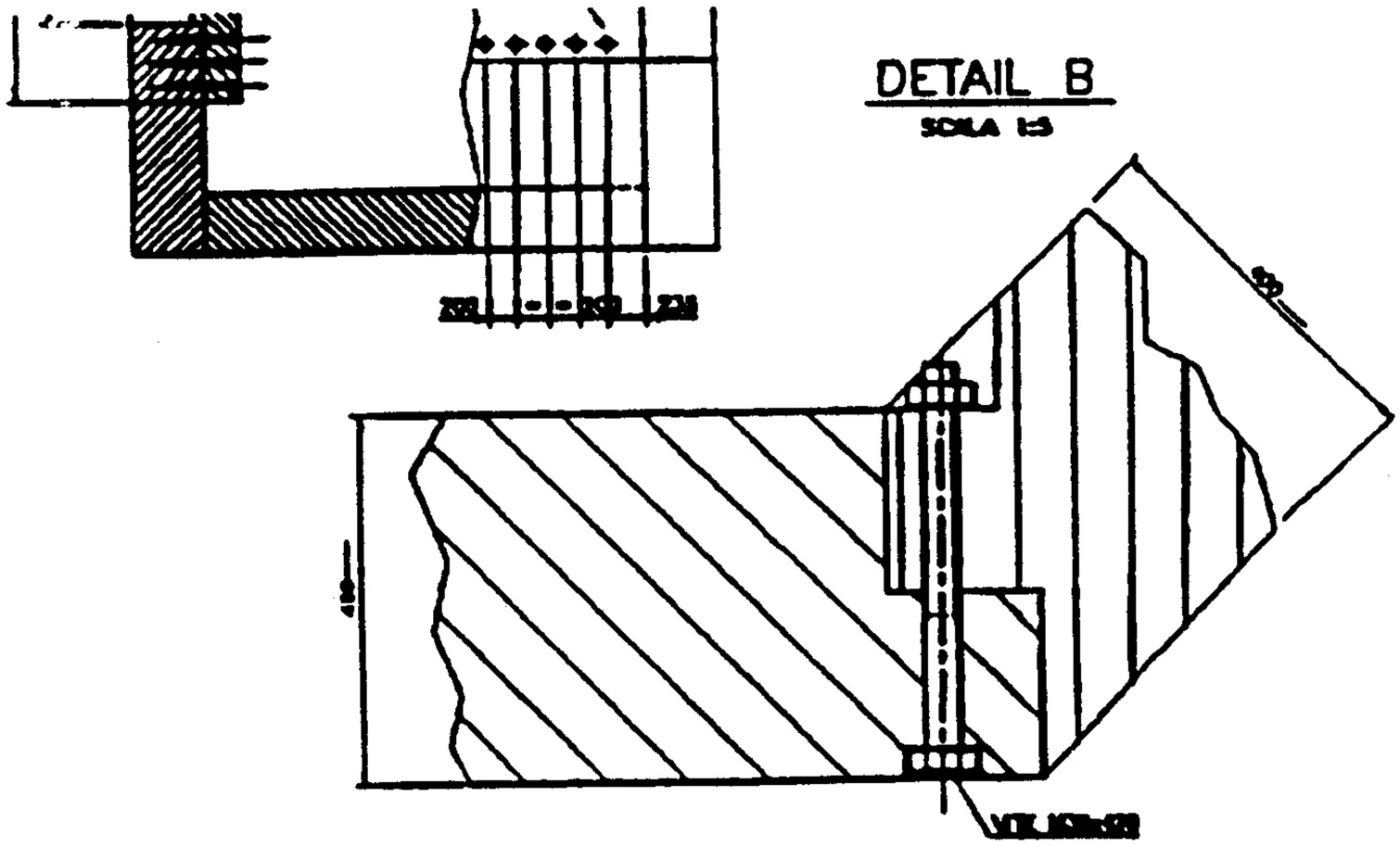

Figure 3.5: Detail of the coupling of the modules forming the octagonal iron prism yoke of FINUDA.

3.2 Coil and field shape

A detailed design of the superconducting coil with a complete analysis of the different operation conditions (steady state, cool down, quench, fast and slow dump) has been performed. The coil has been designed to reach the indicated performances, according to the specifications, with a relevant safety margin. The superconducting coil will have a 2.92 m inner diameter and a length of about 2.1 m. The coil will be vacuum impregnated with epoxy resin, using a special designed winding former used also as a mould, to get a monolithic coil body, that provides good thermal contact between turns and the cooling/constraining cylinder. The cable will be wound on the external surface of the winding former, previously covered with a mylar/tedlar bandage and a suitable thickness of ground insulation. After the coil impregnation, an aluminum cylinder will be shrink fitted on the coil. The aluminum cylinder will contrast the Lorentz force (during coil operation at the nominal field), and will provide the cooling of the coil by means of pipes welded on it. The aluminum alloy cylinder will be suspended by a set of radial tie-rods. The coil is located inside an annular vacuum chamber with helium cooled thermal shields. Of the two possible options for the coil: a one-layer or a two-layer winding, we selected the two-layer option since it has a lower cryogenic consumption and the requested time constant for the fast discharge, 20 s, can be fulfilled with a maximum voltage of 300 V between the coil ends. In the conceptual design, the following basic criteria were fixed:

- the design will have to allow a full safe operation of the magnetic system both in normal and emergency condition. The coil will be self protected, i.e. able to withstand a quench also in case of failure of the active quench protection system;

- the cold mass cooling system will be based on a self regulating thermosyphon loop, able to guarantee a suitable cooling autonomy in case of refrigerator emergency stop. This system does not require any helium pump;

The coil will be made of about 6100 m of pure aluminum stabilized NbTi/Cu superconducting cable, insulated by dry glass fiber ribbon. The cable will be supplied in three single lengths and at least four joints will be necessary for returning the cable to the electrical exit. The magnet design is the result of an optimization process based on the mandatory requirements of the experiment. In particular, to fulfill the FINUDA specifications the current density J increases at the ends of the coil by properly reducing the cable section. The resulting main parameters of the coil are the following:

- central part: length =1170 mm, J = 2850 A/cm^2
- end part: length=464.2 mm (each), J = 4021 A/cm^2
- coil internal radius: 1460 mm, coil thickness: 30 mm

With these choices, assuming that at the origin (center of the solenoid) $B_{z_0} = 1.1$ T, $B_{x_0} = 0$, $B_{y_0} = 0$, the components of the magnetic field inside the tracking volume will have the following uniformities: $|B_z - B_{z_0}|/B_{z_0} < 5\%$, $|B_y - B_{y_0}|/B_{z_0} < 1\%$, $|B_x - B_{x_0}|/B_{z_0} < 1\%$. A field map is given in figure 3.6.

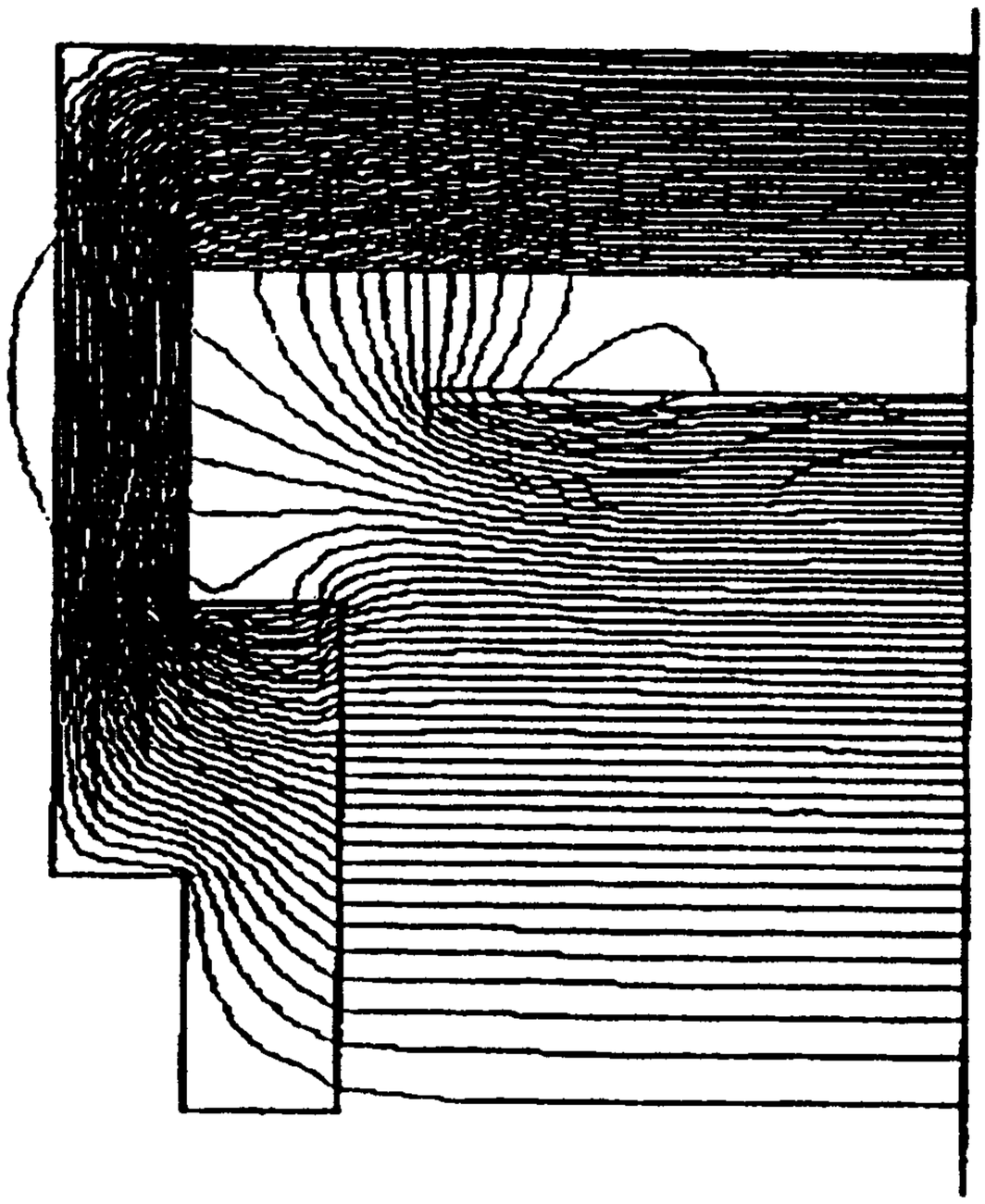

Figure 3.6: Map of the value of the z-component of the magnetic field inside the tracking volume.

In figure 3.7 the profile of the z-component of the field is shown with, in the inset, the region, outside the solenoid, where are placed some of the $DA\Phi NE$ low-beta quadrupoles. The vertical arrow indicates the end of the iron yoke.

In table 3.2 the basic parameters of the coil are given.

3.3 The cryogenic parameters

The superconducting solenoid will be cooled with a net of aluminum alloy pipes welded on the constrain cylinder. The circulation of the helium in the pipes is due to the thermosyphon effect. During the steady state operation, the liquefaction plant has only to maintain a constant level of liquid helium in the turret vessel. The increase of the temperature, due to the hydraulic pressure from the top to the bottom of the magnet, is negligible ($< 65\,mbar$). Using an operating pressure of 1.2 bar in the helium vessel, the temperature in the helium circuit is less than 4.45 K. The shield will be cooled by a separate circuit, using 60-70 K helium gas. The use of liquid nitrogen is possible, but it has been considered not convenient. The warm stream from the current leads will be regulated by two automatic flow controllers, with a remote set point fixed by the computer control as a function of the current. In this way a flow independent from the inside and outside pressure will be guaranteed.

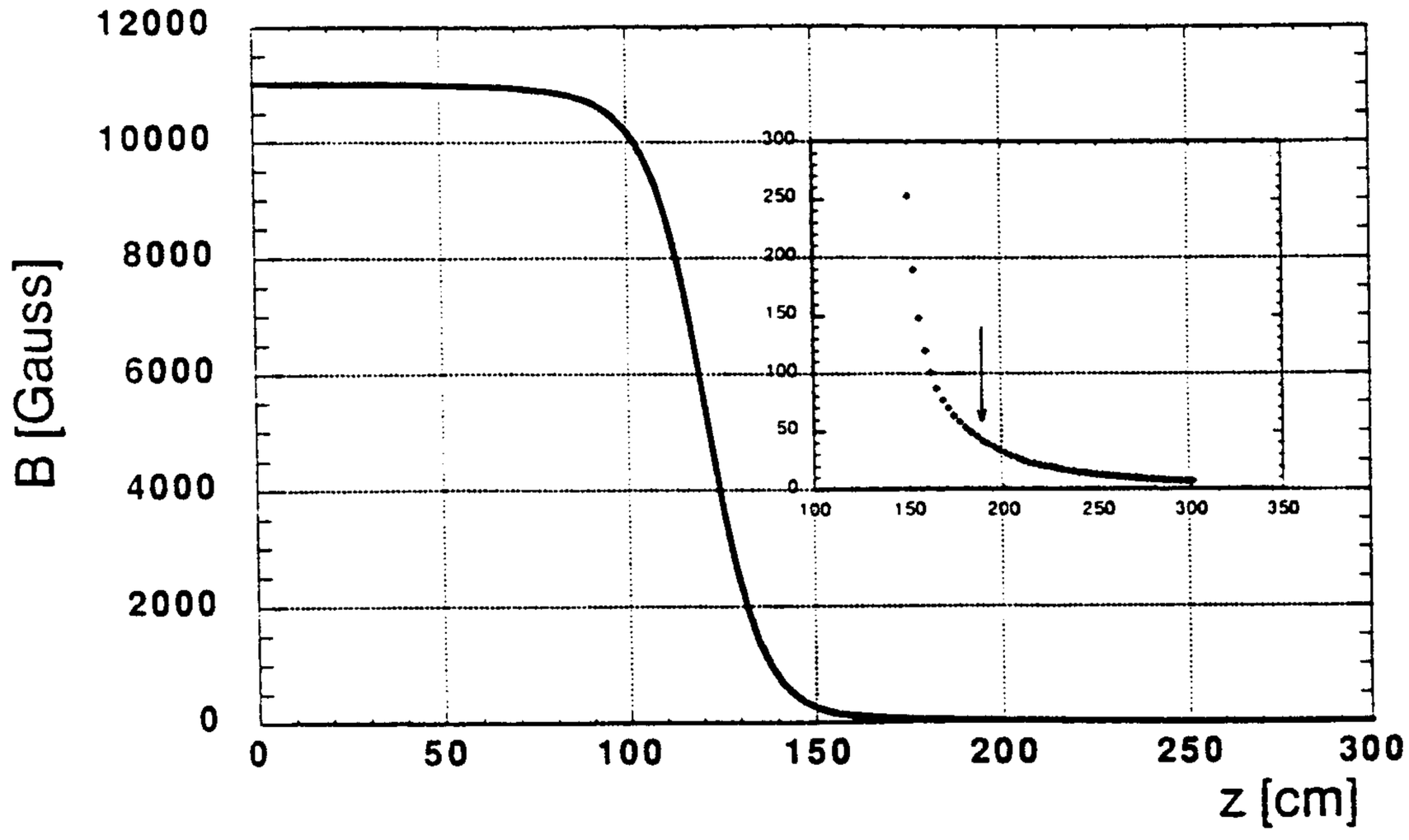

Figure 3.7: Profile of the z-component of the magnetic field along the axis. In the inset the B_z-value outside the iron yoke is shown; the vertical arrow indicates the end of the iron yoke.

Table 3.2: Basic parameters of the FINUDA superconducting coil.

Parameter	value
Inner radius	146 cm
External radius	149 cm
Total length (layer 1) at 4.4 K	211.83 cm
Total length (layer 2) at 4.4 K	211.49 cm
Central length (layer 1) at 4.4 K	115.21 cm
Central length (layer 2) at 4.4 K	120.45 cm
Current density (central part)	2850.0 A/cm^2
Current density (end parts)	4020.9 A/cm^2
Total cable length (central parts)	$1660 \cdot 2$ m
Total cable length (end parts)	$940 \cdot 4$ m
Insulated cable axial dimensions (central parts)	6.536 mm
Insulated cable axial dimensions (end parts)	4.635 mm
Insulated cable radial dimensions	14.9 mm
Max. temp. after quench	20 K
Dump resistance	0.11 Ω
Time constant of discharge	20 s
Max. ext. voltage during discharge	300 V

Table 3.3: FINUDA helium consumption.

Parameter	at 4.5 K	at 70 K
Radial tie-rods	2.16 W	32 W
Axial tie-rods	0.37 W	5.36 W
Radiation	4.9 W	35 W
Conduction	4.5 W	5 W
Total	11.93 W	77 W
Total (with a security factor of 2)	24 W	154 W

All the warm return stream will be connected to a simple collector. A drawing of the FINUDA cryogenic system is shown in figure 3.8.

The chimney has been sized as small as practical to avoid a too large aperture in the iron yoke. Demountable bayonet type cryo-couplings will make easier the disconnection of the magnet from the supply lines when the magnet is moved from the assembly hall to the experimental hall. During the steady state, the foreseen cryogenic consumption for the chosen two-layers option is about 80 W at 70 K, 10 W at 4.2 K plus 0.45 g/s (12.8 l/h) of liquefaction. In the table 3.3 the foreseen helium consumptions of the FINUDA solenoid are summarized.

According the scheme of figure 3.9 two transfer lines are expected to furnish cryogenic helium at the input of the solenoid cryogenic system: one at 300 K and one at 4 K.

During the cool-down phase, the helium flow coming from these two lines will be mixed, through a three-way valve; hence, using a feed-back system (with temperature sensors and electrical heaters), the input helium temperature will be regulated, according to the needs, by the computer control, together with the helium flow through a valve put immediately before a mass flow meter. The input helium flow and temperature will be determined by the computer control system, in such a way to avoid too much high thermal gradients. When the temperature of the magnet will reach about 50 K, the cool-down line will be closed, and the liquid helium will be fed through a dedicated line (indicated in figure with "in 4.2 K"). Two return lines from the magnet are foreseen: one for the recovery of "cold" helium ("out 4.2 K" in figure), and one for the recovery of the "warm" helium ("out 300 K" in figure) during the cool-down. A low hydraulic impedance line is also foreseen ("quench line" in figure) on which security valves will be inserted. For the helium input/output to/from the magnet, two bayonets (one coaxial and one single) are foreseen. The screens will have an independent circuit.

With a constant helium flow of 10 g/s and a constant inlet pressure of 10 bar, a cool-down time (from 300 K to 4 K) of 130 hours is foreseen. All tubes are dimensioned for a maximum pressure of 30 bar, but in the cryostat of the current leads a security valve is foreseen to open at a pressure of 3.5 bar. This means that an appropriate low impedance of the recovery lines will be necessary, so that, during the cool-down, when the pressure can be high, the emergency circuit will not be

/	1	thermal shild	15	/
/	1	thermosifon loop	14	/
/	1	thermal shild	13	/
/	1	pipeline	12	/
/	1	cryogenic valve	11	/
/	1	liquid helium reservoir	10	/
/	1	quench line	9	/
/	1	safety valve	8	/
/	1	burst disk	7	/
/	1	trasfer-line coupling	6	/
/	1	trasfer-line coupling	5	/
/	1	trasfer-line coupling	4	/
/	1	trasfer-line coupling	3	/
/	1	current lead	2	/
/	1	current lead	1	/

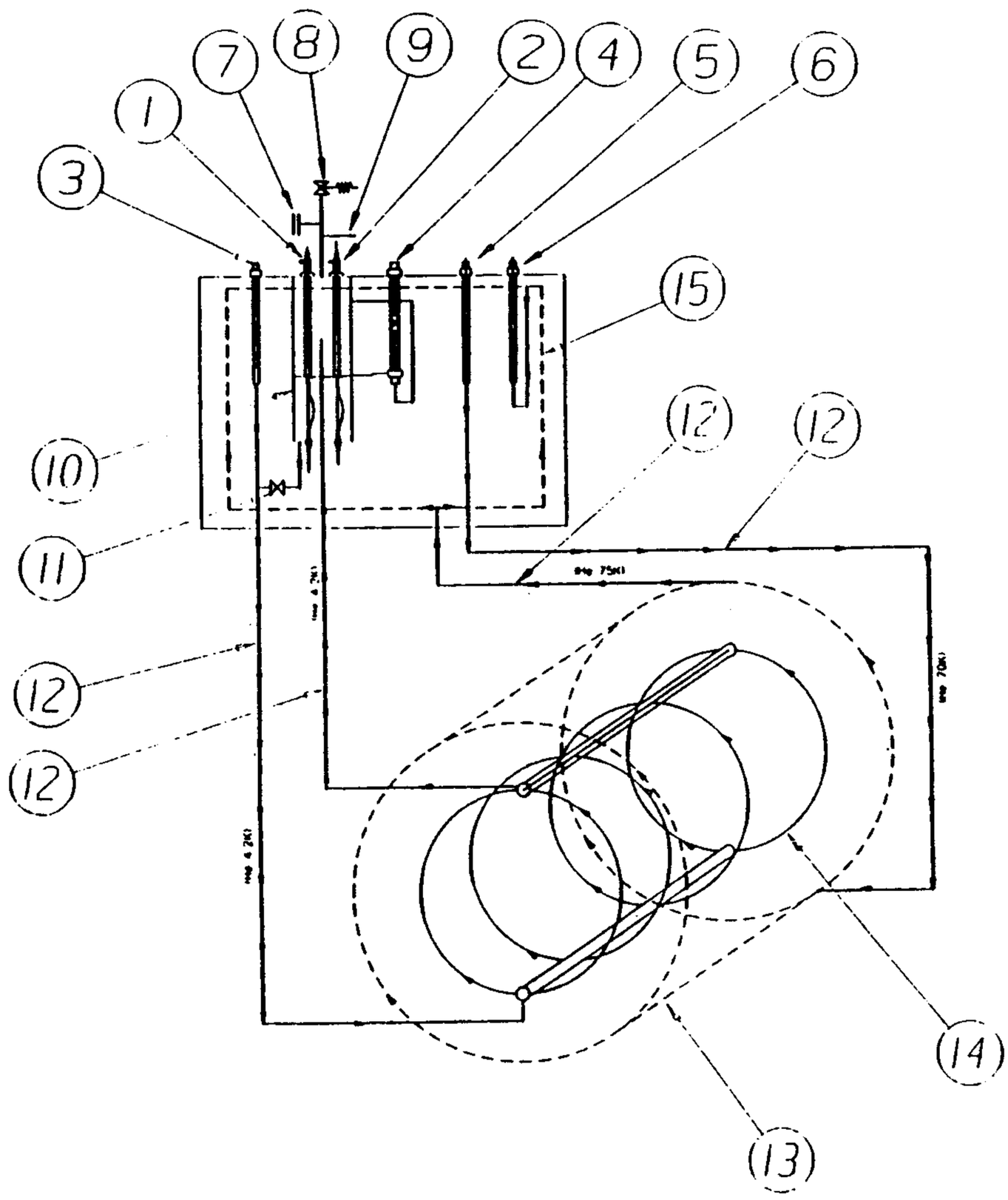

Figure 3.8: Schematic drawing of the FINUDA cryogenic system.

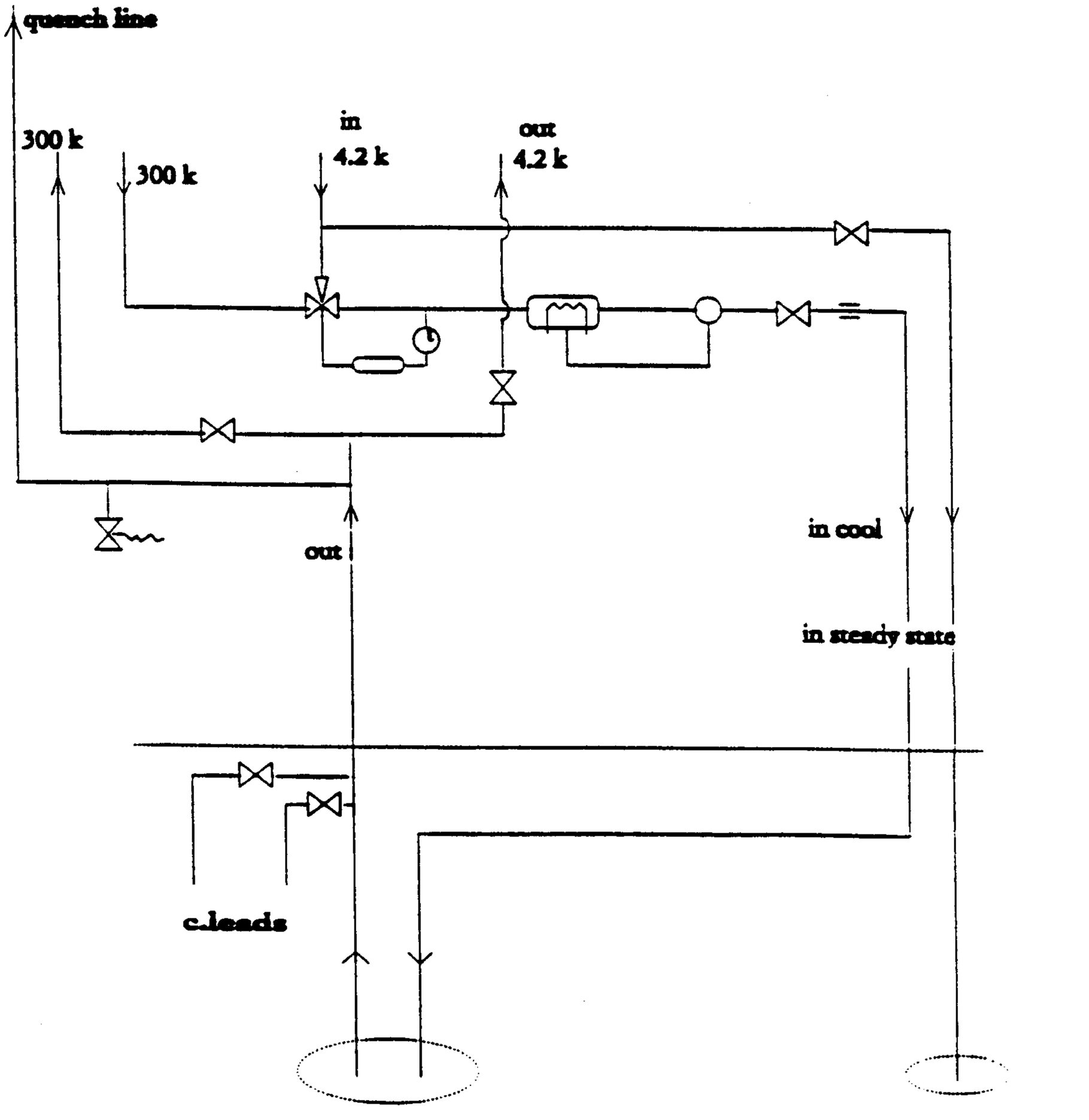

Figure 3.9: Scheme of the FINUDA cryogenic helium circulation, with valves and controls.

activated.

To the cryogenic losses of table 3.3, it must be, of course, added the 0.45 g/s of liquid helium necessary for the current descendents.

3.4 The opening and moving mechanical system

The solenoid, with the included detectors, will be installed inside a pit located in the $DA\Phi NE$ building (see Chap.9). Two types of operations have been foreseen: a) access to all the inner volume of the solenoid; b) lateral displacement out from the beam line of the whole solenoid.

Regarding the operation a), it can be required for an ordinary substitution of the nuclear target, for small repairs of the inner detectors or for the extraction of complete parts of some detectors for repairs in the outside equipped laboratory. To access the inner volume of the solenoid for this type of operations, the opening of the end-caps is foreseen in such a way that the $DA\Phi NE$ beam pipe remains untouched. To accomplish this task, the end-caps are hanged to appropriate supports mounted above the magnet.

The following sequence of movements has been foreseen: 1) each of the two end-caps is moved outwards along the solenoid z-axis for a distance of 330 mm, so that the two inner "noses" have their $|z| = 1530\,mm$, i.e. greater than the halflength of the octagonal iron yoke without end-caps (1435 mm); 2) each of the two end-caps is separated along the vertical symmetry plane in two halves that are transversally slided in opposite directions for a total opening of 2800 mm, so that the whole inner detector region of FINUDA will become accessible. Some special tools are foreseen to open the end-caps against the residual magnetization forces, and dowels to re-close properly them. After the reclosing of the end-caps, the checking of the alignment will be done using the reference marks on them and on the octagonal iron yoke containing the detectors, and on detector marks accessible through the end-caps holes. Operation b) has been foreseen only in the event of some "cathastrofic" situation which could require the complete removal of the solenoid out from the beam line. Moreover the movements of the magnet inside the pit will turn essential in the initial phase of installation of the experiment inside the $DA\Phi NE$ building and for the removal from inside the solenoid of the detector frame (see Chap. 9) with all the inner detectors. The transversal movement of the whole magnet, in the direction opposite to the $DA\Phi NE$ center, will be done using the rails installed on the floor of the experimental pit (see Chapter 9). In this operation, of course, the $DA\Phi NE$ beam line located inside FINUDA will follow the magnet displacement, so that a substitute vacuum pipe has been foreseen.

3.4.1 The precision of alignment and the reproducibility of movements

At the momentum of the installation of the FINUDA detector on the machine, the magnetic axis of the solenoid will be aligned with the beam axis at a precision level of $\leq \pm$ 500 μm, while the magnetic axis will lie inside a circle of 1 mm of diameter at the center of the end-caps.

The system of movements (opening of end-caps and displacement of the magnet from the beam line) ensures a repositioning better than the reported alignment precision. The request of the Machine Group to have a capability of relocating the end-caps geometrical centers with a precision in the 100 μm range with respect to the beam axis is not yet implemented in the project.

3.5 The internal mechanics

3.5.1 Introduction

The present paragraph refers to the mechanical structure supporting the different detectors of FINUDA. The presentation is divided in different parts, basically according to the main detectors. Consequently, the description of the FINUDA mechanical structure is organized as follows:

- 1) the general supporting structure;
- 2) the mechanical structure supporting the TARGETS, ISIM and OSIM;
- 3) the mechanical structure for the DRIFT CHAMBERS (inner and outer);
- 4) the mechanical structure for the STRAW TUBES;
- 5) the support for the outer scintillator array (TOFONE);
- 6) hints about the way of extracting TARGETS, ISIM and OSIM out of the magnet;
- 7) hints about the way of inserting the whole structure inside of the magnet.

3.5.2 The general supporting structure

The general supporting structure is based on the scheme shown in figure 3.10, 3.11.

The cage shaped structure has the multiple purpose of:

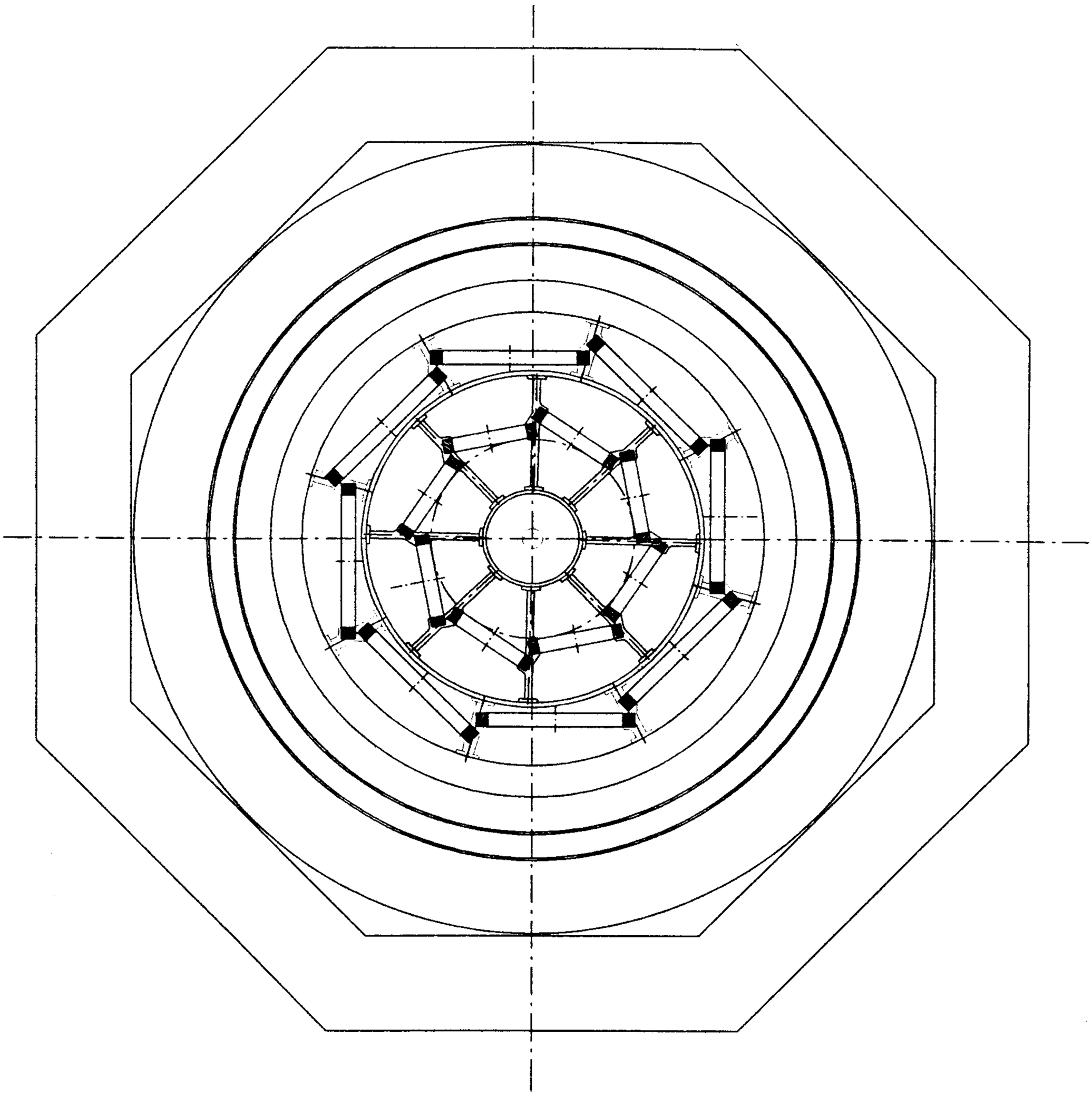

Figure 3.10: The FINUDA general supporting structure (x-y plane view)

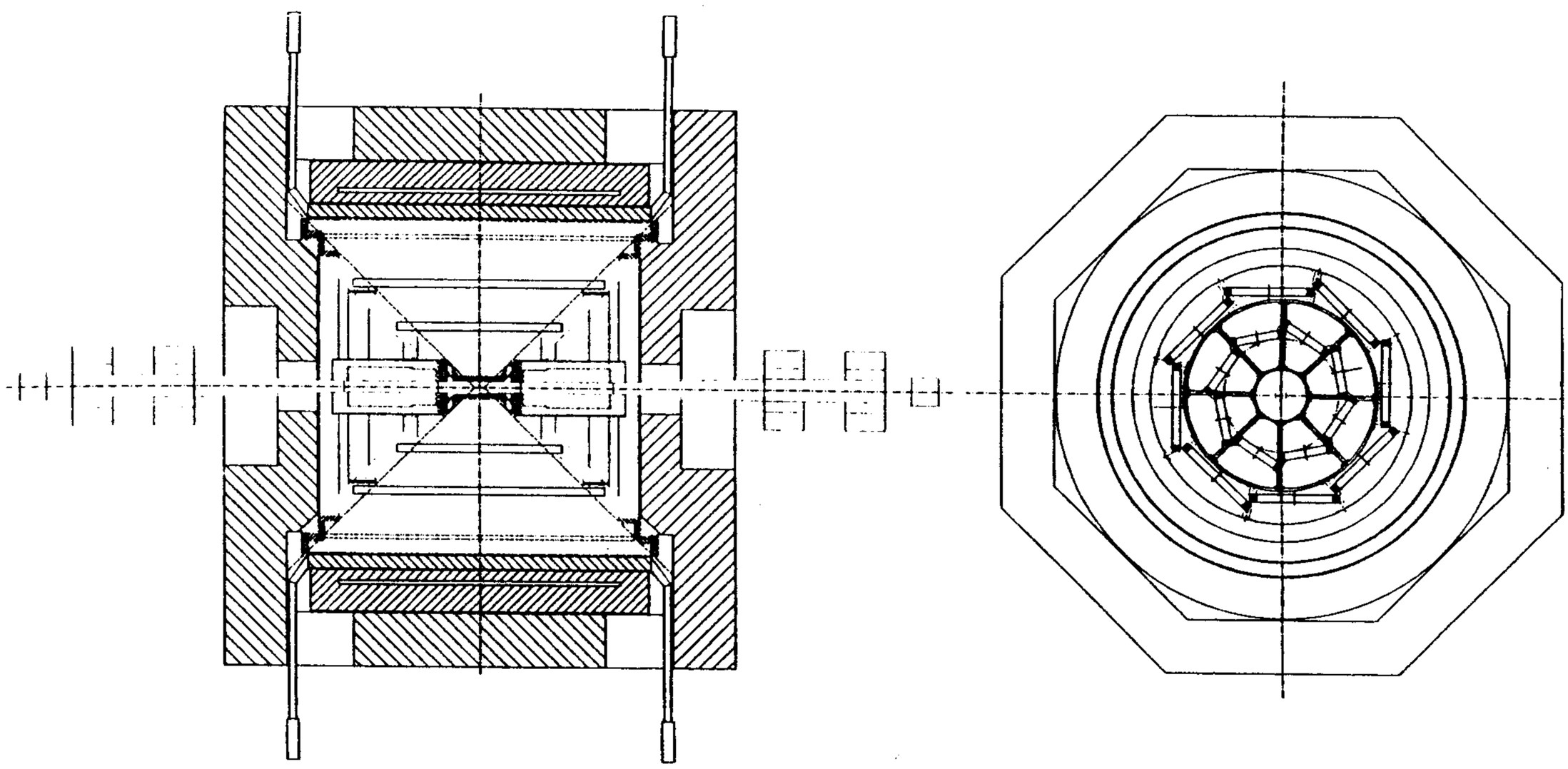

Figure 3.11: The FINUDA general supporting structure (x-z plane view)

- 1) supporting the beam pipe with the two inner pairs of $DA\Phi NE$ quadrupoles;
- 2) supporting the drift chambers;
- 3) supporting the straw tube array;
- 4) allowing the sustain of TOFINO, ISIM, and OSIM detectors, targets and of the beam pipe, thanks to the two inner cylinders connecting the radial spokes on the lateral surfaces of the structure;
- 5) forming a tight structure so that it can be easily inserted inside the magnet.

Other important advantages of the chosen supporting structure can be found in the possibility of discharging the strain given by the straw tubes on the axial links sustaining the drift chambers. In other words, the seats of the drift chambers behave themselves as compression members to support the tension given by the straw tubes (15 N strain max for every straw; about 2500 straw tubes).

Another characteristic of the supporting structure to be underlined, is the inclination of the radial spokes. This solution allows to gain free volume in the lateral surfaces of the structure, leading to two positive consequences: a) more space one has just outside the structure, easier will be to manipulate the inner structures (TOFINO, ISIM, TARGETS and OSIM) to extract them manually or by means of proper tools (automatic or robotized devices); b) the spokes partially behave themselves as compression members which contribute to support the straw tube mechanical tension.

As for the outer part of the structure, the one which would give the right consistency to the structure, both to support the straw tubes strain, and to make the whole system not to collapse due to its own weight, two solutions have been proposed for the moment.

- 1) The first one consists in inserting between the straw tubes area and the outer scintillators (TOFONE) one, a cylindrical skirt (aluminum made) about 1.0 cm thick. The advantage could be the contribution to a very rigid structure, while the disadvantage is to decrease the transparency to the particles going towards the TOFONE.

- 2) The second option suggests to use some compression members forming a sort of outer cylindrical cage. In this way, the transparency of the particles going towards the outer scintillators is increased, but the zones in which the rods are arranged are completely blind for the particles.

As for the mechanical deformations point of view, the two options are very similar, as shown in the simulation schemes obtained by a Finite Element Analysis (FEM) (figure 3.12). These calculations have been made supposing the strain of the straw tubes 4 times the working condition; the structure has a good behavior in both the two options.

A third (now in progress) solution involves to create some room between outer scintillators for compression members. This option decreases the inefficiency of the second solution, but it will make more difficult the TOFONE assembling.

The main parts of the structure can be made up of carbon fiber or inox steel: the first solution allows to have a good mechanical strength and high lightness; however, it is surely more expensive than the second option.

3.5.3 The mechanical structure supporting targets, ISIM and OSIM

In figure 3.13 the scheme of the relative angular position of TOFINO, ISIM, OSIM and targets is draw.

The solution of building ISIM and OSIM in octagonal and decagonal shape, respectively, is due to the use of the same silicon microstrip module for both of them. In this way the length of the side of the two polygons is the same. So, the very light mechanical structure supporting the silicon microstrips forming the ISIM is equal to the one supporting the silicon microstrips of the OSIM.

This structure, pictured in figure 3.14, not only allows the seating of the microstrips, but also the electronic devices (chips) connected to them. The octagonal structure reporting the microstrip of ISIM must allow the seating of the targets at its outer face. In this way two advantages can be achieved:

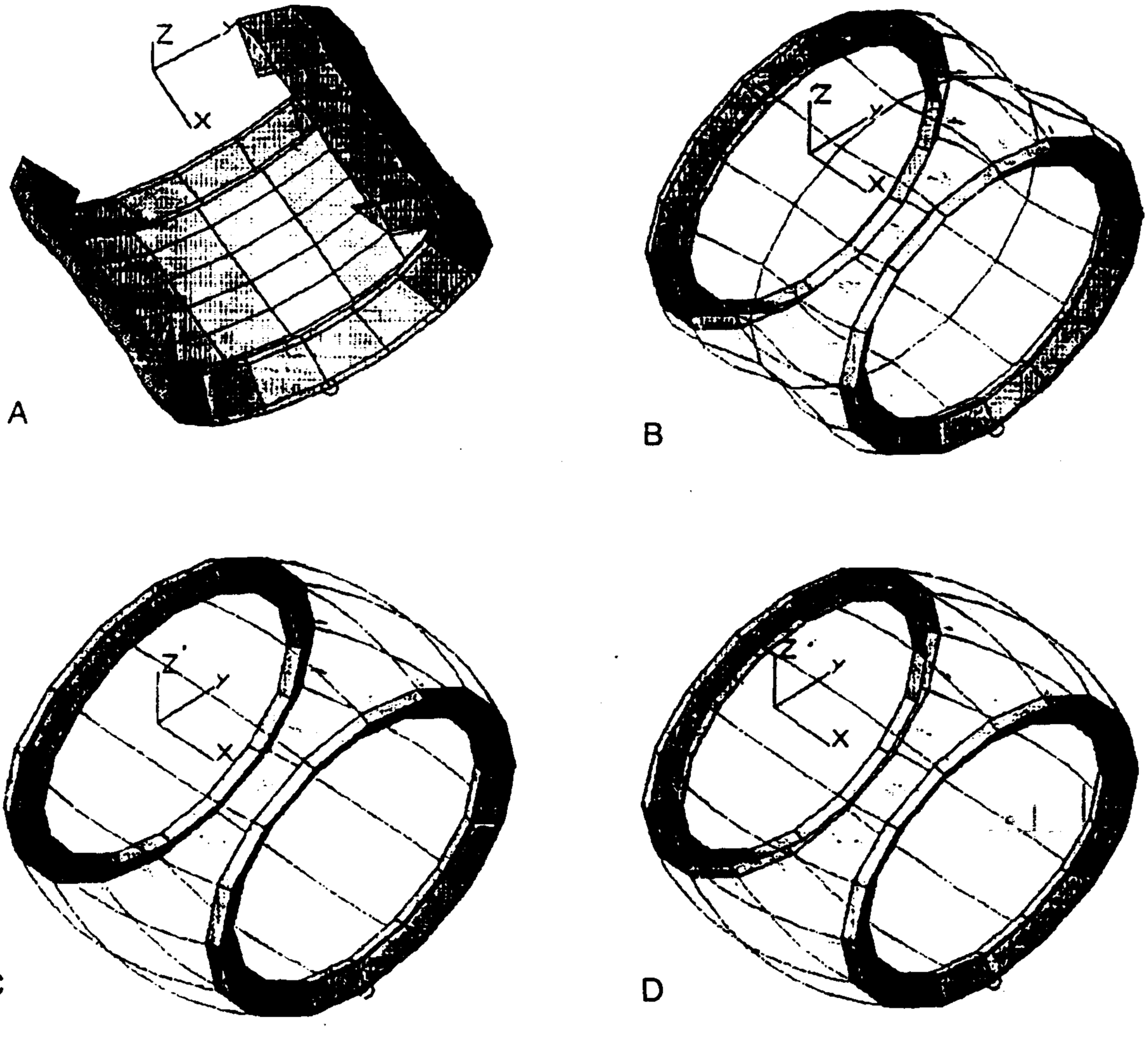

Figure 3.12: Simulation schemes obtained by the Finite Element Analysis.

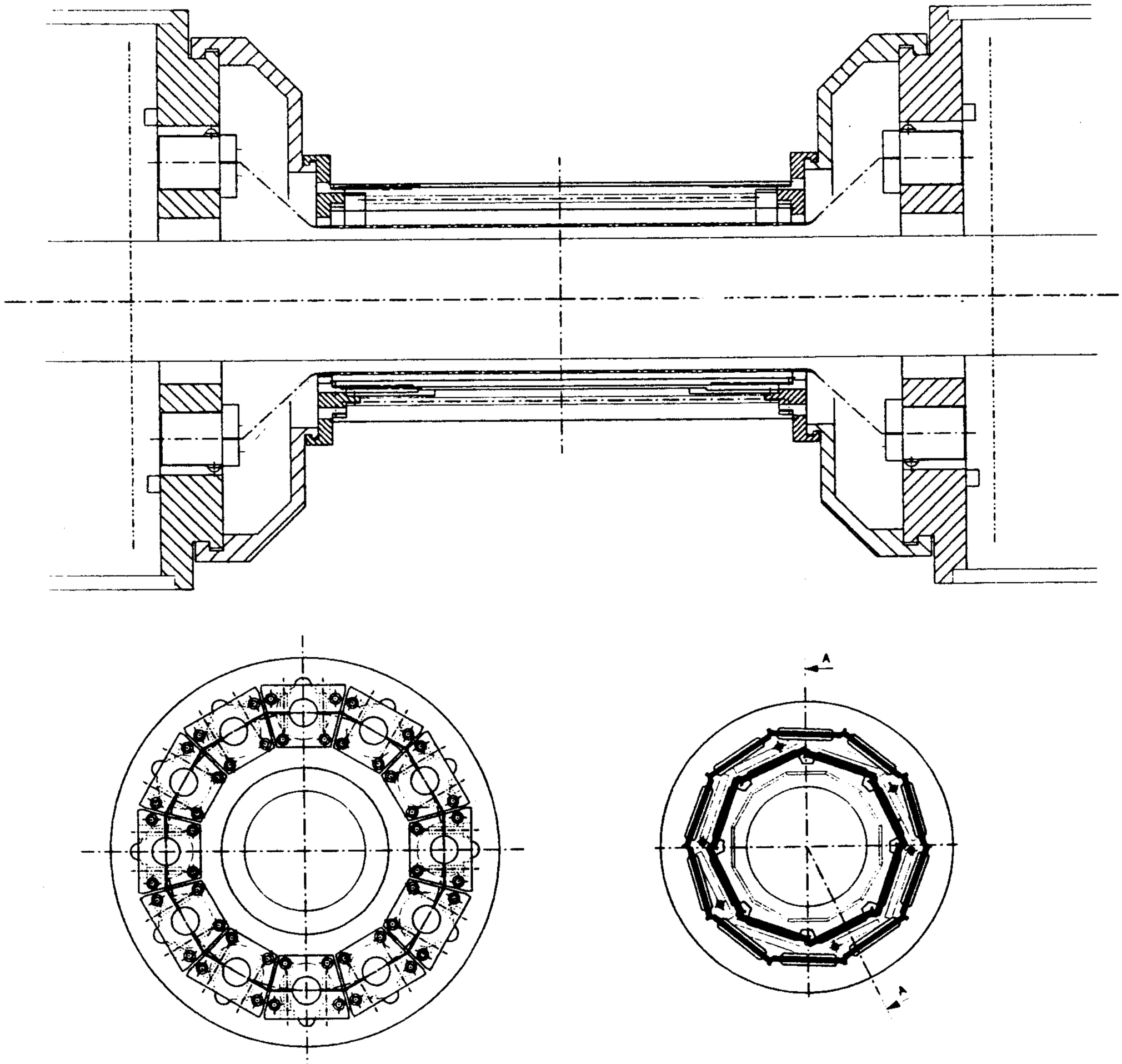

Figure 3.13: Scheme of the relative angular position of the TOFINO, ISIM, OSIM and TARGETS.

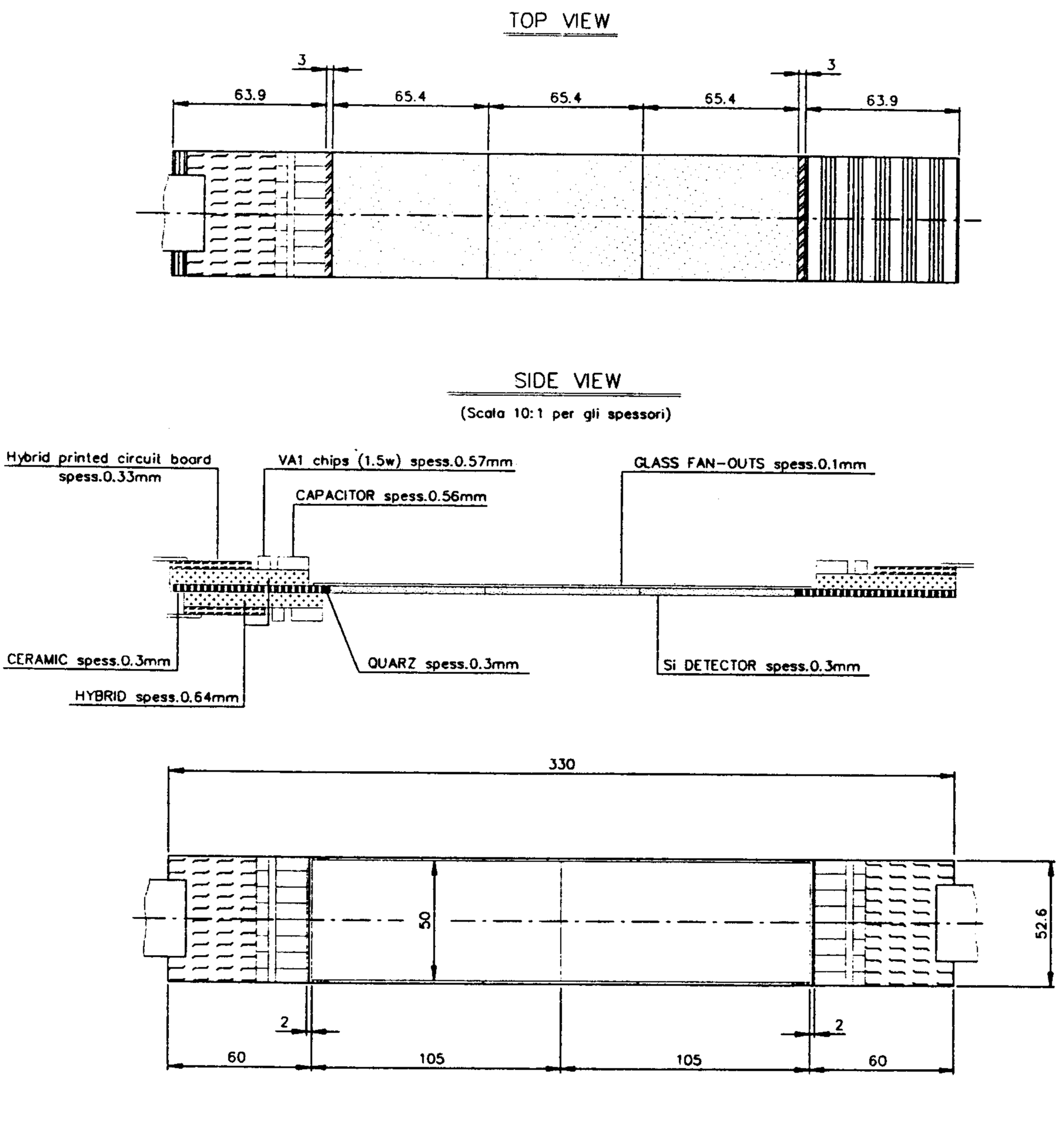

Figure 3.14: The frame on which the silicon microstrips lie stiffened by a supporting structure.

- 1) there is not the necessity of building another supporting structure for the targets;

- 2) it is possible to keep the targets very near to ISIM, that is good for the physics of the experiment.

Both the octagonal shell of ISIM and targets and the decagonal shell of OSIM are provided with proper flanges that will be linked to the inner cylinders of the general supporting structure (see paragraph above). This fact enables us also: a) to satisfy the necessity of disassemble ISIM, OSIM and targets from the structure, allowing the substitutions of the detectors; b) to give a further mechanical solidity for the extraction of the components from the solenoid, manually, or with a proper robotized device.

The two half shells (octagonal (ISIM and targets) and decagonal (OSIM) can be kept together, linked on the flanges, by means of screws and proper dowels. However, another interesting solution under study, is to maintain the two half shells together by means of pneumatic devices. In this case, the mounting and disassembling of the structure could be rather easy.

It has been esteemed that the current passing through the ISIM and OSIM detectors gives a global thermal energy equal to 50 Watt, which needs a forced ventilation to be dispelled. So, in the flanges supporting the ISIM / targets and OSIM frames, holes and pipe lines which fit the purpose are foreseen.

3.5.4 The mechanical structure for the drift chambers

The compression rods constituting the general supporting structure described in paragraph 2, are used to guide the insertion and to realize the supporting of the inner and outer drift chambers. So, the compression axial members and the radial spokes form a sort of frame on which the drift chamber can be seated.

From the physics computer simulations, it results that the best configuration is the one shown in Figure 3.15.

The cross section of the compression members is arranged as shown in Figure 3.16.

This shape of the rods allows the insertion of the drift chamber in their own seats by making them sliding on the rods themselves. By using a trivial description, we can think about the insertion of the drift chambers in the structure as they were "drawers" in their guides. After the insertion operation, proper dowels (possibly parallel pins) will define the exact position of each drift chamber with respect to the general supporting structure, while stops on the guide and proper linkages will block it.

This design has the following main characteristics:

1) It allows to use the compression members in a double function:

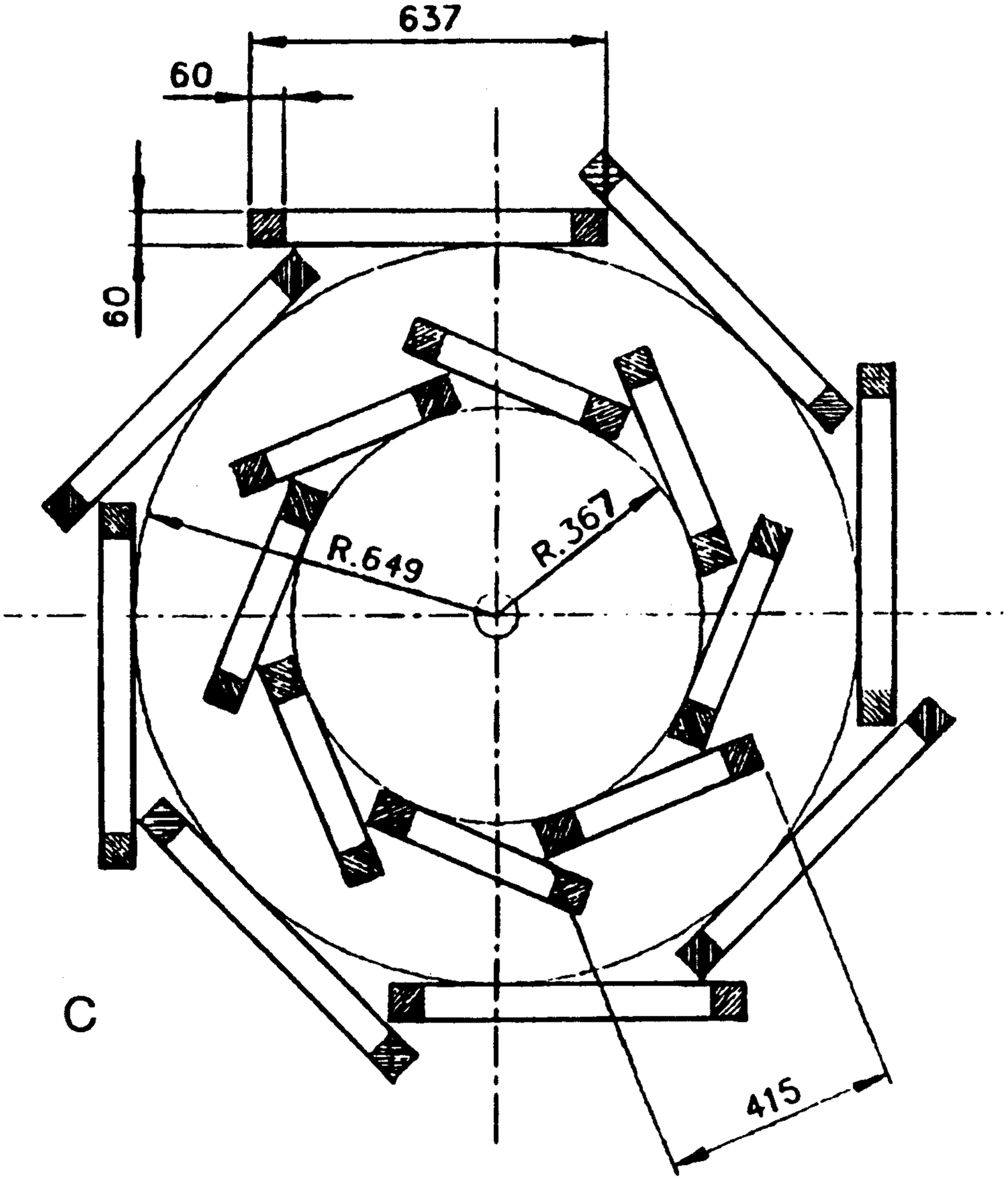

Figure 3.15: Selected configuration of the drift chambers.

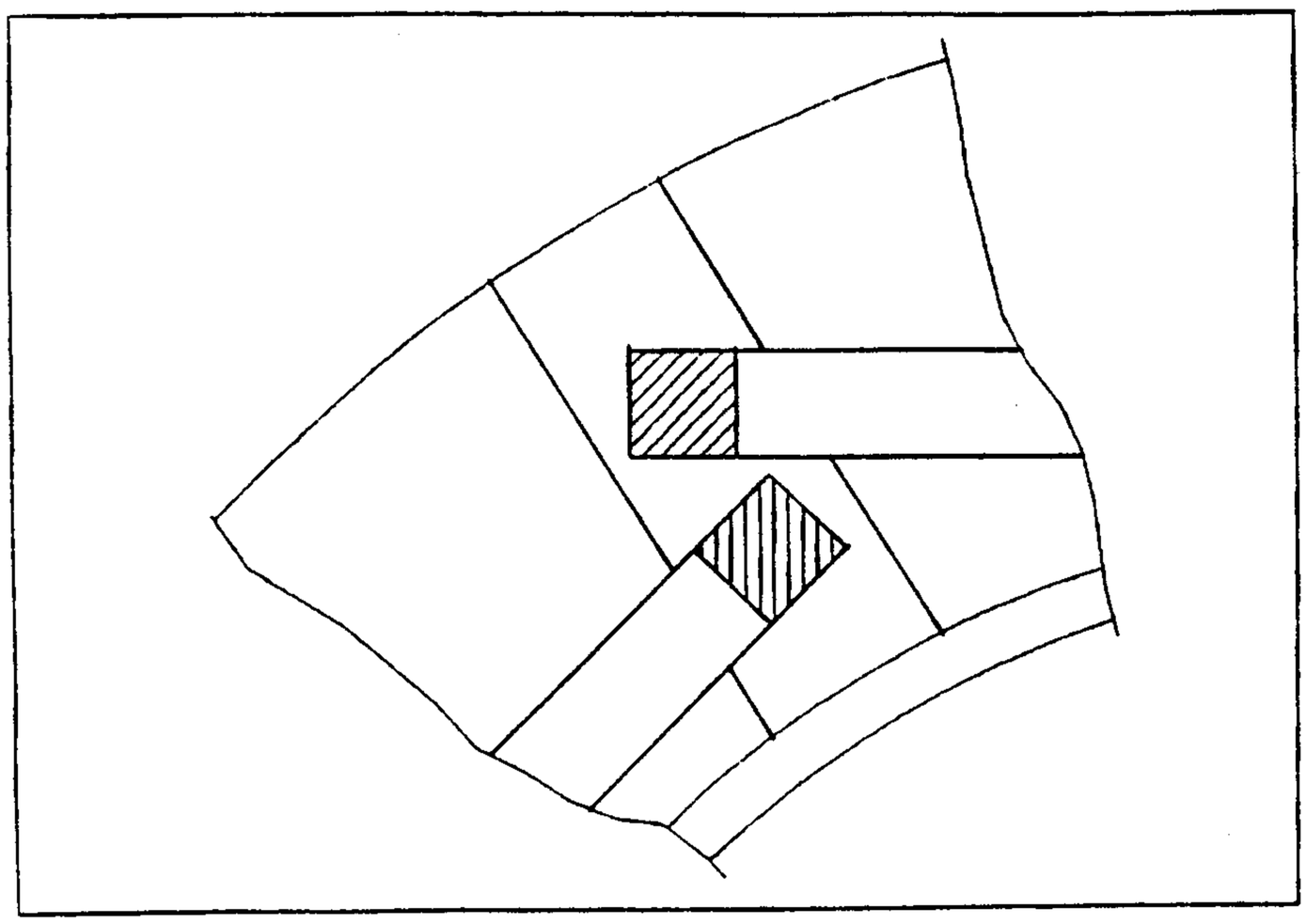

Figure 3.16: Cross section of the arrangement of the compression members.

- a) they are rectilinear guide for the insertion of the drift chamber;
- b) they are the supporting structure of the drift chamber.

2) It allows a very easy way to insert the drift chambers: no rotation is necessary for their insertion, but only translation.

For this operation, a proper tool for the entrance of the drift chambers in their guides must be still designed, but at the moment one can say that its conceptual design is rather easy.

The sliding of the chambers on the guides is obtained by a proper anti-friction solid material (commonly used in the field of tool machines). The possibility of a rather easy insertion of the chambers in the general supporting structure, opens the way towards two interesting options: it is possible to insert the drift chamber into the general supporting structure, when the detector is: a) outside the magnet; b) inside the magnet.

Considering that the weight of every drift chamber is less than 60 kg, and that 16 drift chambers are mounted on the structure, by using option b) the operation of the insertion of the detector inside the magnet would happen with almost 1 ton less in the total weight. This can make easier both the operation of the insertion of the detector in the magnet itself, and the linking of the detector to the magnet (or the cryostat).

3.5.5 The mechanical structure for the straw tubes

The straw tubes form a very important structure from the mechanical point of view, because it results a highly strained structure (15 N strain for every straw;

about 2500 straw tubes). That's why it is necessary to have a strong mechanical structure which can support this tension. The suggested options are the following:

- 1) To insert between the straw tubes area and the outer scintillators (TOFONE) one, a cylindrical skirt (aluminum made) less than 1.0 cm thick;
- 2) to use some compression rods forming a sort of outer cylindrical cage;
- 3) To modify some outer scintillators to make room for the needed compression members.

Advantages and disadvantages of the three solutions have been already discussed above.

Here, it is underlined again that, as for the mechanical deformations point of view, the first two options (the third one has not been completely deepened yet) are very similar as shown in the simulation schemes obtained by a FEM (see Figure 3.12). Observe that considering that the calculations have been made supposing the strain of the straw tubes 4 times than the chosen working condition, the structure has a good behavior in both options. Besides, one must also consider that in the above FEM analysis, the contribution of the compression members supporting the drift chambers has not be considered. So, by the analysis of a more complex model, which considers also the above mentioned compression rods as elements to support the straw tube strain, it will be possible to reduce the thickness of the cylindrical skirt (as for solution (1)) or the number of the compression members forming the outer cylindrical cage (as for solution (2)).

3.5.6 The support for the outer scintillator array (TOFONE)

The scintillators forming TOFONE will be linked to the cryostat by means of proper brackets made up solid to the cryostat by means of threaded holes (see Figure 3.17).

3.5.7 Hints about the way of extracting targets, ISIM and OSIM out of the magnet

This paragraph has been arranged in form of "hints", because different mechanical solution hypotheses have been made, but no one of them is still frozen. In fact the relative merits and proper designs are not yet completely studied.

The way of extracting ISIM, targets and OSIM could be arranged in two main options: 1) manual extraction; 2) robotized extraction.

The first solution is obviously easier to be realized, not expensive, but it is linked to the following requirements:

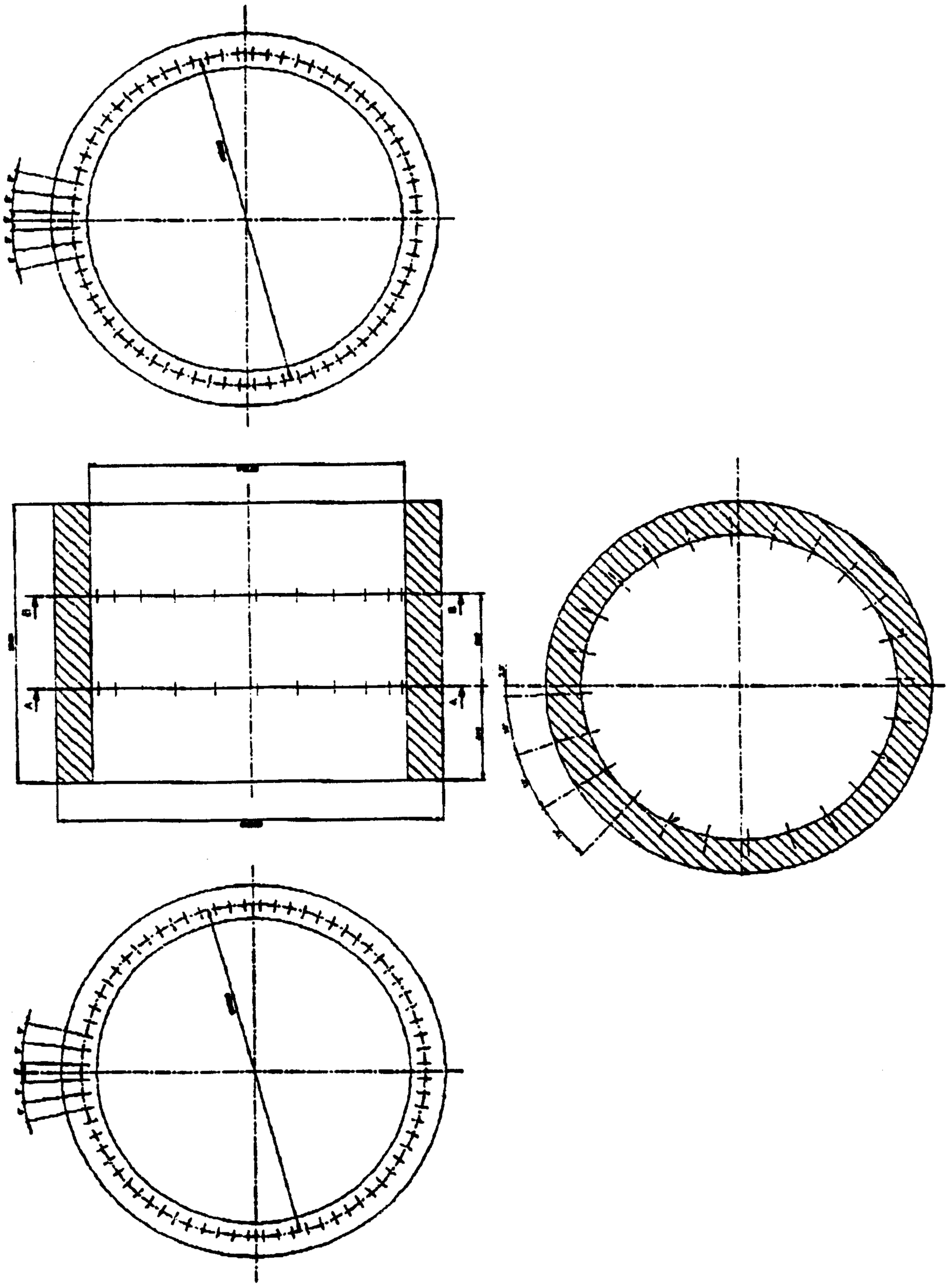

Figure 3.17: The brackets linking the TOFONE to the cryostat.

- a) between the lateral surface of the detector and the machine first quadrupole, one needs the necessary room so that a person can easily work. From the first drawings of the whole structure (Figure 3.18) this seems not simple; however, a complete drawing scaled 1:1 is in progress, so that possible doubts can be driven away;

- b) evaluation of the weight of the structure to be extracted. The question is whether it is possible for one man to sustain the structure. From the first evaluation the answer seems to be positive, but a deeper evaluation of the problem is needed.

The second solution is more difficult to design and realize, and more expensive, but, due to the low space at disposal, seems the best. The questions to be answered to begin the conceptual design of the extracting robotized tool are:

- a) the final relative positions between the octagonal of ISIM and targets and the decagon of OSIM must be frozen;

- b) it must be defined the way of disassembling and extracting the detectors: is there the necessity of extracting the OSIM, or ISIM, OSIM and targets have to be always extracted at the same time?;

- c) the way of connecting cables from the detectors to the front end electronics must be established, to determine if the cables can give problems for the extraction of the detectors;

- d) the extraction can be done in a space between the inner cylinder connecting the radial spokes on the lateral surfaces of the general structure and the inner drift chamber (this is possible if the inner cylinder radius is small) or between the inner cylinder and the beam pipe (this is possible if the inner cylinder radius is big). Both these hypotheses are feasible, and the inner cylinder radius size depends only by the method chosen by the machine group for link their elements to the structure.

In any case, independently from the answer to the questions a) and b), it is possible to think about something like a Cartesian robot which, positioned outside the detector, is endowed with two rectilinear arms which can reach the center of the detector. On this two arms, a proper tool is mounted, having two purpose: 1) it fits to the flanges supporting the OSIM decagon and ISIM/TARGETS octagon, like a sort of sheath containing and protecting the detector structure; 2) it allows the disassembling of the two (octagonal and decagonal) half shells, contemporaneously or in sequence, by acting on the possible screws that keep them linked one another or by acting on a pneumatic circuit (if one thinks about the two shells kept together by pneumatic devices).

Another operation that one has to foresee for the robot is to make it performing an operation of covering the beryllium pipe, when the detectors are out of the structure and leave the beam pipe uncovered.

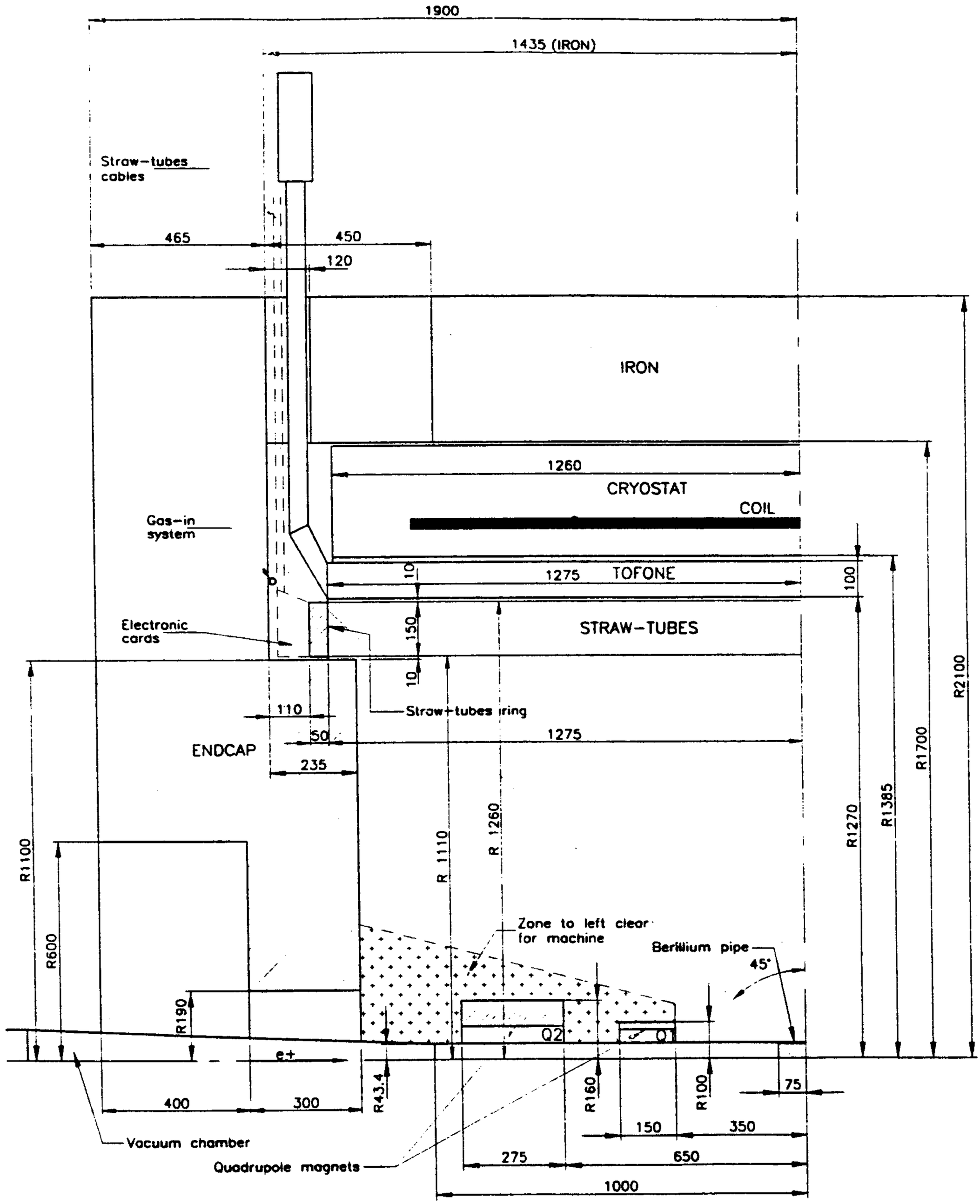

Figure 3.18: The whole FINUDA mechanical structure.

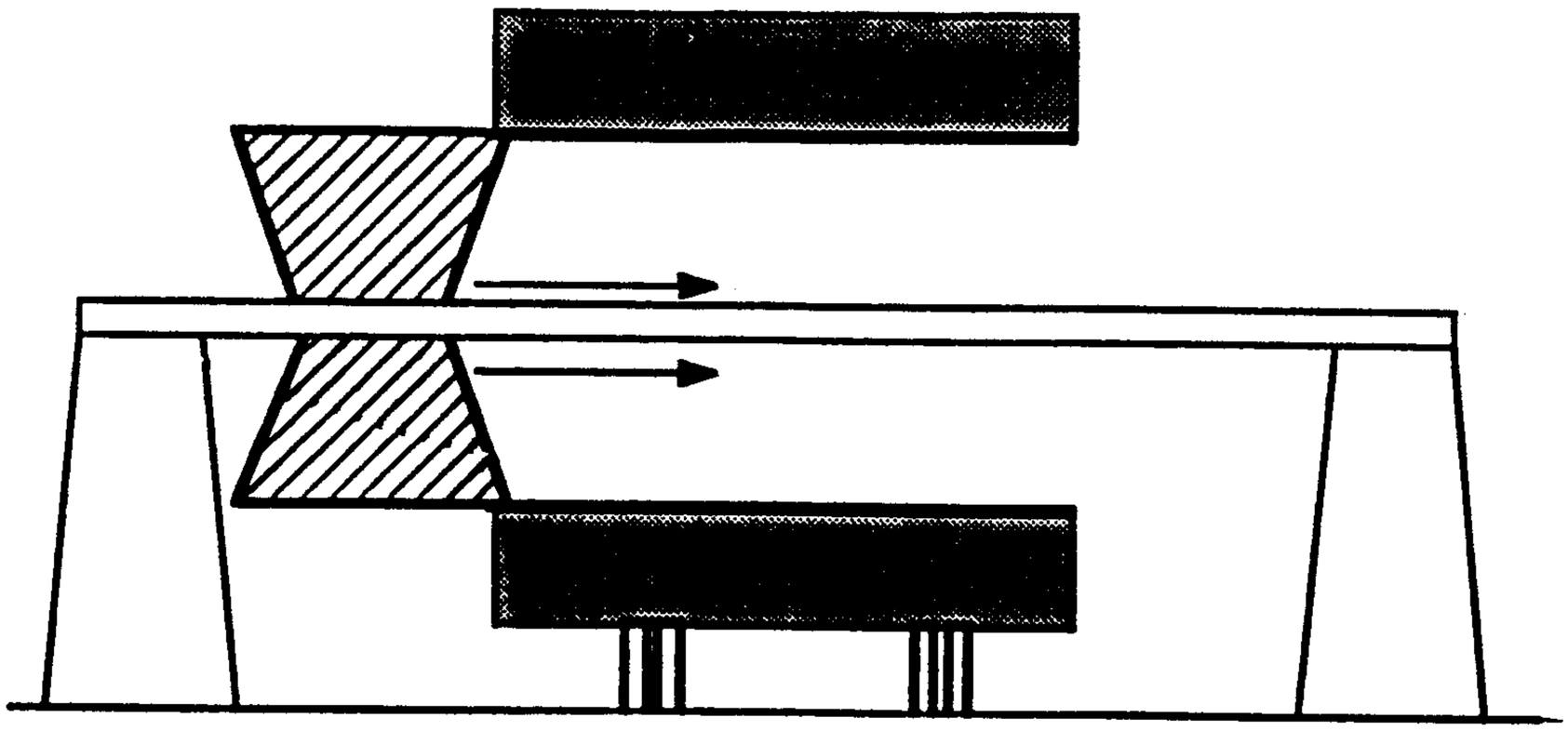

Figure 3.19: A conceptual scheme of the insertion of mechanical structure in the magnet. The actual room situation in the pit and around it is not shown in the concept work.

3.5.8 Hints about the way of inserting the whole structure inside of the magnet

Three solutions are discussed about the way of inserting the detector into the magnet and to keep it still.

1) The first possible solution utilizes three rectilinear guides, placed on the cryostat, which, paired with proper elements embedded on the detector structure, permit a translation movement. This solution is conceptually rather easy, but is subjected to some shortcomings:

- a) the slot of the rectilinear guides on the cryostat needs the modification/elimination of some scintillators of the TOFONE;
- b) once the detector is inside the magnet, it is blocked on the cryostat by two flanges;
- c) a prolongation of the guides outside the magnet must be considered for the entrance of the detector inside the magnet. The junction between the external guides with the internal ones can cause alignment problems.

2) The second options refers to the scheme given in Figure 3.19.

No fixed guides are present on the cryostat, but the sliding of the detector into the magnet is obtained by means of external supports which are removed once the detector has reached the right position. The rectilinear guide can act either on the inner cylinder of the supporting structure, or on the lateral surfaces spokes. Once the detector is inside the magnet, it can be fixed to the magnet by proper flanges.

The advantages obtained by the choice of this solution lie in: a) there is no the necessity of eliminating some scintillators of the TOFONE; b) the sliding system is something external to the detector and can be removed after the detector is inside the magnet.

However, some shortcomings linked to the present solution arise: a) it is possible that the sliding guide bends under the weight of the detector, causing a difficult insertion of the detector inside the magnet; b) it could be difficult to insert the structure on the guide because room in the pit and around it is very limited. Some tools for the entrance must be designed.

3) A third solution, not yet well developed, suggests to use a pneumatic device which sustain the structure while it is inserting into the magnet.

From a first analysis of the three solutions, it seems that the best one is the second one, even if the difficulties above mentioned have to be well studied yet:

Chapter 4

THE TRACKING SYSTEM

4.1 The silicon vertex detector

The hypernuclear physics program at DAΦNE relies on the low-energy $K^-(K^+)$ from ϕ-meson decay at rest: $\phi \rightarrow K^- K^+$ with a branching ratio of ~49%. The kaon kinetic energy is T_K=16 MeV and the two kaons are emitted in opposite directions, $\theta_{K^+K^-} = 180°$. Negative kaons, being moderated by the beam pipe, TOFINO and ISIM media, will stop in selected targets and, therein, form a hypernucleus through the $K^-_{stop} + {}^A X_Z \rightarrow {}^A_\Lambda X_Z + \pi^-_{prompt}$ reaction. The hypernucleus will weakly decay either to ${}^A_\Lambda X_Z \rightarrow^{(A-1)} Y + N + \pi$ (*mesonic* transition) or to ${}^A_\Lambda X_Z \rightarrow^{(A-2)} Y + N + N$ (*non mesonic* transition).

The complexity of the topology of the hypernuclear formation and decay, and the narrowness of hypernuclear states (~0.1 MeV) require a vertex detector finely segmented and capable of operating in high magnetic fields. The vertex detector of FINUDA, ISIM and OSIM (I&O), has been designed to embody these requirements. Figure 2.2 shows the arrangement of I&O around the crossing region of the e^+e^- beams, along with the other elements of the central FINUDA's region: the beam pipe, TOFINO and the target.

The electronics associated with I&O will initiate the charge collection ~1 μs after the arrival of a trigger signal from TOFINO, which is designed to be selective to K^-K^+ pairs. ISIM will trace K^-K^+ events to the target with a resolution of 10-20 μm (FWHM). OSIM, which has the same resolution as ISIM, is the leading device of the tracking system of FINUDA [1]. Furthermore, OSIM, in association with ISIM and with the outer tracking system of FINUDA, will identify the hypernucleus formation and decay spot in the target region.

4.1.1 The ISIM and OSIM detectors

The set up of the vertex detector of FINUDA around the beam pipe is sketched in figure 2.2. It consists of two layers: ISIM and OSIM. Both are arranged along two parallelepipeds, ISIM of octogonal section and OSIM of degagonal section. I&O

are modular; ISIM will be equipped with 8 modules and OSIM with 10 modules. Each module (see fig. 4.1) will be obtained by micro-bonding together 3 units of Si detector. A module will have an active surface of 196 mm (along the z direction, that is, the e^+e^- beam direction) $\times$ 52 (along the ϕ direction, which is normal to z direction) mm^2. The unit detector is the *ALEPH's new detector*[2]: it is a Si detector with strips on both sides, it has a size of 52.6$\times$65.4 mm^2 and a thickness of 300 μm. The pitch between two strips is 50 μm on both sides and the strip width about 6 μm. The rims of the detector have an inactive width of $\sim$0.6 mm, this part will be used to mechanically tighten the detector.

This type of detector is ideal for the purpose of FINUDA, since it:

- has a high granularity. For the detector described above, the resolution on both z- and ϕ-side can be assessed to be 10-20 μm (FWHM) for a readout pitch of 100 μm, for a signal to noise ratio S/N=40-20 and for minimum ionizing particles[3];

- has a low sensitiveness to magnetic fields [4]. It has to be reminded that FINUDA will commonly operate at 1.1 Tesla;

- has low mass, $<$0.1 g/cm^2. The effects of K^- multiple Coulomb scattering are minimized for this detector: a pencil-like kaon beam of 8 MeV crossing the detector is diffused with an angular width of $< 2^\circ$ (rms);

- has a moderate energy resolution. About 50% (FWHM) for minimum ionizing particles[5], see fig. 4.2. However it will allow to identify low-energy $K^-(K^+)$ ($\sim$10 MeV at ISIM) from quasi minimum ionizing π^-_{prompt} (T_π $\sim$160 MeV), and from protons deriving from non mesonic decay ($T_p \sim 85$ MeV);

- can be coupled with electronic circuits which can be enabled by an external trigger: a K^-K^+ event trigger in the case of hypernuclear studies.

- is resistant to radiation. The detectors of I&O as well as the front-end chips and hybrids, will escape most of Bhabha radiation. However, even including a large uncertainty in the background radiation of DAΦNE, the radiation hardness of silicon detectors and front-end electronics renders I&O safe in this respect[6].

The wafers will be produced by CSEM, Neuchâtel. They make use of a fabrication process developed jointly by INFN at Pisa and CSEM itself. Using this method CSEM has previously produced the ALEPH's *old* detectors. An order of four batches is being submitted for a total of about 80 detectors, commonly 70% of them have efficiency over 97%. An initial quantity of detectors should be delivered within the current year, and they will be tested by INFN at Trieste and Bari. The bonding of both I&O and the spare modules will be carried out by MIPOT, Gorizia, for a total of about 350,000 bondings.

The strips on the z-side will be fanned out to the ϕ-side by means of gold layer structures deposited on glass substrates. A substrate will have a surface of 84.5 ($\frac{1}{2}$

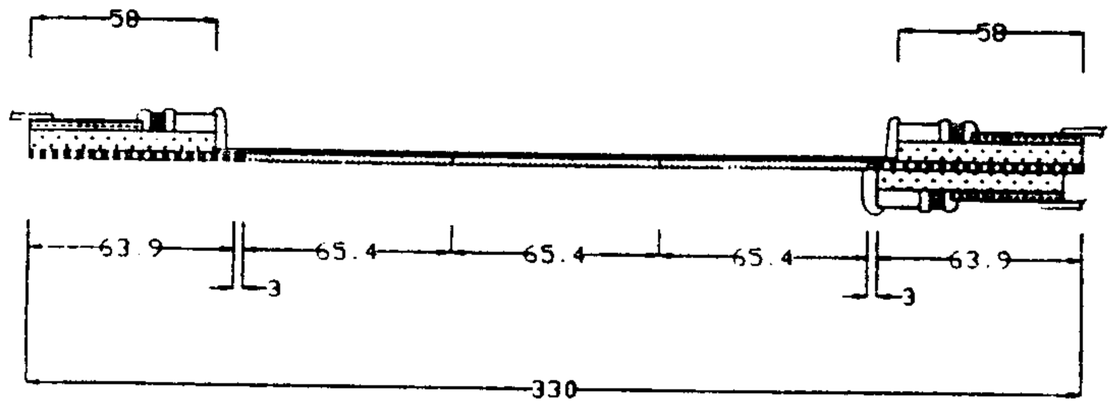

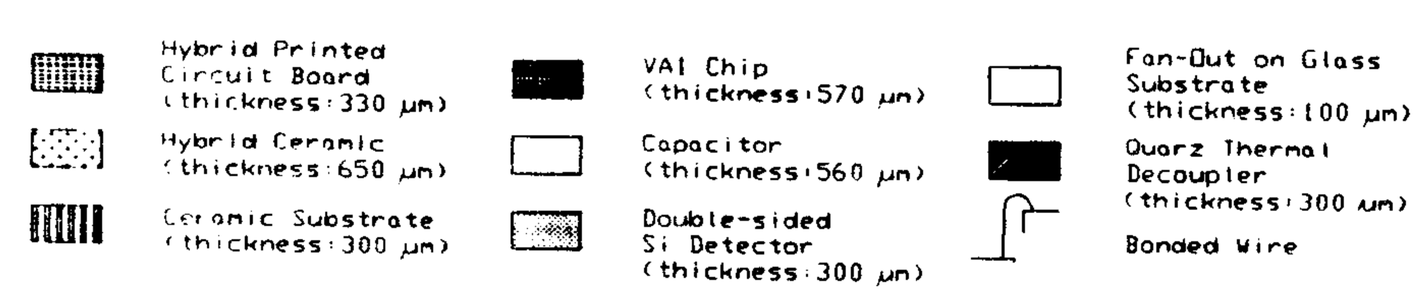

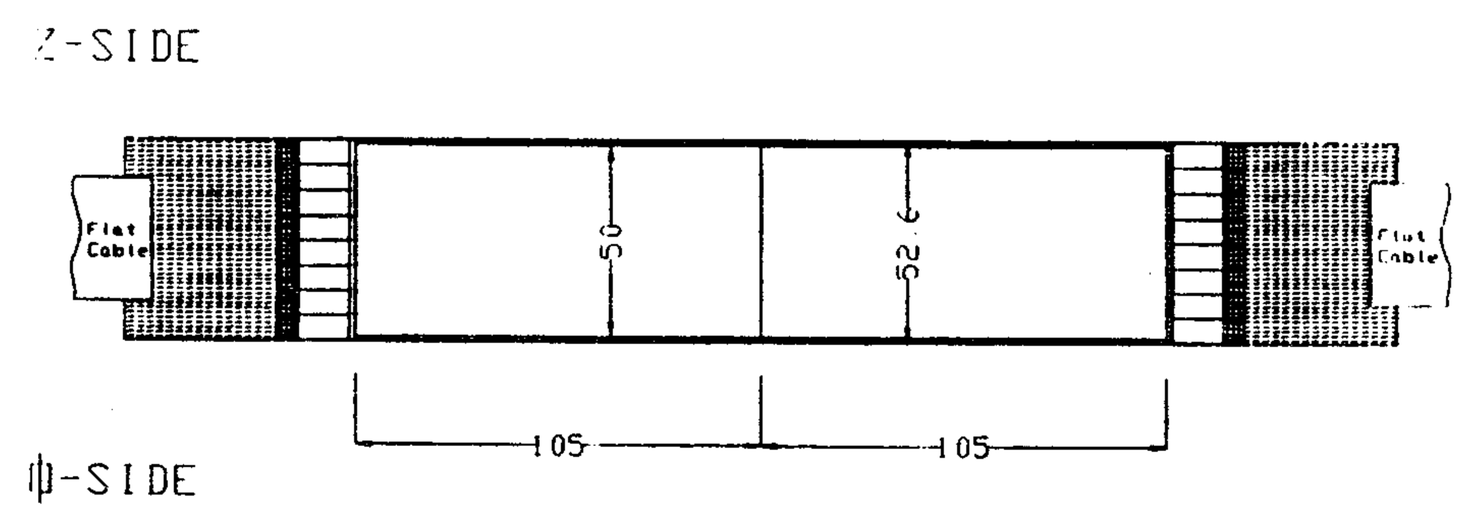

Figure 4.1: ACAD representation of an ISIM (OSIM) module. a) side view with the description of the different parts of the module. b) and c) top and bottom views. Each module ends with two short (about 15 cm) flat cables on one side and one on the other side.

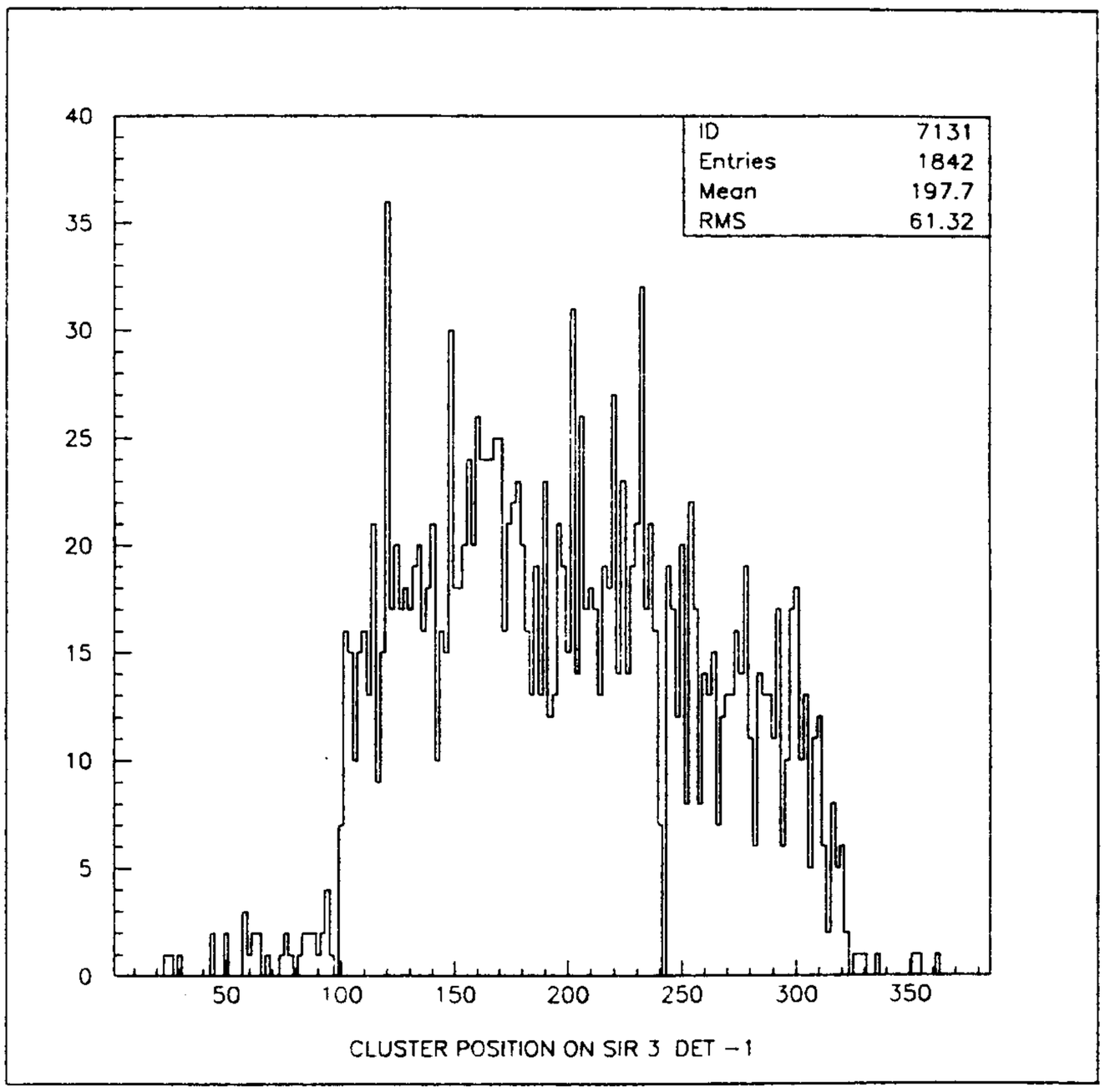

Figure 4.4: Pion beam profile obtained during the May '94 run at CERN. The beam as a y-projection of ~7.5 mm (FWHM). The x-axis is the strip number, the y-axis represents the counting frequencies.

of the full module length)×52.0 mm^2 and a thickness of 100 μm. Two of them will be glued on a module to fully read out the z-side. The glass plates and the masks for the gold strips will be constructed by Baumer IMT, Zurich.

4.1.2 Results of tests on prototypes

A test run on a prototype detector was performed at CERN with minimum ionizing particles (50 GeV/c pions) in May '94. The detector consisted of a double-sided micro-strip silicon detector bearing the same characteristics as the final detector, but being of smaller size, 20×20 mm^2. Furthermore, the electronic chain associated to it was the same that will be used for I&O, but the VIKING chip replaced the VA1 (the VA1 chip will be described in the next paragrapf). Some results of the May '94 test are reported in figs 4.3, 4.4 and 4.5.

Fig. 4.3 shows the response of the prototype detector to a 50 GeV/c pion: the x-axis is the flash ADC channel, and the y-axis is the ADC channel content. Some noisy channels, which stand out from the mean noise, appear at low ADC

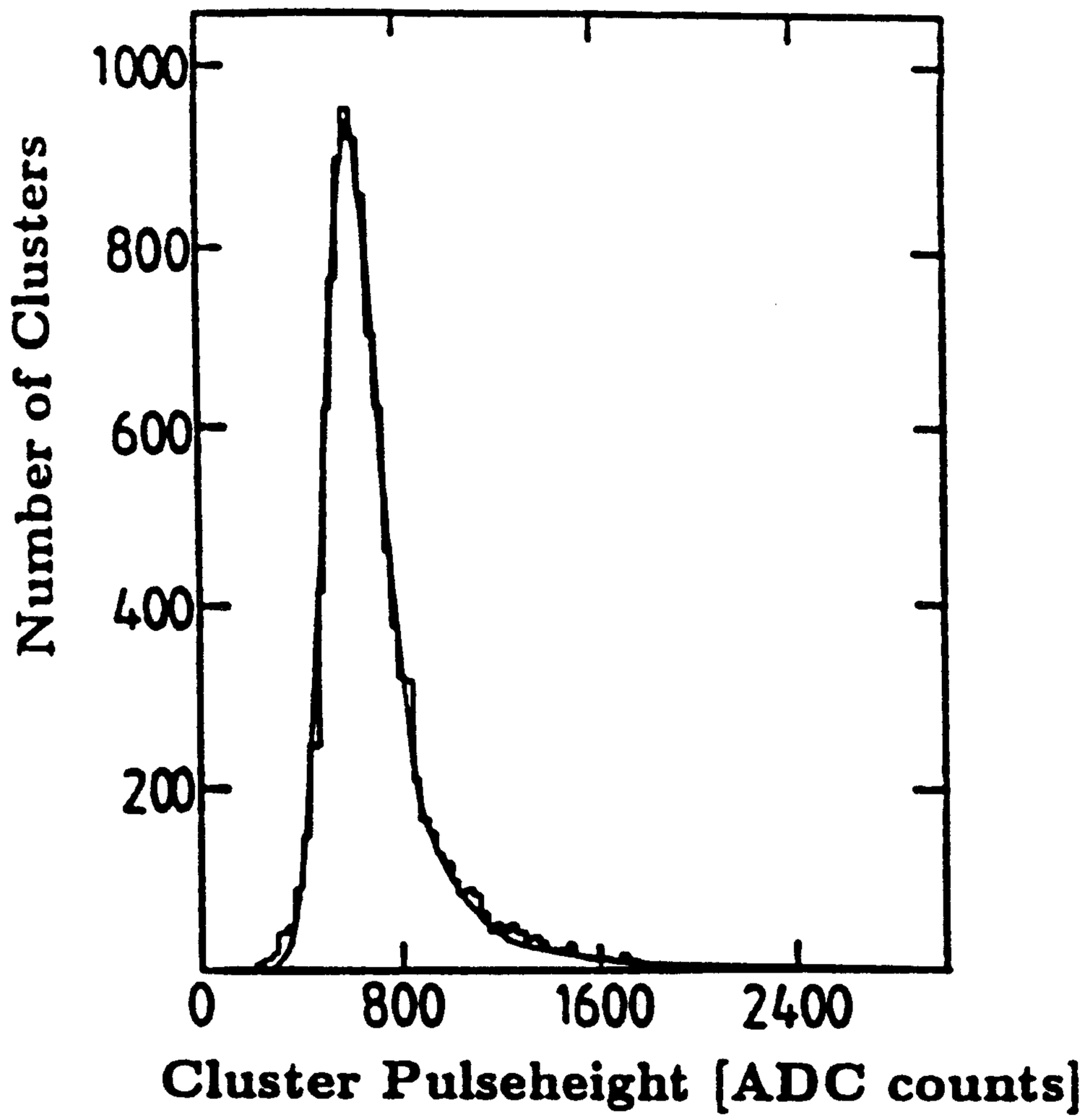

Figure 4.2: Distribution of the energy loss measured in a micro-strip silicon detector 280 μ thick travesed by minimum ionizing particlles. The solid line is a phenomenological calcullation which takes in account the binding energies of electrons and the electronic noise.

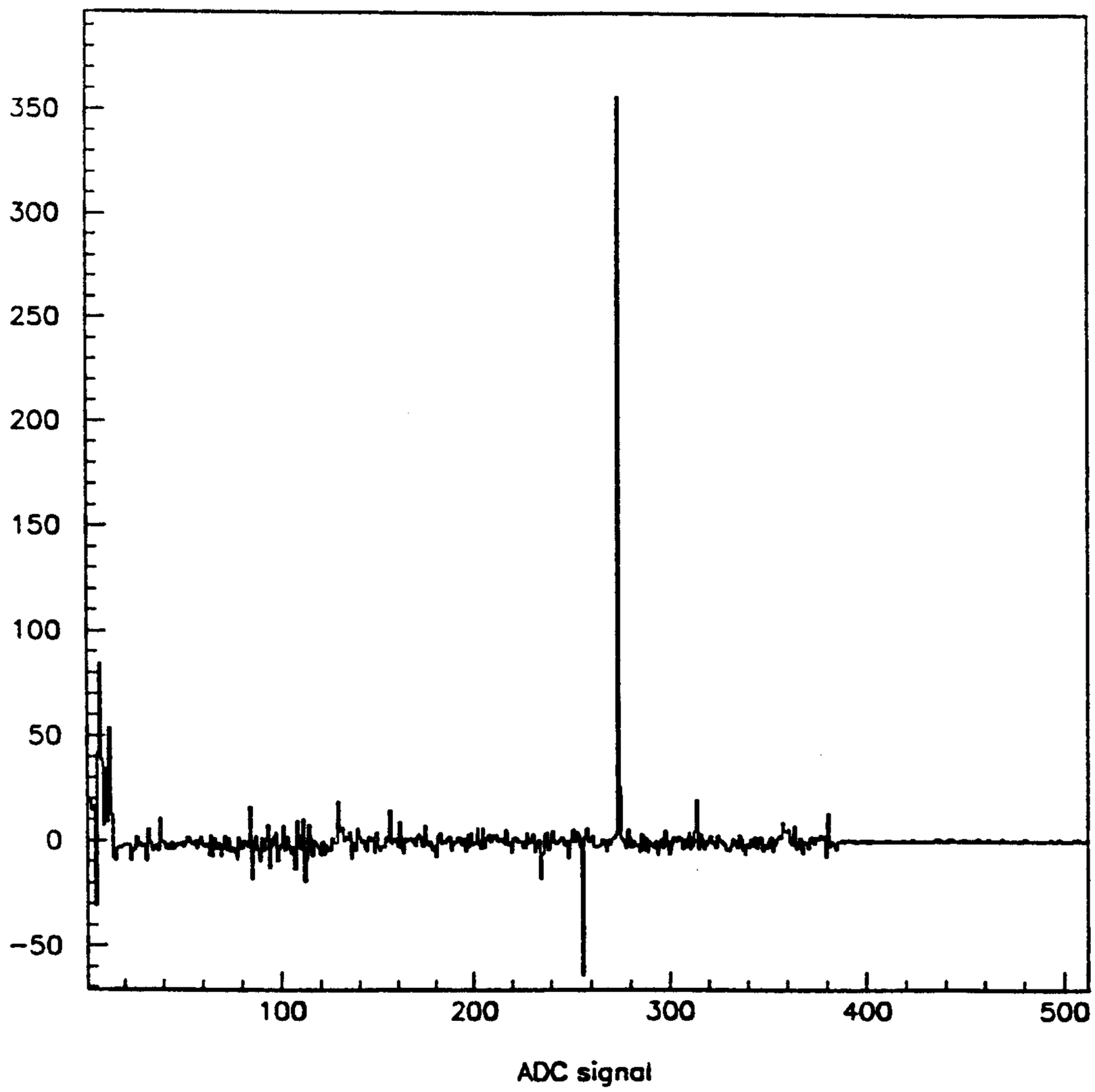

Figure 4.3: Response (raw data) of the prototype silicon detector to a 50 GeV pion from the particle beam. The x-axis in the flas ADC channel and the y-axeis is the ADC channel content.

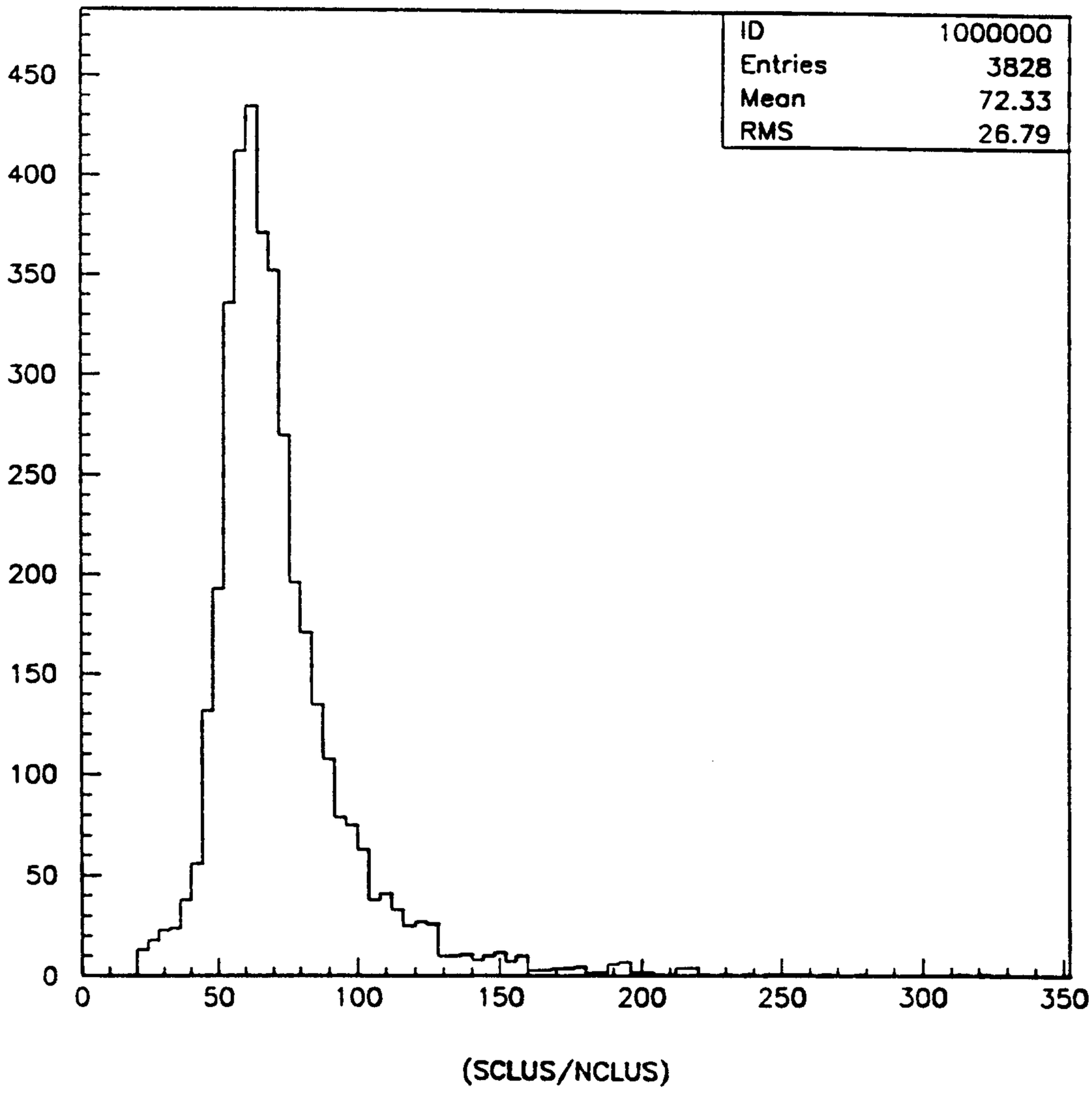

Figure 4.5: Signal to noise ratio distribution for minimum ionizing particles. The mean value is about 70..

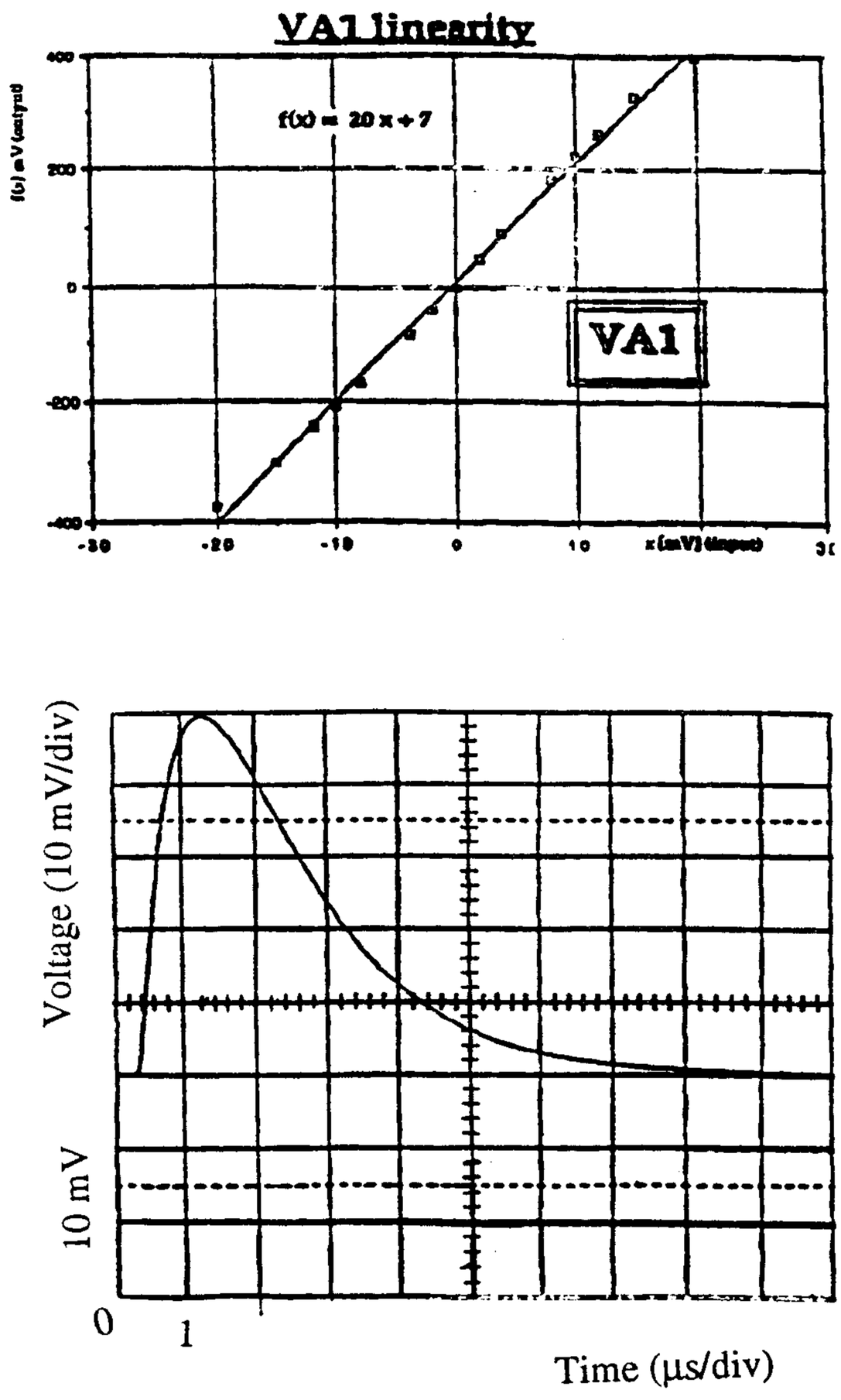

Figure 4.6: Some results from measurements performed on the VA1 chip. The upper figure shows the VA1's linearity, and the lower figure the VA1's output signal. The lower diagram was taken with the Lecroy 7200 High Precision Oscilloscope.

channels, the negative signal at channel 256 marks the end (or the beginning) of the second (third) VIKING and the positive signal is the response of the detector to the passage of a minimum ionizing pion. Fig. 4.4 shows the 100 GeV/c pion beam profile: the data are raw and the threshold is set at the minimum bias. The x-axis is the strip number, and the ordinate represents the counting frequencies. The detector noise is responsible for the counting outside the beam profile region. However, the pedestal subtraction and zero-suppression which are implemented on the CAEN flash ADC's (see the paragraph 4.1.3) will efficiently eliminate any sort of counting due to background signals. Fig. 4.5 shows the signal to noise (S/N) ratio distribution, a mean value of ~70 is obtained for this detector. If a minimum bias is set to S/N~5, then the detector efficiency will slightly be affected while the noise will largely be suppressed (see also fig. 4.3).

More tests are planned. In August 95 a full module will be tested with minimum ionizing particles at CERN. A beam telescope of four small silicon detectors of (the same type used in May '94 test) will check the beam through the module. The spatial resolution to normal and to inclined particle trajectories will be measured as well as the energy resolution of the silicon detector to minimum ionizing particle.

The same beam telescope will be used in Fall '95, when a telescope of two modules will be tested with low- and medium-energy pions at TRIUMF. Pions of low and medium energy will emulate the behavior of 16 MeV kaons and 85 MeV protons on ISIM, respectively, while medium energy pions (100-300 MeV/c) will test the ISIM and OSIM response to π^-_{prompt}. This test will be of importance for particle mass identification: kaons from ϕ-meson decay, protons from non mesonic hypernuclear decay and prompt pions are likely to be identified through their energy release in the silicon detector. These detectors were only tested with minimum ionizing particle[5] giving a moderate energy resolution, $\Delta E/E \sim 50\%$ (FWHM), hence their response to low and medium energy particles must be measured. If the mass identification reveals successful for these particles, then I&O will provide a powerful means of (off-line) particle tagging on a nearly 4π highly granular volume, unlike the TOFINO detector.

4.1.3 The electronics of ISIM and OSIM

The front-end electronics. The I&O detectors will be read out by the VA1 version of the VIKING[6]. This chip integrates and shapes the charge collected by the silicon detector strips, then delivers it upon the arrival of an external trigger signal. The VIKING is capable of reading many strips and, coupled to a hybrid, of multiplexing their outputs into a single readout line. The VA1 characteristics are given in Table 4.1, and some of its performances are reported in fig. 4.6. The measurements were done at CERN with the cooperation of INFN at Trieste.

There are three main sources of noise for a detector channel [6, 7]:

1. The above mentioned noise of the input FET of the preamplifier, $ENC_{preamp} =$

Table 4.1: Characteristics of the VA1 readout chip.

Channels	Pitch(μ m)	Power(mW/Ch.)	Noise(ENCe$^-$)(§)
128	50	1.2	180+7.5e$^-$/pF

§ENCe$^-$: Equivalent Noise Charge, expressed in number of electrons.

$180 + 7.5 \times C_{load}[pF]$, where C_{load} is the external load capacitance;

2. The leakage current of the silicon detector $ENC_{leak} = 130 \times \sqrt{I_{leak}[nA]}$, where I_{leak} is the leakage current for a single channel; and

3. The bias resistor $ENC_{br} = 946/\sqrt{RI_p[M\Omega]}$, where R_p is the parallel resistance of the bias resistor and the feedback resistor of the preamplifier.

By assuming $C_{load} \sim 30pF$, $I_{leak} \sim 0.6nA$ and $R_p \sim 8\Omega$ for I&O, the total noise, ENC_t, is, then obtained by summing in quadrature the ENC_{preamp}, ENC_{leak} and ENC_{br} single noises, and it results to be $ENC_t \sim 520$. This number should be compared with the number of electrons given by a minimum ionizing particle in a Si medium 300 μm thick, ~25,000. Therefore the signal to noise ratio S/N is ~50, somewhat lower than the (mean) S/N~70 obtained during the tests at CERN with the prototype detector (see fig. 4.5). However, this is mainly due to the low capacitance of the prototype detector, being of small size, 20×20 mm^2, with respect to the size of the final detector, 195×52 mm^2.

In the case of hypernuclear studies, the external fast trigger delivered by TOFINO should match the peaking-time of the VA1 output signal which reaches the maximum between 1.0 and 1.5 μs (see fig. 4.6) after a K^+K^- event has taken place.

VA1's are produced by IDEAS, Oslo. The quantity needed (580 chips) will be supplied in Winter '95.

Eight VA1's will be mounted on a hybrid as well as DC capacitors. Three hybrids will equip a module: two for the z direction and one for the ϕ direction. Their performances will be tested both in laboratory and under experimental conditions (at TRIUMF). Hybrids will be connected through flat cables to repeater cards, physically located at about 50 cm from the hybrids. Repeater cards will deliver the multiplexed analog signals through single-wire coaxial cables to flash ADC's, which will be placed outside from the FINUDA magnet. Hybrids will be designed and produced by either IDEAS or MIPOT. The base layout and electronic scheme are those of the ALEPH's new detector. However, they have to be modified to account for the characteristics of the VA1 chip.

The readout electronics. The analog signals from the VIKING (or VA1) and hybrid system are commonly digitized by charge-sensitive flash ADC's (FADC). FADC's must have a built-in zero-suppression system in order not to read out

Table 4.2: Readout of the Vertex Detector of FINUDA

VA1 readout pitch	50 μm
Channels per VA1 chip	128
ϕ-side	
strip pitch	50 μm
readout pitch	50 μm
# of strip read out	1024
# of VA1 chips	8
z-side	
strip pitch	50 μm
readout pitch	100 μm
# of strip read out	2048
# of VA1 chips	16
# of V550-C-RAMS to read out ϕ and z	1 + 1/2

all the strips ($\sim 4 * 10^4$ for FINUDA) once a valid event has triggered the detector. Moreover, a FADC must be a VME module, to meet the FINUDA's standard. FADC's are currently developed by CAEN, Viareggio, that, within July will deliver two prototype boards (named V550 SIROCCO-DRAMS) for tests. The main features of DRAMS's are:

- 2 channels per card;
- 2048 channels per card;
- 2 MHz of conversion rate;
- 10 bit linear conversion;
- zero-suppression and pedestal subtraction;
- fast read-out via VME;
- diagnostic and self-test capabilities.

Table 4.2 summarizes the characteristics of the readout for one module of the vertex detector of FINUDA. It will consist of 18 modules and about 6 of them will be spare.

4.2 The low-mass high resolution drift chambers

4.2.1 General description

Sixteen low mass high resolution drift chambers are the central part of the tracking system. They will be assembled to form two coaxial cylinders of octagonal shape

centred on the beam axis (Fig. 2.2). They are rotated around their common axis by 11^0 and the lateral sides of the frames are overlapped in order to maximize the apparatus acceptance for charged particles of $\sim$ 250 MeV/c. In order to obtain a good momentum resolution it is necessary to reconstruct with high accuracy the track of the particle. In fact [8], [9], [10],

$$\left[\frac{\Delta p}{p}\right]^2 = \left\{\left[\frac{\Delta p}{p}\right]^2_{meas} + \left[\frac{\Delta p}{p}\right]^2_{ms}\right\} \tag{4.1}$$

where $[\Delta p/p]_{meas}$ is the contribution due to the instrumental error of the localizing devices and $[\Delta p/p]_{ms}$ is the contribution due to the multiple scattering.

It follows that a gas with low mass, low electron drift velocity, low electron diffusion and high and stable gain has to be chosen and a very high mechanical precision is needed [11].

4.2.2 Cell and gas choice

In what follows the criteria to identify a gas mixture which best suits the FINUDA conditions, namely best possible localization performance in the presence of a magnetic field of 1.1 Tesla and low atomic number, are described. The last requirement is mandatory not only for the minimization of the multiple Coulomb scattering, but also to reduce the absorption of the low energy photon background, inevitably present at an (e^+e^-) collider.

Helium based mixtures are the obvious candidates and, first of all, we calculated the characteristics of several such mixtures ($He-DME$, $He-CH_4$, $He-C_2H_6$, $He-C_4H_{10}$) at different percentages [12]. $He-DME$ mixtures seemed slightly better than the other ones and then an experimental study with a small–sized drift chamber prototype on a $\sim$ 2 GeV/c π^+ beam at CERN was performed. We do not report here many details of such measurements, already presented at previous Sessions of the Scientific Committee of LNF. We present only the precision on the localization (Fig. 4.7) for perpendicular and inclined (20^0) tracks as well as the efficiency along the cell (Fig. 4.8). It can be seen that the performances are very satisfactory and in agreement with calculations. We notice that these data were taken in absence of magnetic field.

However, in the following, we decided to discard the $He-DME$ mixtures mostly for the risks of inflammability of DME diffusing across the very thin mylar window of the chambers of FINUDA and we decided to use a $He-C_4H_{10}$ (70-30) mixture that was proven to offer safe and stable conditions over two months of operation on a real scale prototype. Fig. 4.9 and Fig. 4.10 show the drift velocity and the diffusion characteristics of the $He-C_4H_{10}$ mixtures.

The accurate operation of a drift chamber depends largely on the precise knowledge of the space–time relationship, which depends on the gas mixture employed and the electric field in the chamber. Drift velocities in helium based gases were

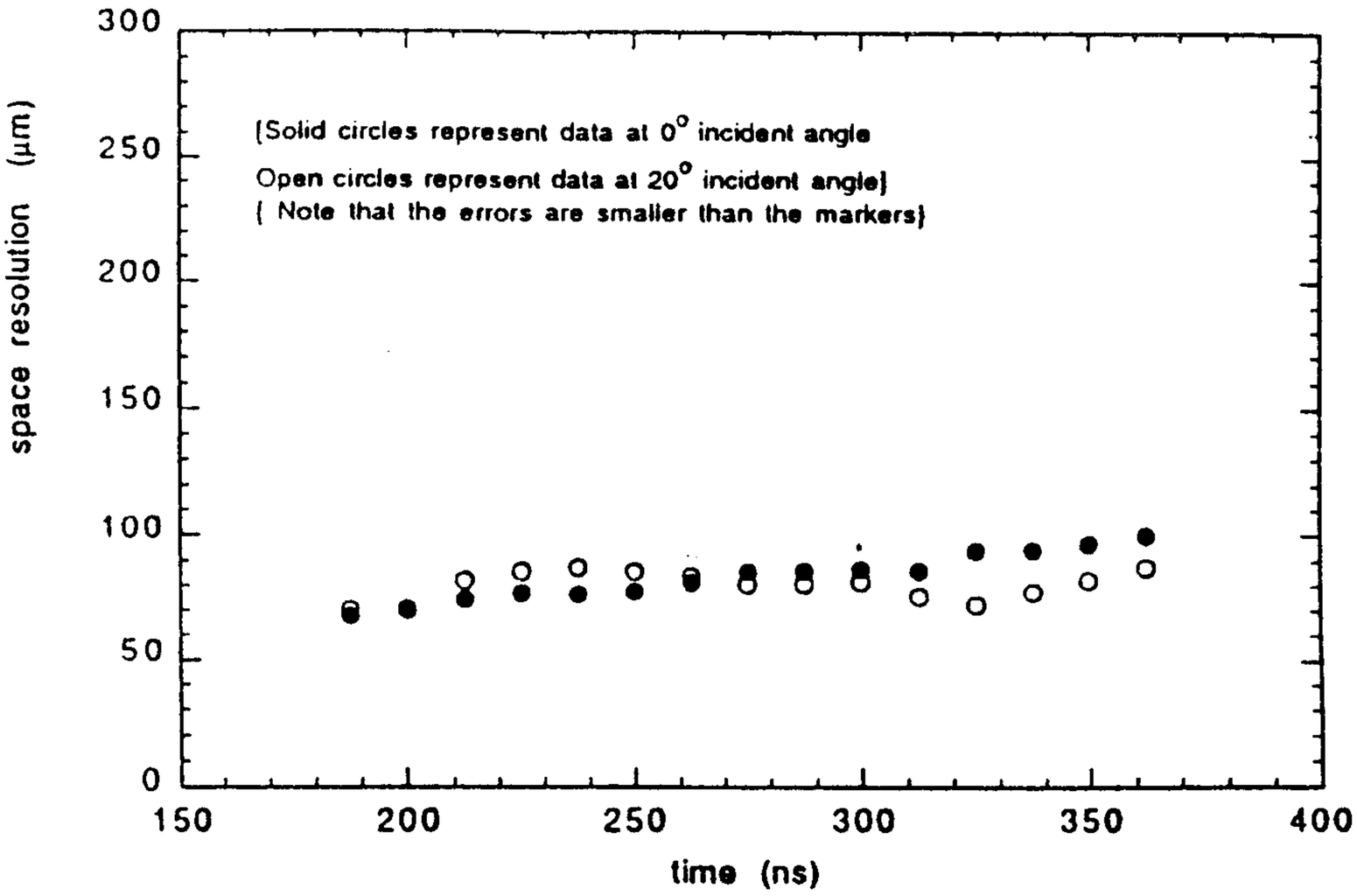

Figure 4.7: Spatial resolution measured with a small size drift chamber prototype filled with a $He - DME$ (70-30) gas mixture with a π^+ beam impinging at 0^0 and 20^0 respectively incident angles.

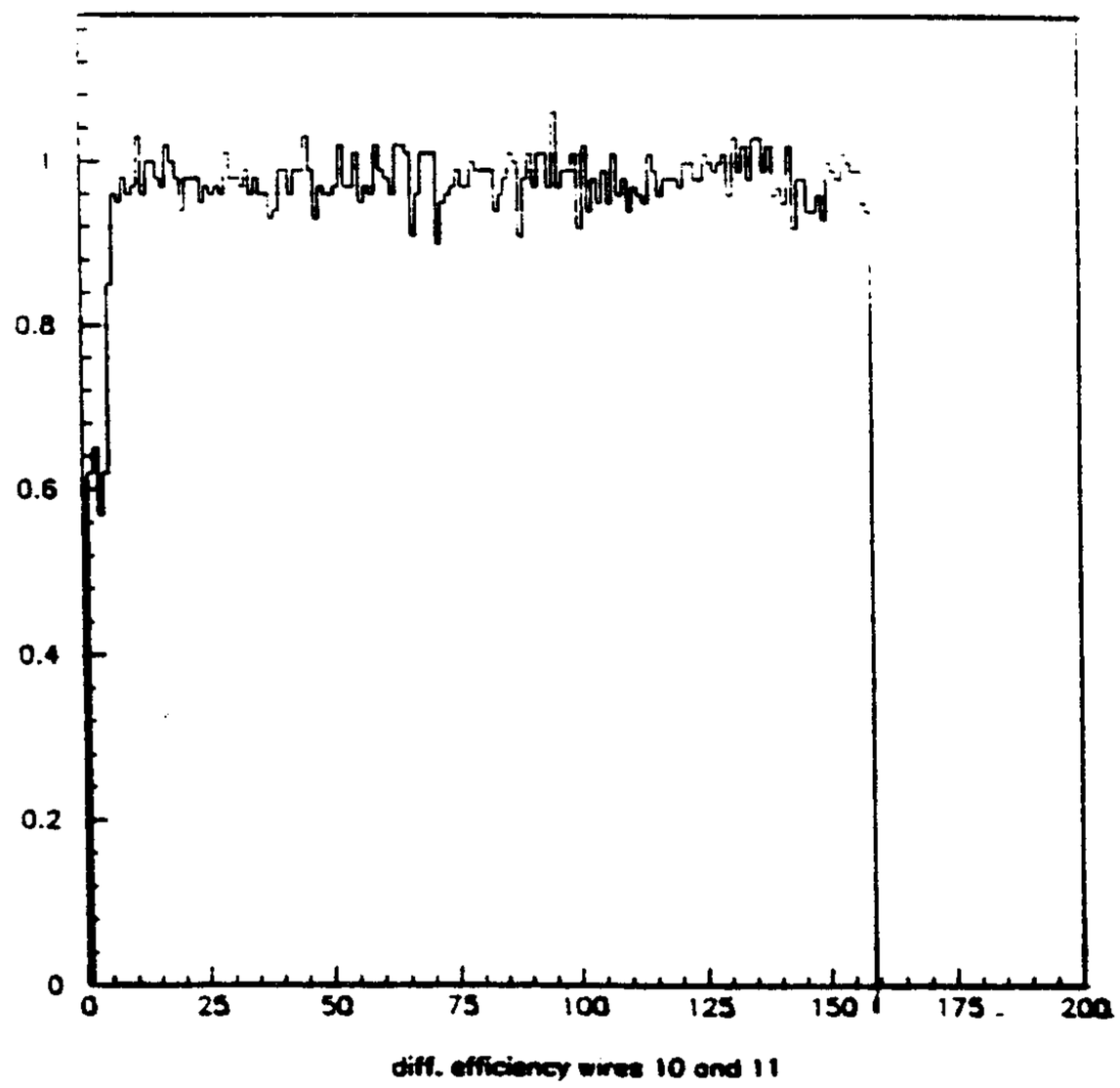

Figure 4.8: Measured efficiency along the cell of a small size drift chamber prototype filled with a $He - DME$ (70-30) gas mixture. (The abscissa of the end of the spectrum correspond to 25 mm)

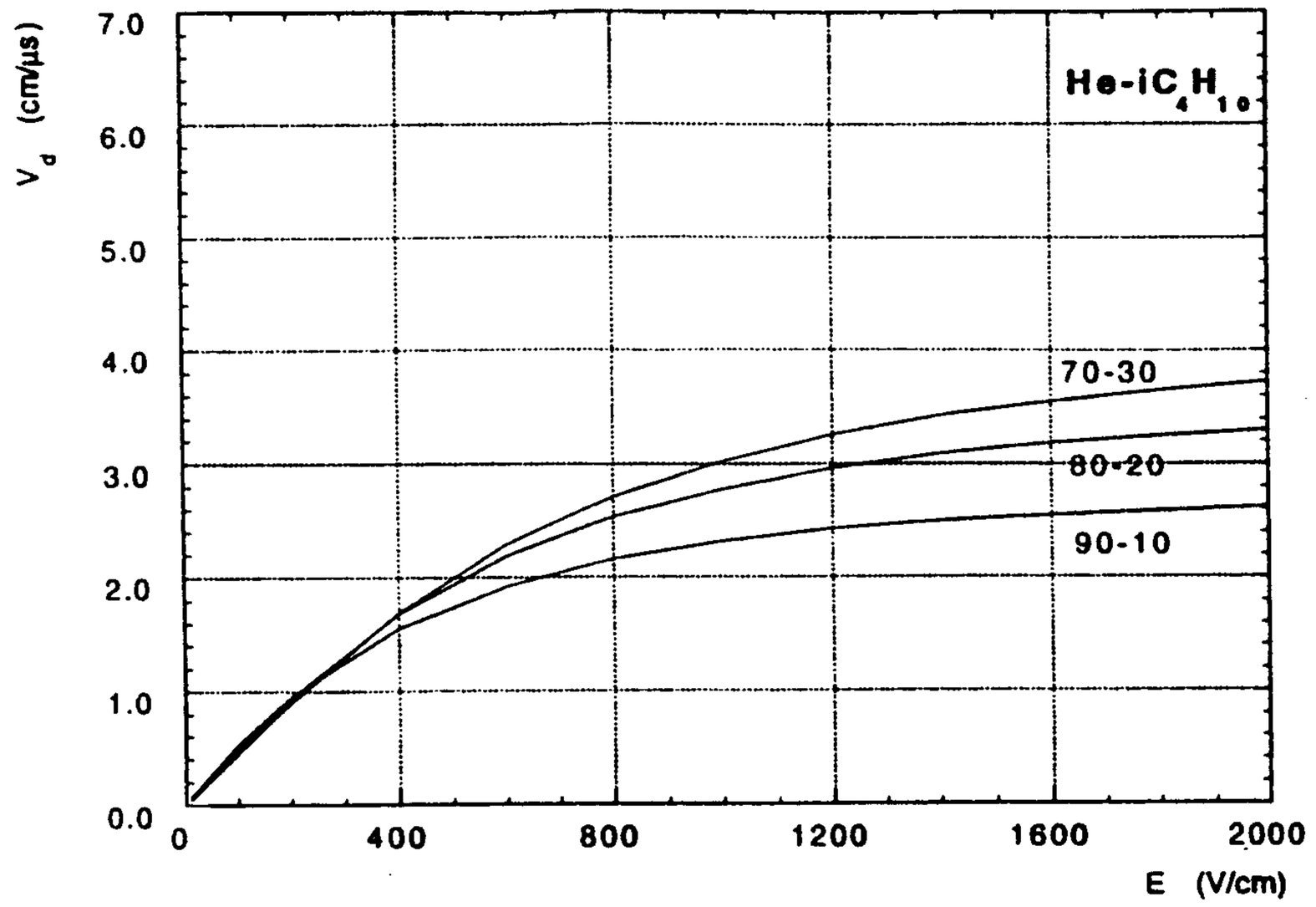

Figure 4.9: Calculated drift velocity of $He - iC_4H_{10}$ mixtures as a function of the electric field.

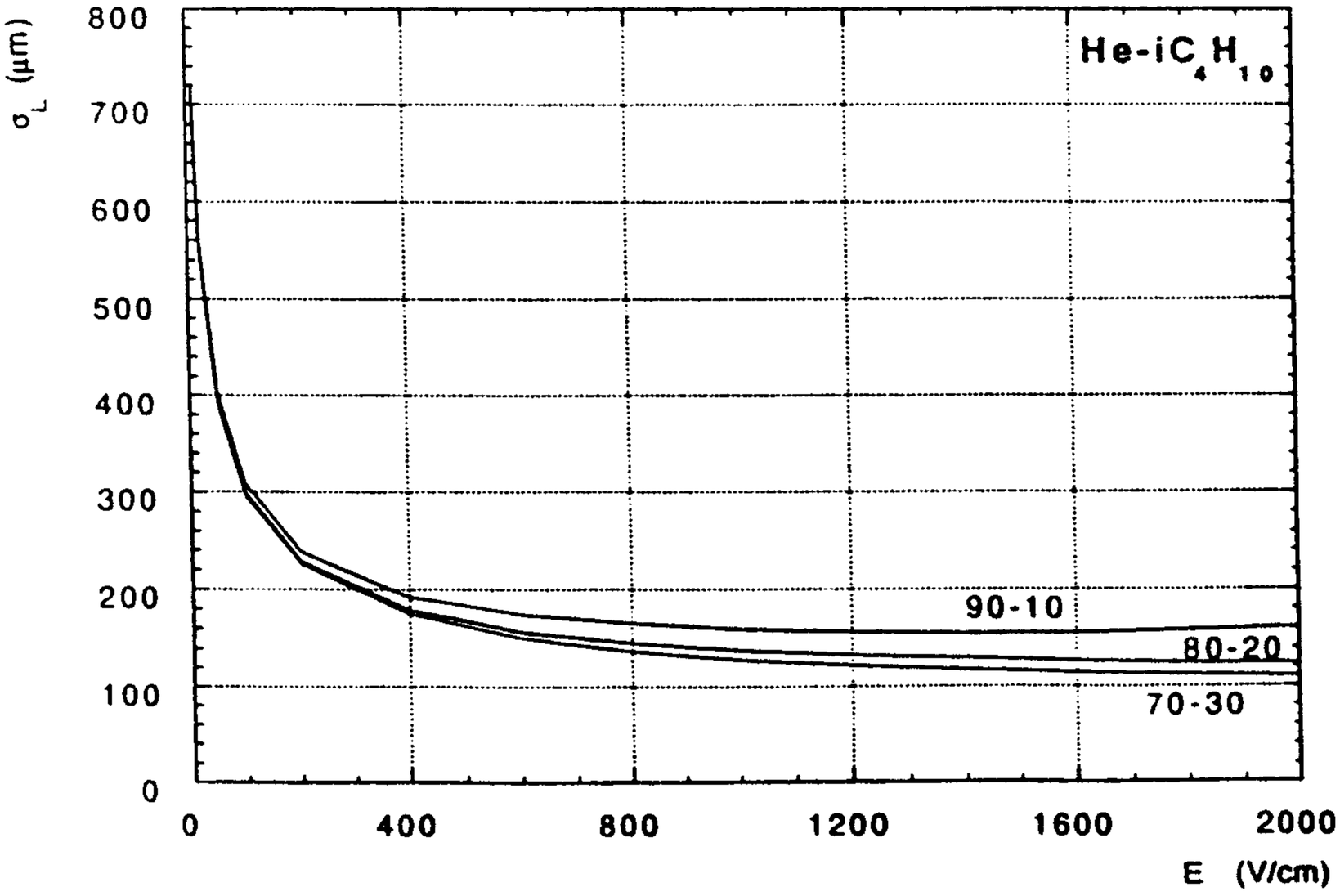

Figure 4.10: Calculated longitudinal diffusion coefficient of $He - iiC_4H_{10}$ mixtures as a function of the electric field.

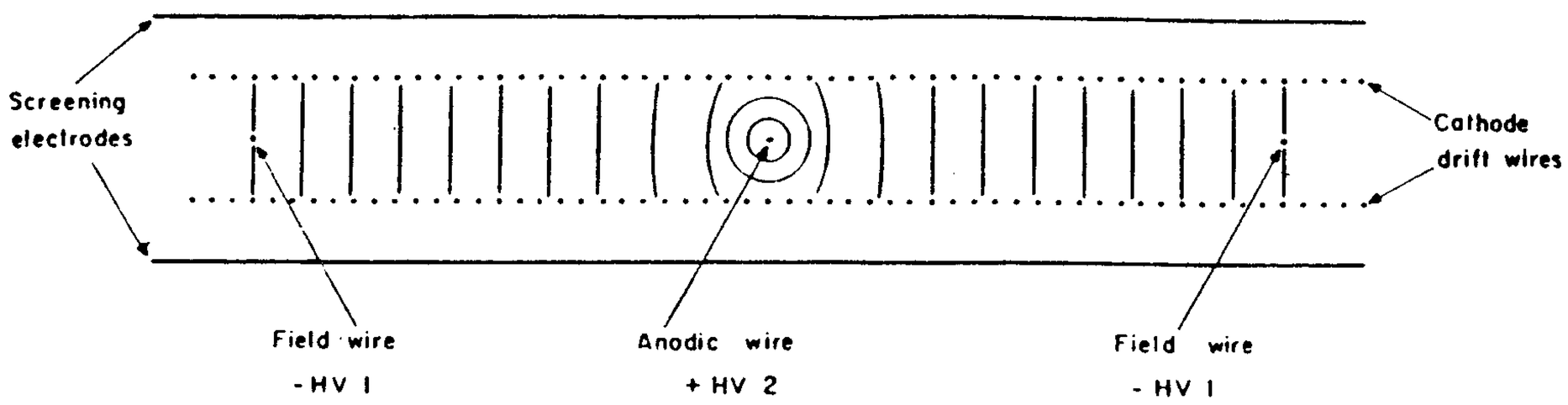

Figure 4.11: Layout of a high accuracy drift chamber cell.

found generally non-saturated even up to electric fields of almost 2 kV/cm [13]. To compensate for this effect the electric field in the sensitive region of the drift cell must be as uniform as possible.

Fig.4.11 shows the layout of a high accuracy drift chamber [14], [15]. A pair of stainless steel anodes, necessary for the solution of the left-right ambiguity, is sandwiched between two cathode planes consisting of Cu-Be wires placed 1 mm apart. Field wires are inserted in the anode plane to avoid low field regions in the sensitive volumes and to maintain a uniform electric field. To compensate for the Lorentz angle in the presence of a magnetic field, a shift, corresponding to the cathode wire pitch, can be applied to the voltage distribution of the cathode planes in order to obtain the equipotential contours as shown in fig. 4.12. All the above calculations for the electric field and electron drift were performed with the GARFIELD code.

The drift chamber characteristics are the following. The cathode wires spacing has been opted to be 1 mm so that the field is not too modulated close to the cathode plane, and distant enough for ease of machining and fabrication of the printed circuit board, and soldering. In a magnetic field, electron drift lines are tilted and we found that $He - C_4H_{10}$ mixtures have the smallest Lorentz angles, not too sensitive to the relative percentage of C_4H_{10}. The resulting electron drift lines and isochrones in the absence and presence of a magnetic field of 1.1 T are shown in Fig. 4.13, 4.14, respectively. The space time relationship is linear for most of the cell, both for perpendicular tracks as well as for tracks with large angles, as seen from Fig. 4.15. Fig. 4.16 shows the Lorentz angle for this gas mixture as a function of electric and magnetic field.

For a good overall chamber resolution a good position accuracy of each of the electrodes is required together with the requirement of minimum B-field non unifor-

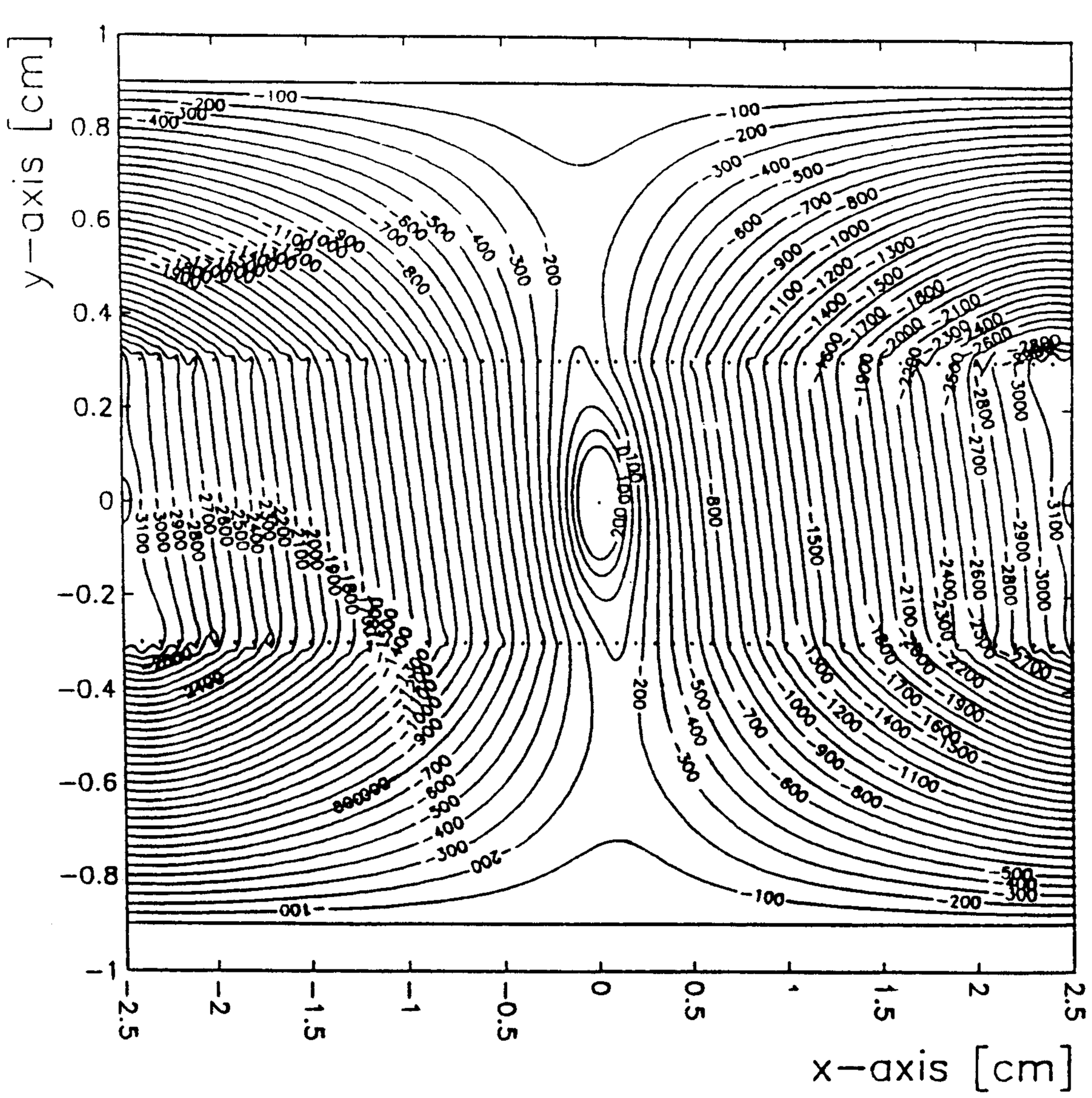

Figure 4.12: Calculated equipotential contours when a shift of 1 mm, corresponding to the cathode wire pitch, is applied to the distribution voltage of the cathode planes, to compensate for the Lorentz angle. V_{anode} = 1.9 kV, $V_{cathode}$ = - 3.7 kV.

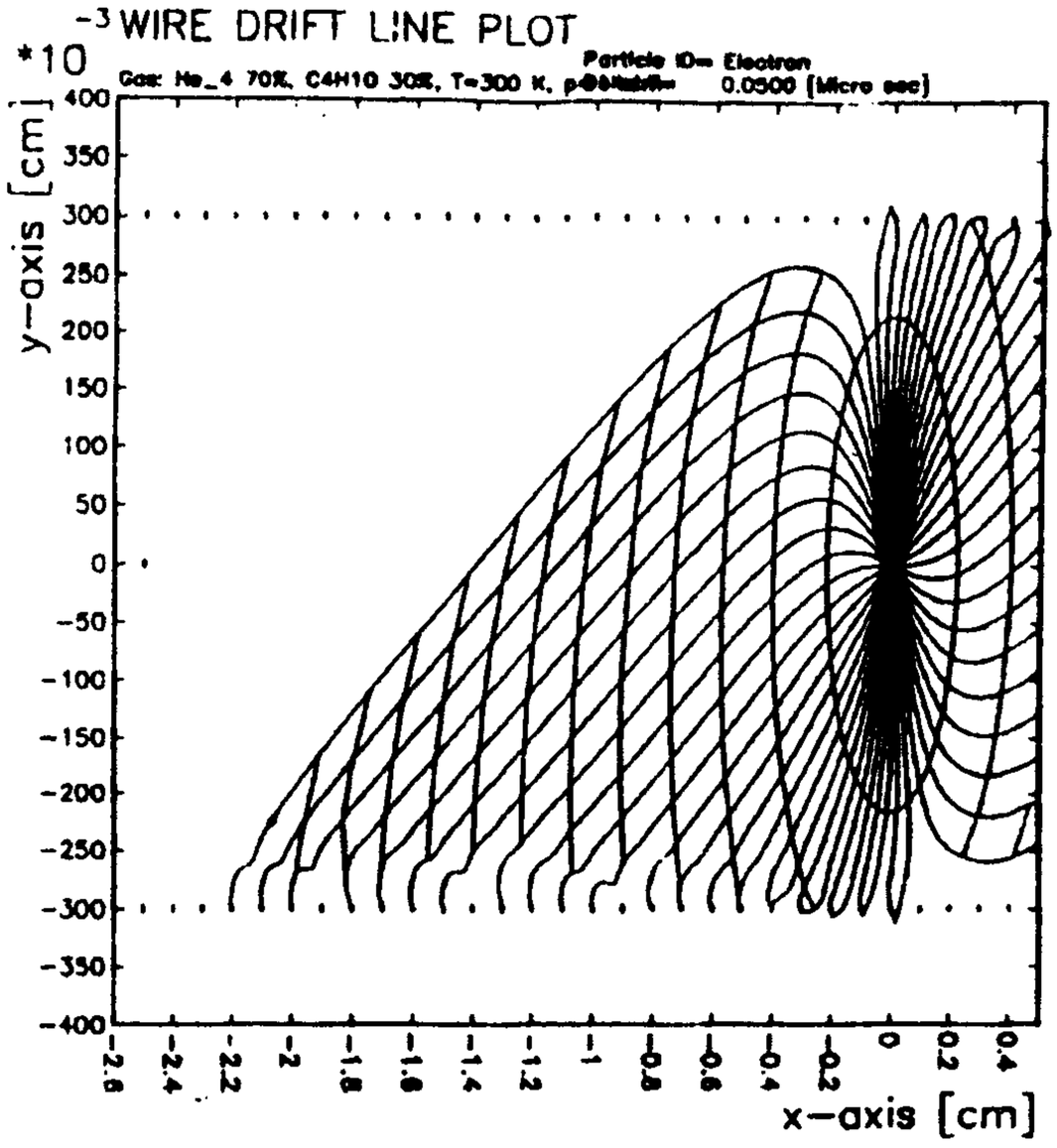

Figure 4.13: Calculated drift lines and isochrones for a $He - C_4H_{10}$ (70-30) mixture with potentials on the cathodes tilted by 1 mm, without magnetic field.

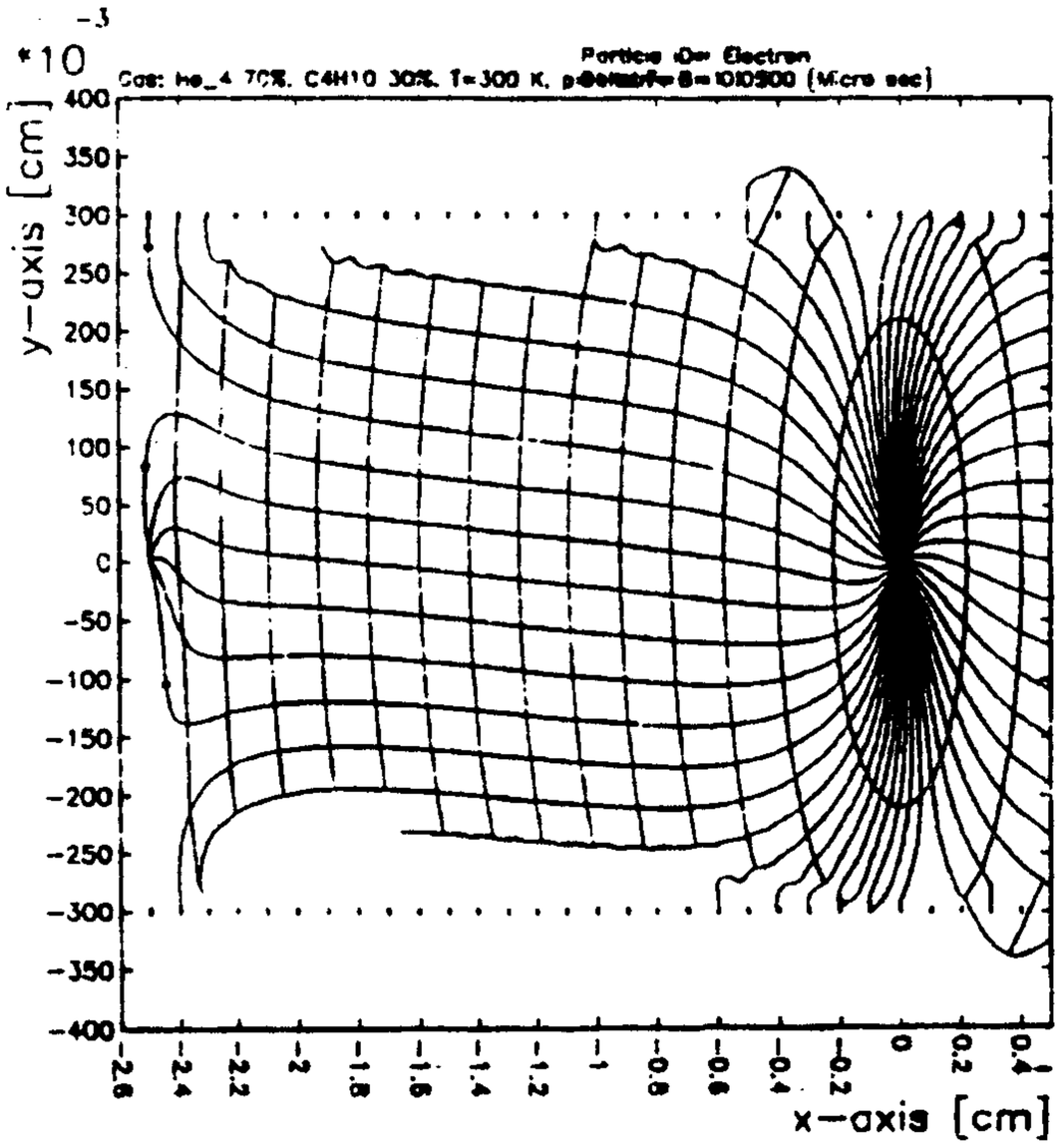

Figure 4.14: The same of fig. 4.13, but with a magnetic field of 1.1 T.

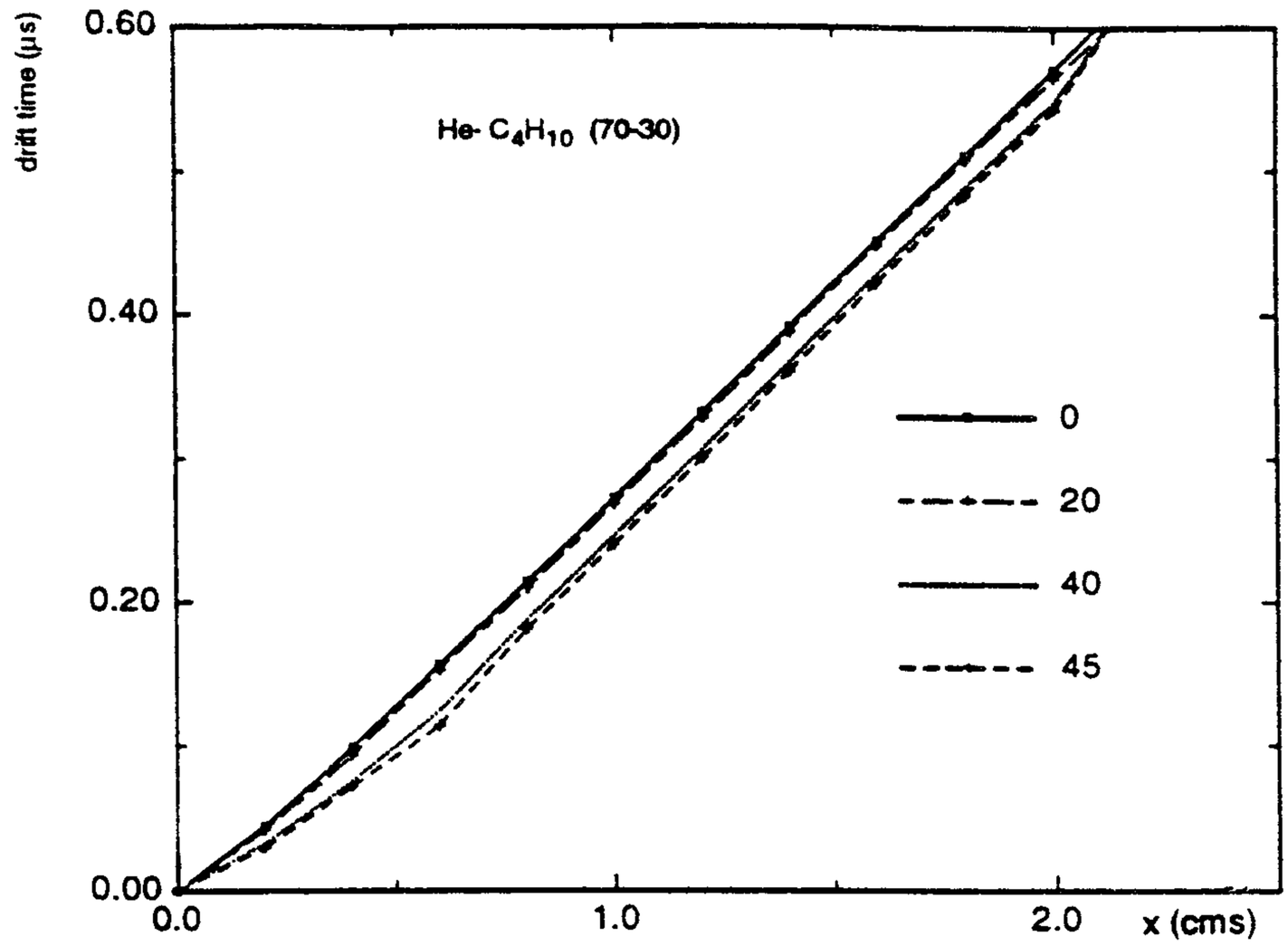

Figure 4.15: Space time relationship for the cell, with a $He-C_4H_{10}$ (70-30) mixture, for perpendicular tracks as well as for tracks incident at different angles.

mities both in magnitude and in angle, since they can change the Lorentz angle as well as other transport properties of the gas.

In the following a study on how the mechanical precision of the elements of a drift cell affect the performance of a drift chamber is presented.

The deviations of the reconstructed space coordinates arising from errors in positioning are computed.

First of all, the effect of a displacement of 100 μm in x and 500 μm in y in the positioning of the anode is studied. The differences of the minimum drift time for electrons arriving with a track normal to the plane of the chamber with respect to the normal geometry are plotted in fig. 4.17 (a,b,c). The displacements in y can be a consequence of electrostatic forces and seems the more significant source of error, which can be 50 μm or more depending on the drift velocity ($\sim$ 2.5 cm/μs).

Displacements for the field wire and cathode wires were similarly studied by displacing the field wire by 500 μm in y and two cathode wires at each extremity of the cell by 50 μm in x and y. The deviations from normal geometry, for perpendicular tracks, are shown in fig.4.18, and no significant effect is apparent.

Rather large angles of incidence of incoming tracks to the drift chambers due to low momenta are expected, as shown in fig. 4.19. In some cases these angles exceed 40 degrees. To have an accurate tracker, it is necessary that the performance in terms of spatial resolution of the drift chambers is not too much degraded in going from perpendicular tracks to tracks at large angles. In case of standard gas, namely argon-isobutane (methylal), it has been seen that the spatial accuracy worsens from $\sim$100 μm to $\sim$150 μm in going from perpendicular tracks to tracks at 45 degrees. Since a helium based mixture is slower, in addition to its lower primary ion statistics, this worsening is expected to be greater.

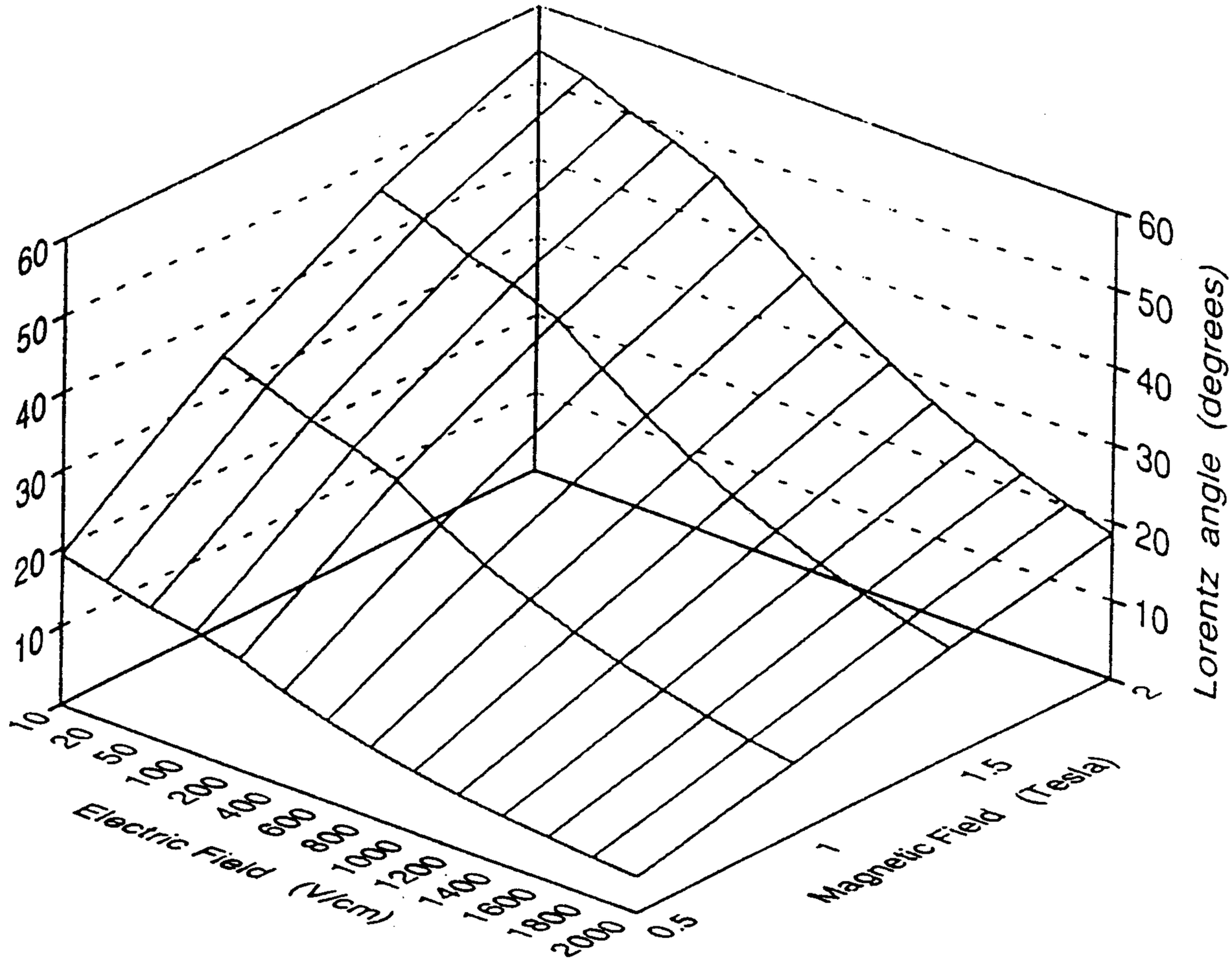

Figure 4.16: Lorentz angle as a function of electric and magnetic field for a $He - C_4H_{10}$ (70-30) gas mixture.

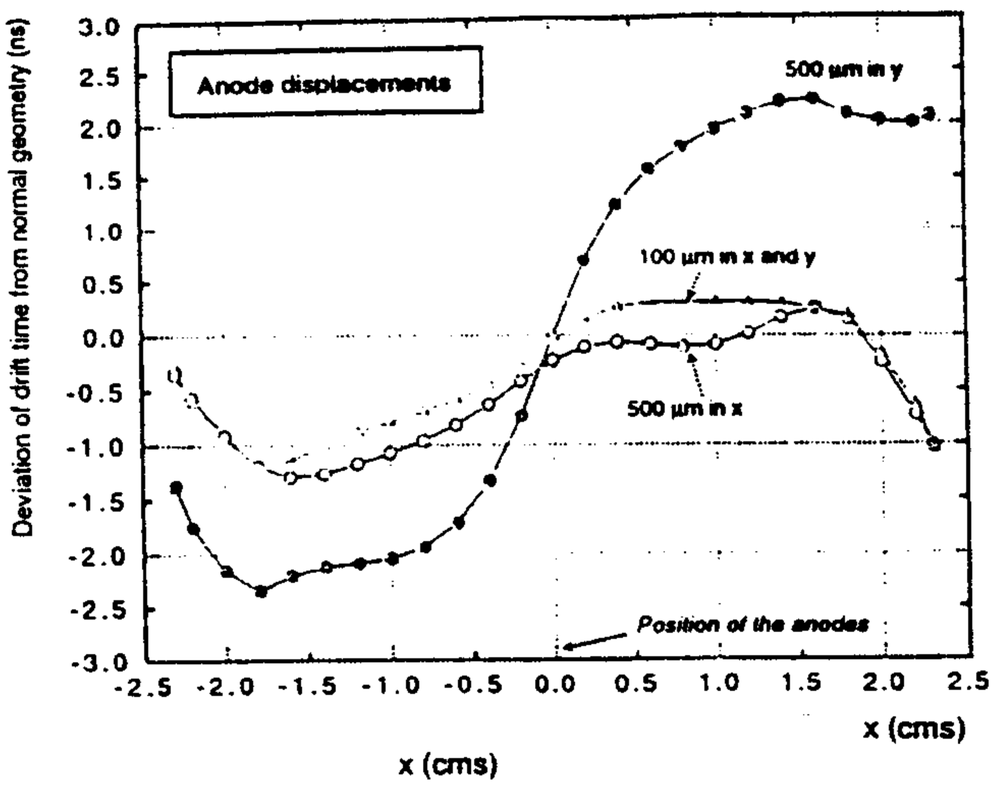

A

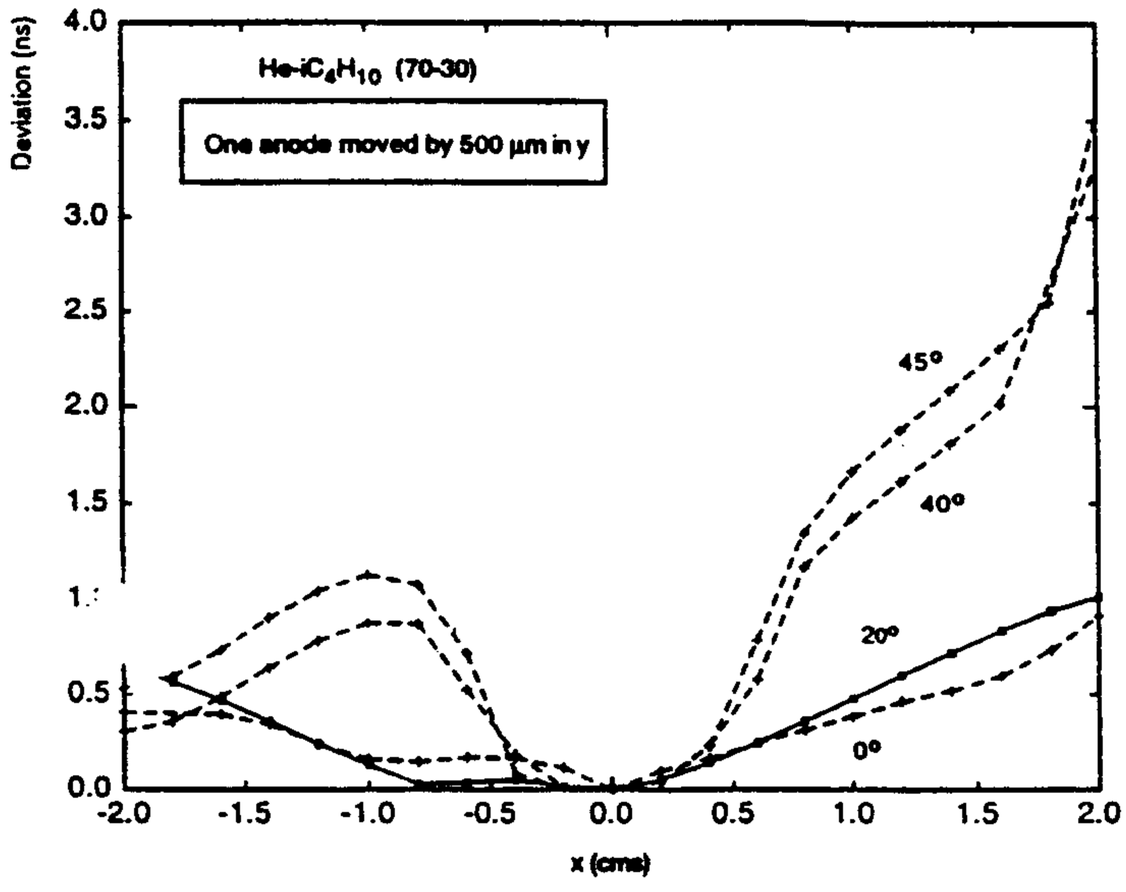

B

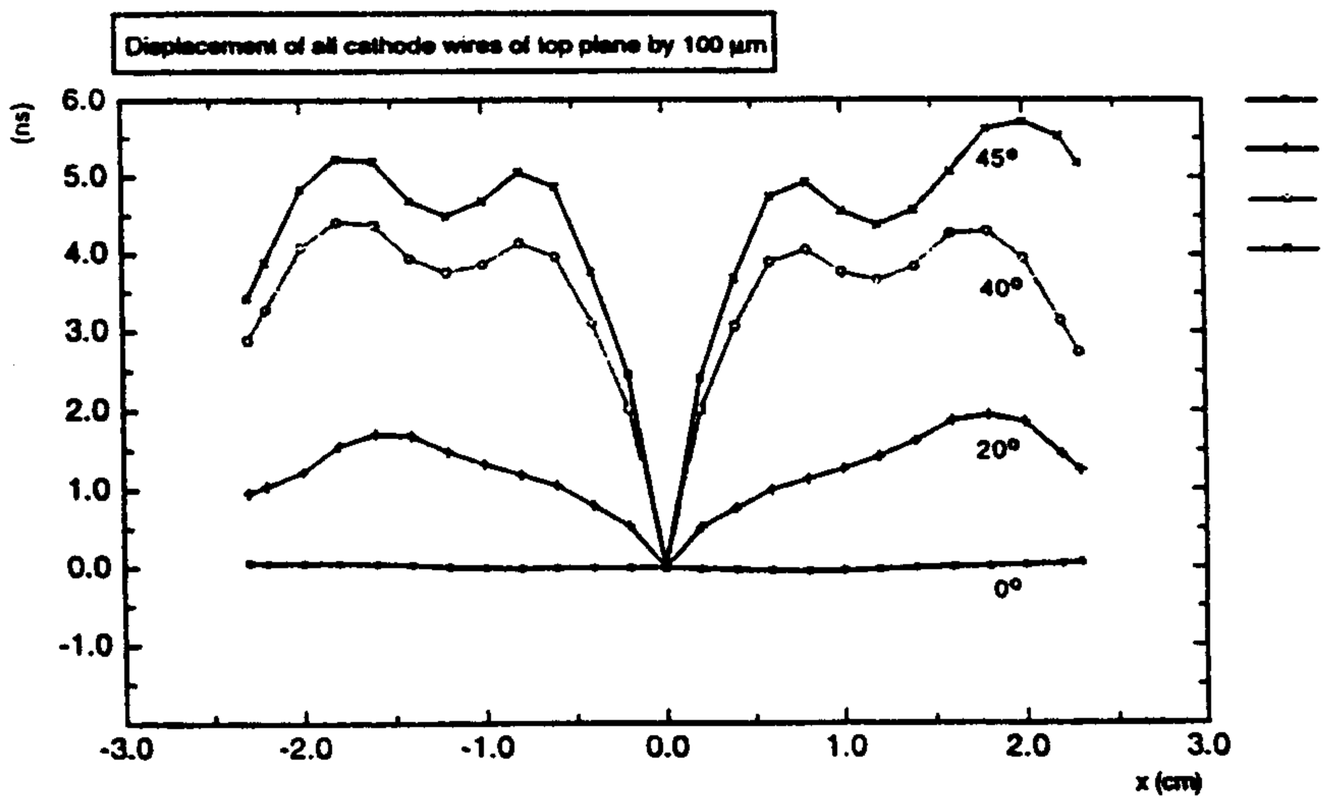

C

Figure 4.17: Differences in drift time from normal geometry for some anode and cathode displacements.

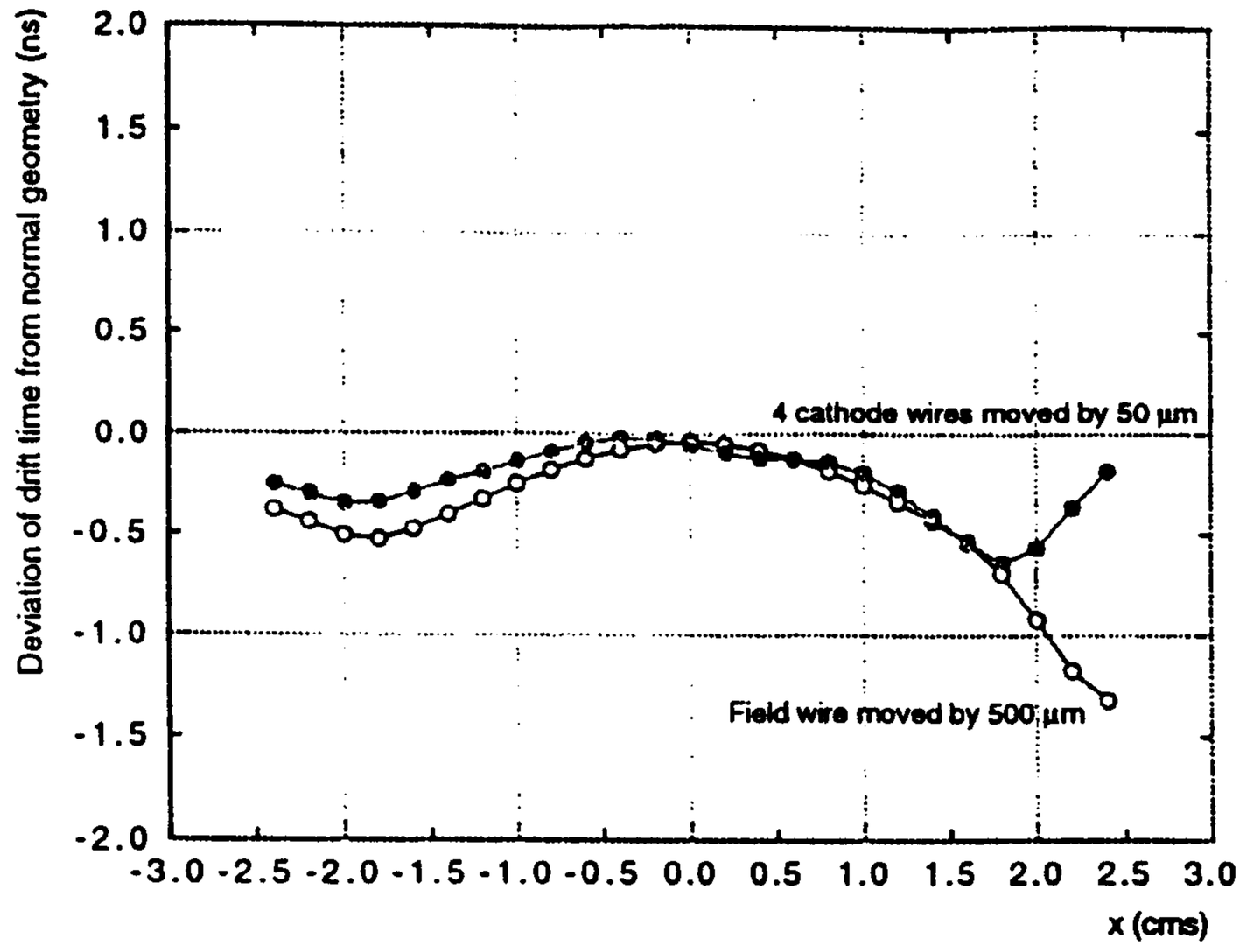

Figure 4.18: Differences in drift time from normal geometry for a field wire displacement of 500 μm in y and two cathode wires at each end of the cell displaced by 50 μm.

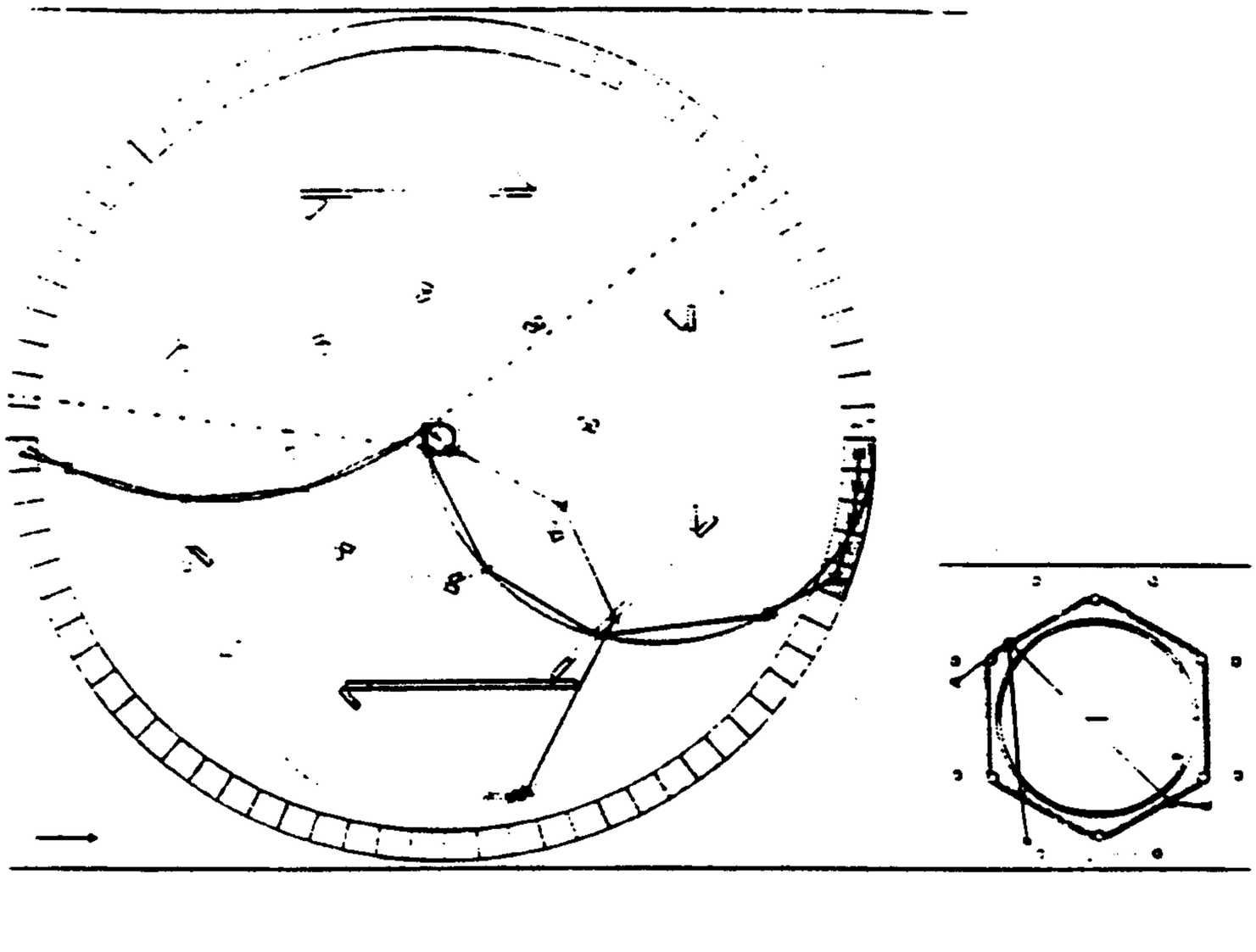

Figure 4.19: M.C. simulation of a typical event in FINUDA.

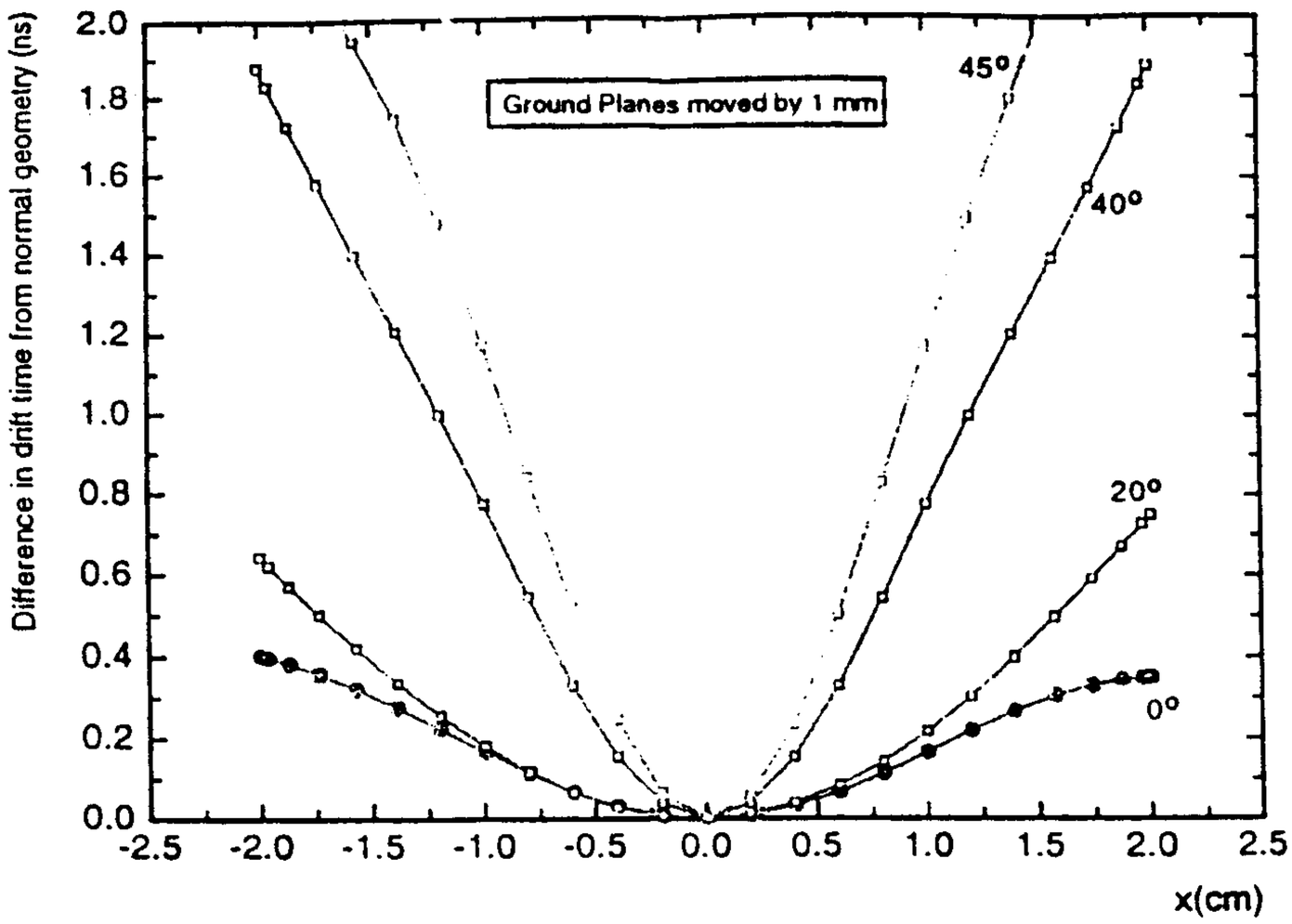

Figure 4.20: Difference between drift time of normal geometry and that with ground planes moved by 1 mm.

Due to the pressure differences in the two regions of the chamber, there may be a sagitta in the ground plane foil. The results are shown in fig. 4.20 for tracks at 20°, 40° and 45°. However, we recall that, knowing the incident angle from the rough data, we may apply further software corrections which include the above effects and finally arrive to a precision of $\sim$ 150 μm also for the inclined tracks.

4.2.3 Drift Chamber prototype

General description

Each drift chamber is built up by five glass fiber frames (fig.4.21) supporting mylar, cathode and anode wires, and two external aluminum frames necessary to reinforce the structure and to give the exact position for the anode and cathode frames with locating pegs. This material is the most commonly used because it gives a good electrical insulation and avoids ageing effects with the gases usually utilized; its weight is quite low and does not produce significant out-gassing pollutant [16]. The frames are sandwiched and strongly clamped with screws in order to obtain a rigid structure and to squash the sealant o-rings. The frames are specularly sandwiched with respect to the anode frame.

Starting from the outside, there are the two aluminum frames, then two glass fiber frames, called cover frames, on which mylar sheets on both sides are glued. Then there are the glass fiber cathode frames, on which the Copper-Beryllium cathode wires of 50 μm diameter are soldered, and finally the anode frame on which the Stainless Steel anode wires of 25 μm diameter and Copper-Beryllium field wires of 50 μm diameter are soldered. Our choice to separate anode from cathode planes is to better control the positioning of the wire to form a correct cell. The wires are

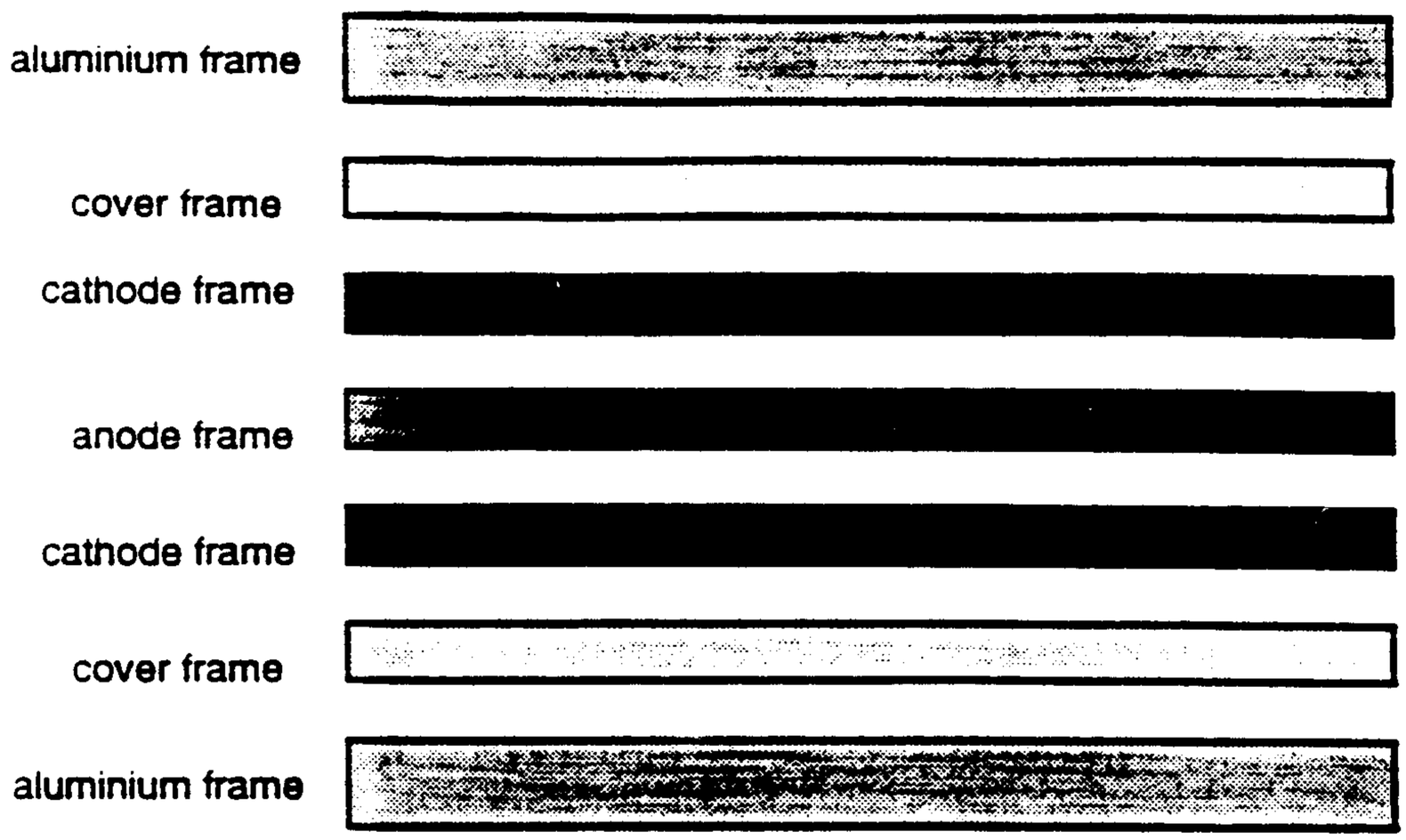

Figure 4.21: Order of the drift chamber frames.

parallel to each other and the drift chamber will be placed with the wires parallel to the beam axis.

General dimensions

For the glass fiber prototype the external dimensions, excluding the printed circuits, are shown in fig. 4.22. The total length is 1450 mm and the width is 720 mm. Including the printed circuits glued on the anode and cathode frames, the length increases from 1450 mm to 1530 mm. The total thickness of the five glass fiber frames is 30 mm.

The free length of the cathode and field wires is 1150 mm. The free length of the anode wires is 1150 mm but the total length between the two soldering point is about 1180 mm.

Weight

The weight of each frame is indicated in Table 4.3. Then the total weight of all the frames is about 41.5 Kg. Adding screws, o-rings and gas connectors the total weight is about 45.0 Kg.

Cover frames and mylar sheets

The two cover frames are designed to close the drift region in order to permit the gas to flow inside the drift chamber and to get a better uniformity of the electric field obtained with a thin aluminum coating on the mylar sheet (fig.4.21).

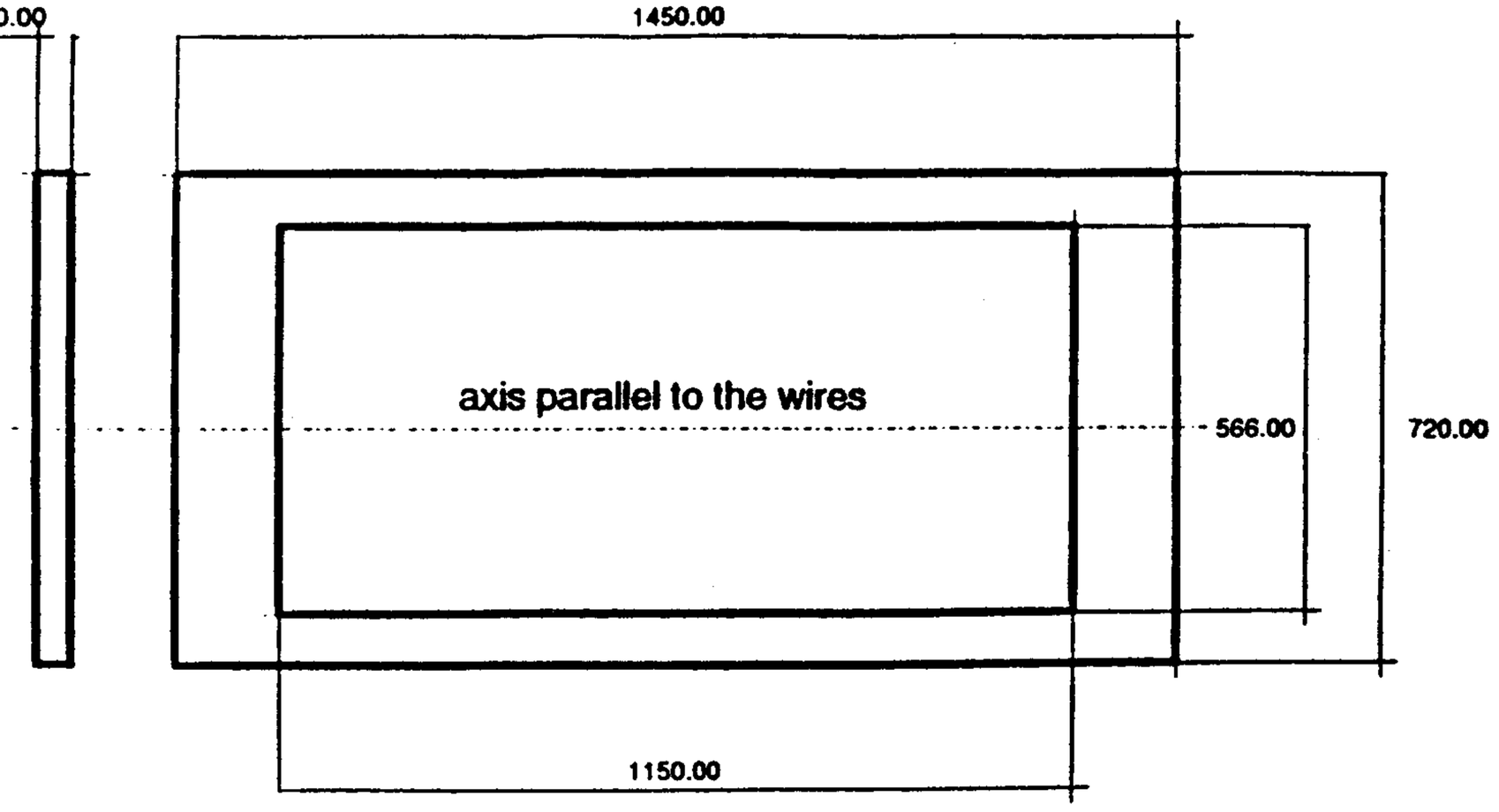

Figure 4.22: Dimensions of the Drift Chamber Prototype.

Table 4.3: Characteristics of the frames of the drift chambers

Frame name	material	Dimensions (mm)	weight (Kg)
Supporting frame	aluminum	1450x720x10	9.5
Cover frame	glass fiber	1450x720x6	4.5
Cathode frame	glass fiber	1450x720x6	4.5
Anode frame	glass fiber	1450x720x6	4.5

For this purpose, on the cover frame, an aluminized mylar sheet , 12 μm thick, was glued with the aluminum layer faced inward the drift chamber, and a 6 μm thick aluminized mylar sheet was glued on the other side, with the aluminum coating faced outward the drift cell. In this way we obtain a good electric contact with the ground. On the other cover frame, an aluminized mylar sheet, 12 μm thick, was glued faced inward the drift chamber. On the other side a not aluminized mylar sheet, 50 μm thick, was glued to have the possibility of observing the displacement of the internal mylar sheet. A displacement of less then 1 mm when the gas was flowing in the chamber was measured. For the final chamber we will ensure that the displacement of the internal mylar plane will be well less than 1 mm by reducing the pressure difference between the two gas volumes.

Gas flow

A series of grooves, designed to optimize the gas flow inside the drift chamber, are placed on both ends of the chamber, as shown in fig. 4.23. The gas enters directly the drift chamber on one end, and goes out on the other end of the chamber through the grooves. Then it enters the two external volumes. This flow guarantees that the internal pressure is kept higher with respect to that one of the external volumes. So the internal mylar sheet can't be displaced towards the cathode wires, avoiding electric discharges between the cathode and the mylar plane. The force acting between the mylar and the cathode plane is negligible [17].

Between each frame there is an o-ring to avoid the leakage of the gas mixture. As said before the o-ring material (EPDM) has been chosen such as to give no significant out-gassing pollutant also after a long period of operation and radiation exposure [18].

The gas leakage occurs mostly across the 6 μm thick aluminized mylar sheet, and not from the o-rings and the mechanical gas connectors.

Cell dimensions and description

The disposition of wires and mylar sheets constituting the cell is illustrated in fig. 4.24. The picture is obtained by sectioning the drift chamber with a plane orthogonal to the wires.

The cell is built up of two parallel layers of cathode wires at a relative distance of 6 mm with two anode wires placed in the center. In the prototype, four cells with stainless steel anode wires with a diameter of 25 μm, 200 μm apart, and seven cells with stainless steel anode wires with a diameter of 32 μm were made. In three of the latter seven cells the anode wires were placed at a distance of 200 μm, in two cells the wires are 300 μm apart, in the last two cells, they are 400 and 500 μm apart, respectively. Two anode wires are needed in order to eliminate the left-right ambiguity. Copper-Beryllium field wires, 50 μm diameter, close the cell. The distance between the two field wires is 50 mm and the cathode wire pitch is 1 mm.

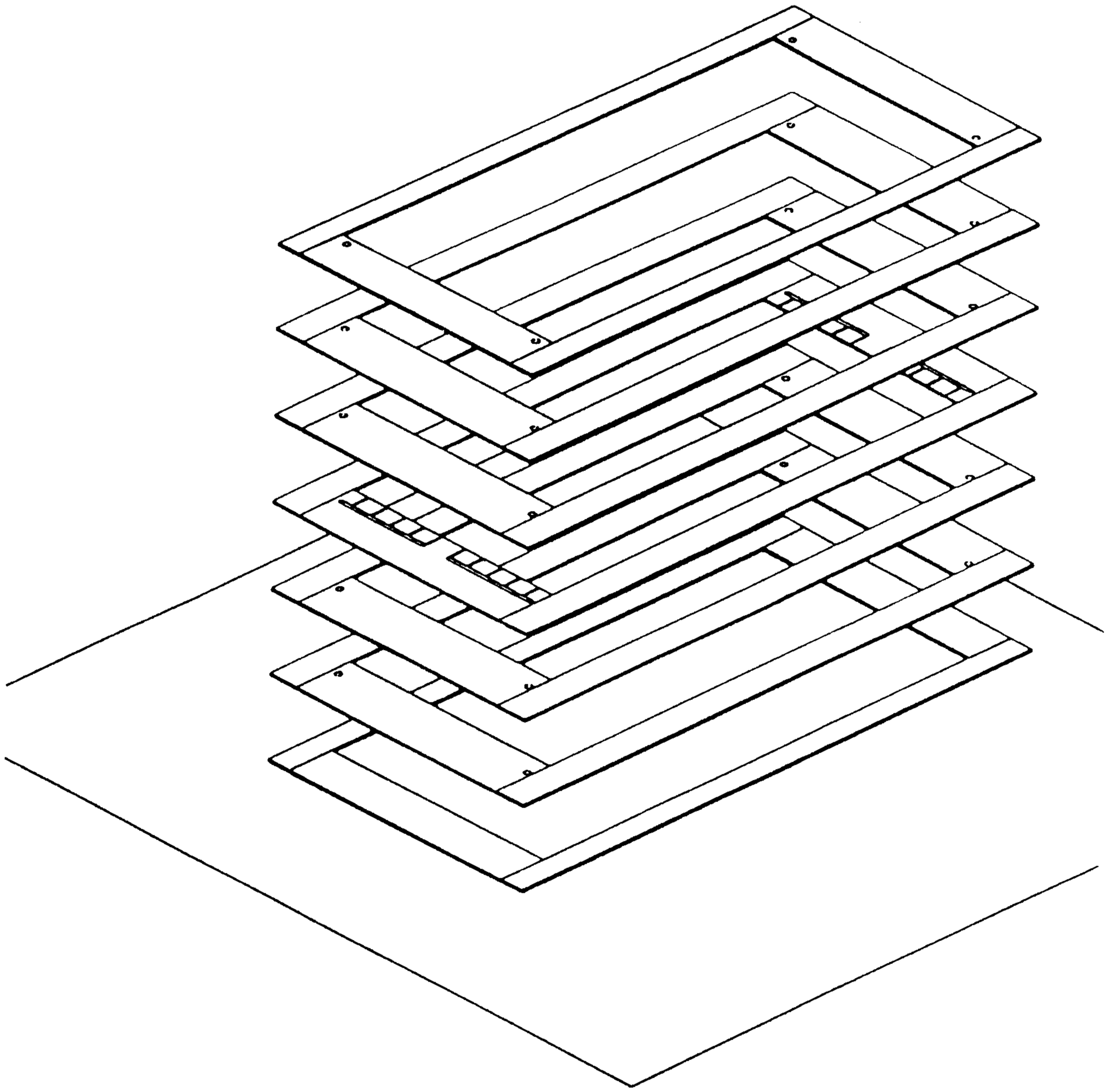

Figure 4.23: Exploded view of the drift chamber frames and gas grooves.

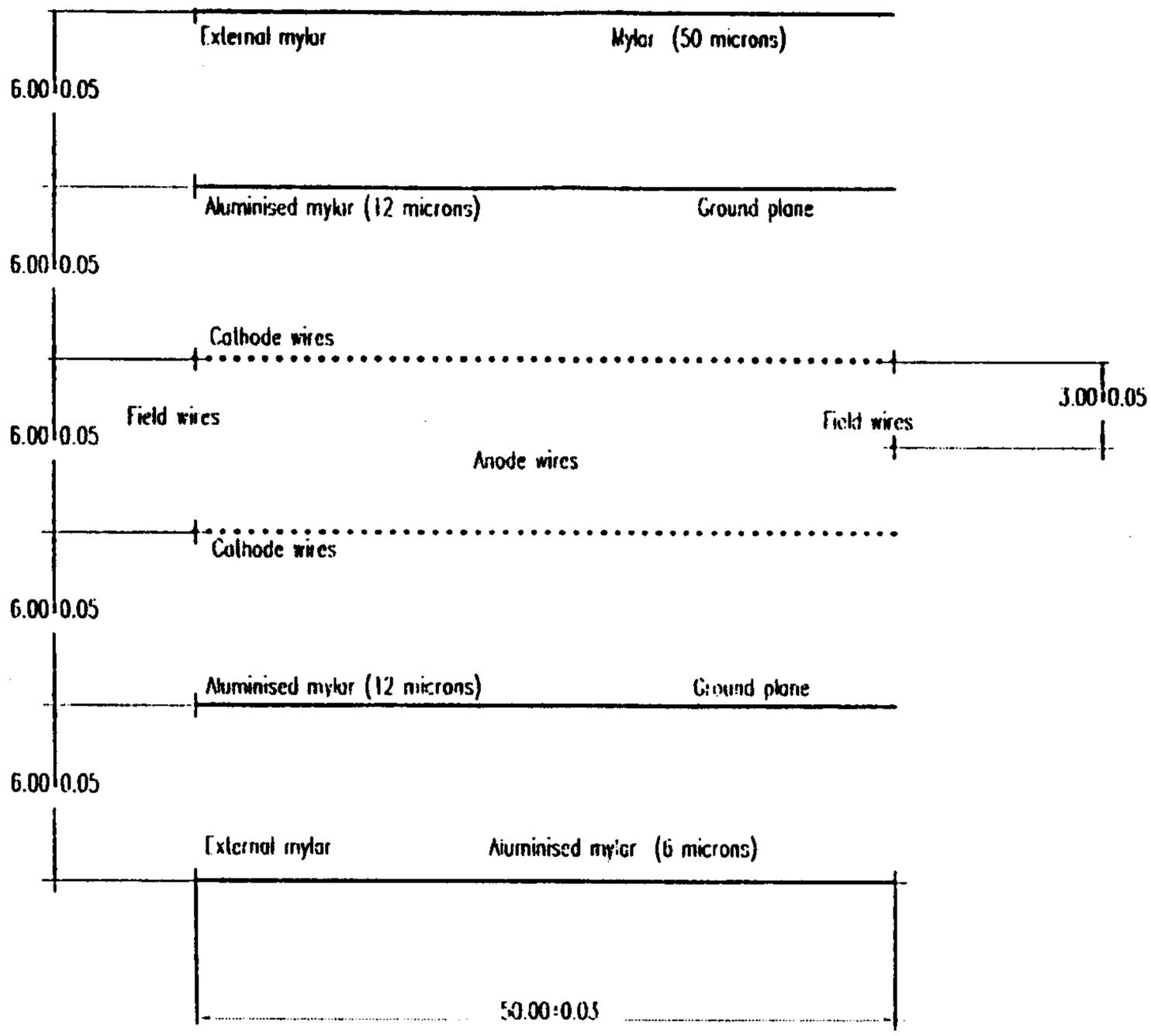

Figure 4.24: Drift chamber cell layout with dimensions and mechanical tolerances.

Aluminized mylar, with an aluminum coating layer $\sim$ 300 $\AA$ thick faced inward, close up and down the electric field.

Wires

In table 4.4 the mechanical characteristics and the mechanical tension chosen for each kind of wire used in the prototype are reported.

Mechanical and electrostatic wire stability

The electrostatic stability has been checked according to the equation [19]:

$$L_{max} = \frac{d\, ln(d/r_0)}{26.6\, V}\sqrt{T} \tag{4.2}$$

where:
L_{max} is the maximum wire length for stable operation [m]
d is the distance from the wire to ground planes [mm]

Table 4.4: Mechanical characteristics and tension for each wire used in the prototype

Material	Cu-Be Microfil Ø50 μm	Stainless steel Microfil 304 V Ø32μm	Stainless steel Microfil 304 L Ø25μm
Ultimate tensile stress of the material (N/mm^2)	996	2280	1763
Density (g/cm^3)	8.7961	7.87	7.87
Maximum tensile stress of the wire (g, N)	199.25 g 1.954 N	186.92 g 1.8337 N	105.14 g 1.0314 N
Wire tension for the prototype (g)	120	120	60

r_0 is the wire radius [mm]
V is the potential on the wire [kV]
T is the tension on the wire [g]

For our prototype:

cathode Ø= 50 μm Cu-Be wire:

assuming V = 4 kV, d = 6 mm, $r_0 = 0.025$ mm, T = 120 g.

$$L_{max} = 3.37\ m$$

anode Ø= 25 μm stainless steel wire:

assuming V = 2 kV, d = 3 mm, $r_0 = 0.0125$ mm, T = 60 g,

$$L_{max} = 2.4\ m$$

well above the length of our wires.

Sagitta wire measurement

For an horizontal wire fixed at one end and pulled from the other end by means of a slide with negligible friction, in the hypothesis that the load per unit length is uniform (own weight), the sagitta in the center position of the wire is given by the relation;

$$f = \frac{p\,L^2}{8\,H} \tag{4.3}$$

where:
p is the load per unit length
H is the mechanical tension applied at the wire extremities
L is the length between the two anchorage wire points.

Using the above equation we obtain
for Copper-Beryllium ϕ 50 μm
$p = 8.7961 \cdot 1.9625 \cdot 10^{-5} = 1.7262310^{-4} \quad g\,cm^{-1}, \quad L = 115\,cm, \quad H = 120\,g$

$$f = 23.81 \mu m$$

for Stainless steel ϕ 25 μm
$p = 7.87 \cdot 4.5239 \cdot 10^{-6} = 3.56 \cdot 10^{-5} \quad g\,cm^{-1}, \quad L = 115, \quad H = 60\,g$

$$f = 9.81 \mu m$$

for Stainless steel ϕ 32 μm
$p = 7.87 \cdot 8.04310^{-6} = 6.33 \cdot 10^{-5} \quad g\,cm^{-1}, \quad L = 115, \quad H = 120\,g$

$$f = 8.71 \mu m$$

Fig. 4.25 shows the calculated and measured sagitta for the Cu-Be wires.

Mechanical force on the mylar sheet

A small partial pressure difference can cause the movement of the ground plane outward or inward, with the maximum value of the sagitta being at the center. Using the following equation ;

$$f = \left[\frac{3\,a^2}{8\,Es}(1-\nu)\left(Pa^2 - 4N_0 f\right)\right]^{\frac{1}{3}} \tag{4.4}$$

where:
f is the sagitta
E is the modulus of elasticity of the material

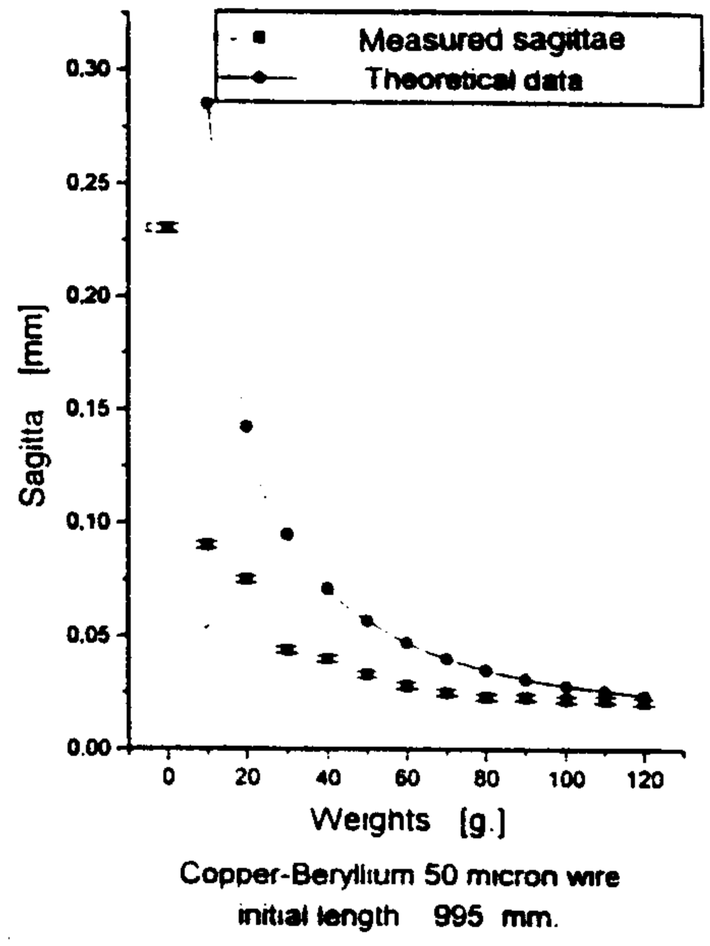

Figure 4.25: Calculated and measured sagitta for Cu-Be wire.

ν is the Poisson number
s is the thickness of the foil
P is the pressure
N_0 is the linear stretching tension
a is the membrane radius

Eq. (4.4) is valid for a circular membrane, and taking $s = 12\ \mu m$, $p = 0.4\ mb$,$N_0 = 588\ N/m$, $E = 380\ Kg/mm^2$ and $\nu = 0.3$, we obtain f = 231 μm. Taking into account the results shown in fig. 4.20 we may see that this deformation introduces a negligible effect on the localization precision.

Electrostatic forces

We evaluated with approximate equations taken from [11], [17] the maximum sagitta that we could expect on the cathode and anode wires due to electrostatic forces acting between the different elements. We found that in all cases these displacements introduce errors on the drift time measurement that are negligible apart two cases; 1 - the cathodes at voltages larger than 2000 V, in particular for inclined tracks. We have to investigate experimentally with beam how to apply software corrections, if necessary.
2 - the repulsive force among two adjacent anodes, 200 μm apart, that introduce a large sagitta (of the order of 3 mm), not tolerable. To overcame this effect, small araldite drops were placed every 11.5 cm for these anodes and we found that in this case the maximum sagitta is less then 40 μm.

Thermal expansion calculations

Linear thermal expansion coefficient (T range 20÷ 100 ° K)

Al:	$24 \cdot 10^{-6} \circ K^{-1}$
Stesalit 4411W:	$11.5 \cdot 10^{-6} \circ K^{-1}$
G10:	$1.6 \cdot 10^{-5} \circ K^{-1}$

Al

1000 *mm* Al	gives 0.024 *mm* per °K
1450 *mm* Al	gives 0.0348 *mm* per °K
700 *mm* Al	gives 0.0168 *mm* per °K

G10

1000 *mm* G10	gives 0.016 *mm* per °K
700 *mm* G10	gives 0.0112 *mm* per °K

Stesalit 4411W

1000 *mm* 4411W	gives 0.0115 *mm* per °K
700 *mm* 4411W	gives 0.008 *mm* per °K

4.2.4 First results obtained with the drift chamber prototype

Routine tests

After completion of the mechanical assembly of the chamber, we performed routine tests (leakage, high voltage) with mixtures of Ar-CO_2 (50-50) and Ar-C_4H_{10} (75-25). We did not observe any localized gas leakage. There was obviously a gas leakage through the 6 μm mylar window of $\sim$ 3 liters/hour. The pressure acting on the internal mylar window was 0.4 mb. We reached the maximal high voltages on the cathodes (-3700 V) and anodes (2200 V) without problems and we observed good signals both with ^{55}Fe and ^{106}Ru sources.

Tests and measurements

First tests with a He-C_4H_{10} (90-10) mixture were unsuccessful. We could observe signals with a source of ^{55}Fe but not with the electrons of a ^{106}Ru source, that deposit $\sim$ 10 times less energy in the gas. Increasing the anode voltages to more than 1800 V a high dark current and discharges were observed. Consequently the percentage of C_4H_{10} was increased to 30%. The chamber was stable, holding high voltage both on the cathodes and the anodes and continuous tests in these conditions for more than a month were performed. Fig. 4.26 shows a picture of the signals

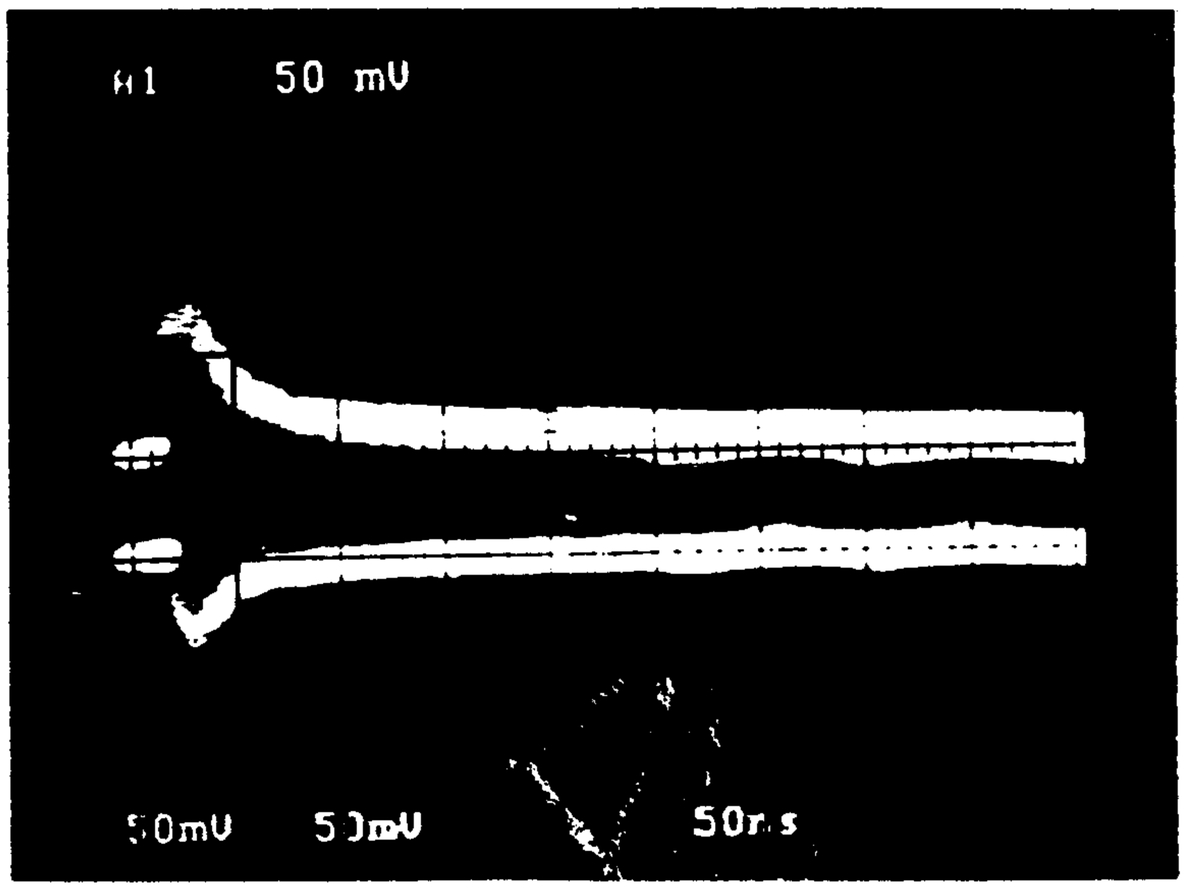

Figure 4.26: Signal observed on one end of an anode pair when the cell was irradiated by a ^{55}Fe source, placed at the opposite extremity of the anode wire, (with He-C_4H_{10} (70-30) mixture)

observed on an anode pair when the cell was irradiated with a ^{55}Fe source placed at one extremity of the wires, that opposite to the side on which the signals were observed (the worst case). We observe quite nice signals both on the wire collecting directly the charge (positive signal, due to the preamplifiers inversion of polarity) and the adjacent one (negative signal). Furthermore we investigated the behavior and performances of the chamber with a ^{106}Ru source, selecting electrons passing through the chamber by means of two thin scintillators. The electronic logic is shown in fig. 4.27.

First of all we checked the behavior of each cell since the diameter of the anode and the spacing among the anode pair is slightly different from each other, as explained before. We found that the wires of 25 μm diameter, spaced by 200 μm, gave the best results concerning charge and time spectra. A typical ADC spectrum showing the expected Vavilov distribution for electrons is shown in fig. 4.28. Fig. 4.29 shows a typical TDC spectrum, exhibiting the expected flat behavior. Both measurements were done with an un-collimated source. In the following we studied the localization properties of the chamber along the wire direction (z-direction) as obtained by the charge division method. By measuring the ADC spectra from both ends of the same anode wire and defining Q_l and Q_r respectively the charge collected at the left and right sides of the anode, the z-coordinate (taking the center of the wire as origin of the coordinates) is given by the relation;

$$z = [(Q_l - Q_r)/(Q_l + Q_r)] \cdot (Z_i + R_o * l/2)R_o$$

where :
Z_i is the input preamplifier impedance
R_o is the wire resistivity

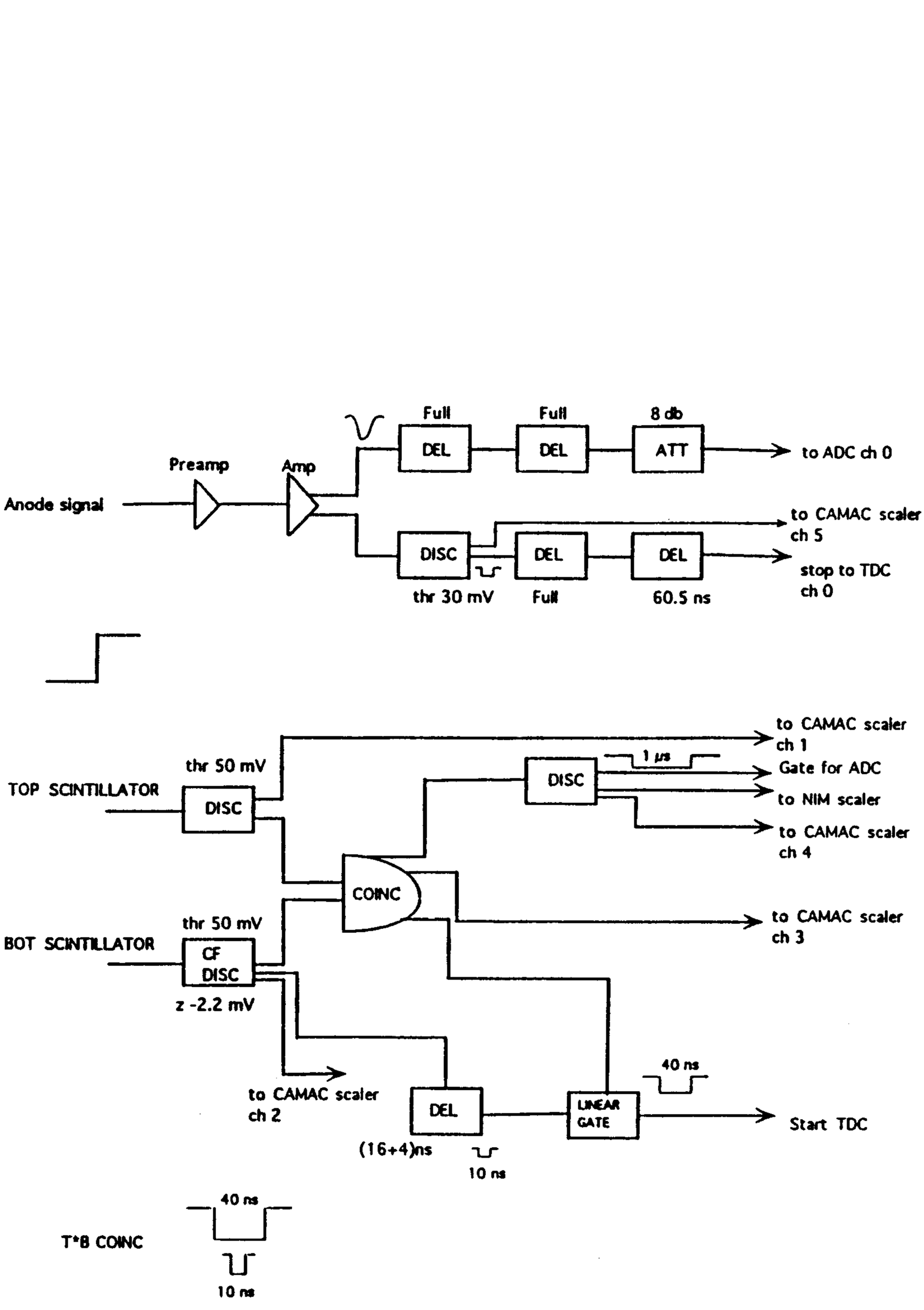

Figure 4.27: Trigger set up for the tests with a ^{106}Ru source.

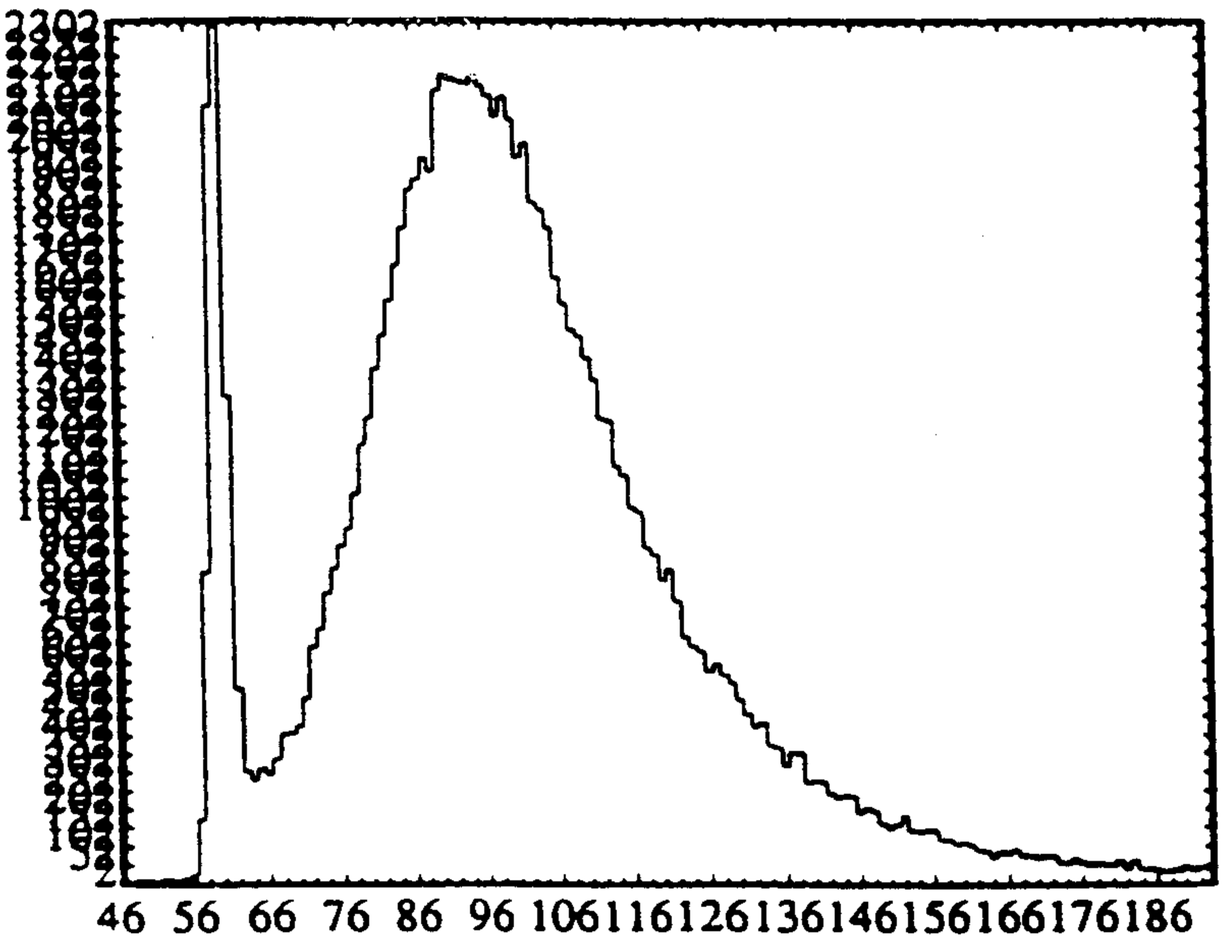

Figure 4.28: A typical charge spectrum.

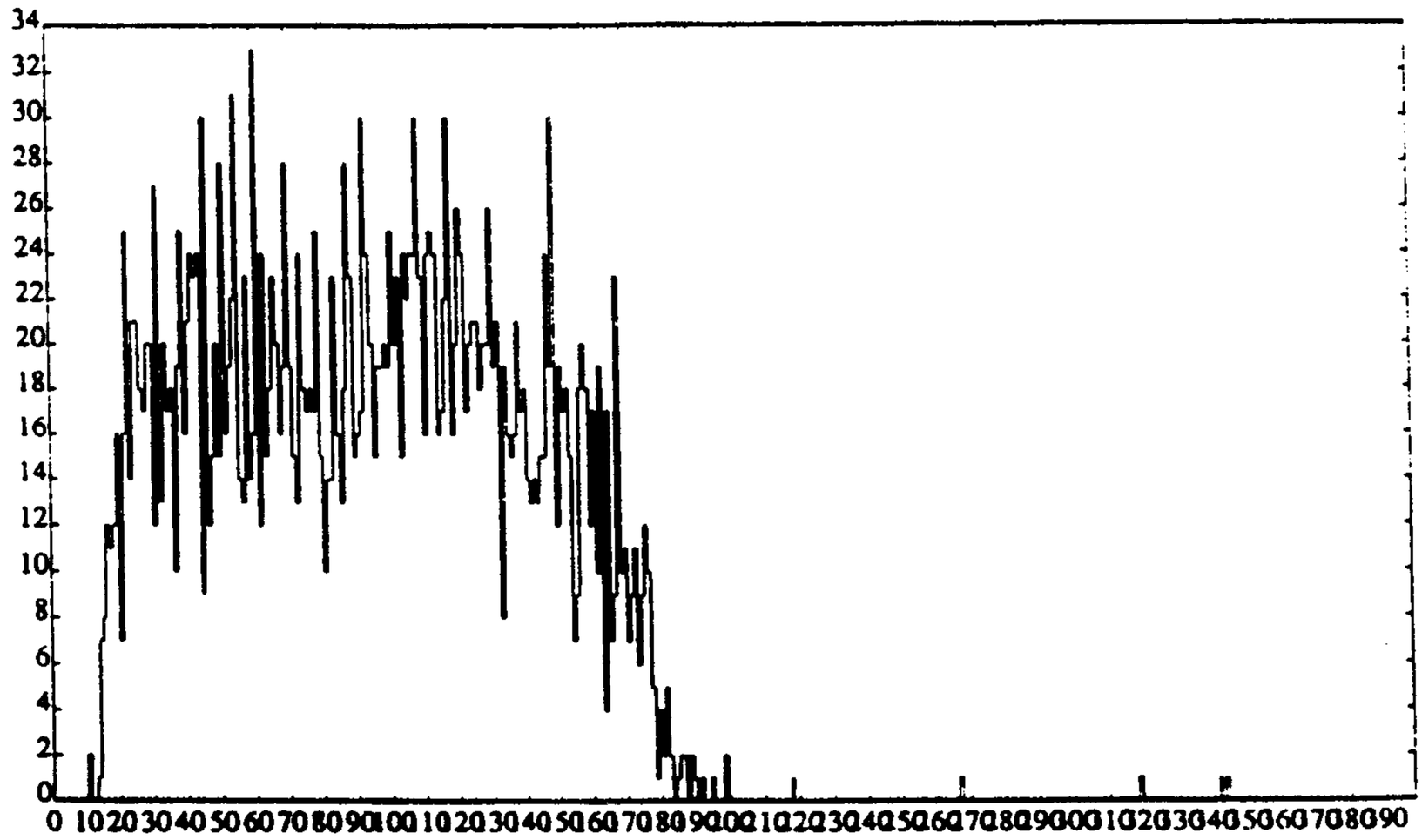

Figure 4.29: A typical time spectrum.

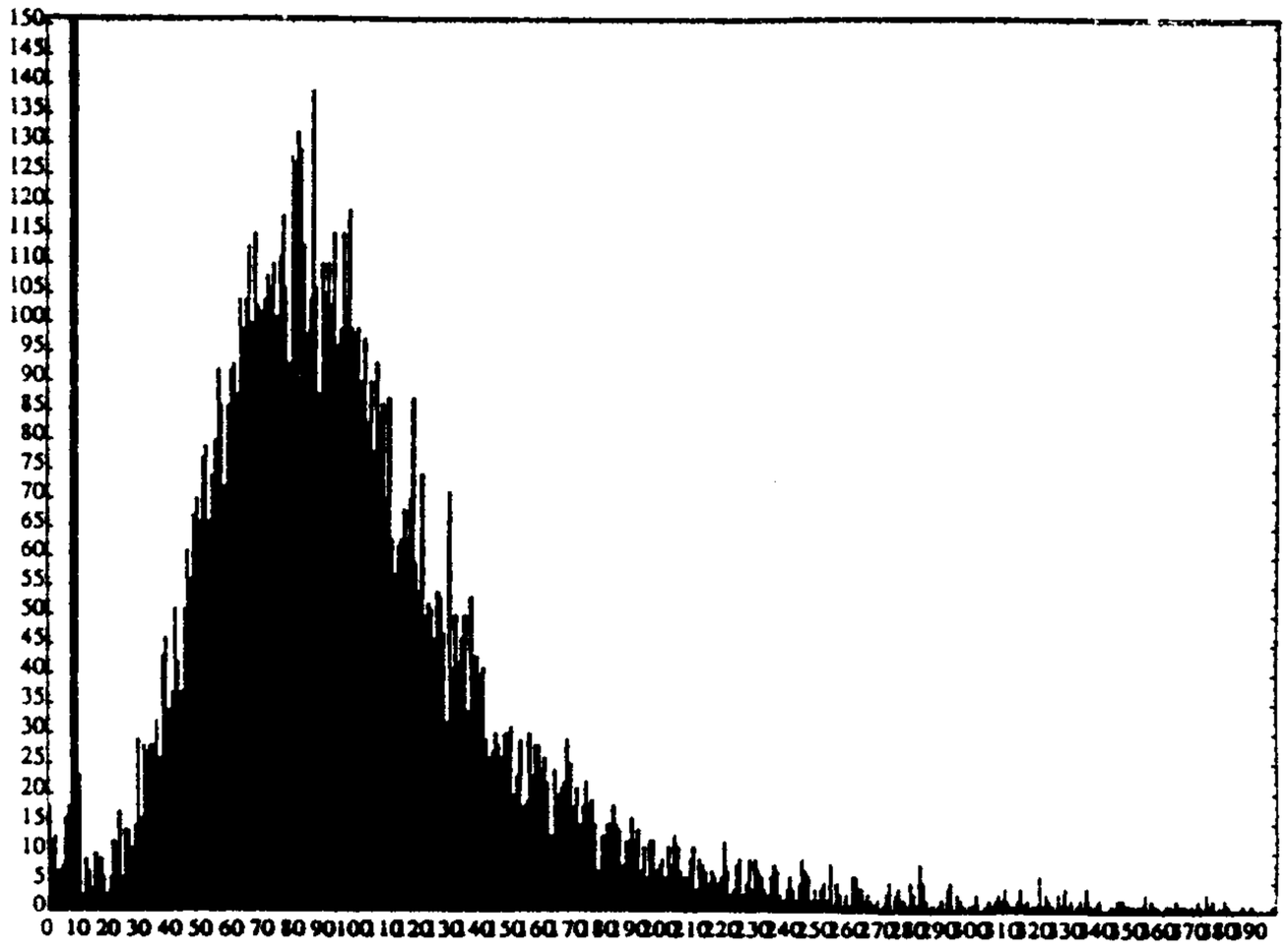

Figure 4.30: Charge spectrum obtained with a collimated ^{106}Ru source.

l is the total wire length.

Fig. 4.30 shows the ADC spectrum obtained with a collimated ^{106}Ru source. Fig. 4.31 shows the distribution of the measured z-coordinate when the collimated source was placed at the center of the wire. The FWHM of the distribution is 14 mm (corresponding to a σ of $\sim$ 6 mm), which is a good result if we consider that the length of our anode is 1180 mm. Fig. 4.32 shows the results taken at different positions on the wire. A very good linear relationship is observed, with a worsening of the resolution at the edge of the wire.

It is well known that the efficiency and the localization precision are hardly measured with an electron source. At the center of the cell we measured an efficiency of 96 $\pm$ 2%. We plan to perform extensive measurements at a beam test scheduled in November 1994.

In conclusion we are very satisfied of the results so far obtained. To our knowledge a drift chamber of large dimensions, filled with He based mixtures with anode pairs exceeding 1 meter of length and with very thin windows (6 μm) was never operated before. We decided then to pass to the stage of mass production of the chambers, and the final characteristics of the cell are given in Table 4.5.

4.2.5 Final choice of the FINUDA drift chamber

General dimensions

Internal drift chamber

The eight drift chambers, assembled in the inner octagonal shaped cylinder, are smaller than the external ones. The external dimensions are shown in fig. 4.33,

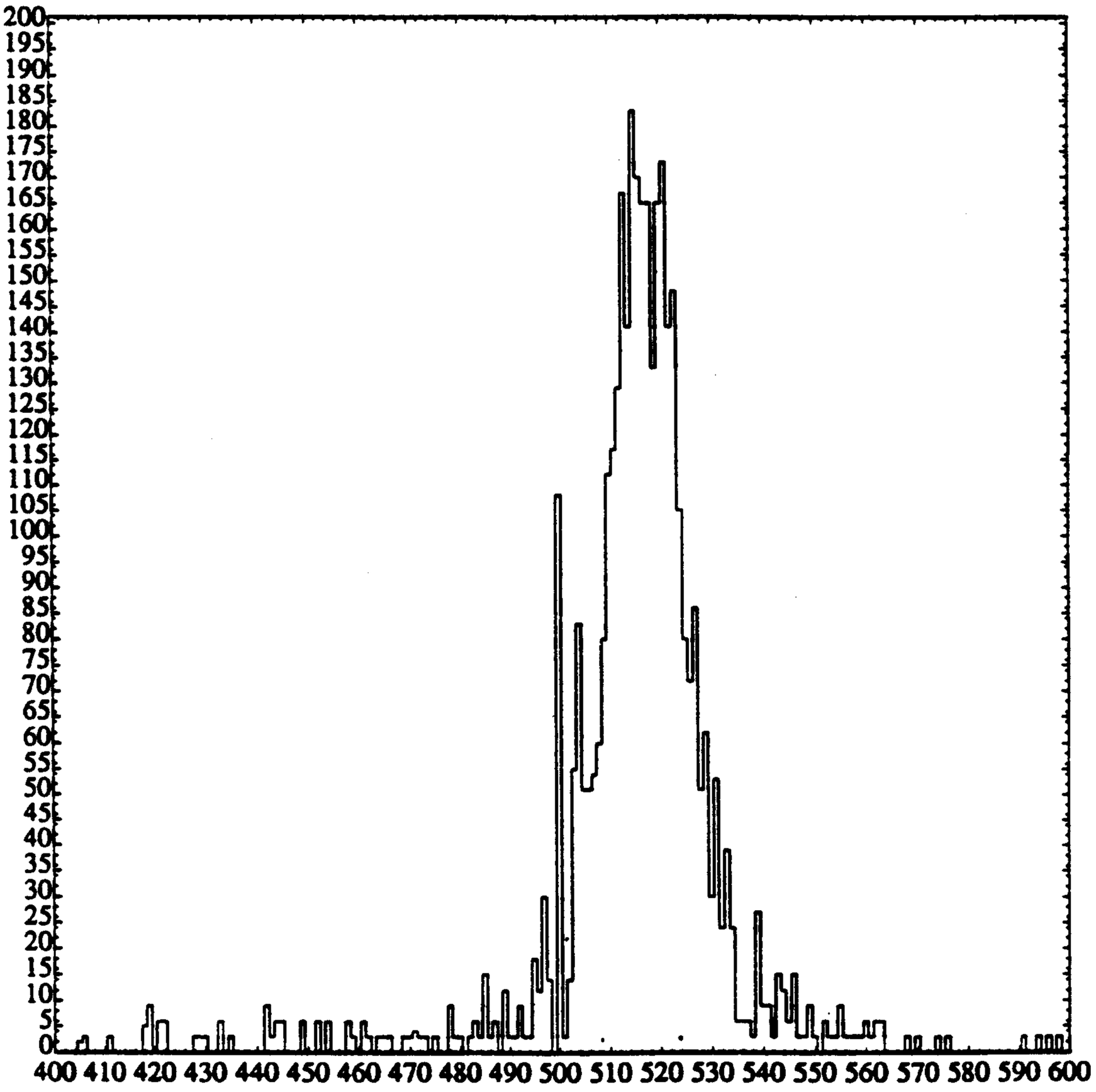

Figure 4.31: The z-coordinate given by charge division in the center of the drift chamber.

Z cm	Z measured	FWHM	Sigma		
0	0	1.41	0.6		
9.5	9.5	1.41	0.6		
22.5	22.4	1.59	0.68		
45	44	3.6	1.55		
The Z coordinate is in the center of the chamber					

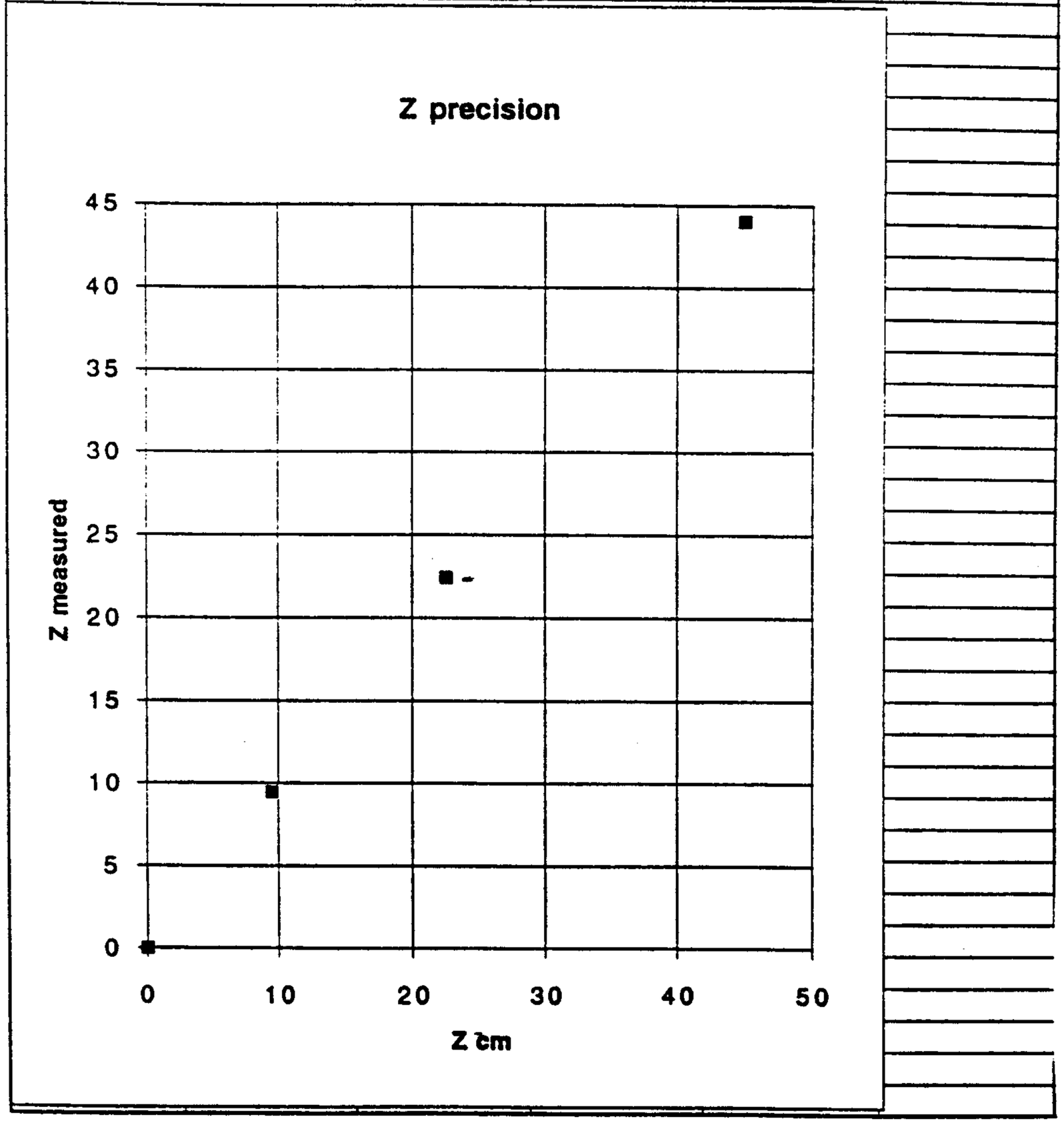

Figure 4.32: The z-coordinate given by charge division for several z value.

Table 4.5: Final characteristics of the cell

Sense wire diameter	25 μm
Sense wire pitch	50 mm
Field wire diameter	50 μm
Field wire pitch	50 mm
Cathode wire diameter	50 μm
Cathode wire pitch	1 mm
Material of the ground planes	Mylar + 300 Å of aluminum
Thickness of the ground planes	6 μm
Gas mixture	He-C_4H_{10} (70-30)
Accuracy for perpendicular tracks	100 μm
Total thickness of gas mixture	$1.9 \cdot 10^{-5} X_0$

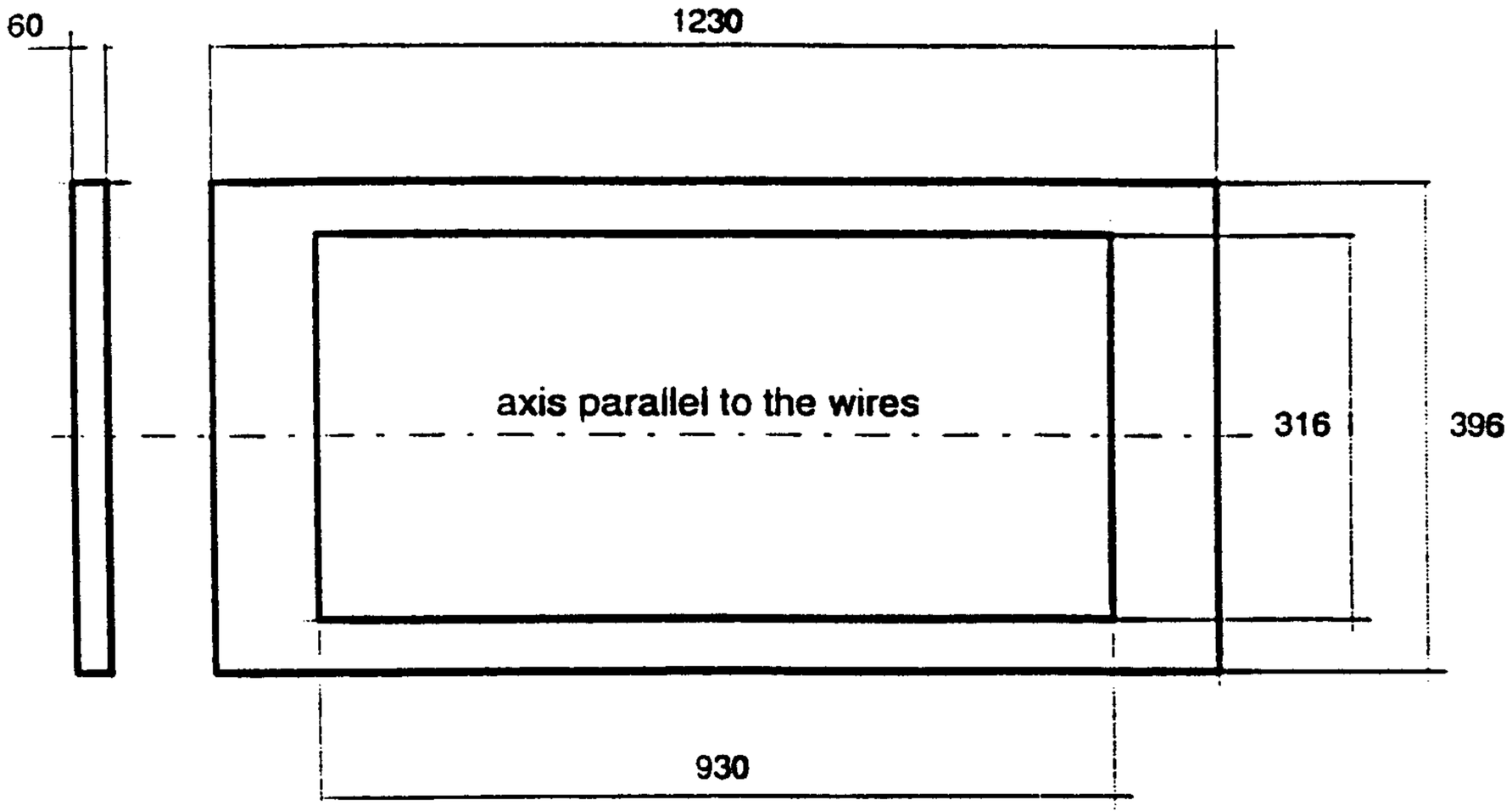

Figure 4.33: Dimensions of the small Drift Chamber.

excluding the printed circuits. The total length is 1230 mm and the width is 396 mm. The total thickness of all the five glass fiber frames is 30 mm, while the aluminum frame will have a thickness of 15 mm. The gas flows inside the chamber across tubes and connectors placed parallel to the wires in order to reduce the total thickness. The free length of cathode and field wires is 930 mm. The free length of anode wires is the same, but the total length between the soldering points is about 960 mm.

Weight

The weight of each frame is indicated in Table 4.6. The total weight of all the frames is about 24.9 Kg. Adding screws, o-rings and gas connectors the total weight is about 28.0 Kg.

External drift chamber

The eight external chambers are assembled in the outer octagonal shaped cylinder. The external dimensions are shown in figure 4.34, excluding the printed circuits. The total length is 1870 mm and the width is 686 mm. The total thickness of all the five glass fiber frames is 30 mm, while the aluminum frame will have a thickness of 15 mm. The gas flows inside the chamber across tubes and connectors placed parallel to the wires in order to reduce the total thickness. The free length of cathode and field wires is 1570 mm. The free length of anode wires is the same, but the total length between the soldering points is about 1600 mm.

Table 4.6: Weight of each frame of the internal drift chambers.

Frame name	Material	External dimensions (mm)	Weight (Kg)
Supporting frame	aluminum	1230x396x15	6.9
Cover frame	glass fiber	1230x396x6	2.2
Cathode frame	glass fiber	1230x396x6	2.2
Anode frame	glass fiber	1230x396x6	2.2

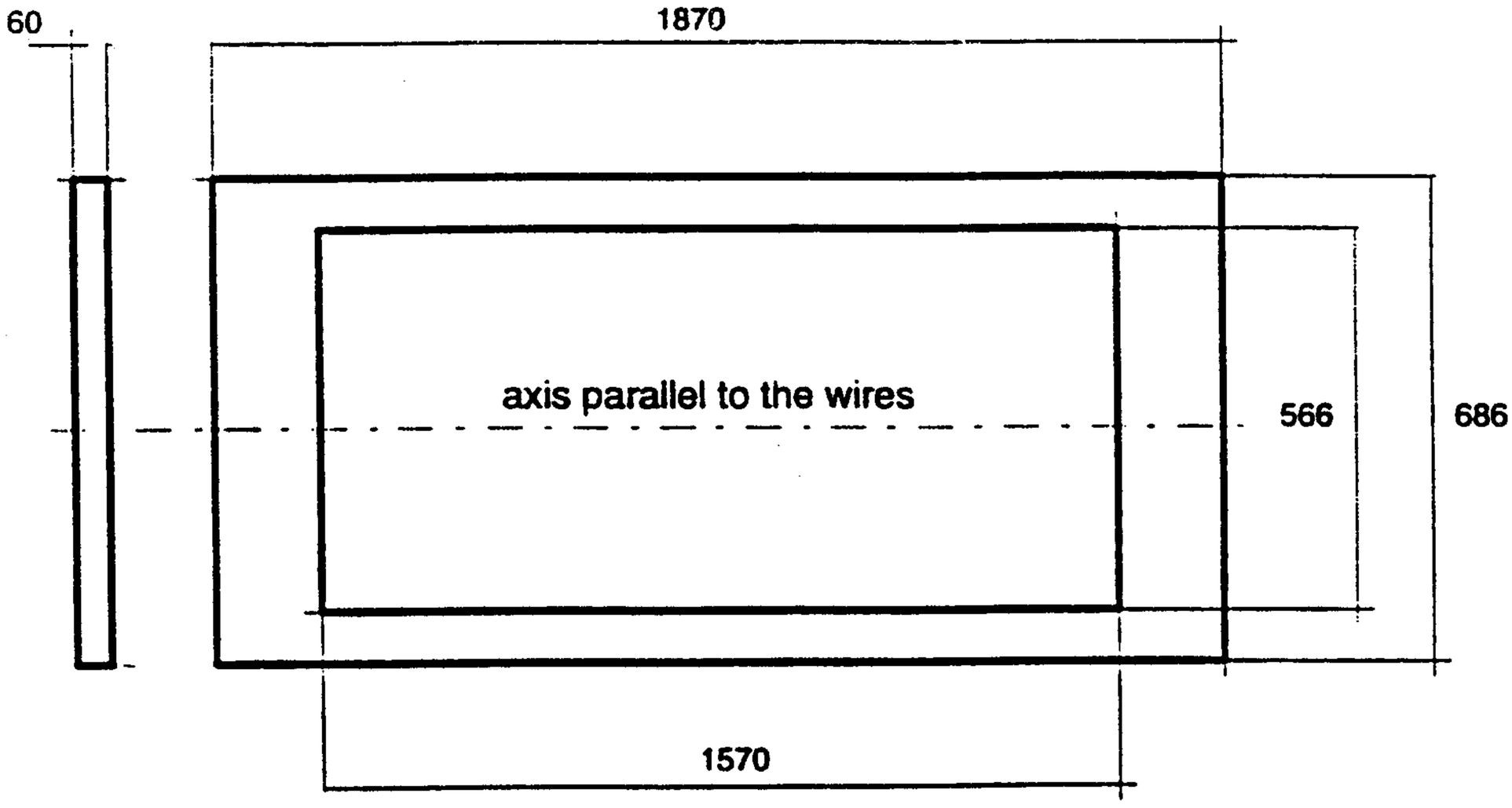

Figure 4.34: Dimensions of the big drift chamber.

Table 4.7: Weight of each frame of the external drift chambers

Frame name	Material	External dimensions (mm)	Weight (Kg)
Supporting frame	aluminum	1870x686x15	14.2
Cover frame	glass fiber	1870x686x6	4.5
Cathode frame	glass fiber	1870x686x6	4.5
Anode frame	glass fiber	1870x686x6	4.5

Weight

The weight of each frame is indicated in Table 4.7. The total weight of all the frames is about 50.9 Kg. Adding screws, o-rings and gas connectors the total weight is about 55.0 Kg.

Cell dimensions and description

The disposition of the wires and the mylar sheets constituting the cell are illustrated in figure 4.35. This picture is obtained by sectioning the drift chamber with a plane orthogonal to the wires. The anode wires will be positioned at a distance of 200 μm.

Wires

25 μm diameter stainless steel will be used for anode wires and 50 μm diameter Copper-Beryllium will be used for the cathode and the field wires.

The mechanical tension chosen for the wires is:

120 g for the Copper-Beryllium cathode, field wires;

60 g for the Stainless Steel 25 μm anode wires.

Table 4.4 reports all these values and also the mechanical characteristics of each kind of wire.

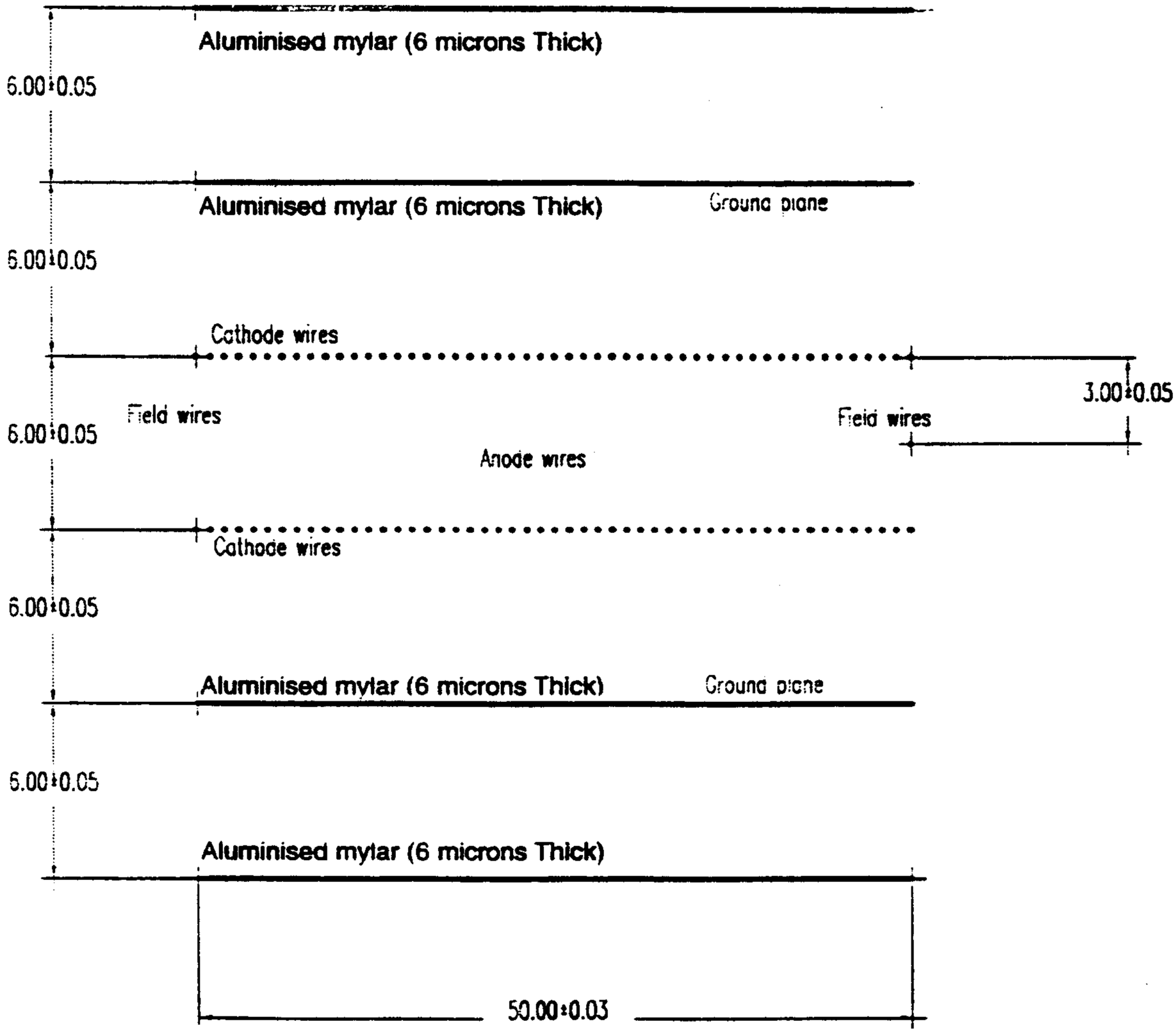

Figure 4.35: Final drift chamber cell layout with dimensions and mechanical tolerances.

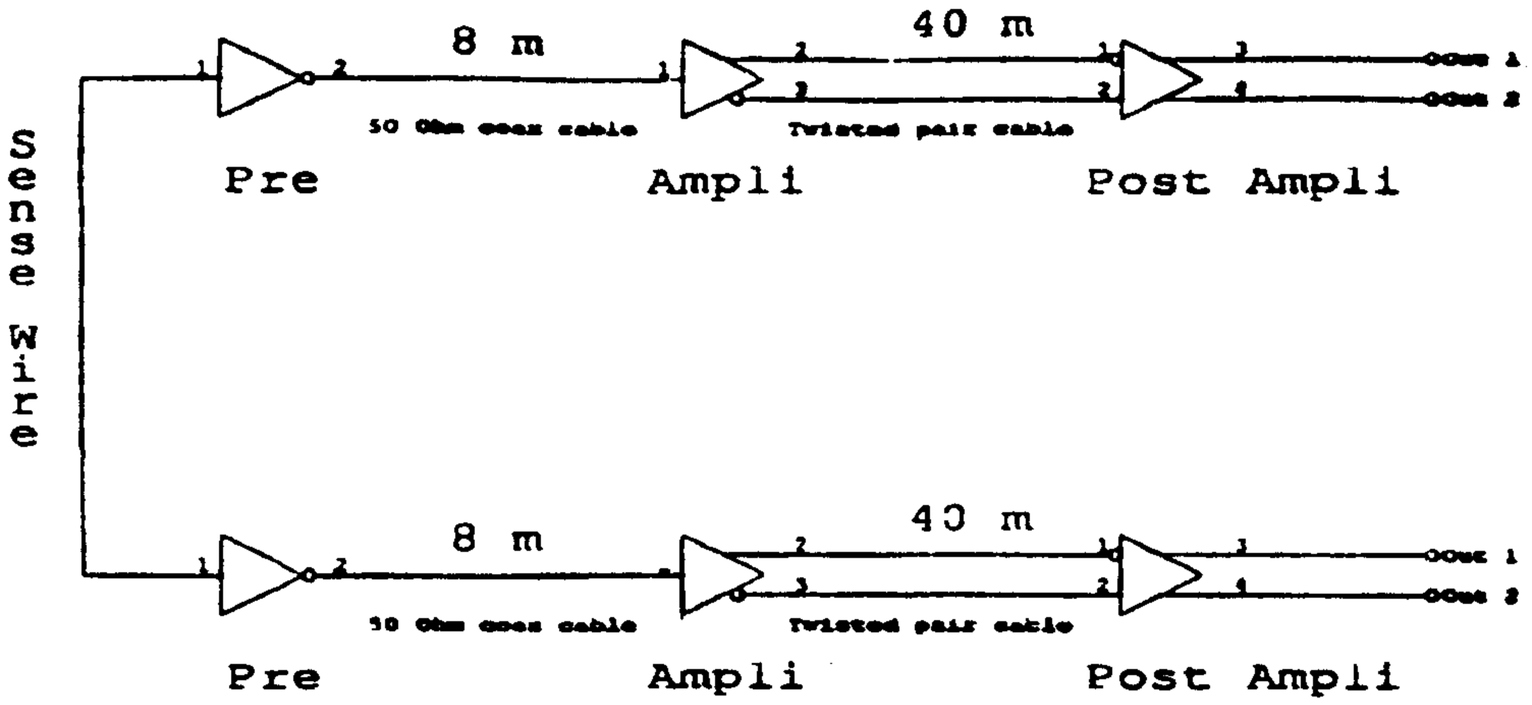

Figure 4.36: The front-end linear electronics for a single channel

4.2.6 Front-end electronics for the drift chambers

The analog front end of the FINUDA drift chambers

The front-end linear electronics for a single channel consists (see fig. 4.36) of a current-voltage preamplifier mounted on the side of the chamber and connected to the voltage amplifier through a 10 m long 50 Ω coaxial cable. The amplifier is positioned near the magnet and it is connected to the postamplifier through 30-40 m long twisted-pair cables.

In order to make easier to reach the drift chambers for maintenance, a very light coaxial cable (gore type CXN 1214) will be used, whose peculiar characteristics are: weight 2.2 kg/km, capacity 90 pf/m, propagation delay time 4.4 ns/m, attenuation 64 $db/100m$ at 100 MHz, diameter 1.27 mm, dielectric constant of gore-tex ϵ_r = 1.3, characteristic impedance 50 Ω. The 30-40m twisted-pair cable is a flat cable which contains 8 independent channels screened from each other, with a 10 MHz bandwidth, 5.17 ns/m propagation delay time, polipropilene dielectric constant ϵ_r = 2.29 with AVG 28 copper wire, 100 Ω characteristic impedance.

Linear amplifying chain of the signal

In the current-division method for z coordinate measurement, the current pulses coming from each end of the sense wire must be measured, since the hit position along the wire is proportional to their asymmetry. The accuracy is limited by the electronic noise. In large detectors with some hundreds of long sense wires, the noise

of the preamplifiers is out-weighted by other factors:

- large capacitances of the sense wires;
- difficulty to avoid ground loops in the connections of the high and low voltage power, magnet power supply, integration with other spectrometer components;
- environmental noise generated by other experiments and accelerator.

The philosophy that will be adopted is the following: all grounds everywhere connected together, so the eventual ground-loop effects are reduced by the very low resistance of the apparatus ground. The noise that can be accepted, for 1% charge division resolution, is ENC = 15.000 electrons for 100 fC mean charge released. The same ENC noise can be accepted to have $2ns$ of time resolution.

The preamplifier

In fig. 4.37, the current-voltage preamplifier is presented. No circuit innovations are introduced, but it is possible to maximize the performances by using appropriate components and layout: rise time, noise, power consumption, linearity, temperature drift, reliability and constant characteristics.

The circuit is a common base amplifier followed by two emitter followers and coupled in AC connection to a fast voltage amplifier. The current to voltage amplification is given by the resistor R5, that also controls the rise time of the signal due to the parasitic capacitance connected to the collector Q_1. The input impedence is measured by switching a part of the input signal current in a well known resistance and computing the new gain. The input impedence for a steady current of 0.53 mA in Q_1 is $(85 \pm 2)\ \Omega$.

The input impedence is controlled by the resistors R_7 and R_4. Applying a pulse at the test input (R1 resistor) with $R_5 = 2.7\,k\Omega$, an amplification of 6.5 $mV/\mu A$ and a rise time less than 20 ns is obtained; while with a delta pulse charge a rise time of 3 ns is obtained.

The noise of the preamplifier is 40 nA r.m.s. and it can be neglected if compared to that one presumably introduced by the experimental area environement. The ENC_0 (Equivalent Noise Charge without detector) is 2500 e when 0.53 mA flow in Q_1.

The test input can supply $1\mu A$ to the preamplifier when 22 mV are applied. The power dissipation is 150 mW per channel; no cooling is needed, since, in first approximation, the gain of the preamplifier is independent of the transistor characteristics: $\Delta G/G < 1\%$ for $\Delta T = 5°C$.

The amplifier and the line driver

As shown in fig. 4.36 the amplifiers and line drivers are housed near the magnet inside a VME-like unit. A unit will contain 24 amplifiers.

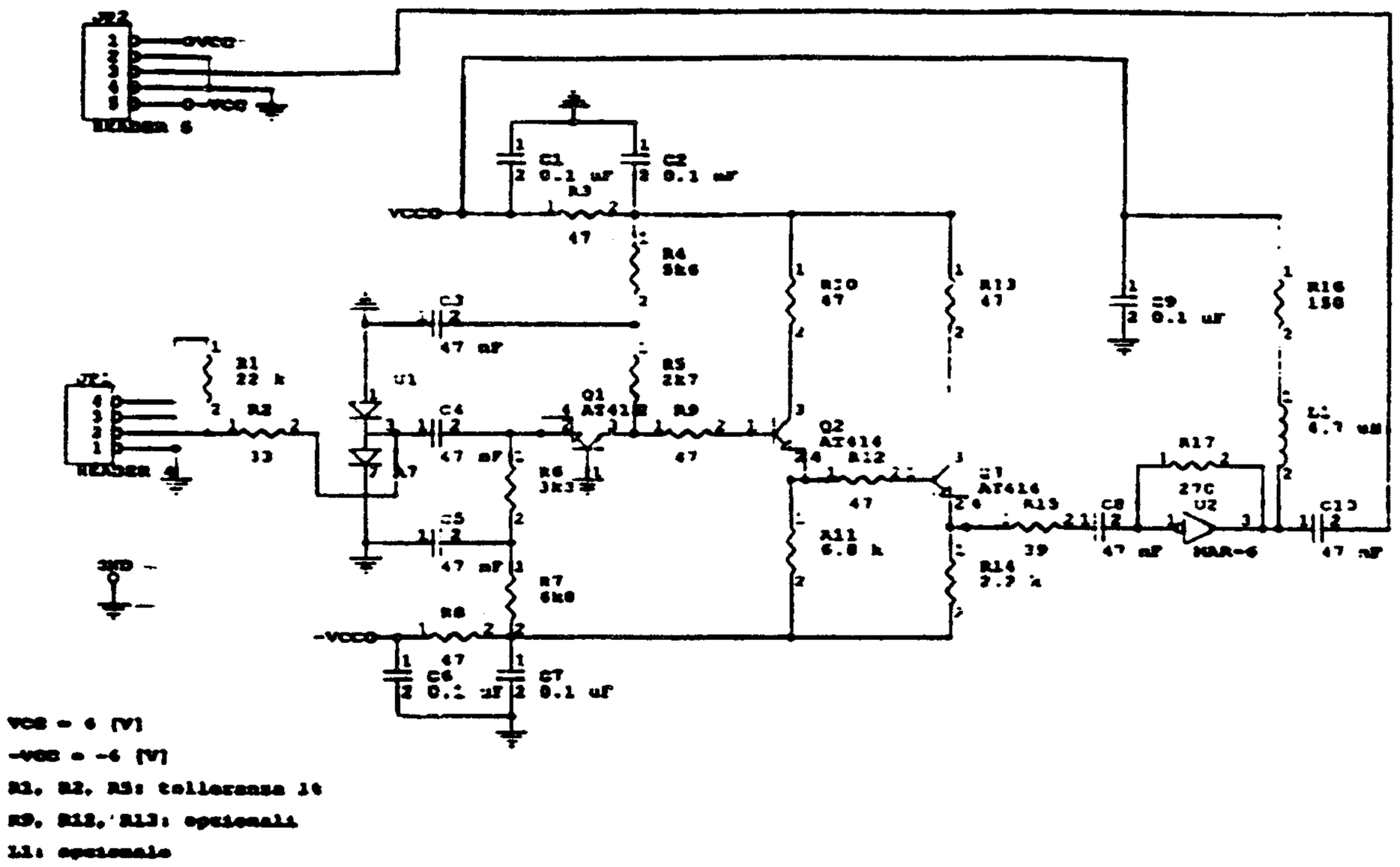

Figure 4.37: The current-voltage preamplifier

In the rear panel there is the input connector (type Burndy 30P 007 00E9) and the power supply connector. In the front panel there is the differential output of the amplifiers via 3 Cannon 37 pin connectors.

The voltage amplification is 10 and an over compensation is needed for twisted cable low frequency transmission (10 MHz). The outline is presented in fig. 4.38.

The receiver and the post-amplifier

The receivers and post-amplifiers are housed in the counting room in two crates VME-like. They consist of wide band differential amplifiers with over compensation and two 50 Ω outputs: one is sent to discriminators and then to TDCs for drift time measurement, the other one to ADCs for charge division measurements. The discriminators will be standard VME with programmable thresholds.

Readout System

The READOUT system consists of TDCs (for drift time measurement) and ADCs (for charge division measurement). The signal is read-out at both ends of the anode wires, that means the total number of channels, spares included, is 700 (700 channels of ADCs and 700 channels of TDCs).

For our purposes we need TDC with a resolution of 0.5 ns/ch and a full scale of 1 μs (11 bits of dynamic range).

At the moment on the market we can find either analog TDC (with a time

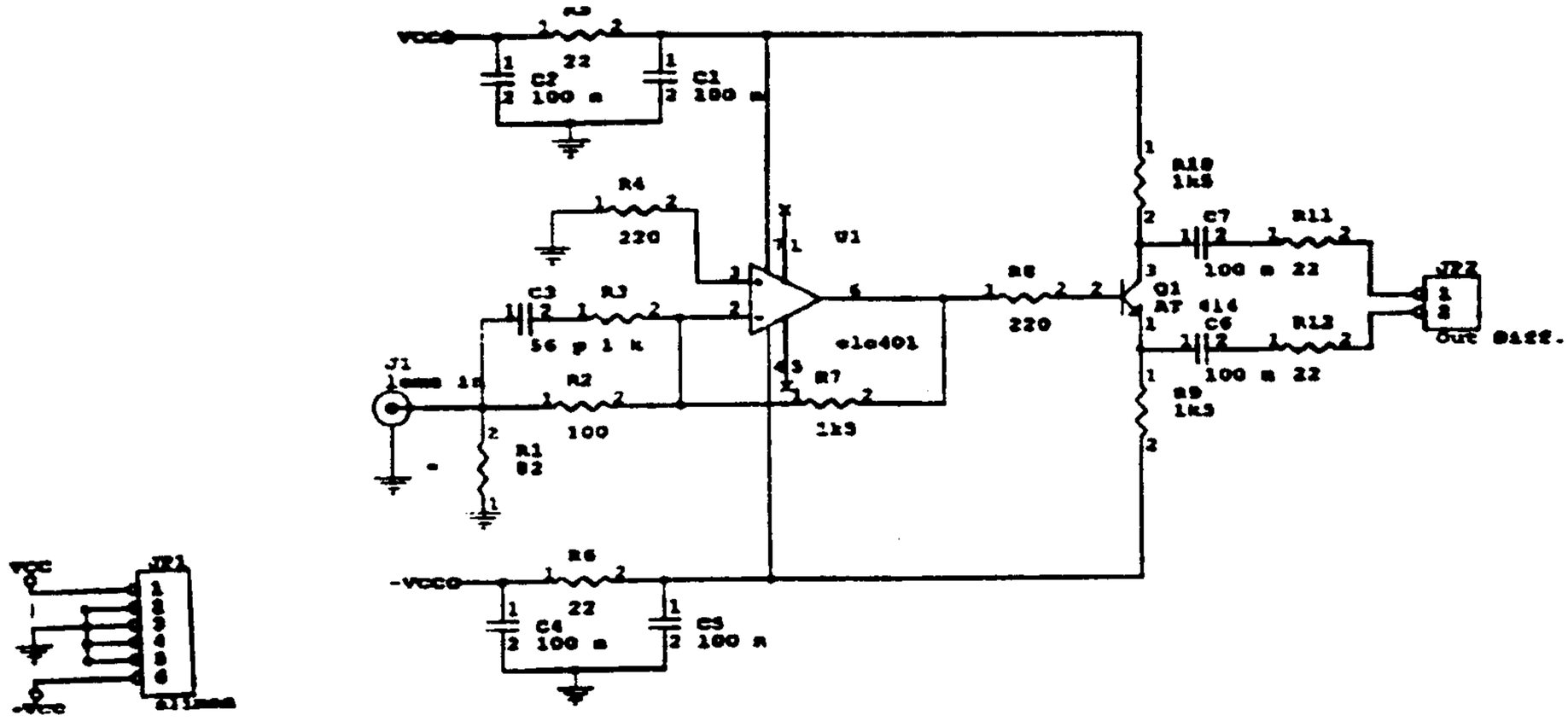

Figure 4.38: The amplifier.

resolution down to .5 ns/ch, a dynamic range of 11 bits) and digital TDC based on CMOS chip (with a fixed resolution of 1 ns/ch and a dynamic range of 16 bits). Some firms are developing a digital TDC with a fixed resolution of .5 ns/ch and a dynamic range of 16 bits. But we are waiting for the final release on the market.

The second option is cheaper and more compact than the first one. All the READOUT system of FINUDA is VME based. Using digital TDC we can house up to 96 channels per 9U VME card (standard 6U VME can have 16 channels per module), that means we just need 1 VME crate.

The TDCs can work on common stop mode and for this purpose we plan to use, like stop signal, the OR of the twelve MT signals (MB) coming from TOFINO, gated by the trigger signal, in that way we don't need to put any delay on the signals.

For the analog spectrum we will use ADC with a resolution of 0.10 pC/ch and 12 bits of dynamic range (400 pC of full range).

We plan to use standard modules on 9U VME with 64 channels per module housed in 1 crate.

4.3 The straw tubes array

The performance requirements on the last tracking detector of FINUDA for the measurement of the fourth point of each charged track are a space resolution of 100 μm in $r - \phi$ plane and 500 μm in z–coordinate. Being the last tracking device, the requirement of low-mass can be partially released.

The proposed solution is an array of aluminized mylar straws. Three super–layers (one axial and two $\pm 15^{\circ}$ stereo super–layers) each with two sub–layers of staggered straws are being considered. Aluminized mylar straws offer many important advantages for measuring the last point of FINUDA tracking system:

- The modular construction procedure is simple and offers flexibility to make a cylindrical tracking detector providing all three space coordinates.
- With straw lengths smaller than 50 cm a space resolution better than 50 μm has been previously reached [20], [21], [22], [23]. For straw lengths exceeding two meters [24],[25],[26], the device is still expected to provide the needed space resolution of ~ 100 μm. For very large detection area (8 m^2) the cost is comparatively low.
- The dead zone caused by a broken wire is limited to one straw only.
- As the wires are shielded by the aluminum cathode, cross talk is small.

4.3.1 Topology of the array and mechanical structure

The conceptual mechanical structure of the straw tube detector is shown in fig.4.39. It has an inner radius of 111 cm and an outer radius of 125 cm, with a full length (L) of 255 cm. The basic array element is a 0.03 mm thick mylar straw with an inner diameter of 15 mm. 2472 straws are arranged in three super–modules A, B, C moving out from the interaction vertex (fig4.40).

The straws are positioned between two aluminum end plates having the shape of a circular ring. The two layers of the inner super–module are assembled with their axis parallel to the beam direction (z-axis) along two concentric cylinders. The tubes in outer super–modules form an angle of $+15^{\circ}$ and -15° with respect to the z-axis for stereo reconstruction of the coordinate of the hitting track.

The same number of straws ($N_{str} = 412$) is contained in each layer, the angle

$$\delta = 2\pi / N_{str}$$

subtended by two adjacent straws in each sub–layer is 0.8738° as shown in the enlarged view of fig.4.40 at one end plate side. The inter-axis distance between two adjacent tubes of the same layer increases from $1.71cm$ at the innermost layer to $1.89cm$ at the outermost one.

The radial distance R of the stereo layers decreases going from the end plates ($z = \pm L/2$) to the center of the detector ($z = 0$) with a maximum displacement of about $5cm$. Radial distances from the center of the apparatus, together with the inter-axis distances d at each layer are listed in table 4.8 at the end plates and at the center of the detector. A mechanical constraint of having a minimum inter-axis distance corresponding to one straw-diameter plus 2 mm has lead to choose the proposed cell structure.

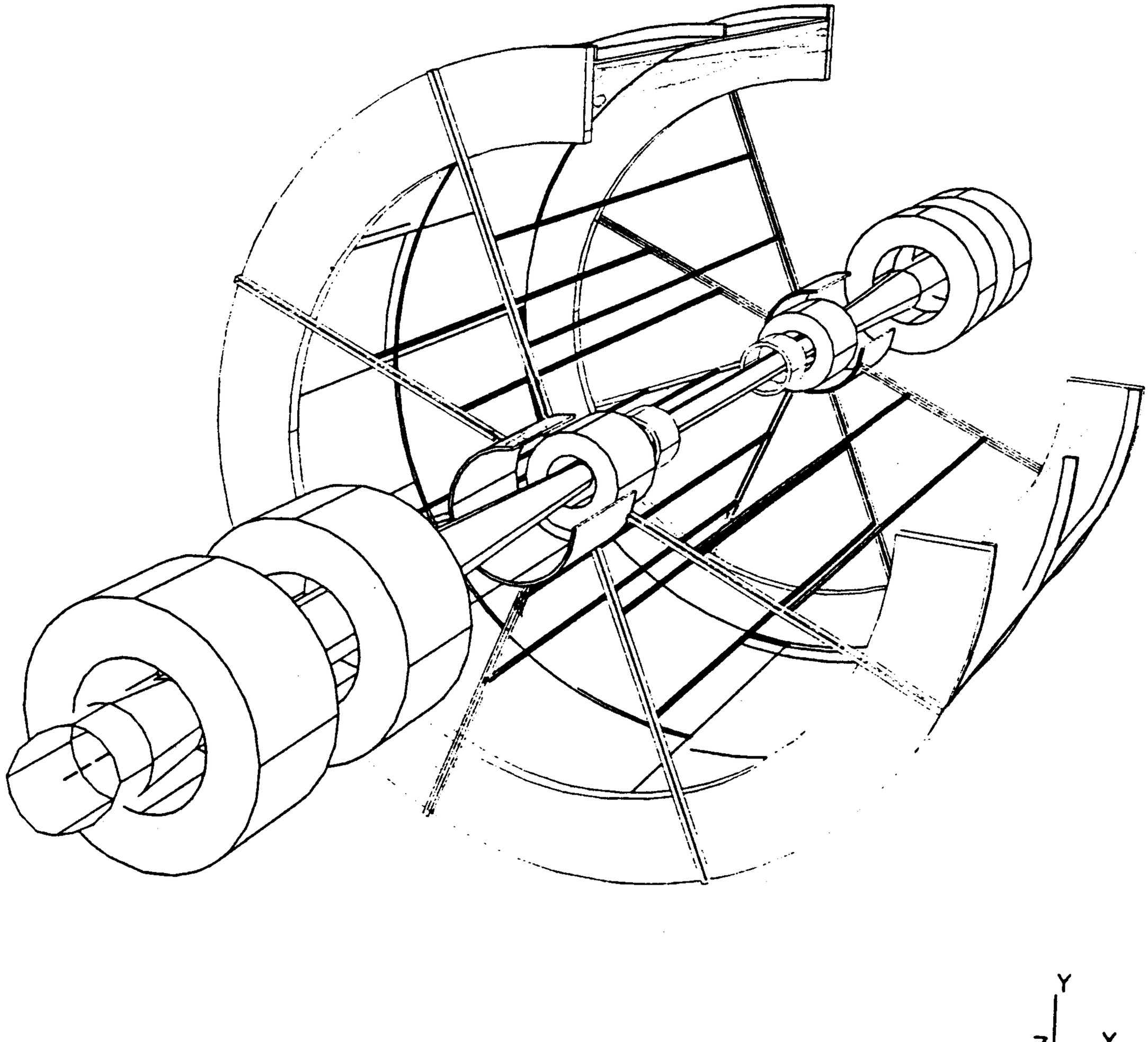

Figure 4.39: A version of the FINUDA detector frame with the straw tube end–plates included. Note that the actual conceptual detector frame, as described in chapter 3, is somewhat different from this version.

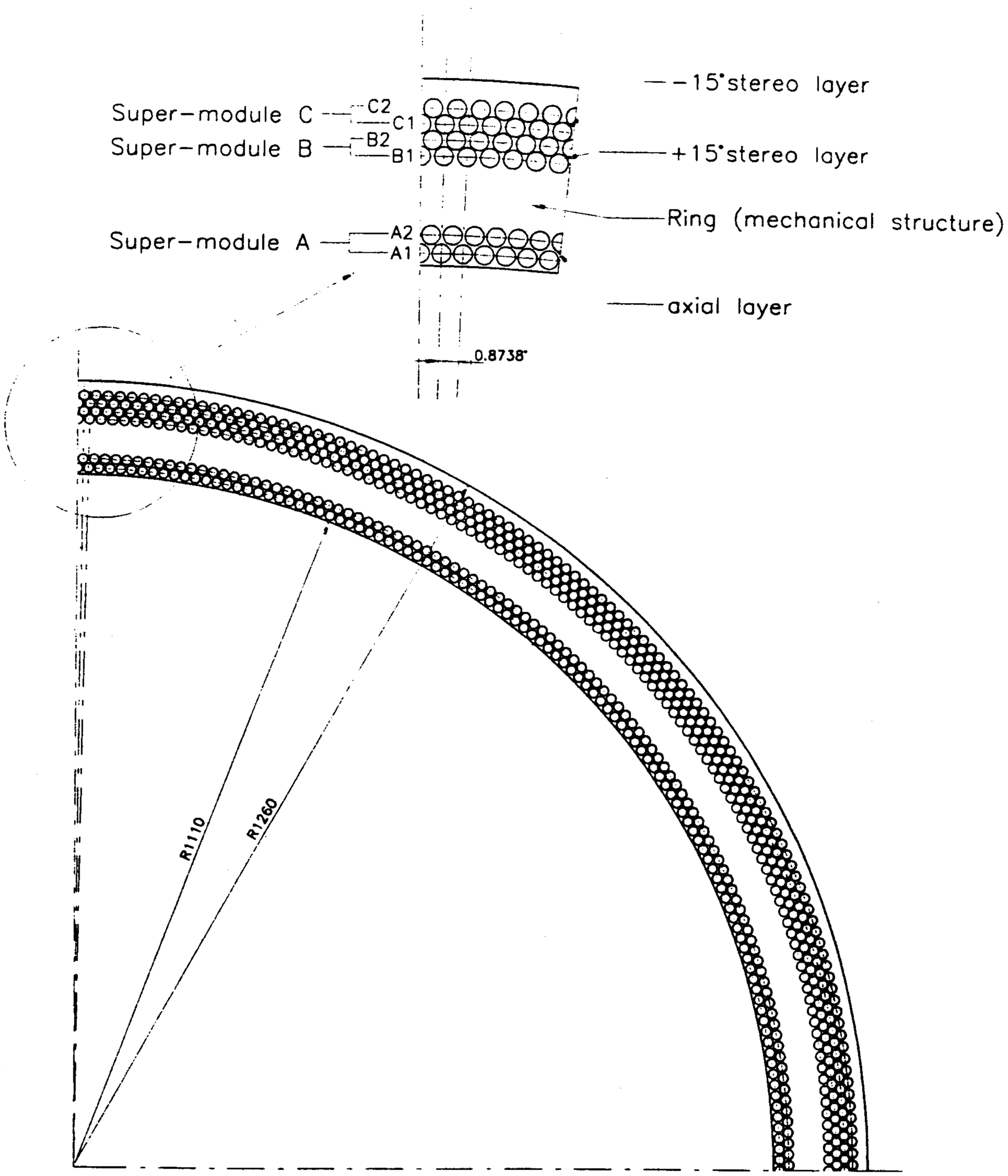

Figure 4.40: Straw tube tracker of FINUDA: front view, at one end plate side, of 1/4 of the array (detail in the enlarged view).

Table 4.8: Basic layer parameters (in *cm*). A1, A2, B1, B2, C1, C2 refer to the first and second sub–layers of super–modules A, B and C respectively.

	A1	A2	B1	B2	C1	C2
$R(z = L/2)$	112.00	113.48	119.80	121.23	122.66	124.08
$R(z = 0)$	112.00	113.48	114.83	116.32	117.81	119.28
$d(z = L/2)$	1.71	1.73	1.83	1.85	1.87	1.89
$d(z = 0)$	1.71	1.73	1.75	1.77	1.80	1.82

4.3.2 Design overview

Generally the straws are glued to metallic plugs (feedthrough) at the two ends and tensioned between two rigid end plates. A number of mechanical and electronic design elements like: feedthrough, pins, wire, preamplifier, discriminator and TDC are needed to be optimized for the particular experimental situation. Guidelines for making this optimization in the context of the FINUDA apparatus are mentioned in this paragraph.

For a realistic selection of these design parameters, intense prototyping with two meter long straws with inner diameters of 10 mm and 20 mm has been started at Frascati since the beginning of 1994. The results obtained with the prototypes demonstrate that with normally incident particles, a space resolution better than 40 μm can be reached and reproduced for the entire straw length. According to our knowledge, this is the best spatial resolution ever obtained with two meter or longer straws.

The final selection of design components is based on experience gained with the existing prototypes. The executive designs for the mechanical/electronic components have been passed onto external firms and will be evaluated on the next test beam scheduled to take place in December this year at TRIUMF with a prototype employing $\sim$ 150 straws.

Mechanical components

The straw length as determined by the geometric acceptance is about 2.5 meters. The number of channels is reduced by using larger diameter straws, but at the same time, contribution due to electron diffusion and gravitation sag due to weight density need straws of smaller diameter. The design efforts have been focused to select straw diameters from 10 to 20 mm. Aluminized mylar straws with inner diameter of a few tens of mm and a wall thickness down to 20 μm are commercially available.

The selection of anode wire is determined by the requirement of long term stability and minimization of gravitational sag. As we are not interested in charge division, wire resistance is irrelevant. A smaller wire diameter renders it more vulnerable to mechanical misuse but at the same time permits higher gain at equivalent operating voltage.

The feedthrough has multiple functions. It should provide means for mechanically positioning and tensioning the straws. At the same time the gas flow and electrical ground are provided by the feedthrough. The wire is crimped in by metallic pins positioned at the center of the feedthrough. The pins provide the electrical connection to the wire for high voltage and signal. In order to compensate for gravitational and electrostatic effects which tend to offset the wire from the straw center, it is common to place a wire support at the center of the straw. The support should precisely position the wire at the center of the straw and should have a small weight.

The gas should provide a small diffusion and Lorentz angle with a high ionization. Since we expect very low straw occupancy (< 0.01 %), pile up (low drift velocity) and ageing do not constitute a concern.

Although the required space resolution can be reached with conventional gas mixtures like Ethane and Argon, the initial attention has been focused towards the use of pure Dimethyl Ether. Pure DME has the advantages of a minimum electron diffusion ($\sim 7\mu m$ per mm of drift distance) and a very small Lorentz angle (less than 2^0 at a magnetic field of 1 Tesla [21]). It has a low drift velocity, implying less stringent requirement on the timing system performance.

Electronic components

Using DME we expect to reach a gas gain of $\sim 10^6$. The preamplifier is therefore needed to provide a moderate charge gain while matching the straw characteristic impedence to the input impedence of the discriminator circuitry. It is required to have a bandwidth large enough for an output rise time of $2{\sim}3$ ns.

Straws of 10–20 mm internal diameter when operated at an anode voltage of a few kV will give rise to electric field values for which the drift velocity v_d of the electrons varies from ~ 2 $\mu m/ns$ at the straw surface to about 60 $\mu m/ns$ near the wire. An rms error of δ_t in time measurements contributes to the space resolution by $v_d \times \delta_t$. It is therefore necessary to contain time jitter within ~ 2 ns, if its contribution to the space resolution is to be kept less than 100 μm even for small drift distances. The dynamic range of the time measurements is determined by the maximum drift time and is about 3 μs.

4.3.3 Straw tube prototype

In order to investigate the straw tube performance, and to freeze the design parameters, a prototype using several straw tubes [27] with diameters of 10 and 20 mm and 2 meters long was assembled at LNF to the beginning of 1994. All the mechanical parts were produced at LNF and the mechanical tolerances were kept to their best possible values [28]. Various characteristics of the prototype are listed in Tab. 4.9.

Operating with DME, signal characteristics, single's count rate plateau and gas gain were studied and preliminary studies with cosmic rays were carried out. Straw

Table 4.9: Prototype mechanical characteristics.

	10 mm straws	20 mm straws
Number of straws	8	4
Wire diameter	30 μm	30 μm
Inter-axis	10.2±0.01 mm	22.2±0.01 mm
Staggered straws	Yes	No
Operating voltage	3.2 kV	3.5 kV
Gas over pressure	20 $mbar$	20 $mbar$
Preamplifier gain	1–3 V/mA	1–3 V/mA

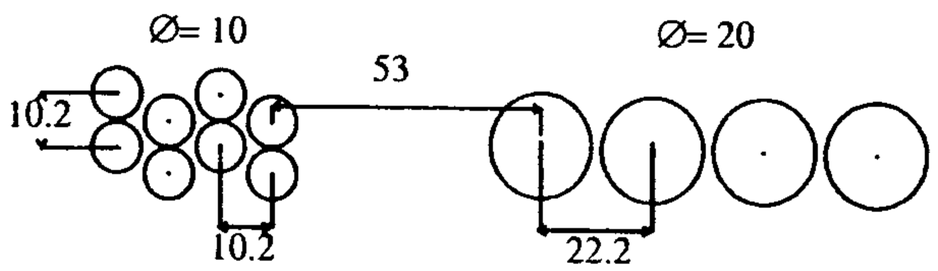

Figure 4.41: Geometrical details of the prototype array (units: mm).

efficiency, space resolution and systematic effects were further studied while testing the prototype with a 1 GeV/c π^- beam at CERN.

Prototype components and assembly

The geometrical details of the prototype array are shown in fig.4.41. It consists of eight straws with an inner diameter of 10 ± 0.05 mm and four 20 ± 0.05 mm diameter straws. The 10 mm straws are arranged in four staggered layers, containing each 2 straws. The layers are staggered by about one straw radius (5.1 mm). The four 20 mm straws were all aligned and placed at $\sim$ 5 cm away from the staggered straws.

The straws we used are produced by spiral wrapping of a 0.012 mm thick vacuum aluminized mylar strip on a mandrel. The thickness of the Al deposit is 0.1 μm. A coat of polyester based epoxy is applied on the wrapped strip and a second, 0.012 mm thick, mylar strip is wrapped over it. The overall straw thickness is 0.03 ± 0.01 mm, which represents about 1×10^{-4} radiation lengths. The linear weight density is $\sim$ 13 mg/cm for 10 mm diameter straws and 26 mg/cm for 20 mm diameter straws.

As envisaged for FINUDA, the straws are supported at the two ends only. In order to minimize the gravitational sag, they are subjected to a pulling force which actually is limited by the straw elasticity. As the straws are pulled, their length is

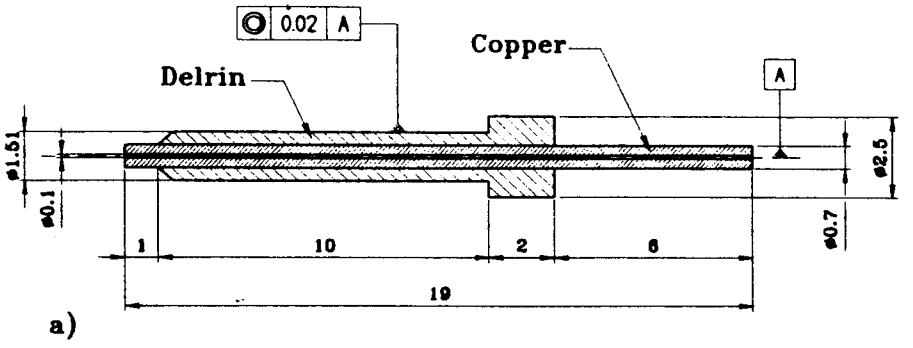

Figure 4.42: Design of the pin used for the prototype. All dimensions are in *mm*.

increased, with each *kg* of tension giving rise to an instantaneous relative elongation of ~ 0.2 %.

Gold plated Tungsten wires (LUMA) with a diameter of 0.03 *mm* have been used as anode. The wire resistance is measured to be 85 Ω/m and the maximum mechanical load of a wire is 1.8 *N*.

The anode wire is crimped in gold plated copper pins shown in fig.4.42. The pin has an inner hole of 0.1 ± 0.02 *mm* with a 6 *mm* long crimping zone which has an outer diameter of 0.7 ± 0.01 *mm*. The 10 *mm* long conic section of the pin, covered by Acetal resin, gives the mechanical rigidity and locates it in the straw feedthrough.

Two of the 20 *mm* straws employ also an internal wire support shown in fig.4.43. The wire support is realized by working a delrin piece on a lathe machine. The outer diameter has a tolerance of 0.01 *mm* with a concentricity for the central hole of 0.1 *mm*. The overall weight of the support is 700 mg.

The feedthrough, as shown in fig. 4.44, consists of an aluminum cylinder which on the straw side has an external diameter (tapered by 10% at the beginning) equal to the straw inner diameter with a tolerance of 0.01 *mm*. The inner surface of the straw is glued on to the feedthrough using a silver based conductive glue. The end plate side of the feedthrough is externally threaded in such a way that, when tightened with the corresponding nut, it permits the feedthrough to move along the axis of the end plate hole while pulling the straw to the required tension. The feedthrough contains an inner delrin body which accommodates the wire pins and provides the gas inlet/outlet for the straws.

The diagram of the preamplifier circuit used with the prototype straws is shown in fig.4.45. It has an input impedance of 300 Ω. Three different preamplifier gain

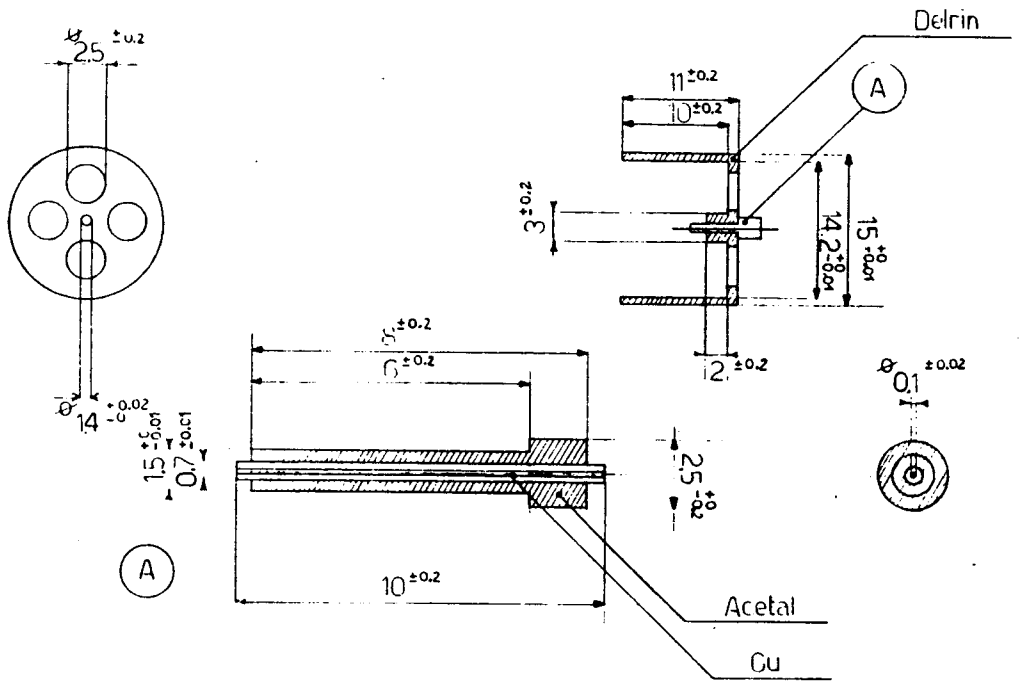

Figure 4.43: Wire support design. All dimensions are in *mm*.

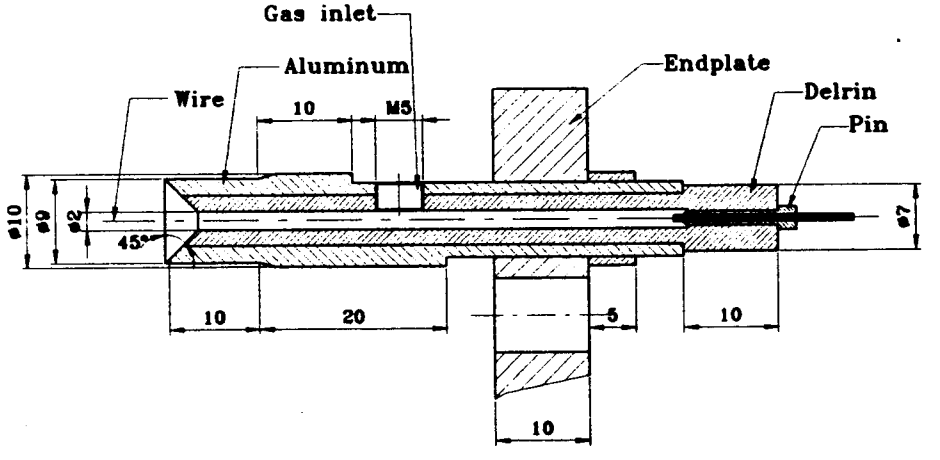

Figure 4.44: Feedthrough used for the prototype. All dimensions are in *mm*.

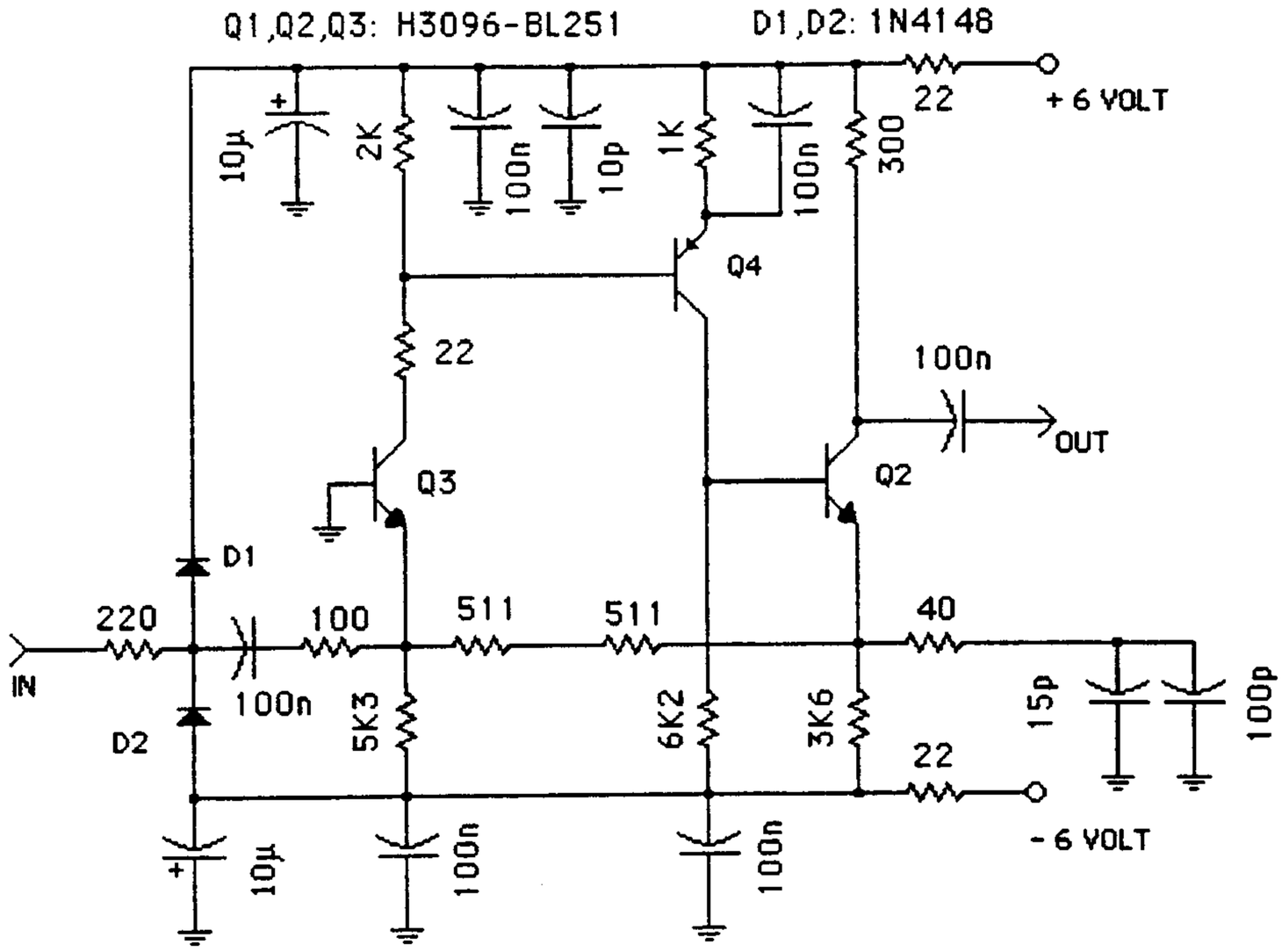

Figure 4.45: Circuit diagram of the preamplifier used with the prototype.

values (1, 2 and 3 V/mA) have been employed on the prototype. The circuit operates with $\pm$ 6 V dissipating 50 mW per channel. The maximum output pulse height before saturation is 2 V. In addition to signal amplification, a high voltage filter is also incorporated in the same circuit. The preamplifier characteristics are summarized in Table 4.10.

Table 4.10: Preamplifier characteristics.

Input impedance	300 Ω
Gain	1–3 V/mA
Charge gain	20–60
Dynamic range	2 V
Output rise time	2 ns
Power supply	$\pm$6 V
Power consumption	50 mW

The preamplifiers were developed at LNF and mounted on PCBs using SMD components. In order to provide e.m. shielding the preamplifiers were enclosed in brass boxes and connection to straws were provided by $\sim$ 5 cm long coaxial cables with grounded shield.

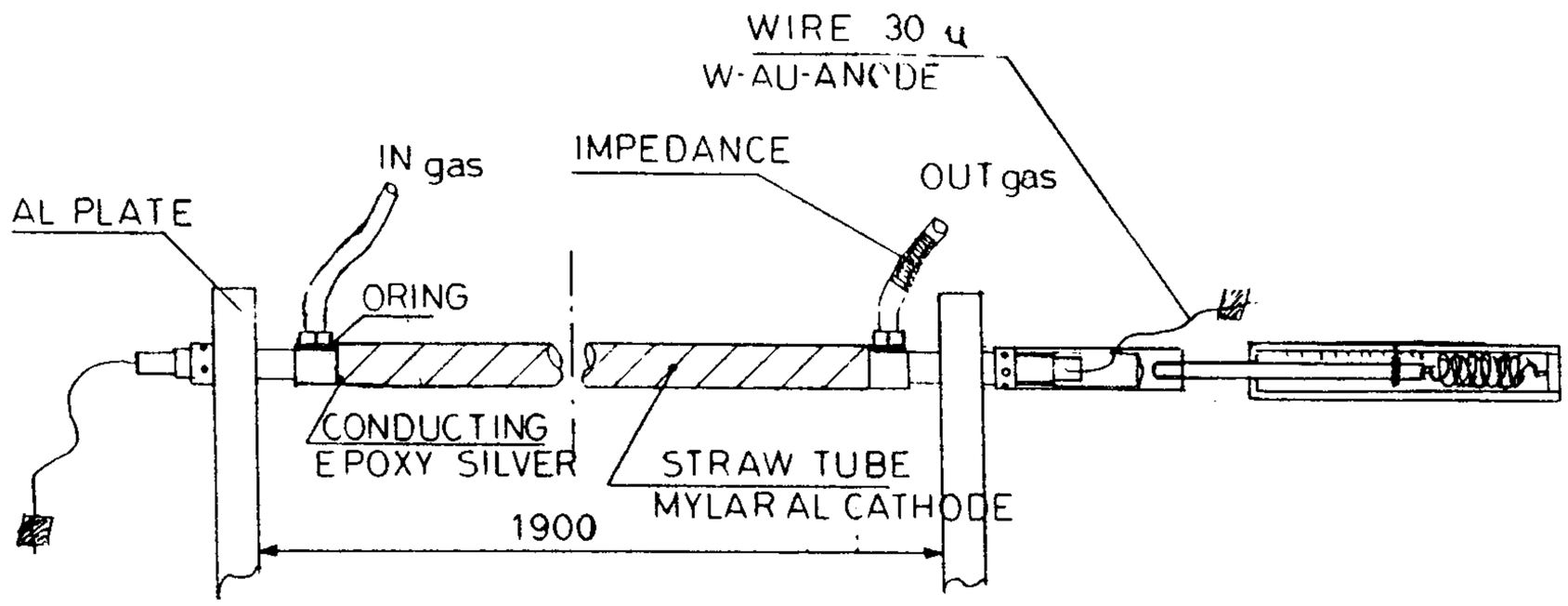

Figure 4.46: An artistic illustration of assembly procedure.

The prototype assembling procedure is illustrated in fig.4.46. The wire is initially strung through the straw, feedthroughs and the pins without any mechanical tension. The inner surface of the straw on the two ends is now glued on to feedthroughs. The setting time of the glue is 16 hours at room temperature and once hardened it can support a maximum load of 126 kN/cm^2. Once the glue is hardened, feedthroughs are inserted in the end plates and the straw is manually tensioned to 25 N. After blocking the feedthroughs against the end plates, the wire is crimped inside the pin on one side, tensioned to 1 N and crimped on the opposite side.

Signal characteristics and gas gain

The gas used in the prototype is 99.8% pure (DME) at a pressure of 1.02 bar. The high voltage was switched on after five volume changes, and a constant flow of 2 volumes/day has been used during normal data taking.

All the 10 mm diameter straws reach a single's count rate plateau at about 3 kV and in most cases the plateau is more than 800 V long (fig.4.47a). The plateau knee, for 20 mm straws is found at 3.2 kV. The signals for cosmic rays and ambient radioactivity, observed at the output of preamplifier with anode at 500 V above the plateau knee show a pulse height of about 200 mV with a rise time of 3 ns (fig.4.48).

Gas gain was measured using pulses originated by single electrons produced by photoemission from the cathode surface. By illuminating the straw with a torch light, an electron emission rate of 8 kHz was produced, which was much higher than the single's rate so that the gain measurements were not biased. On the other hand this rate was low enough to ensure that the probability to integrate more than one pulse in the same ADC gate was negligible. The ADC charge distributions for a 10 mm straw at two different voltages is shown in fig.4.49. The gain variations

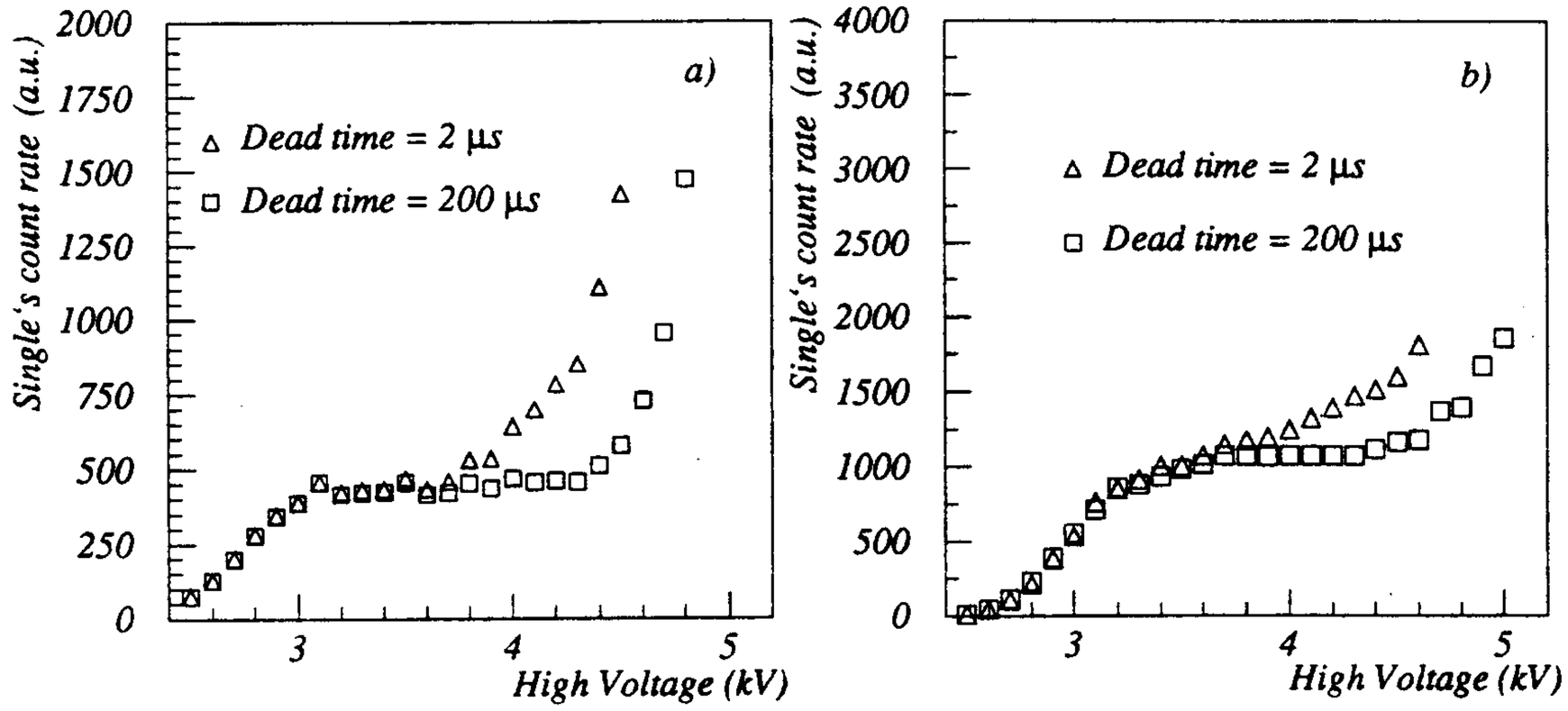

Figure 4.47: Single's count rate plateau curve for a) 10 *mm* straw b) 20 *mm* straw.

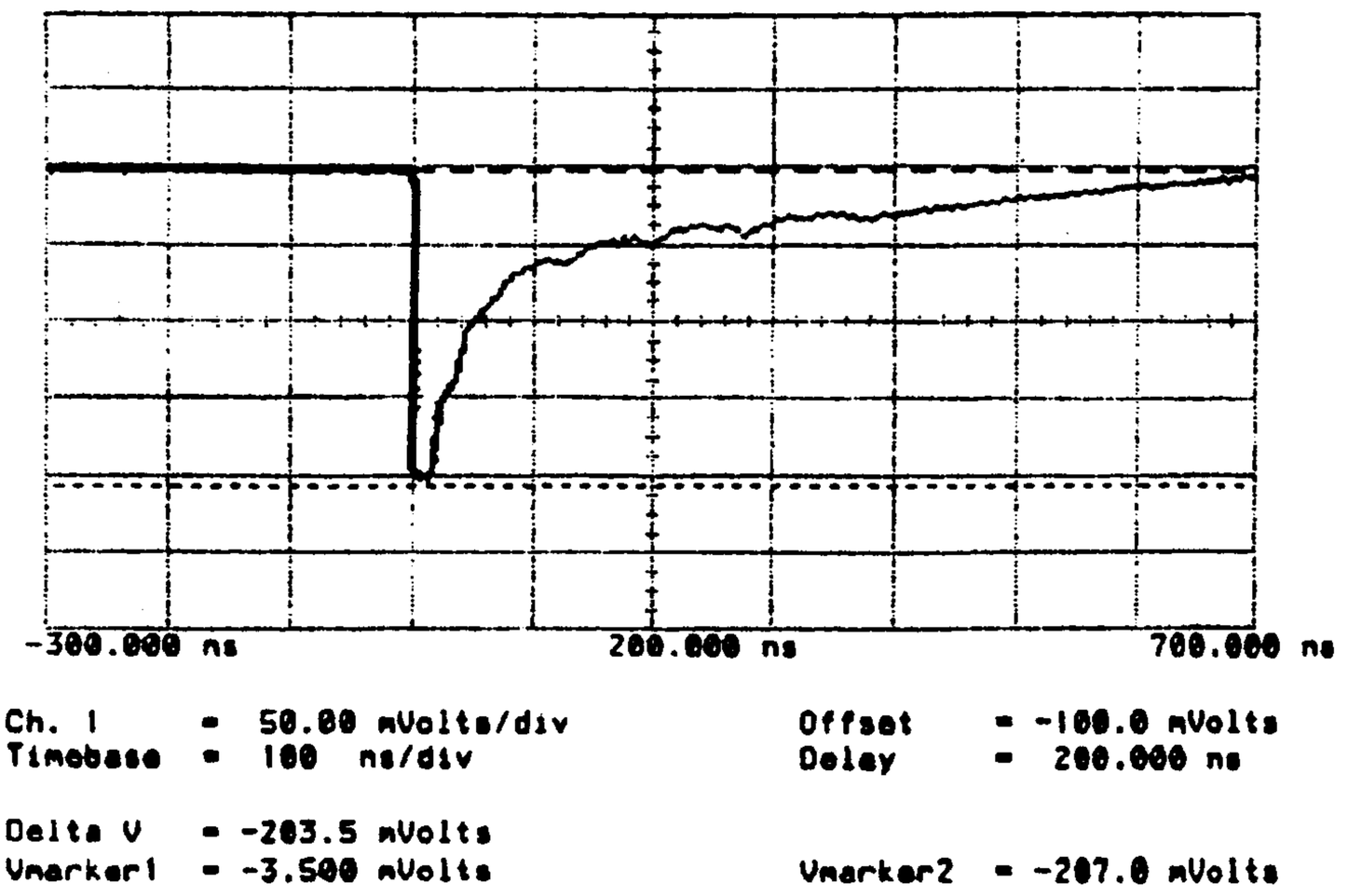

Figure 4.48: Average signal at 500 V above the plateau knee for a 10 *mm* straw.

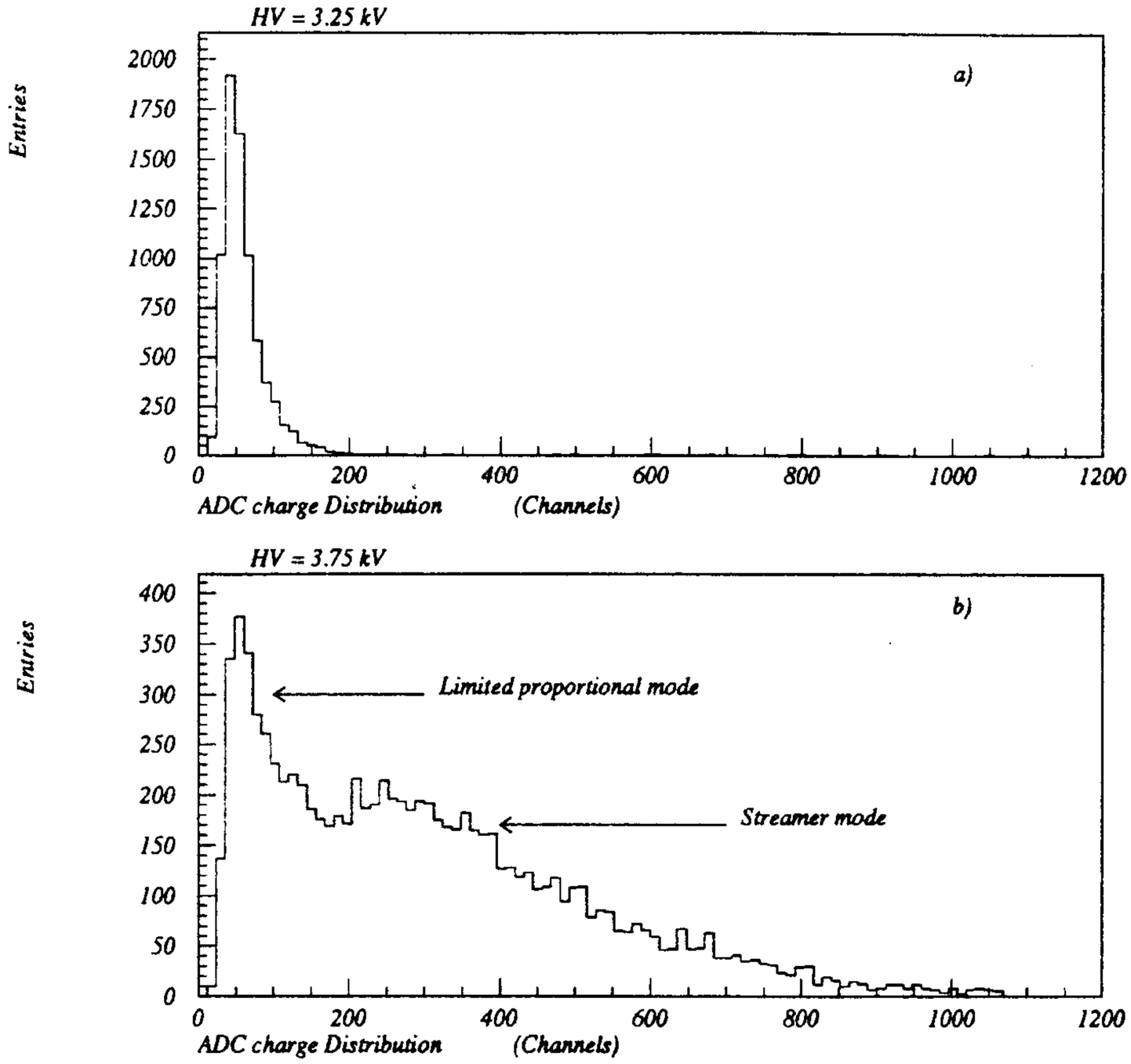

Figure 4.49: ADC charge distributions for avalanches started by single electrons obtained by photoemission from Al cathode.

with straw voltage are shown in fig.4.50.

To investigate the mode of operation we additionally used the signal from a ^{55}Fe source. The ^{55}Fe source with its characteristic 5.9 keV X-ray emission is expected to produce a tight cluster of $\sim$ 200 electrons. The average value of ADC charge against applied voltage is shown in fig.4.50 for the ^{55}Fe source and is compared with single electron signals. At 3.7 kV the single electron signals show a jump in gas gain, reaching almost the same value of ^{55}Fe signals, which indicates a transition from limited proportional to streamer mode.

4.3.4 Results of tests on the prototype with a pion beam

The prototype performance has been studied by means of a 1 GeV/c π^- beam (T10) at CERN PS [29]. The goal was to characterize the performance of the straw tubes

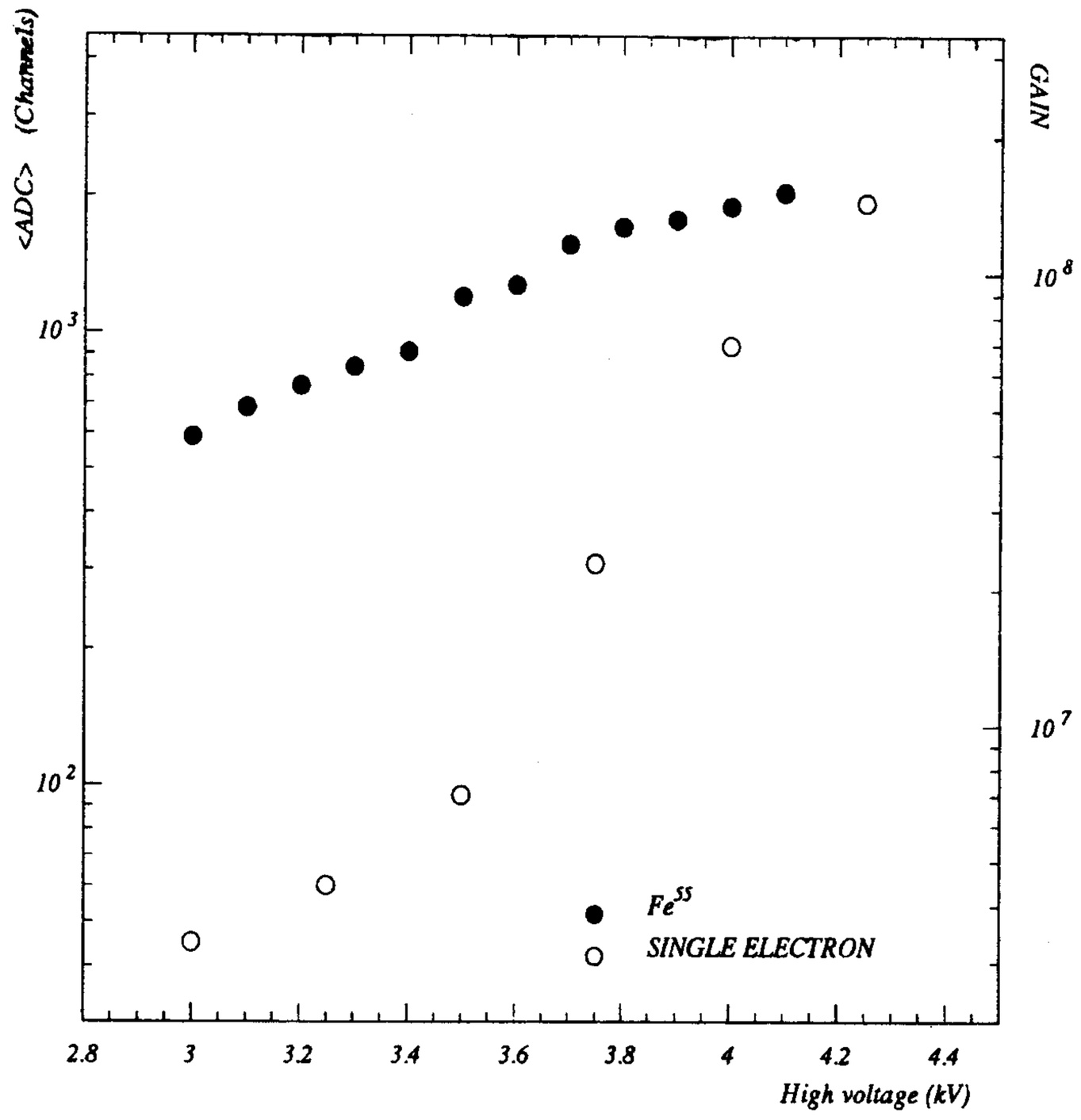

Figure 4.50: Average ADC charge for single electron and ^{55}Fe source signals. The gas gain to be read with single electron signals is shown on right.

studying the efficiency, space resolution and track reconstruction. In the following paragraphs we describe the test beam setup and the results from the prototype. A simple method of correcting for systematic effects has been developed and, once applied, a space resolution better than 40 μm was obtained over the entire straw length.

Experimental setup

The test beam setup is shown in fig.4.51. The 20 mm diameter straws were facing the incoming beam direction and were followed by 10 mm diameter straws. The prototype was mounted on a support movable both in horizontal and vertical direction, which permitted us to scan the prototype along the wire axis. The straws were operated with pure DME (99.8%) at an overpressure of 20 $mbar$. The anode voltage was set to 3200 V for the 10 mm straws and to 3500 V for the 20 mm straws.

The preamplifiers were mounted at the straw ends. The amplified straw signals were brought to discriminators usually operated with a threshold of -30 mV, by $\sim$ 6 m long RG–58 cables. CAEN model N96 low threshold discriminators were used for 10 mm diameter straws and we used CAEN N224 discriminators for the 20 mm straws. The discriminator output was brought to the stop input of TDCs by $\sim$ 40 m long RG–58 cables. Drift times were read for both 10 and 20 mm straws using 12 bit TDCs (CAEN C414) operated in common start mode. In order to have the maximum drift time within the TDC range with the best possible single bit time resolution, the TDC full scale was set to 2 μs for 10 mm straws and to 5 μs for the 20 mm straws (corresponding to a single bit resolution of 0.5 ns and 1.25 ns, respectively).

A pair of scintillator counters was used to define a 15×15 mm^2 beam spot. Their coincidence gave the start signal to TDCs.

Time to space conversion

A typical TDC distribution for 10 mm straws is shown in fig.4.52. The delay due to signal propagation on wire and through preamplifier and discriminator, T_0, is determined from the offset of the starting edge of the TDC spectrum. The time to drift distance relationship is computed using the parameters given in [32]. The T_0 subtracted TDC values are accordingly transformed into drift distances which define the drift circles for the hit straws.

Track fitting

The procedure of track fitting [30] (in the x–y plane as shown in fig.4.51) starts by isolating 10 mm straws with a TDC value below the overflow. Only those events are further considered for which at least three drift circles could be defined. A common tangent to drift circles is identified and a linear track is fitted while minimizing the function:

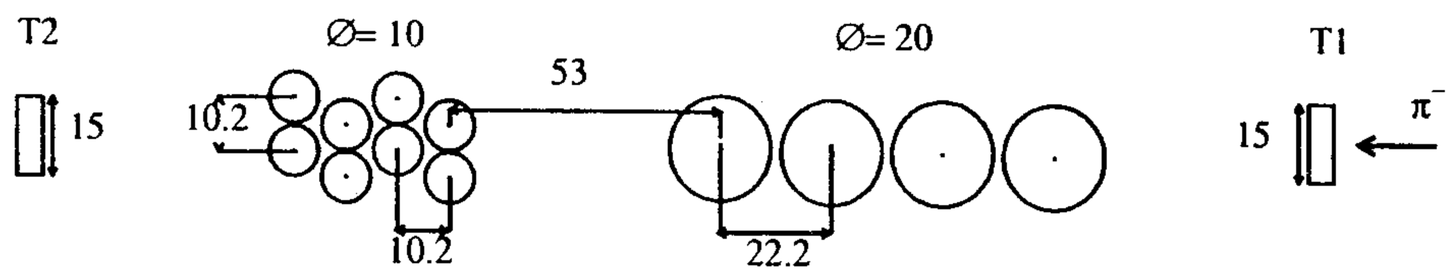

Figure 4.51: CERN test beam setup.

$$\chi^2 = \sum_i \frac{(r_i - \rho_i)^2}{\sigma^2(r_i)}$$

where ρ_i is the distance of closest approach of the fitted track from the i^{th} wire for which the observed drift radius is r_i. The radial dependence of space resolution is described in a following section and for $\sigma(r_i)$, the same radius dependence shown in fig.4.63 is used.

Unlike staggered 10 *mm* straws, the 20 *mm* straws themselves can not eliminate the left-right ambiguity. The track fitted with 10 *mm* straws is projected to the 20 *mm* straws and this ambiguity is therefore removed. A linear fit is then performed working with 20 *mm* straws only. Typical tracks are shown in fig.4.53.

The two parameters chosen to define the linear tracks are the the intercept X_{int} and the angle θ with the x-axis (see fig.4.53 for the axis definition). The distribution of parameter θ (see fig.4.54) can be interpreted as beam divergence, and indicates that the beam had an angular spread of 5 *mrad*.

Straw efficiency

The reconstructed tracks are used to investigate the straw efficiency. For a radial distance between r and r+dr, the efficiency is defined as:

$$\epsilon(r) = \frac{N_{hits}}{N_{tracks}}$$

where N_{tracks} is the number of times a track passed through the selected radial distance and N_{hits} is the number of times a hit was found. A few straw efficiency

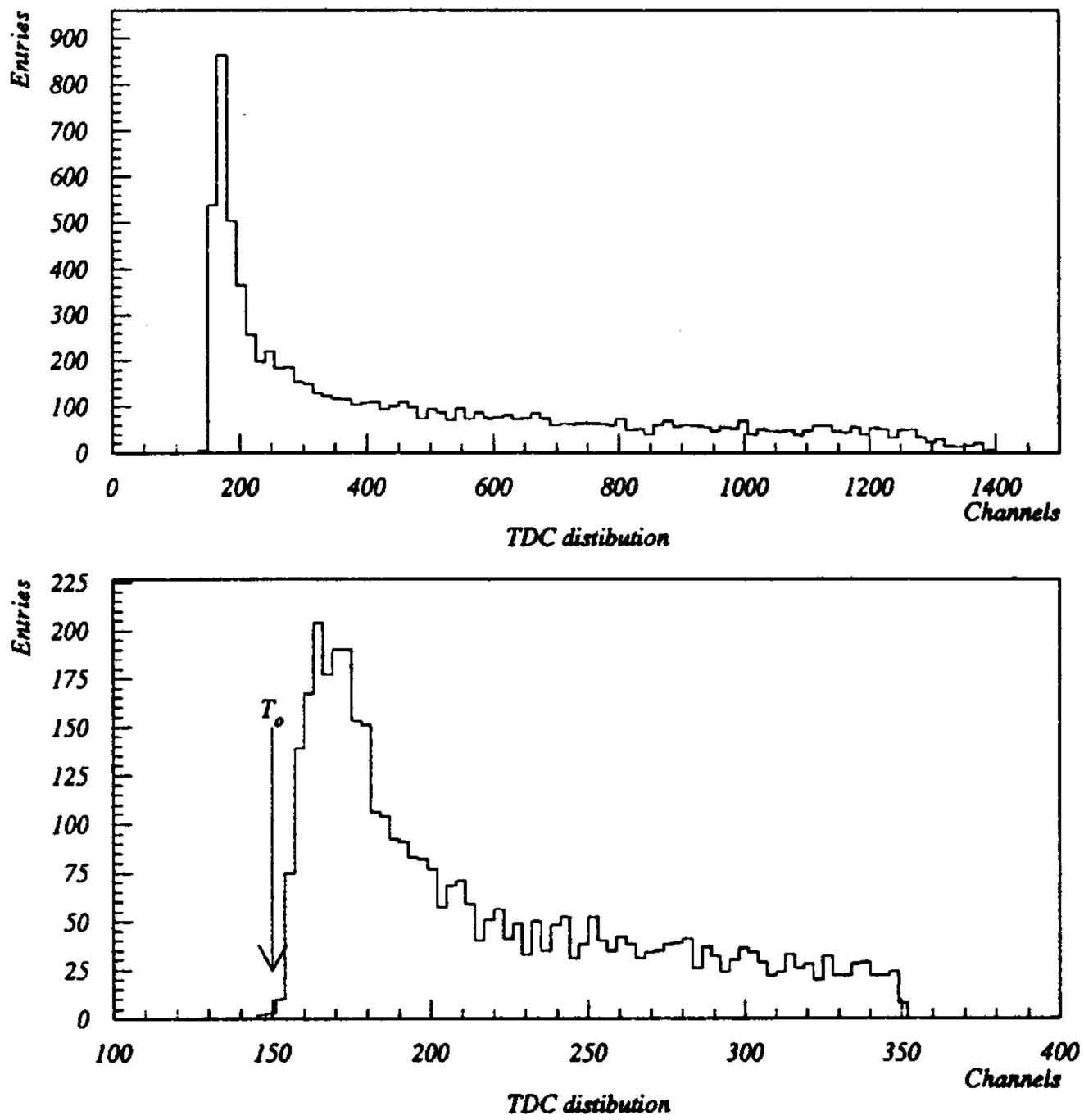

Figure 4.52: Typical TDC distributions for a 10 mm straw and T_0 determination.

profiles are shown in fig.4.55. Integrating the efficiency profiles, the average efficiency for different straws is shown in fig.4.56. With a preamplifier gain of 3 V/mA and at the usual operating voltage during the test (3200 V for 10 mm and 3500 V for 20 mm straws) we had $\epsilon \geq 99\%$.

Two of the 20 mm straws had a wire support at the center, as shown in fig.4.43. While moving the straws across the beam a fine scan was performed in the zone of the wire support. The loss in efficiency caused by the support is indicated by the results shown in fig.4.57. It is to be noticed that a 1 cm long wire support introduces a zone of reduced efficiency which is about 5 cm long.

Local space resolution

As illustrated in fig.4.58a, for three aligned straws the drift radius r of the central straw is equal to the average drift radius $(r_1 + r_2)/2$ of two external straws. In order

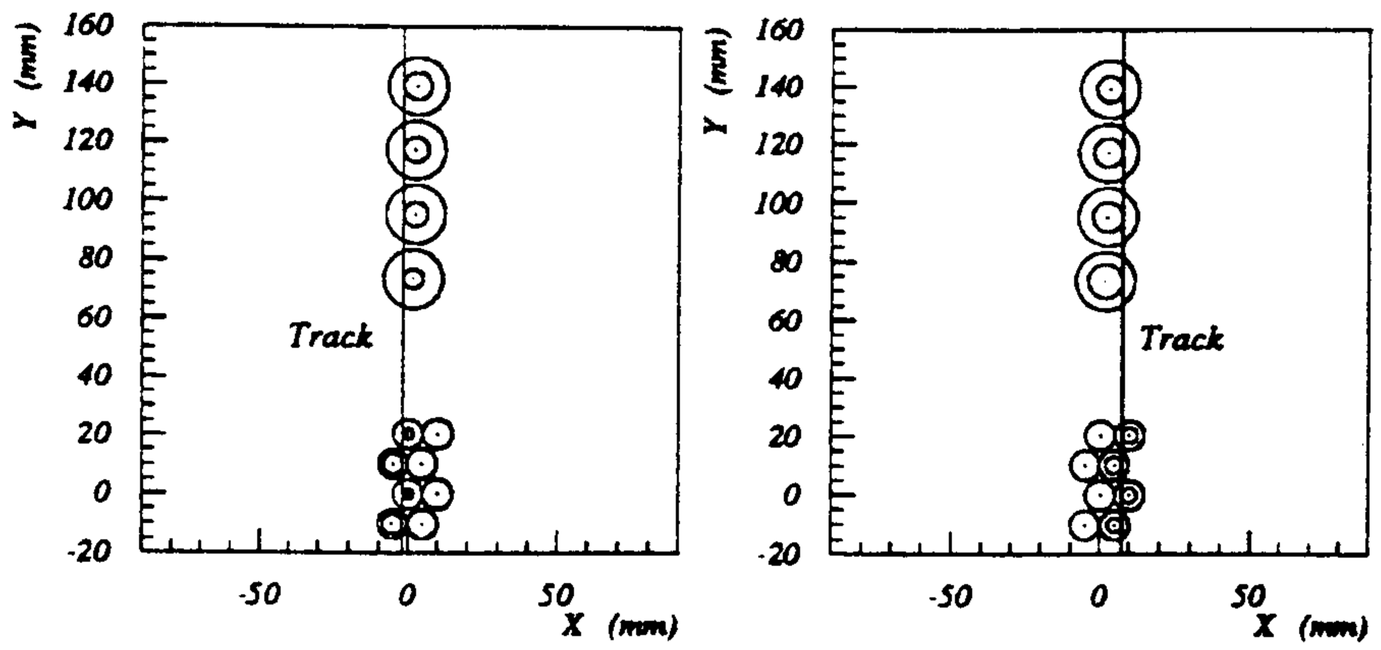

Figure 4.53: Typical tracks.

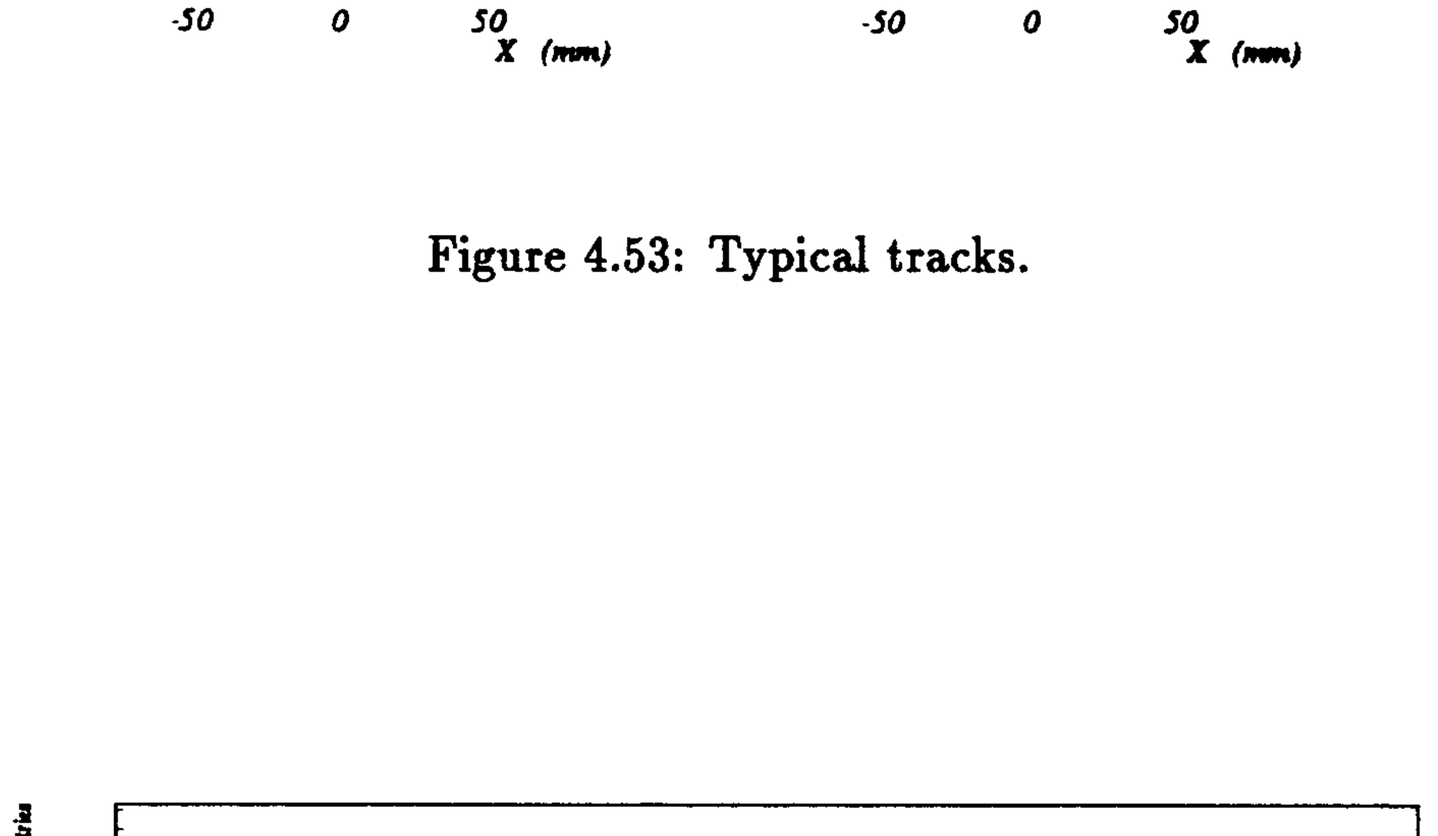

Figure 4.54: Beam divergence as obtained from fitted tracks.

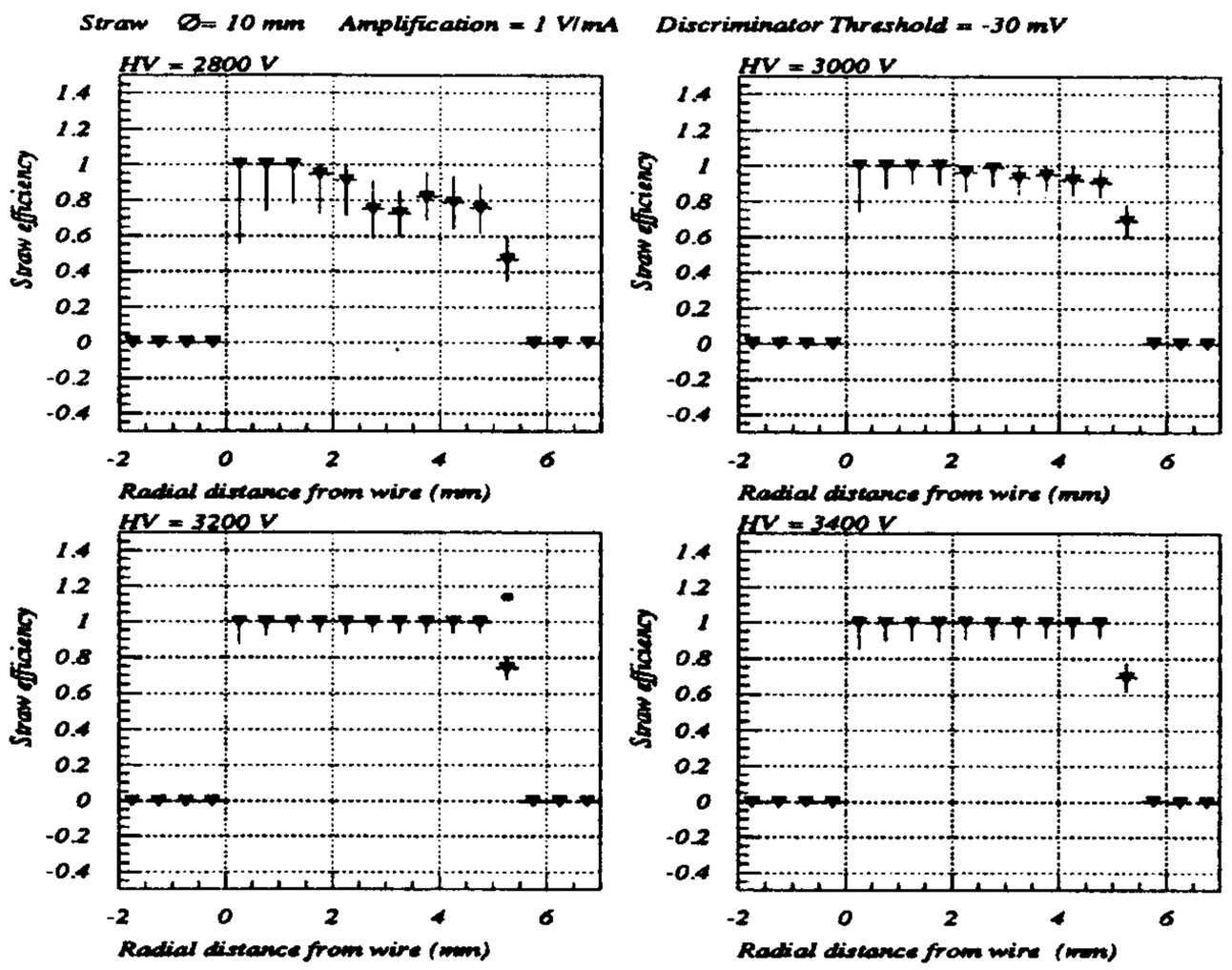

Figure 4.55: Efficiency profiles for a 10 mm straw with different operating voltages.

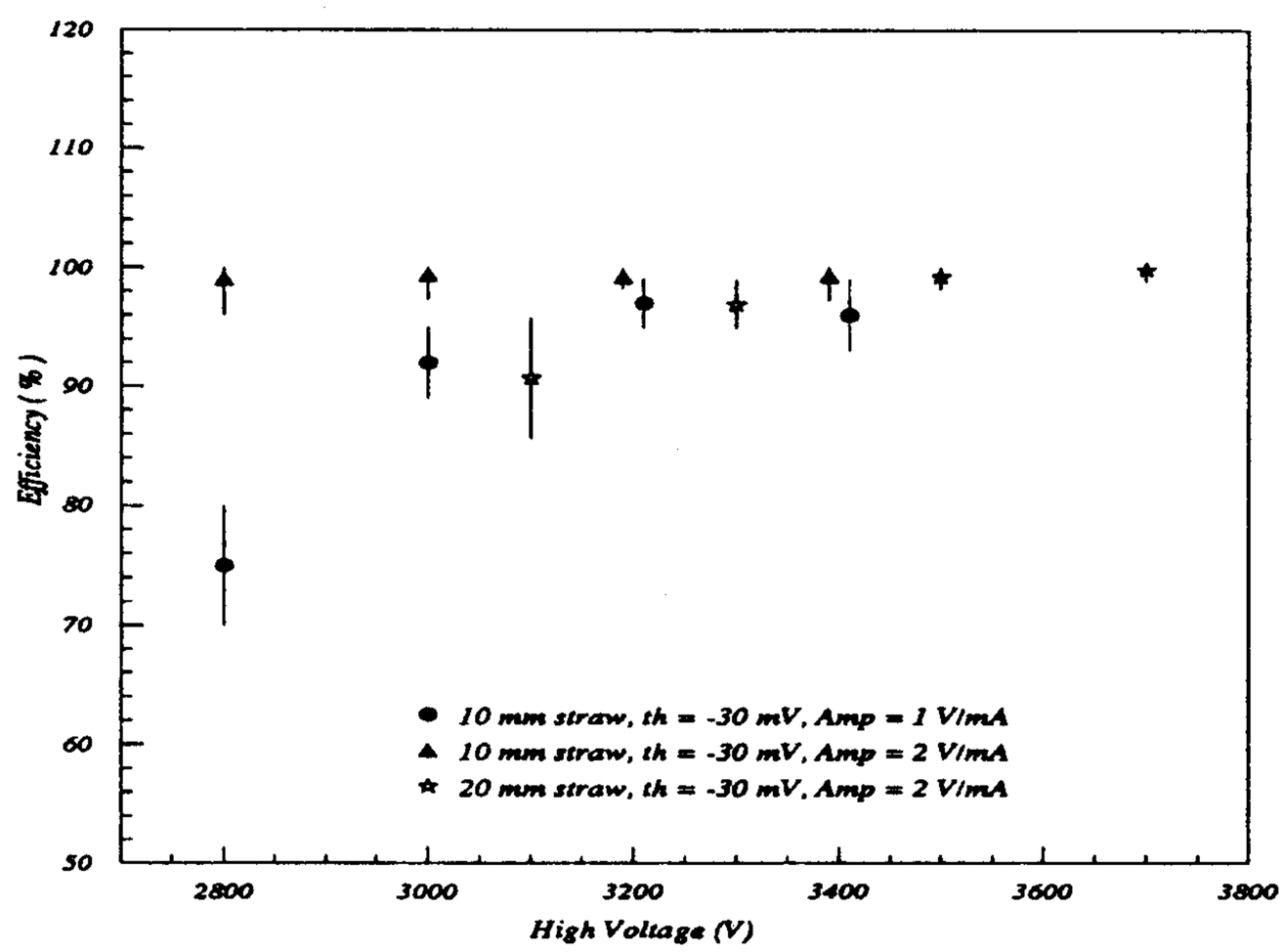

Figure 4.56: Average efficiency curves for 10 and 20 mm straws.

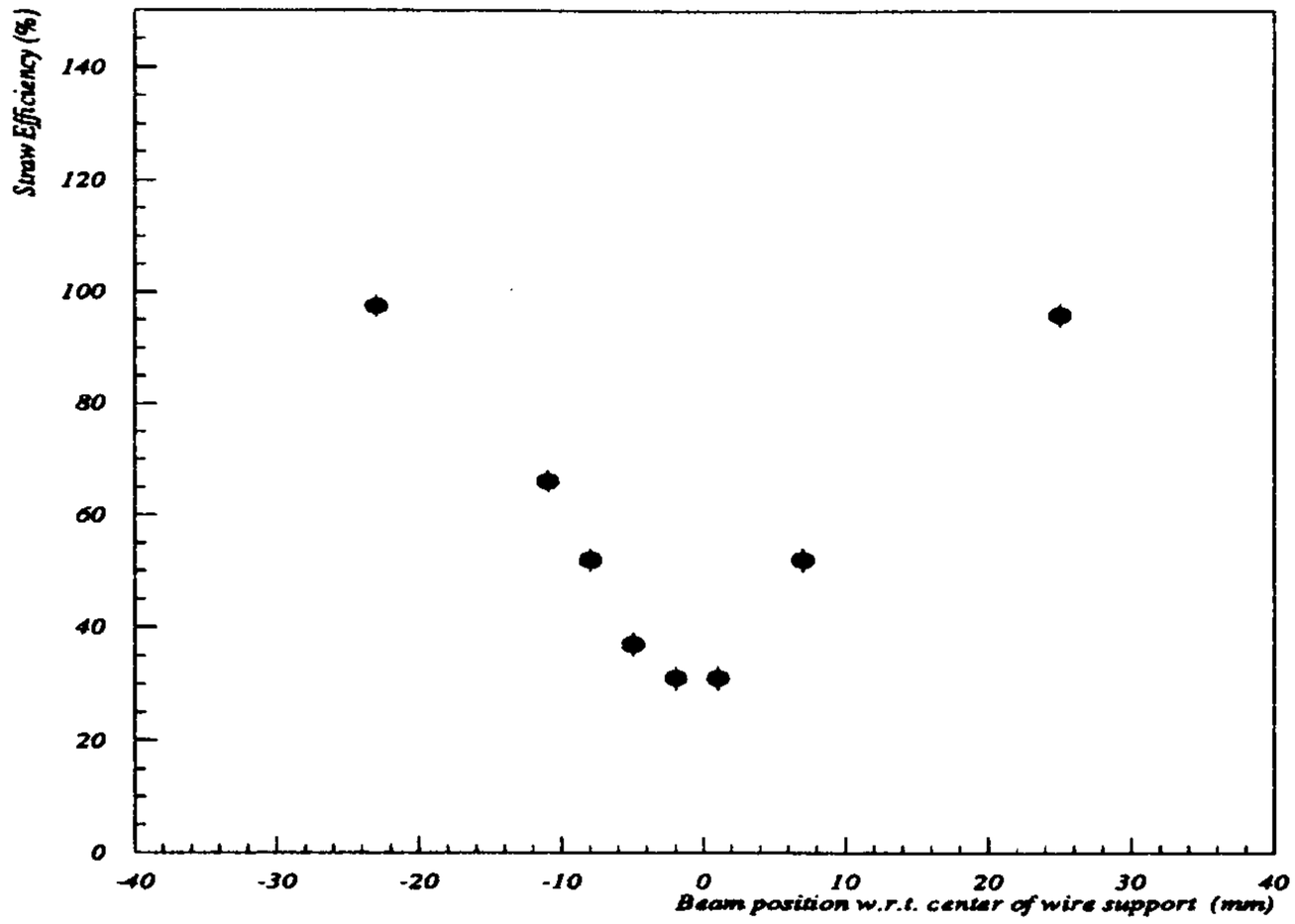

Figure 4.57: Straw efficiency as a function of the beam position along the axis of wire support.

to determine the straw space resolution one can define a function $R^A(r)$ as:

$$R^A(r) = (r_1 + r_2)/2 - r$$

The rms of the function $R^A(r)$ is determined by the precision with which individual drift radii are measured. The assumption that the three straws have the same dependence of the space resolution on the drift distance, given by the function $\sigma(r)$, combined with the results (fig.4.54) that the tracks were almost parallel to the y-axis ($r \sim r_1 \sim r_2$ and therefore $\sigma(r) \sim \sigma(r_1) \sim \sigma(r_2)$) yields:

$$\sigma_{R^A(r)} = \sqrt{3/2} \times \sigma(r) \tag{4.5}$$

where $\sigma_{R^A(r)}$ represents the rms of the function $R^A(r)$ which can be obtained from experimental data. The radial variation of the straw space resolution i.e., the function $\sigma(r)$ can than be determined by inverting Eq. (4.5).

Using the symbolism of fig.4.58b, a similar function $R^S(r)$ can be defined for staggered straws, where:

$$R^S(r) = (r_1 + r_2)/2 + r$$

As in the case of aligned straws, the rms of the function $R^S(r)$ can be related to the straw space resolution $\sigma(r)$. For tracks passing at a distance r from the

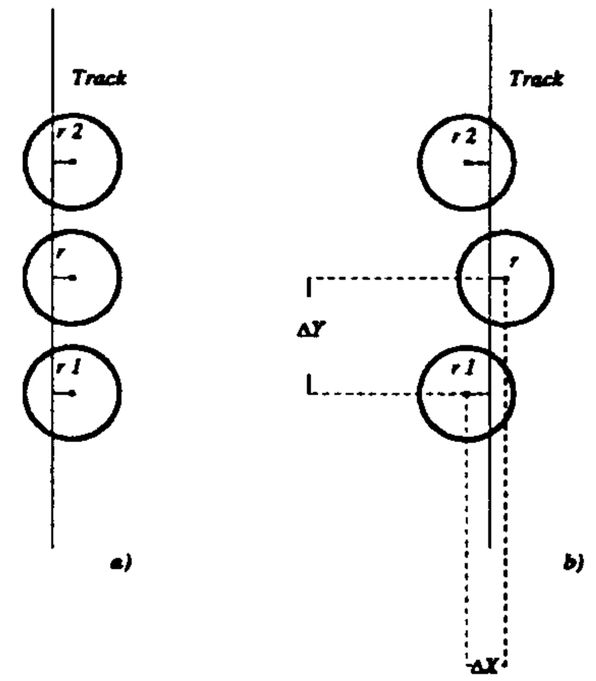

Figure 4.58: A graphical illustration of how to construct variables using drift radii of a) aligned and b) staggered straws to obtain straw space resolution.

central wire, the drift distance is measured with a resolution of $\sigma(r)$ by the central straw whereas the two external straws measure the drift distance with a resolution $\sigma(\Delta_x - r)$. It can be shown that for the test beam data:

$$\sigma_{RS(r)} = \sqrt{\frac{(\sigma(\Delta_x - r))^2}{2} + (\sigma(r))^2} \tag{4.6}$$

Trivially, the expected value of the function $R^A(r)$ is zero and that of the function $R^S(r)$ is given by:

$$< R^S(r) >= \Delta_x$$

where Δ_x, the stagger distance between the straws, is 5.1 mm for the prototype.

In fig.4.59 we plot the function $R^A(r)$ for three of the 20 mm straws against r. It is found that the events are separated in two separate bands. Using the information from track fitting, the two bands are found to be associated with tracks passing above and below the wire and the observed separation in two groups can be explained by a misalignment of the three wires. The fact that the two bands of events in fig.4.59 are not parallel to each other shows that the expected value of the function $R^A(r)$ depends on r and indicates the extent of systematic effects of wire eccentricity and the corresponding lack of accuracy in the time–to–space relationship used. The systematics, if not corrected, will dominate once the straw

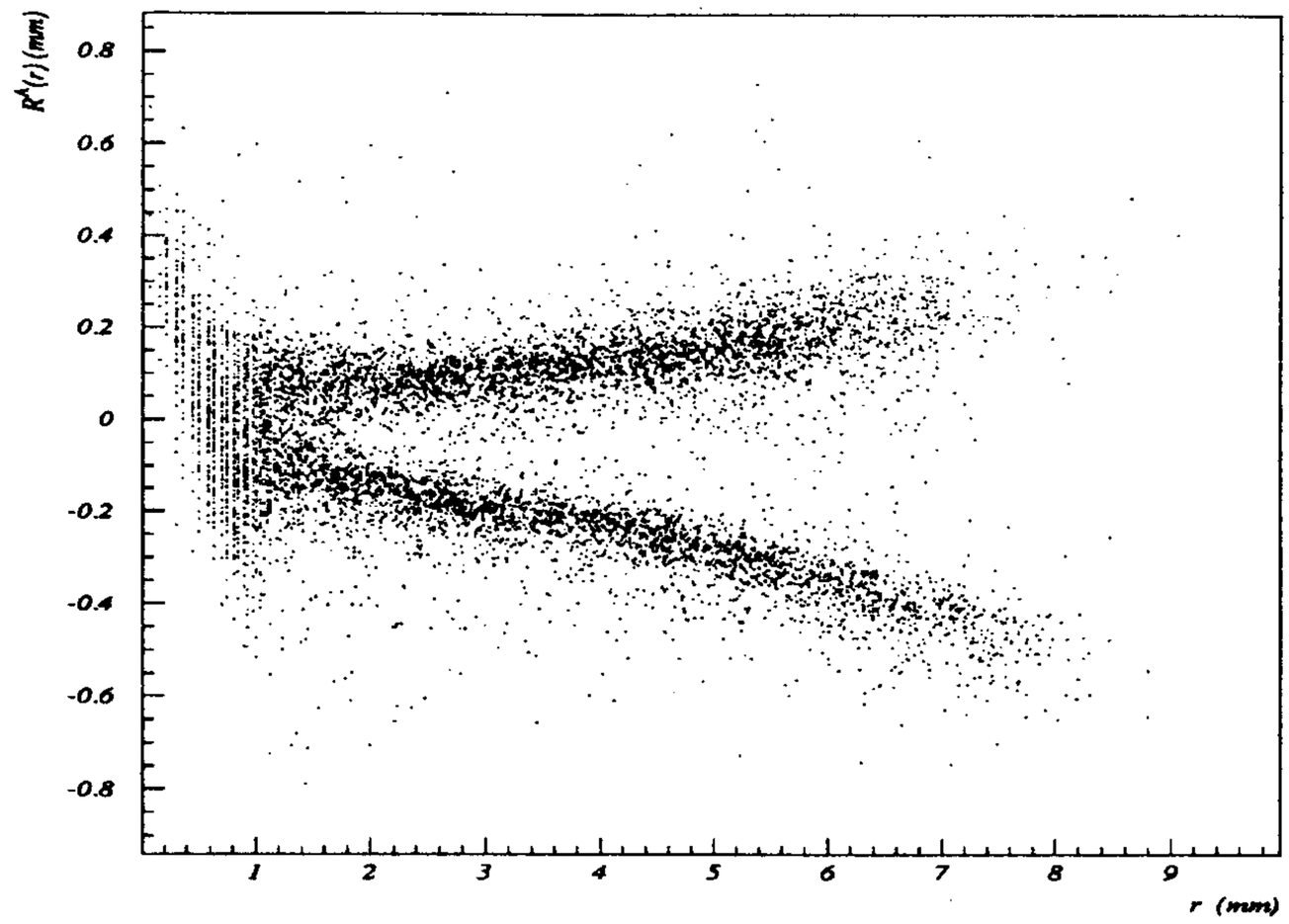

Figure 4.59: The scatter plot of $R^A(r)$ vs r for the 20 mm straws.

performance over the entire radius is considered. However, taking one of the bands at a time and for a fixed value of r, these will only change the expected value of the function $R^A(r)$ and its rms is still related to *local space resolution* $\sigma(r)$ by Eq. (4.5).

To determine the local space resolution the two bands of fig.4.59 are divided in small bins of r and distributions for the function $R^A(r)$ are obtained. The $\sigma_{R^A(r)}$ obtained by Gaussian fits to these distributions is plotted in fig.4.60a against r. It is to be noticed that the empty and filled symbols of fig.4.60a correspond to the upper and lower band of the scatter plot shown in fig.4.59 for the same set of straws and they show a similar trend. A similar analysis procedure is repeated for the 10 mm straws and the $\sigma_{R^S(r)}$ as obtained by Gaussian fits, is plotted in fig.4.60b.

As implied by Eq. (4.5), the local space resolution $\sigma(r)$ for the 20 mm straws is obtained from the $\sigma_{R^A(r)}$ values multiplied by a constant factor $\sqrt{2/3}$ and is shown in fig.4.61. The results shown in fig.4.61 correspond to different straws and different distances of the beam along the wire axis and they all show the same dependence of local space resolution on drift distance. For the major part of the straw radius, $\sigma(r)$ is smaller than 60 μm, and there is a sharp deterioration in local space resolution as one approaches the wire (smaller drift distances). For drift distances greater than 3 mm, the local space resolution deteriorates almost linearly with increasing drift radii.

The local space resolution $\sigma(r)$ for the 10 mm straws is obtained from the $\sigma_{R^S(r)}$ values by inverting Eq. (4.6). The function $f(r)$ (a third order polynomial in r)

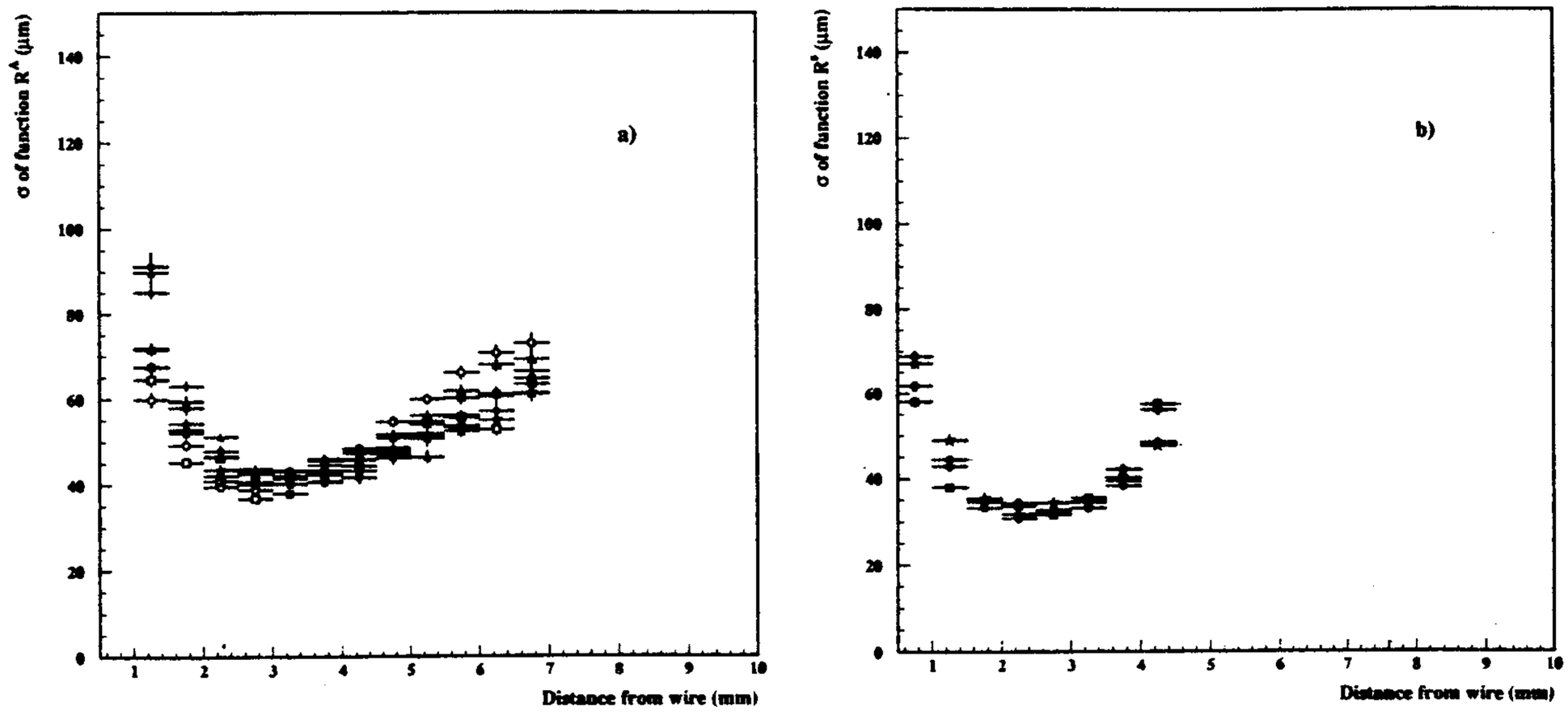

Figure 4.60: The rms of the function a) $R^A(r)$ for the 20 mm straws and b) $R^S(r)$ for the 10 mm straws. The empty and filled symbols correspond to the upper and lowe bands of the scatter plot shown in fig.4.59 for the same set of straws.

is used to approximate $\sigma(r)$ and the data of fig.4.60b are first fitted by a function $S(r)$, where:

$$S(r) = \sqrt{\frac{f^2(\Delta_x - r)}{2} + f^2(r)}$$

The deconvoluted local space resolution as shown in fig.4.62 is then obtained by:

$$\sigma(r) = \frac{f(r)}{S(r)} \times \sigma_{R^A(r)}$$

A comparison of fig.4.61 with fig.4.62 shows that the local space resolution obtained with the 10 mm straws is better than that of 20 mm straws. The dependence of the local space resolution on drift distance is largely determined by three factors: diffusion of electrons, variation in distance between adjacent clusters, and jitter in the time measurements introduced by electronics (discriminator and TDC). These three contributions can be separated from each other [29] and the results are shown in fig.4.63. It is to be noticed that for drift distances smaller than 2~3 mm the dominant contribution to the local space resolution comes from jitter of time measurements, whereas for longer drift distances local space resolution is largely determined by electron diffusion. The better performance of the 10 mm straws can

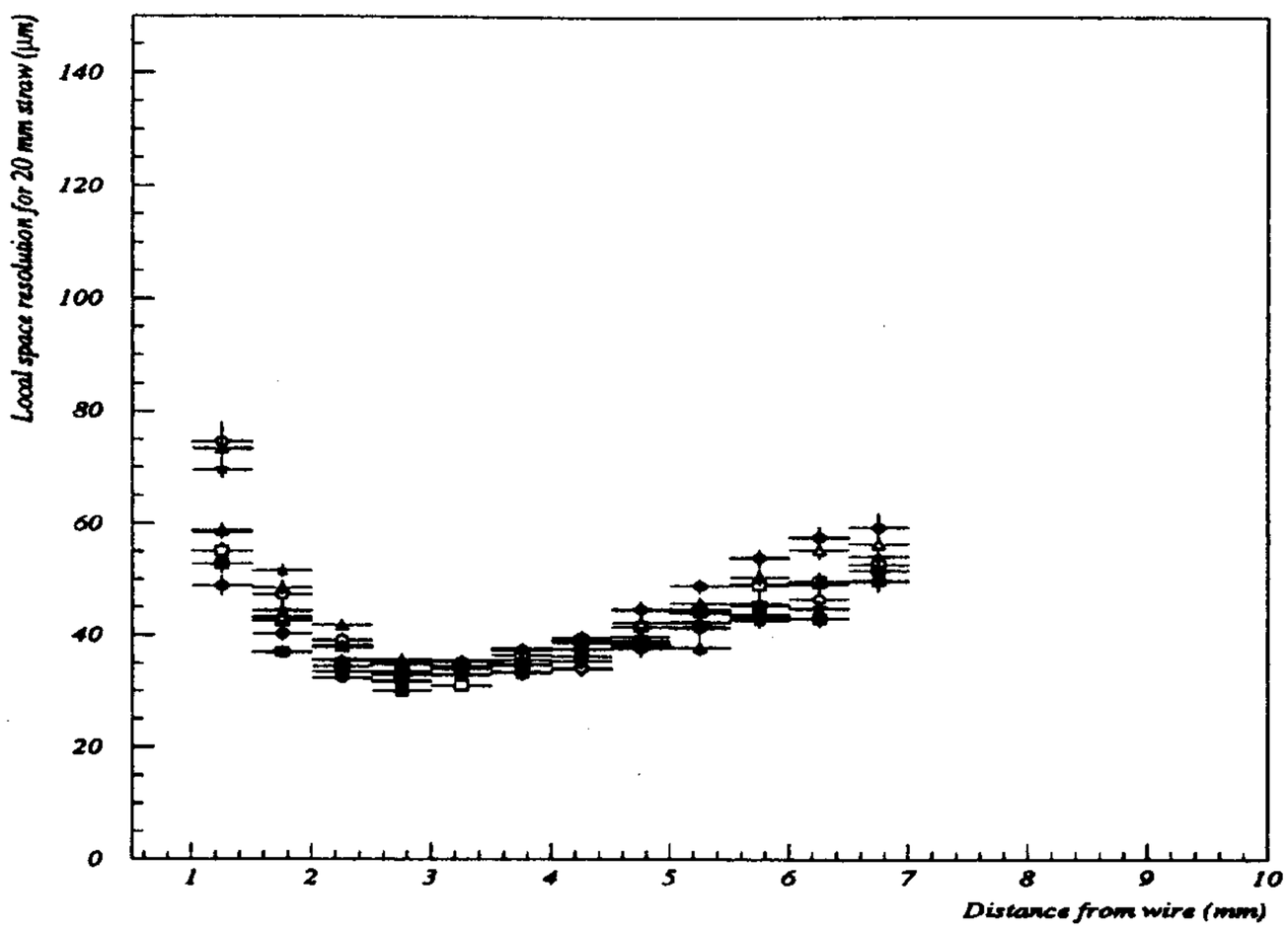

Figure 4.61: The dependence of local space resolution on drift distance for the 20 *mm* straws.

therefore be understood in terms of a smaller jitter in time measurements for the 10 *mm* straws, 1.6 *ns* as compared to 3.9 *ns* for the 20 *mm* straws.

Global space resolution and straw systematics

To get a measure of the straw performance averaged over the entire straw radius, the usual procedure is to consider the distribution of $R^A(r)$ or $R^S(r)$ over the entire radius and take the *global space resolution* as $\sqrt{2/3}$ times the rms of these distributions. An alternative treatment is to consider the residual $(r-\rho)$ distributions, where ρ is the distance of closest approach of the track fitted with the straws themselves and r is the distance determined by drift time measurement. Depending upon the number of straws participating in the fitting procedure, the rms of the residuals can be related to the global space resolution. In the following, we will use these methods, but it should be noticed that their application lacks mathematical exactness since the underlying assumption in such treatments is that local space resolution does not depend on the drift distance.

A typical distribution for the quantity $R^S(r)$ over the entire straw radius for the 10 *mm* straws is shown in fig.4.64. The beam is at 50 *cm* from the straw center for the data shown in fig.4.64. The rms of the distribution as obtained by a Gaussian fit is found to be 90 μm and once multiplied by a factor of $\sqrt{2/3}$ it shows a global

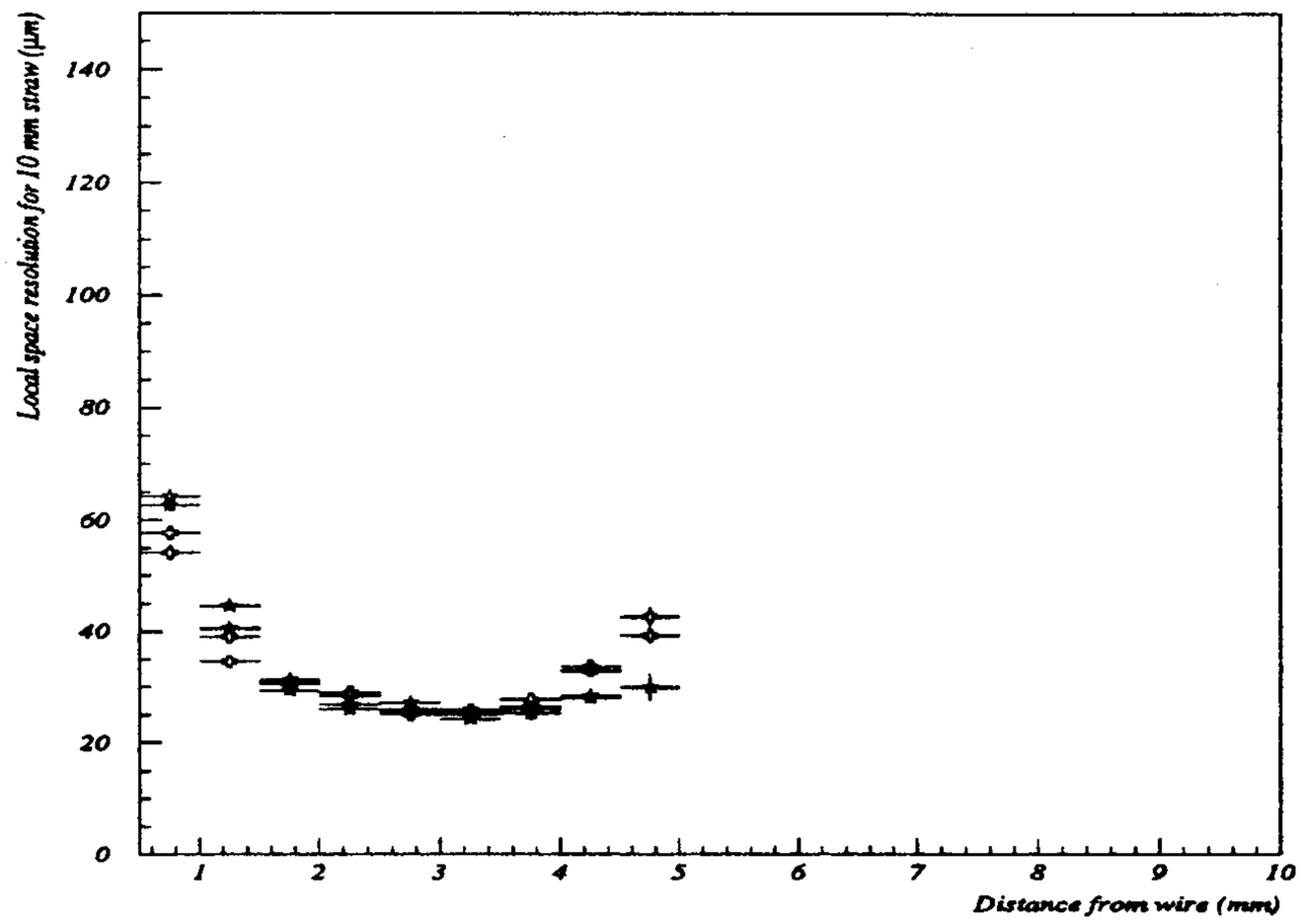

Figure 4.62: The dependence of local space resolution on drift distance for the 10 mm straws.

space resolution of 73 μm, which is about two times higher than the average local space resolution values shown in fig.4.62. The results obtained for the global space resolution by this method for the 10 mm straws are shown in fig.4.65 for different values of the beam position along the wire axis with respect to the straw center. The global resolution is $\sim 50\mu m$, when the beam is very close to the straw end and deteriorates up to 80 μm when the beam is at the center of the straw.

A typical residual distribution (over the entire straw radius) for the 10 mm straws, with beam at 50 cm from the straw center, is shown in fig.4.66. It can be shown that, in our case, the global space resolution is given by $2 \times \sigma_{(r-\rho)}$ for the external straws (with respect to y–axis) and by $\sqrt{2} \times \sigma_{(r-\rho)}$ for the central straws, where $\sigma_{(r-\rho)}$ is the rms of the residual distribution. The rms obtained by a Gaussian fit to the distribution of fig.4.66 thus indicates a global space resolution of 85 μm. The global space resolution obtained in this way for 10 mm straws, with various values of the beam position along the straw axis, is shown in fig.4.67.

The fact that global resolution depends on the beam position along the wire axis and is worse than the average local resolution ($\sim$ 40 μm) is quite as expected. The method used to determine the local space resolution probes similar straws with a small variation in drift distance for tracks and therefore yields the resolution values which are relatively immune from systematics introduced by straw eccentricity and the corresponding inaccuracy of the used time–to–space relationship. Of course the systematics is responsible for the worsening of the global resolution with respect to

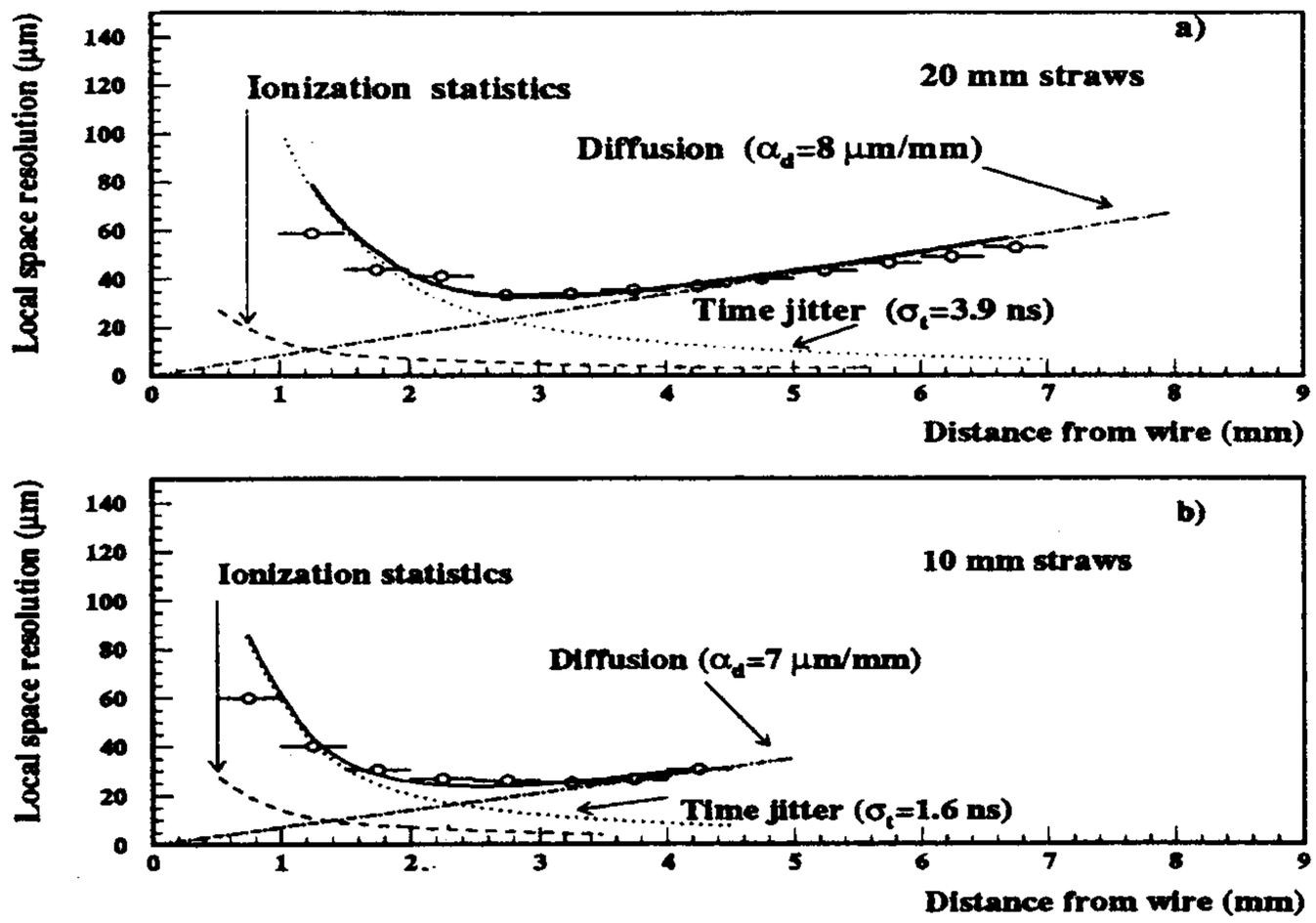

Figure 4.63: Contribution of different terms in the local space resolution of 10 and 20 *mm* straws.

the local one, but also for the deviation of everage value of R^A from its true value.

A simple method can be used to experimentally determine the straw eccentricity and correct for the corresponding systematic effects. For the test beam data, using the information from track fitting the tracks passing above and below the wire can be separated and the corresponding TDC distributions are shown in fig.4.68. For the prototype a maximum eccentricity up to $500 \sim 600$ μm is expected at the straw center [31]. The straw eccentricity creates an asymmetry in the electric field resulting in zones of low and high field as compared with an ideally concentric straw. The behavior of the TDC distributions is qualitatively evident, the drift velocity is lower than the ideal case for the tracks passing through the low field region (below the wire) and therefore the TDC distribution extends beyond the maximum value for the ideal case. On the other side, the drift velocity is higher than the ideal case for the tracks passing through the high field region (above the wire) and correspondingly the TDC distribution terminates before the maximum value for the ideal case. The electric field for an eccentric straw can be computed by using the method of images and the calculated end–points of the TDC distribution for the high and low field regions (T^M_{high} and T^M_{low} respectively) as a function of the straw eccentricity are shown in fig.4.69. In fig.4.70 the correlation between T^M_{high} and T^M_{low} values for different values of straw eccentricity are shown together with experimental data for different straws and for different values of the beam distance from the center of the straw.

By observing the T^M_{high} and T^M_{low} values, the eccentricity for each straw can there-

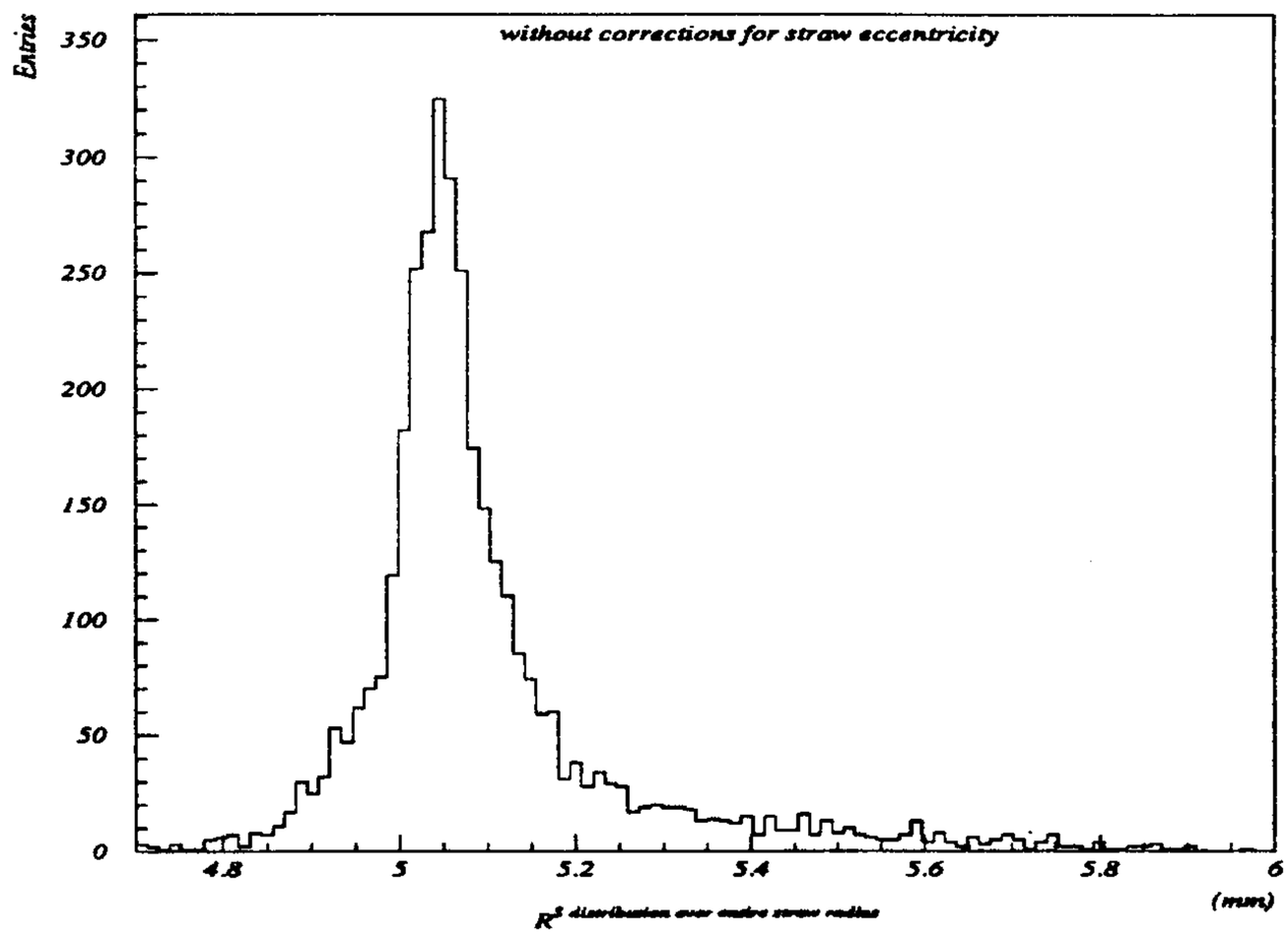

Figure 4.64: A typical distribution of the function $R^S(r)$ over the entire straw radius for 10 mm straws. The beam is 50 cm away from the straw center.

fore be determined (fig.4.71). Once the eccentricity is known, the electric field and the corresponding time–to–space relationship can be computed correctly. The influence of such a correction algorithm is shown in fig.4.72. An improvements of a factor two in the global space resolution is obtained. The global space resolution obtained after having corrected for the straw eccentricity for different values of the beam position along the straw axis is shown in fig.4.73. The global space resolution obtained from track residuals after having corrected for systematics is shown in fig.4.74. The results obtained with both methods, as presented in fig.4.73 and fig.4.74 show that after correcting for systematics, a global resolution better than 40 μm can be reached and is well maintained for the entire straw length. Obviously, as the expected value of the $R^S(r)$ function does not depend any more on the drift radius, the measurement accuracy is also guaranteed by the correction procedure.

The straw length is an important parameter in determining the eccentricity and consequently the systematics and the global space resolution. Global resolution values better than 40 μm have been previously reached [20], [21], [22], [23] but with straw lengths smaller than 50 cm. The previous works with straw lengths greater than 2 m, have obtained global resolutions ranging from 100 to 200 μm [24],[25],[26]. However, as demonstrated in this section, if systematics are properly treated, global space resolution better than 40 μm for straw length of $\sim$ 2 m can be maintained. The results presented here were obtained for tracks almost perpendicular to the wires, however, the systematic correction procedure for the inclined tracks is quite

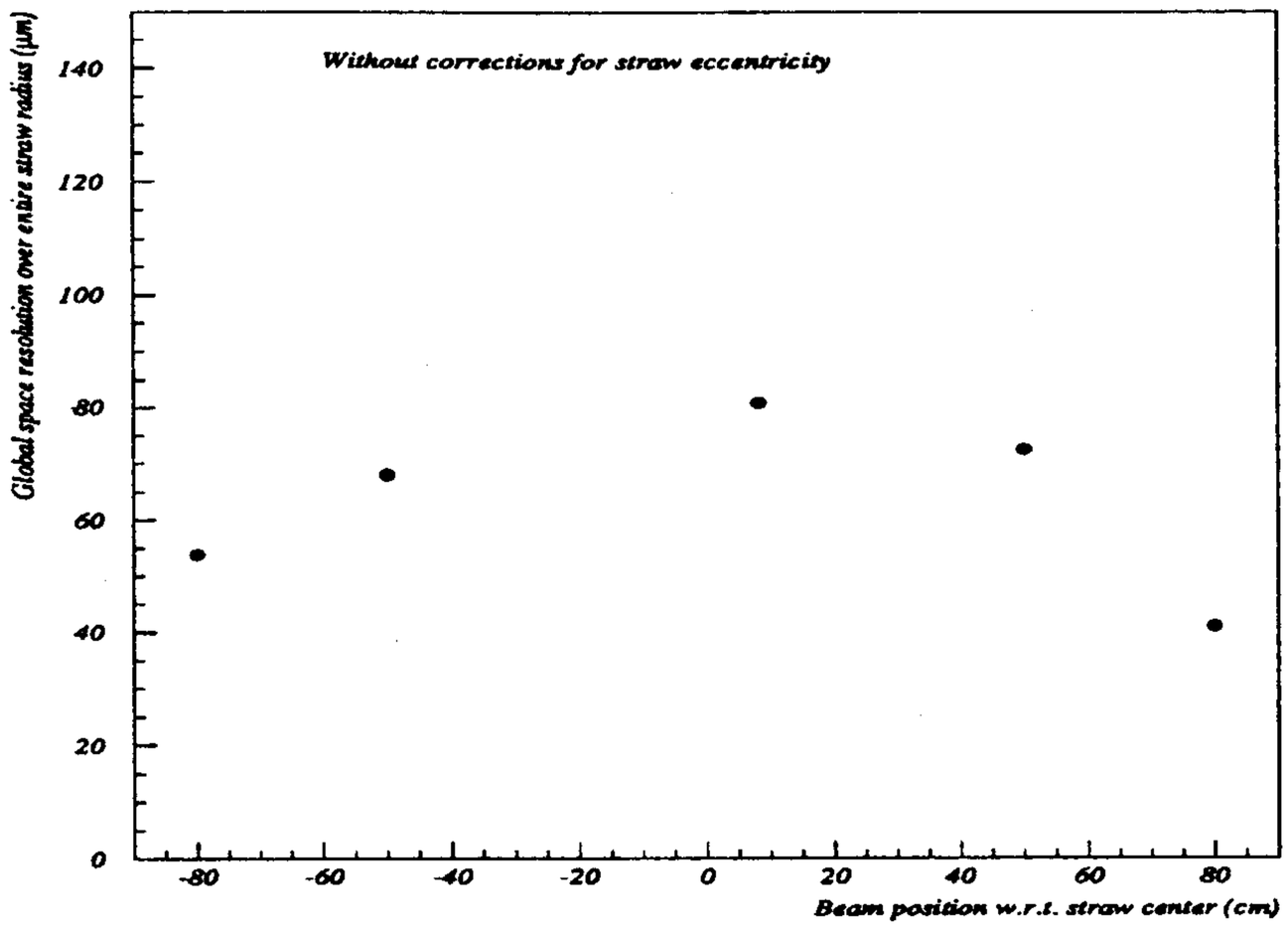

Figure 4.65: The global space resolution for the 10 mm straws for different beam position from the straw center, as obtained from the rms of the $R^S(r)$ distribution over the entire radius.

straightforward extension of the existing algorithm, and will be tested in December 94 test beam at TRIUMF. We believe the space resolution of the FINUDA straw tube detector will comfortably be better than 100 μm.

4.3.5 Proposed solutions for the components of the design

The results obtained with the prototype have been used to select the design components of an array employing 150 straw tubes that will be tested in December this year a test beam at TRIUMF before freezing the final design.

Straws

The contribution in space resolution due to electron diffusion is determined by the straw diameter. As shown in fig.4.63, each mm of drift gives an electron diffusion of about 7$\sim$8 μm. As demonstrated by the prototype data, the straw systematics can be kept under control and the performance goal of 100 μm of space resolution can therefore be maintained by straw diameters of up to 25 mm. The actual design is however based upon straws with an inner diameter of 15 $\pm$ 0.05 mm and the wall thickness is 0.03 $\pm$ 0.01 mm leaving us a very large design margin.

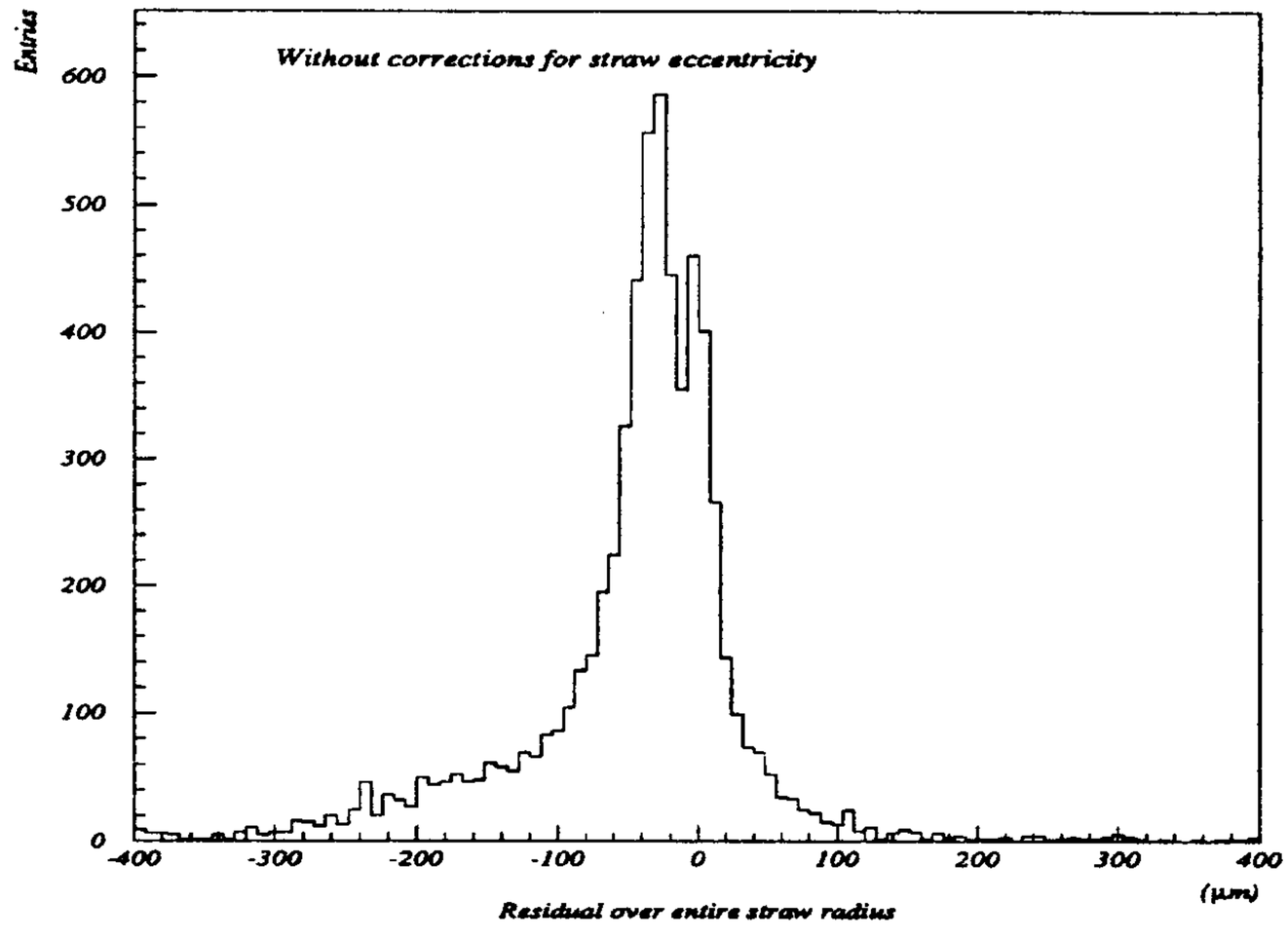

Figure 4.66: A typical residual distribution for 10 mm straws over the entire straw radius. The beam is 50 cm away from the straw center.

Wire

A suitable candidate is to use Gold plated Tungsten wires with a diameter of 0.03 mm. The maximum load of such wires has been measured to be 1.8 N at the breaking point. A safe wire operating tension is 1 N. The long term stability in length is also well known for Tungsten wires.

Pin and feedthrough

The pin and feedthrough used for the prototype are somewhat modified for the present version. The new pin design is shown in fig.4.75. It has an inner hole of 0.08 ± 0.02 mm with a 5 mm crimping zone. The outer diameter in the crimping zone is 1 ± 0.01 mm and it becomes 1.6 ± 0.01 mm for the rest of the length. The 1.6 mm diameter part provides mechanical rigidity to the pin, and is appropriate to accept standard female connectors for high voltage.

Also the feedthrough design has been modified (fig.4.76). A cylindrical housing for the electronics has been added to the features of the feedthrough used on the prototype. The new feedthrough consists of an aluminum cylinder with external diameters of 14.99 ± 0.01 mm on the straw side and 12 ± 0.03 mm on the end plate side. The aluminum cylinder contains a concentric delrin body, which accommodates the wire pins and provides the gas inlet/outlet for the straw. In the final feedthrough

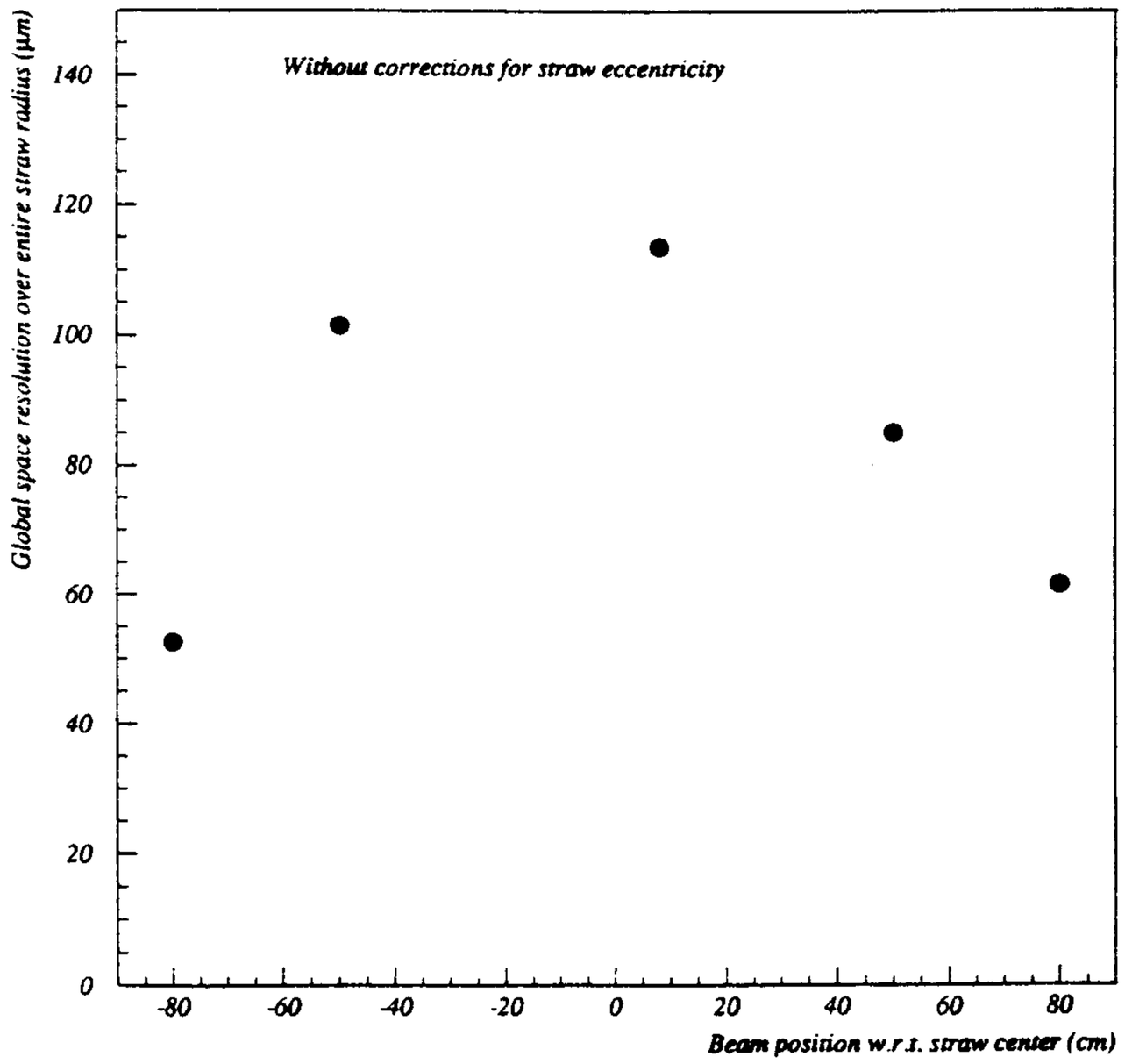

Figure 4.67: Global space resolution for the 10 mm straws as obtained from track residuals for various values of beam position along the wire axis.

design we envisage to reduce the space occupied by the preamplifier circuit. In this scheme the cylindrical housing for the preamplifier board is located inside the end plate hole.

Preamplifier

As shown in fig.4.56 a preamplifier gain of 2 V/mA is sufficient to guarantee a full straw efficiency. The actual design provides a gain of 3 V/mA. Also the rise time of 2 ns is enough to maintain the signal quality. Therefore the main features of the circuit developed for the prototype preamplifier have been maintained in the final design (fig.4.77). The trans–impedence amplifier based on transistor Q_1, Q_2 and Q_3 has an open loop gain of 25000. The current feedback resistance of 3 $k\Omega$ is determined by the resistors $R11$ and $R12$. The current output from the Q_3 collector is used to drive the 50 Ω coaxial cable.

In addition to signal amplification, a calibration signal to the preamplifier input is fed through the transistor Q_4. It permits us to make a rapid calibration for the time alignment and to identify any circuit failure during operation. An HV filter consisting of $R1$, $R2$ and $C1$ is also incorporated in the preamplifier card.

The miniaturized circuit implementation is based on thick film technology using SMD components. The final circuit board has a dimension of 5×1.2 cm^2. A few prototypes of the miniaturized preamplifier board have been developed at LNF and found to satisfy the needed performances.

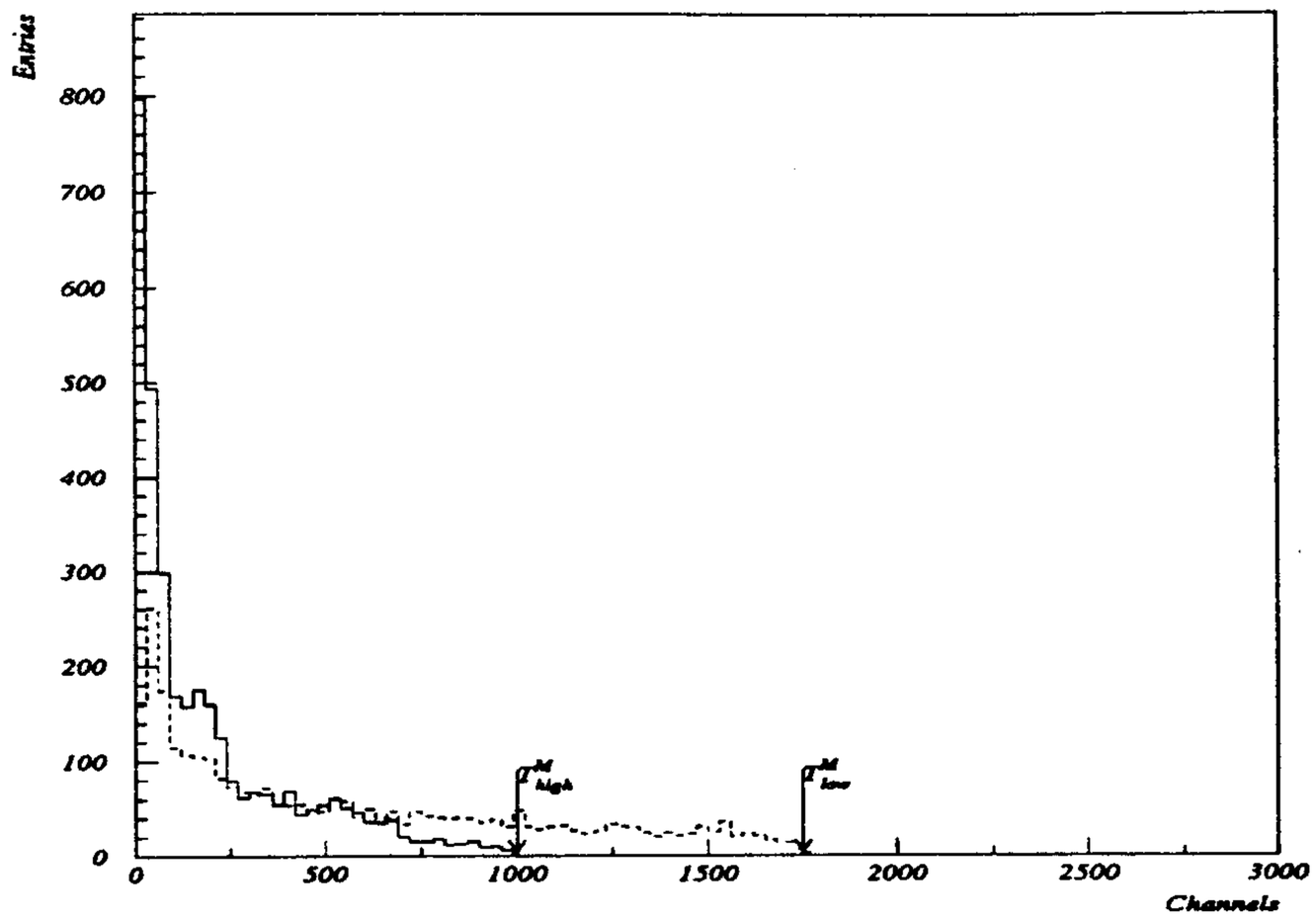

Figure 4.68: The TDC distributions for high and low field zones for a 10 mm straw with an eccentricity of $\sim$ 400μm.

Discriminators

The design goal for readout electronics is an accuracy of 2 ns in time measurements which does not impose very stringent performance requirements on discriminator and TDC circuitry.

The discriminator circuit prototype being designed at LNF is shown in fig.4.78. The analog signal from the preamplifier is actively split in two equal parts. One of these analog parts is provided as an output for an eventual use for charge analysis. The other part is fed to two comparators through an adjustable gain stage. The low threshold comparator is used to generate the clock, while the high threshold comparator is used to enable the flip flop. After discrimination, a 50 ns wide output signal is formed in the differential current mode. A minimum threshold level of 10 mV with a time walk less than 1 ns for the entire dynamic range is provided. The circuit is implemented with a modularity of 32 channels per 9U VME slot. Table 4.11 summarizes the characteristics of the discriminator.

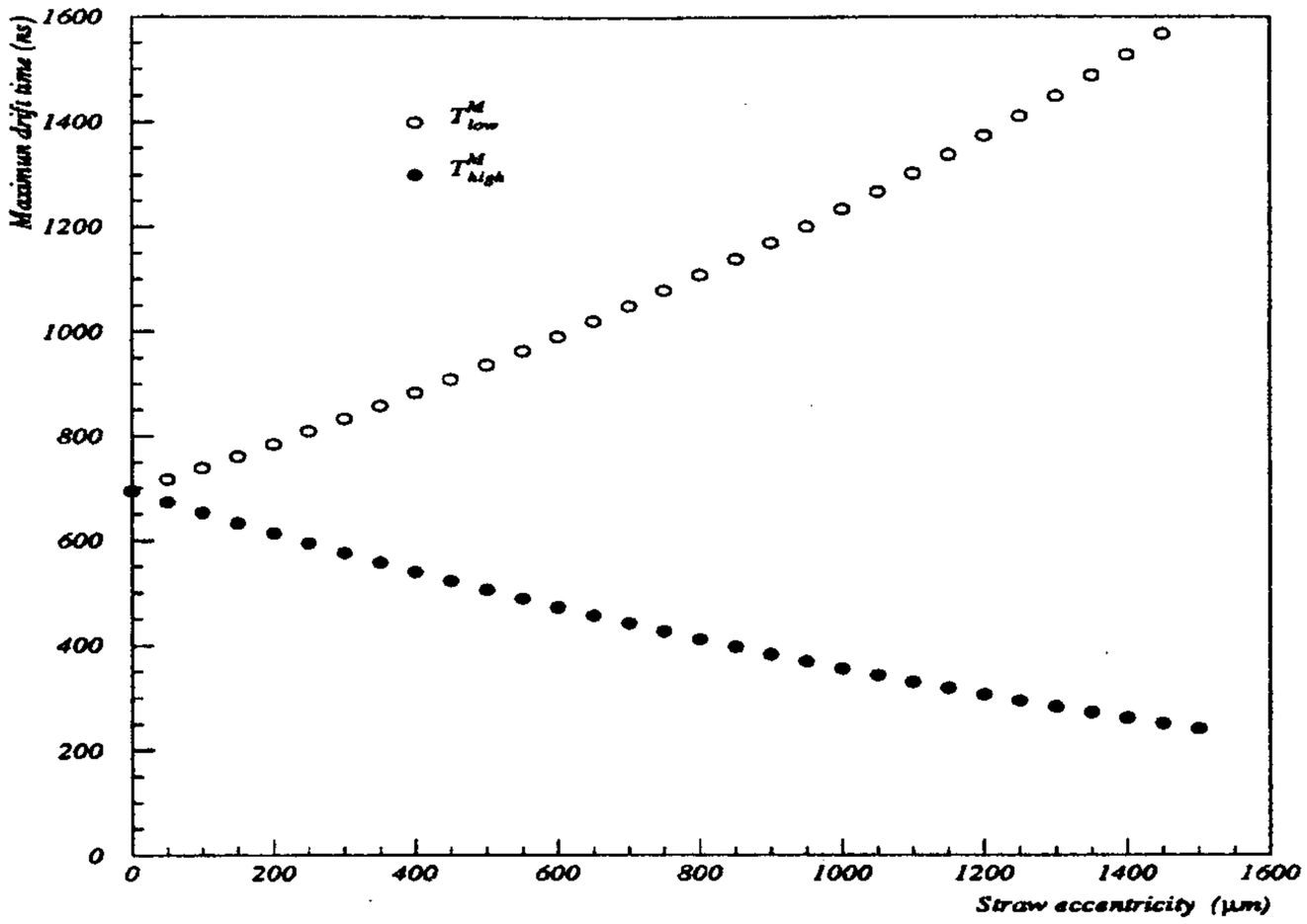

Figure 4.69: The end–point of TDC distributions for high and low field zones as a function of eccentricity for 10 mm straws.

Table 4.11: Straw tube discriminator.

Input	negative, 50Ω
Dynamic range	800 mV
Minimum threshold	10 mV
Output signal	50 ns wide ECL
Power per channel	1 W
Supply	$\pm$ 5 V, $\pm$ 12 V

TDC

The requirements for the straw readout can be satisfied with TDCs having a single bit resolution of 1 ns and a dynamic range of 2 μs. A commercially available option of a digital TDC based on CMOS chip with a fixed single bit resolution of 1 ns and a dynamic range of 16 bits is under consideration.

This option is inexpensive and compact. Using digital TDC we can house up to 96 channels per 9U VME card. The TDCs will be operated in common stop mode with the stop signal provided by the OR of the twelve MT signals coming from TOFINO, gated by the trigger. Consequently, the straw signals do not need to be delayed.

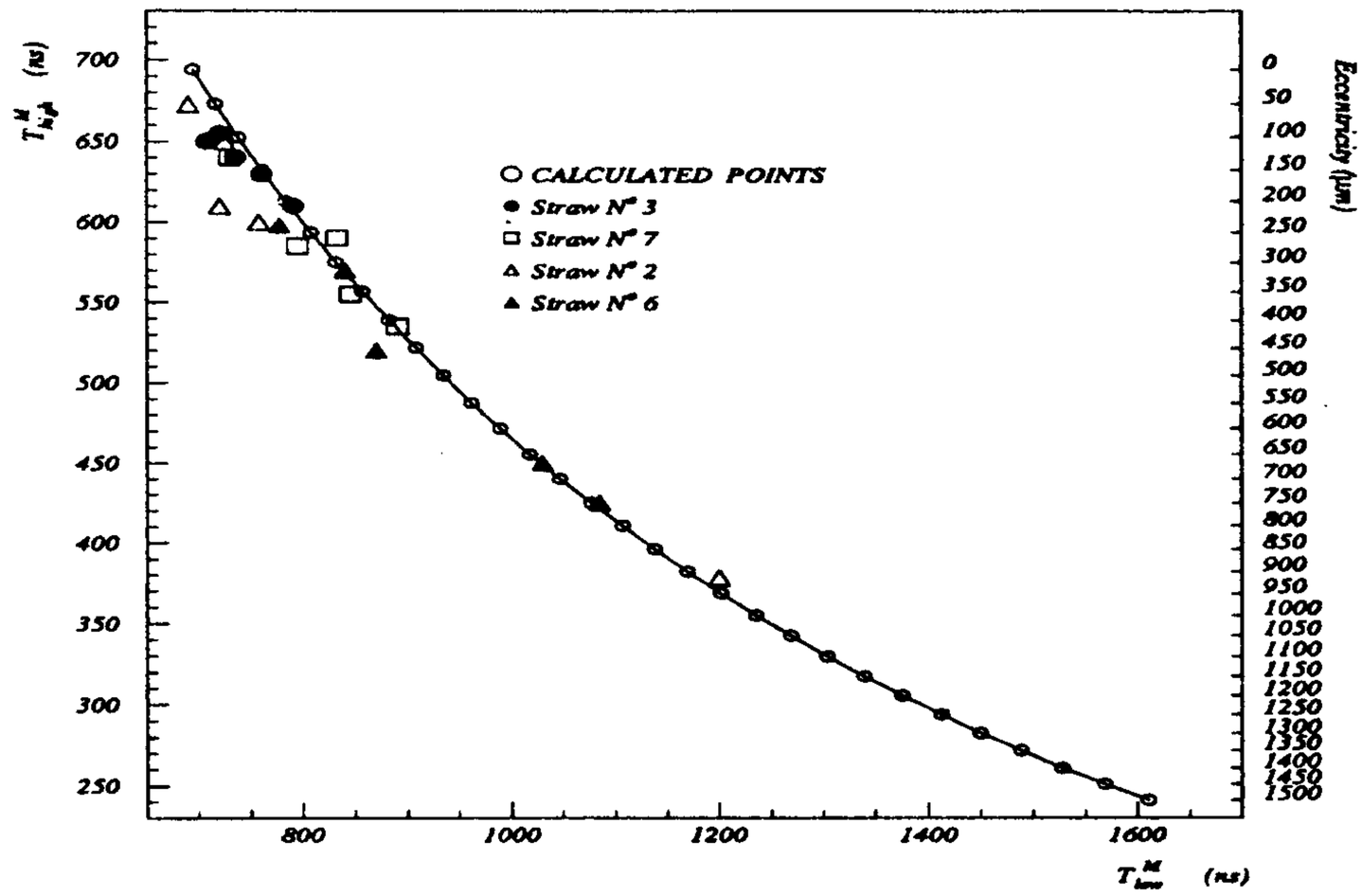

Figure 4.70: Determination of wire eccentricity from the end–points of TDC distributions for high and low field zones for 10 mm straws.

High voltage system

The proposed HV system is shown in fig.4.79. Both the master supply and distributor board are envisaged to be interfaced with CPUs, permitting a remote software monitoring and control.

The master HV supply is required to provide:

- Programmable HV setting of a maximum of 5 kV with steps of 1 V.
- Voltage monitoring with a resolution of 1 V.
- Current monitoring with a resolution of 1 μA.
- Programmable ramp up and ramp down.
- Programmable current limiting and hardware trip.
- Single channel ON/OFF capability.

Whereas at the distributor level we provide:

- Modularity of 30 straws/master channel.
- Current and voltage monitoring with 10 nA and 1 V resolution.

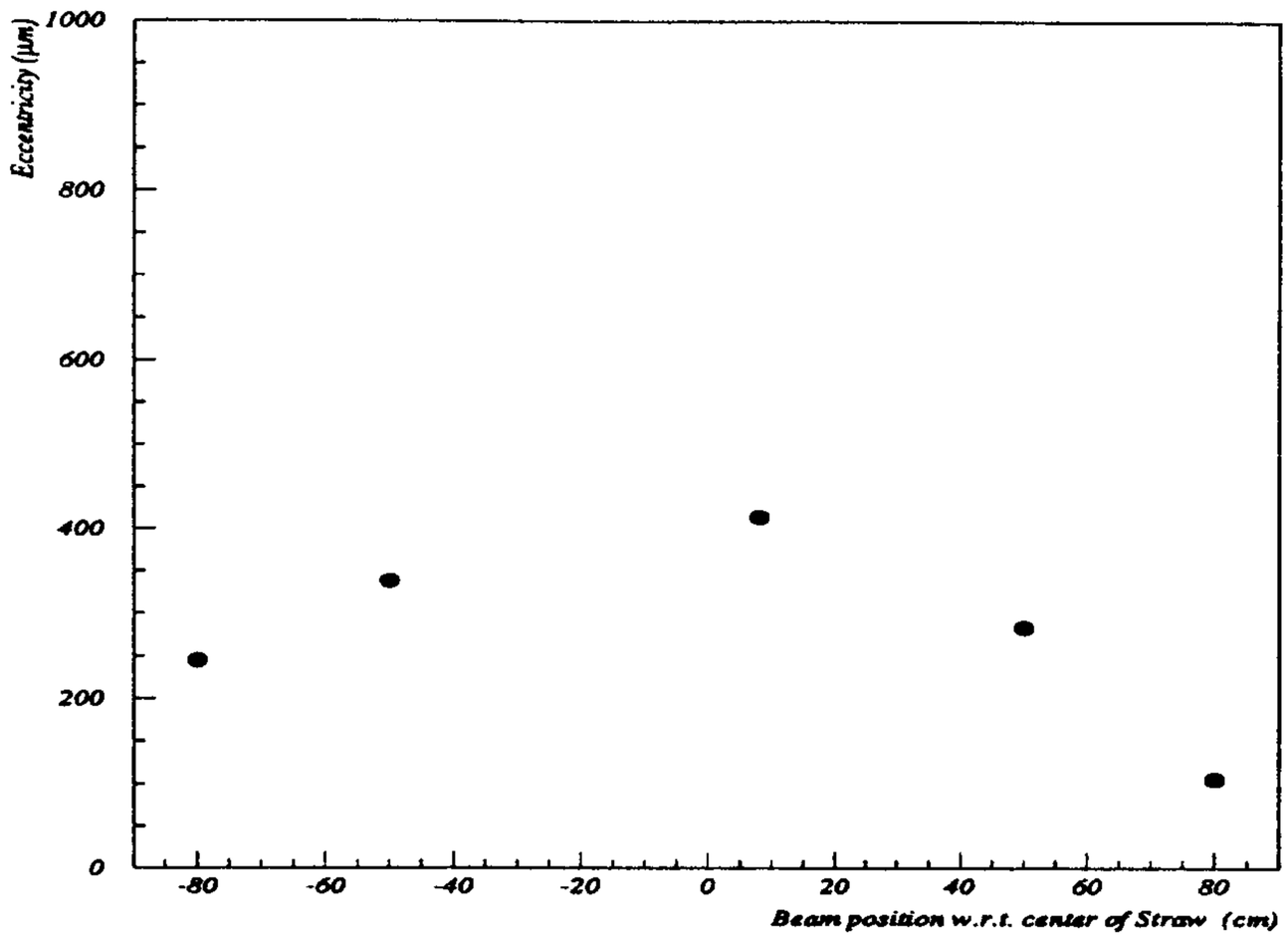

Figure 4.71: Eccentricity for 10 mm straws as a function of distance from the straw center.

- Hardware current limiting.
- Manual single channel ON/OFF capability.

4.3.6 Assembly procedure and monitoring

Assembly procedure

A parallel assembly of the straws is envisaged in which all the components (straw, wire, pin, and feedthrough) are assembled together in fixtures, tested for quality control and then inserted in the final end plates.

The wire is initially strung through the straw, feedthroughs and the pins without mechanical tension. A smooth unrolling of wire is ensured in order to avoid any possible kink and the wire is passed through a slit of a soft lint free material. To make it pass through the straws, one of the wire ends is clamped in an iron cart with plastic wheels which is moved along the straw using an external magnet. Once the wire is strung, the inner surface of the straw is glued on to feedthrough using a silver based conductive epoxy. With the glue hardened, the straw is tensioned and the feedthroughs are blocked against the fixture end plate. Now the wire is crimped on one side, tensioned to 1 N and crimped on the opposite side.

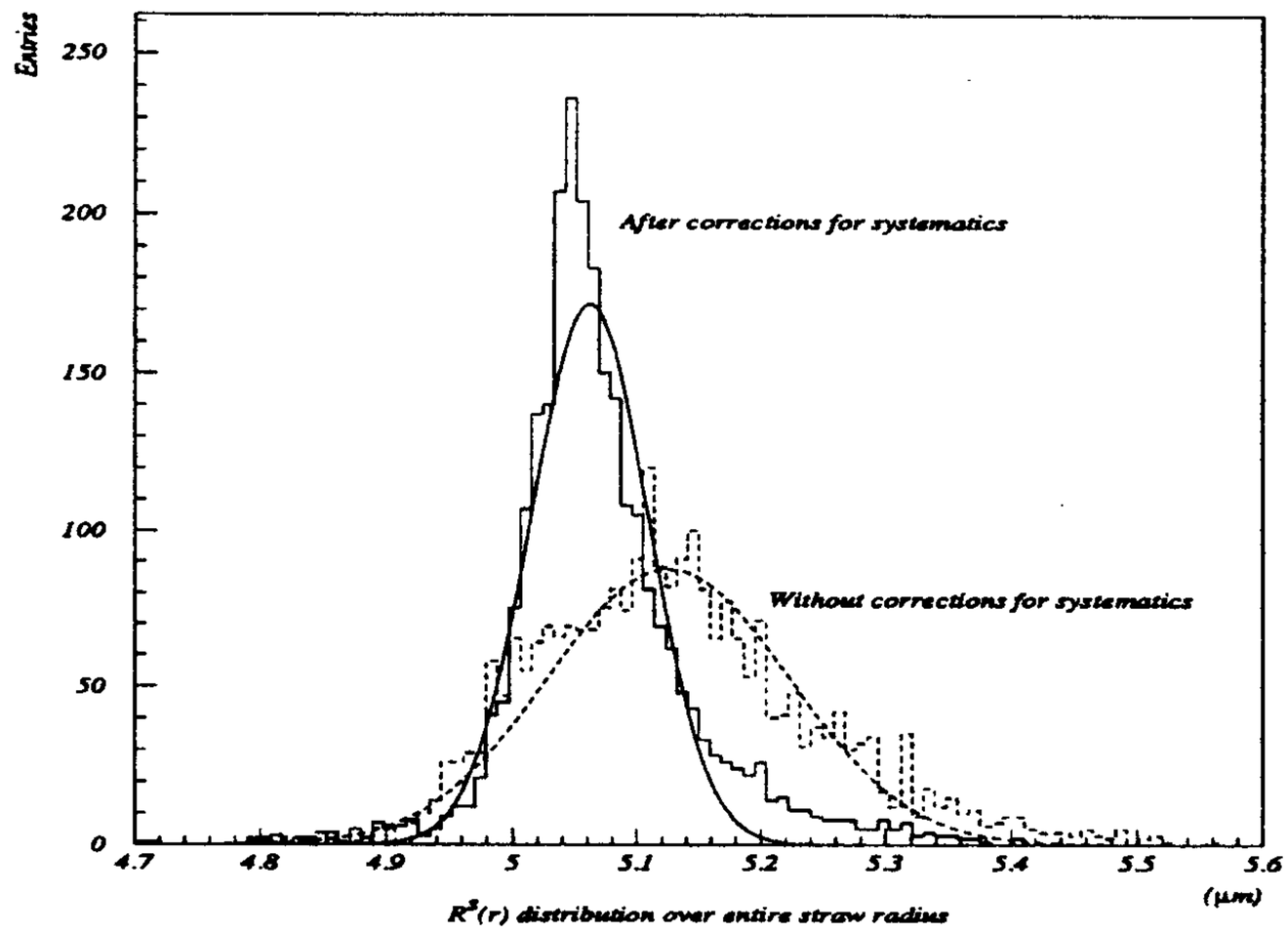

Figure 4.72: The distribution of the function $R^S(r)$ over the entire straw radius for 10 mm straws with (solid histogram) and without (dashed histogram) corrections for systematics.

The electrical continuity of wire and straw is tested and their resistances are measured. Gas tightness is quantified for each straw by sealing it with an overpressure of 100 *mbar* and monitoring the pressure drop for the following few days. On successful completion of these tests, the straw is mounted on actual end plates and preamplifier connections are made.

As the straws are mounted on final end plates, in parallel a performance test with cosmic rays will be realized on mounted straws. The single's count rate plateau, straw efficiency and space resolution will be monitored.

Monitoring

During the running of the experiment, the delay introduced by preamplifiers, wires and discriminator for each straw, T_0, will be monitored by injecting regular calibration pulses at the input of the preamplifier and recording their arrival time to the TDC. We expect that a T_0 determination better than 1 ns can be achieved by this method.

Analog signals from a small number of channels will be integrated by ADC. Once combined with the tracking information, it will provide us with a measure of the gas gain.

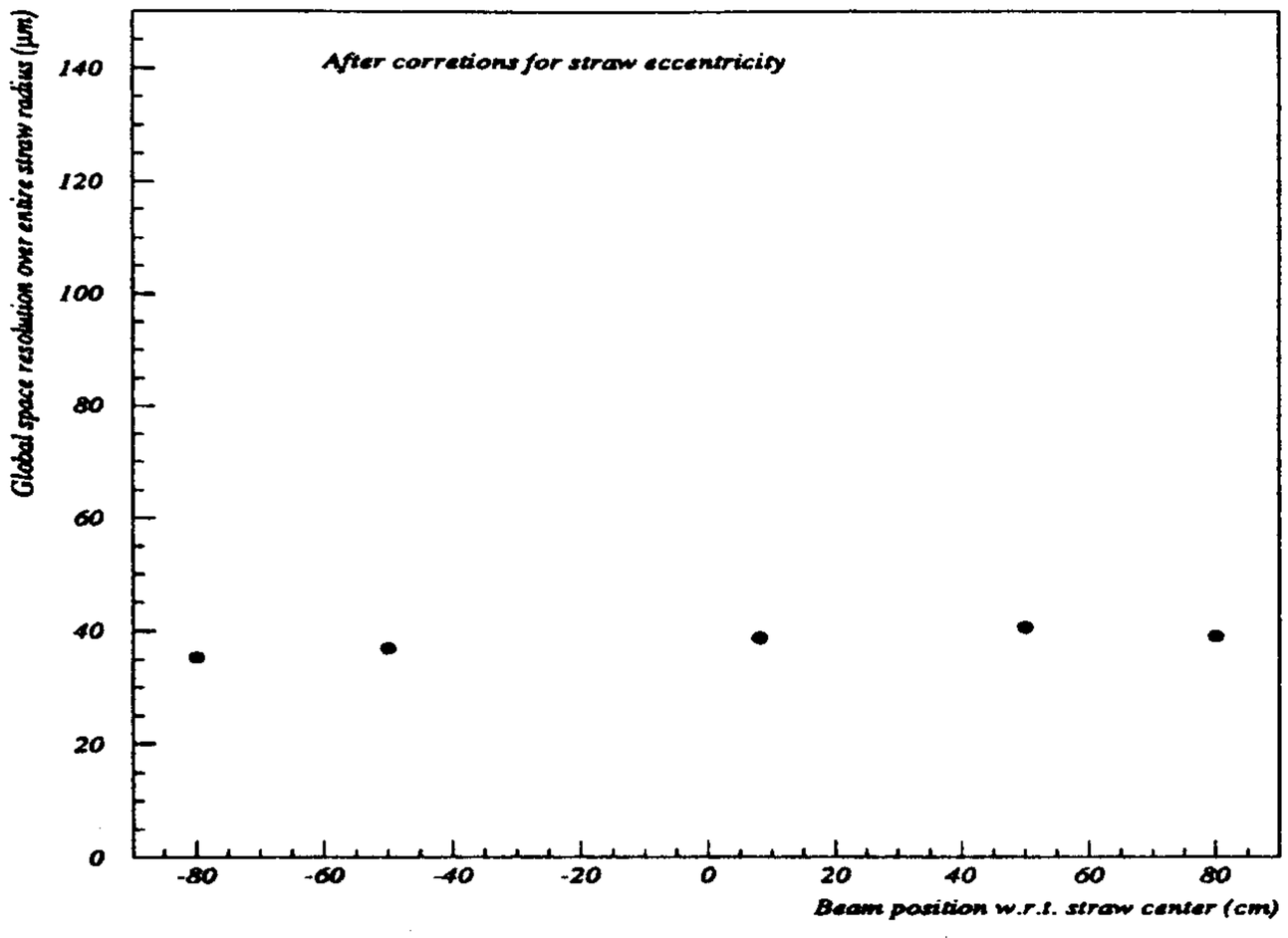

Figure 4.73: Global space resolution for the 10 mm straws as obtained from $R^S(r)$ distribution over the entire radius for different values of the beam position after having corrected for systematics.

In addition, to monitor gas gain and drift velocity, a small chamber built with 10 straws 25 cm long each, will be used. The monitor chamber is operated in parallel with the main straw detector using the same gas and it will be equipped with TDC and ADC readout. Its performance will be monitored by cosmic rays and gas gain measurements will be repeated periodically.

The requirement for monitoring pressure and temperature of gas is determined by the fact that a one percent variation in pressure (temperature) causes a maximum variation of the drift time of 1%, which corresponds to a 40 μm systematic contribution.

4.4 Tracking system calibrations

In order to reach the design momentum resolution of FINUDA, it is necessary that the tracking detectors, besides reaching the expected localization performances, be positioned with a precision less than 100 μm. This task could be reached on one side by a precise mechanical alignment and survey of all the detectors (see Chap. 9), on the other side by a strategy of continuous calibrations with physical signals. We have not yet elaborated in detail such a strategy, and we describe here some guide lines on which we intend to proceed.

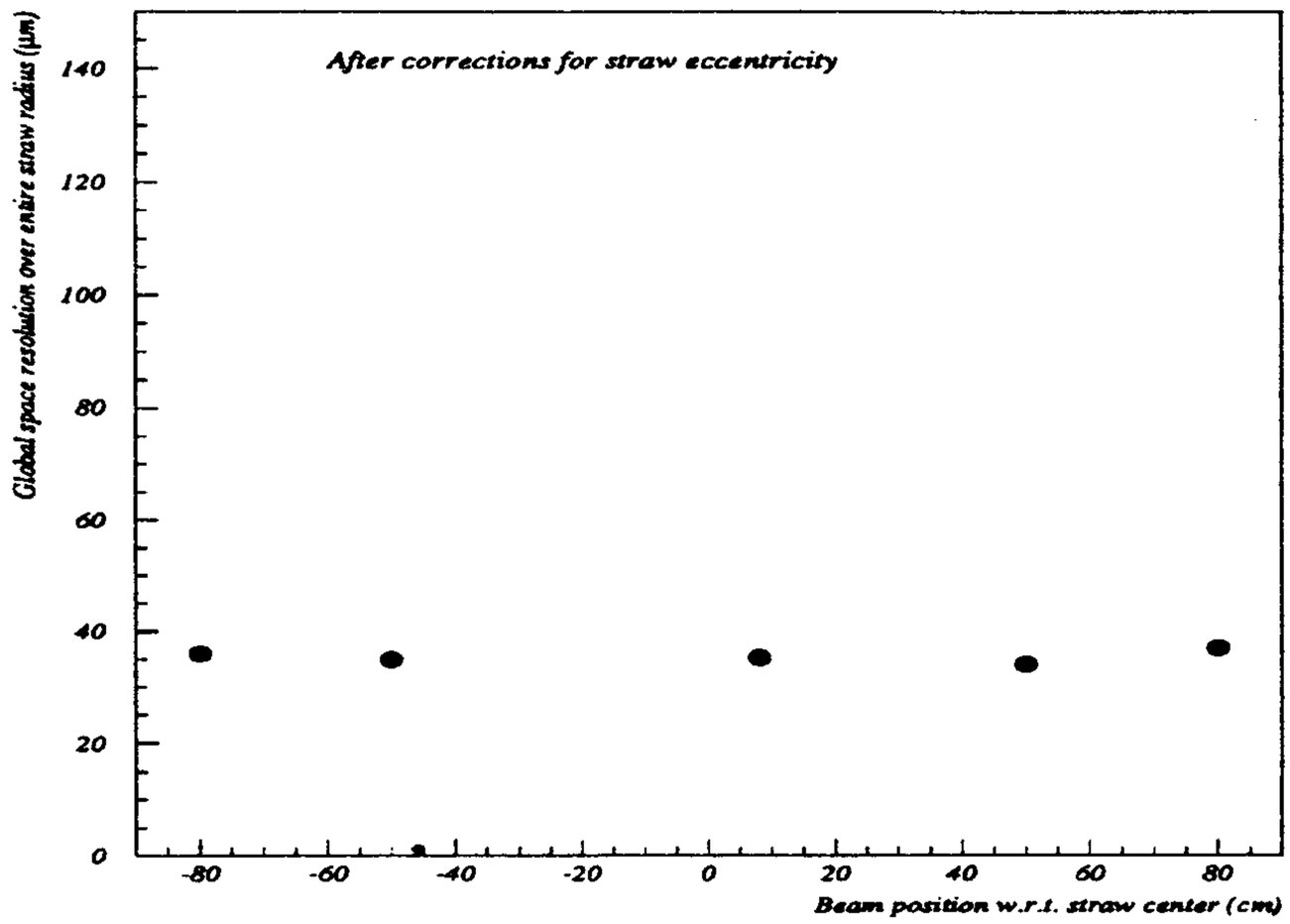

Figure 4.74: Global space resolution for the 10 mm straws, as obtained from track residuals for different values of the beam position, after having corrected for systematics.

The physical signals that can be used for the alignment of all the sub-detectors of the spectrometer are:

- cosmic rays with magnet off
- K_{μ_2} decays from K^+ stopped in the target with magnet on (1.1 T)

Given an acquisition rate of 100 Hz, in a week we may collect more than 5×10^7 cosmic rays events corresponding to straight tracks traversing the spectrometer, and triggered by TOFONE (MUL ≥ 2) or TOFINO*TOFONE (see Chap. 6). Taking in mind that a cosmic ray traverses in average ~ 5 straw tubes, we may collect $\sim 10^5$ events per straw tube and obtain then a positioning of the straw tubes with a precision better than 100 μm.

When triggering with a TOFINO*TOFONE coincidence, we may obtain an alignment of the subdetectors of the tracking device (ISIM+OSIM), LMDC and ST again to a precision better than 100 μm.

We will collect these data during the periods of shut down of $DA\Phi NE$. During the runs, the decay K_{μ_2} with a branching ratio of 63.5 % produces a monochromatic μ^+ of 236 MeV/c. As described in Chapter 6, we can quite easily acquire such events at a rate of ~ 50 Hz, without interfering with the true event acquisition. It means that in one day we could collect more than $\sim 4 \times 10^6$ K_{μ_2} events.

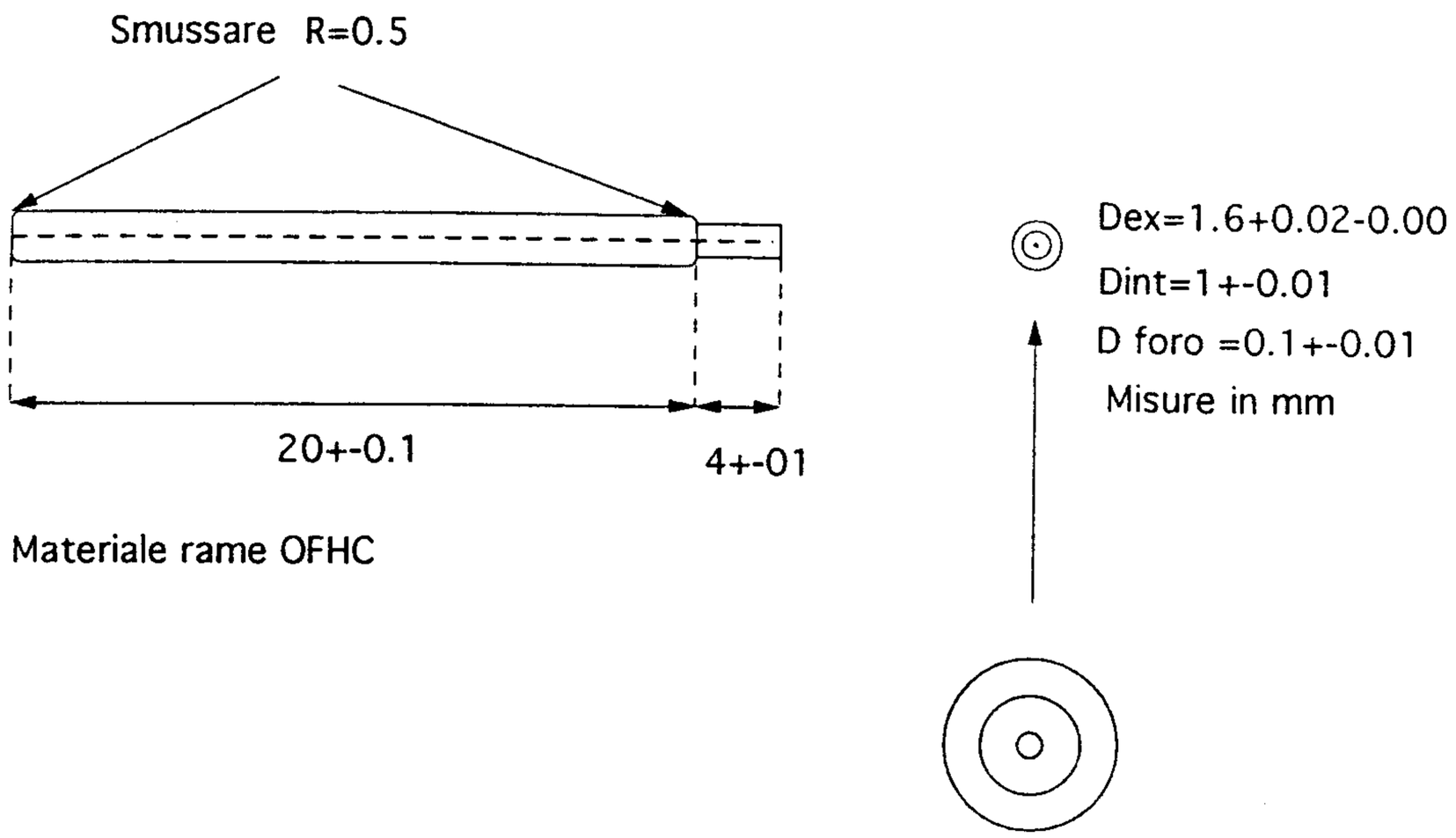

Figure 4.75: Proposed pin design. All dimensions are in *mm*.

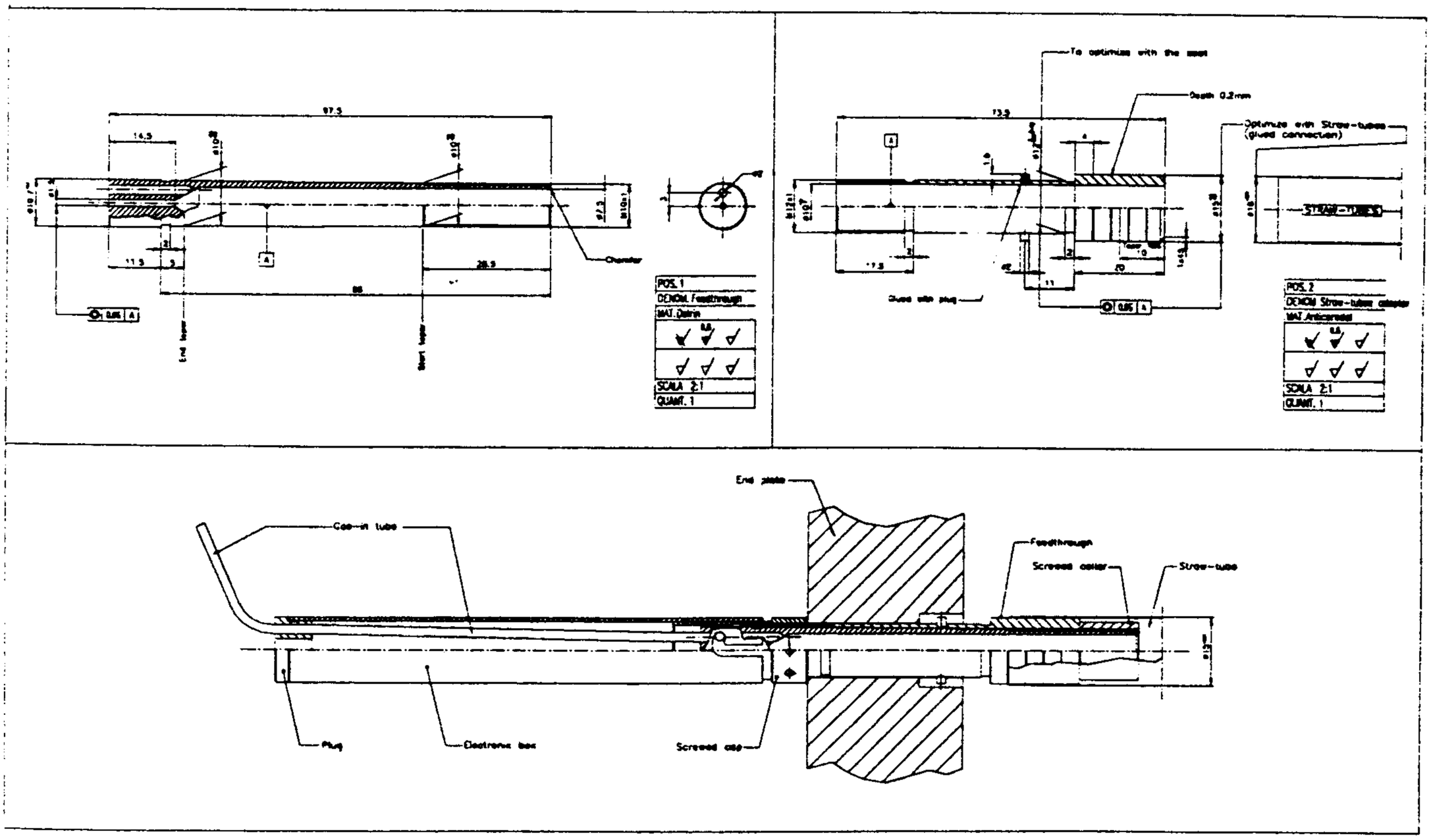

Figure 4.76: Proposed feedthrough design. All dimensions are in *mm*.

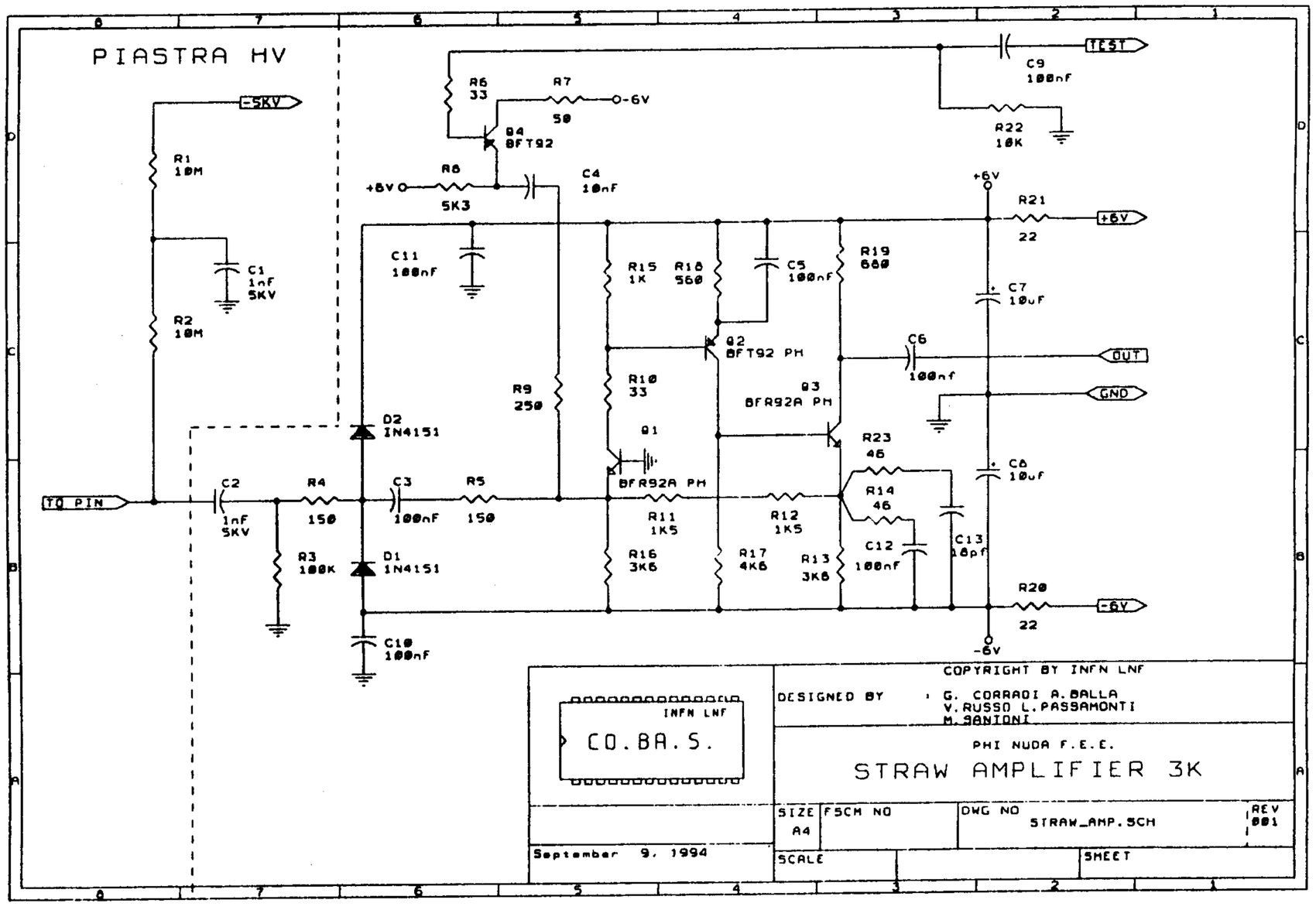

Figure 4.77: Proposed circuit of the preamplifier.

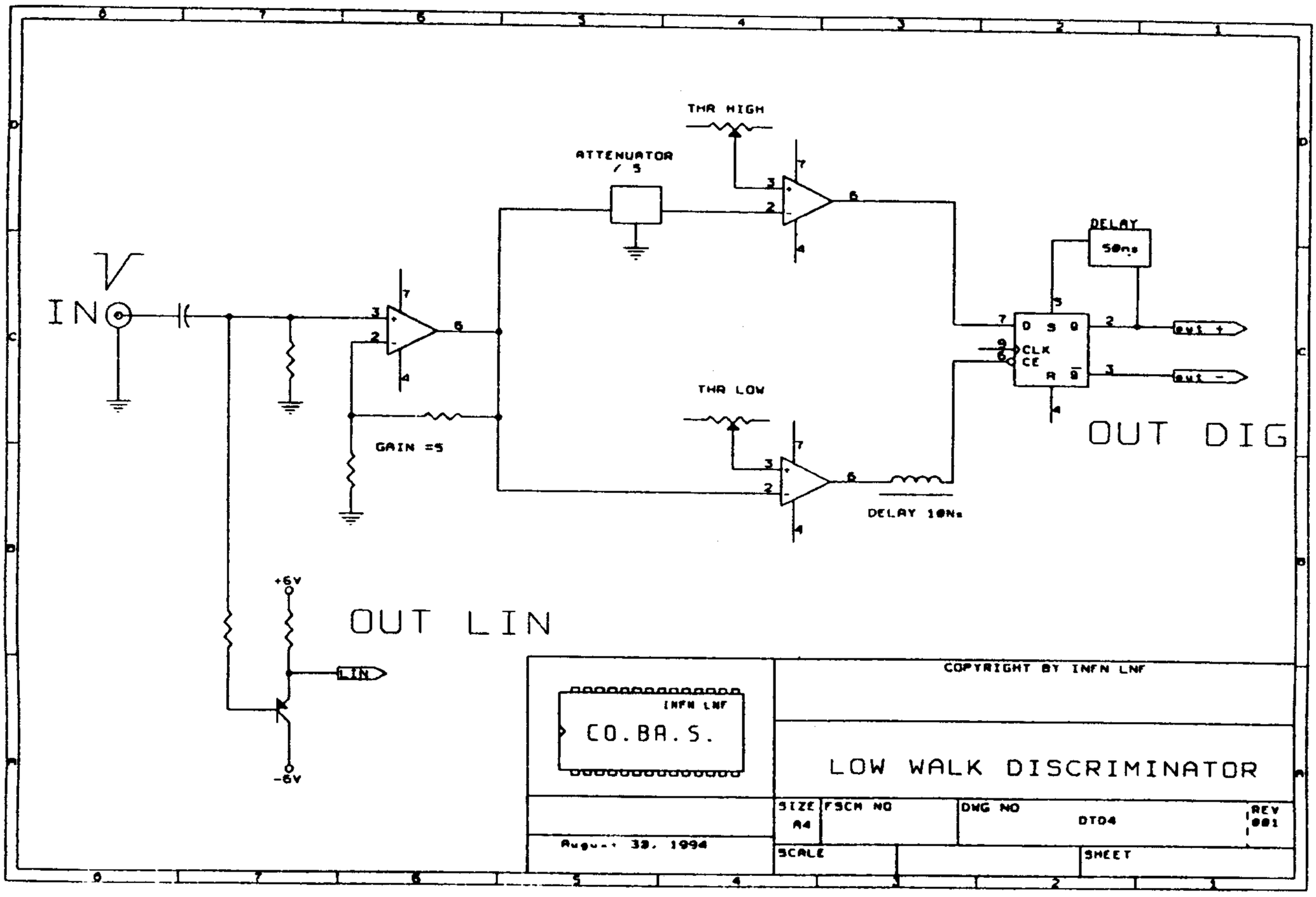

Figure 4.78: Schematic diagram of the discriminator circuit.

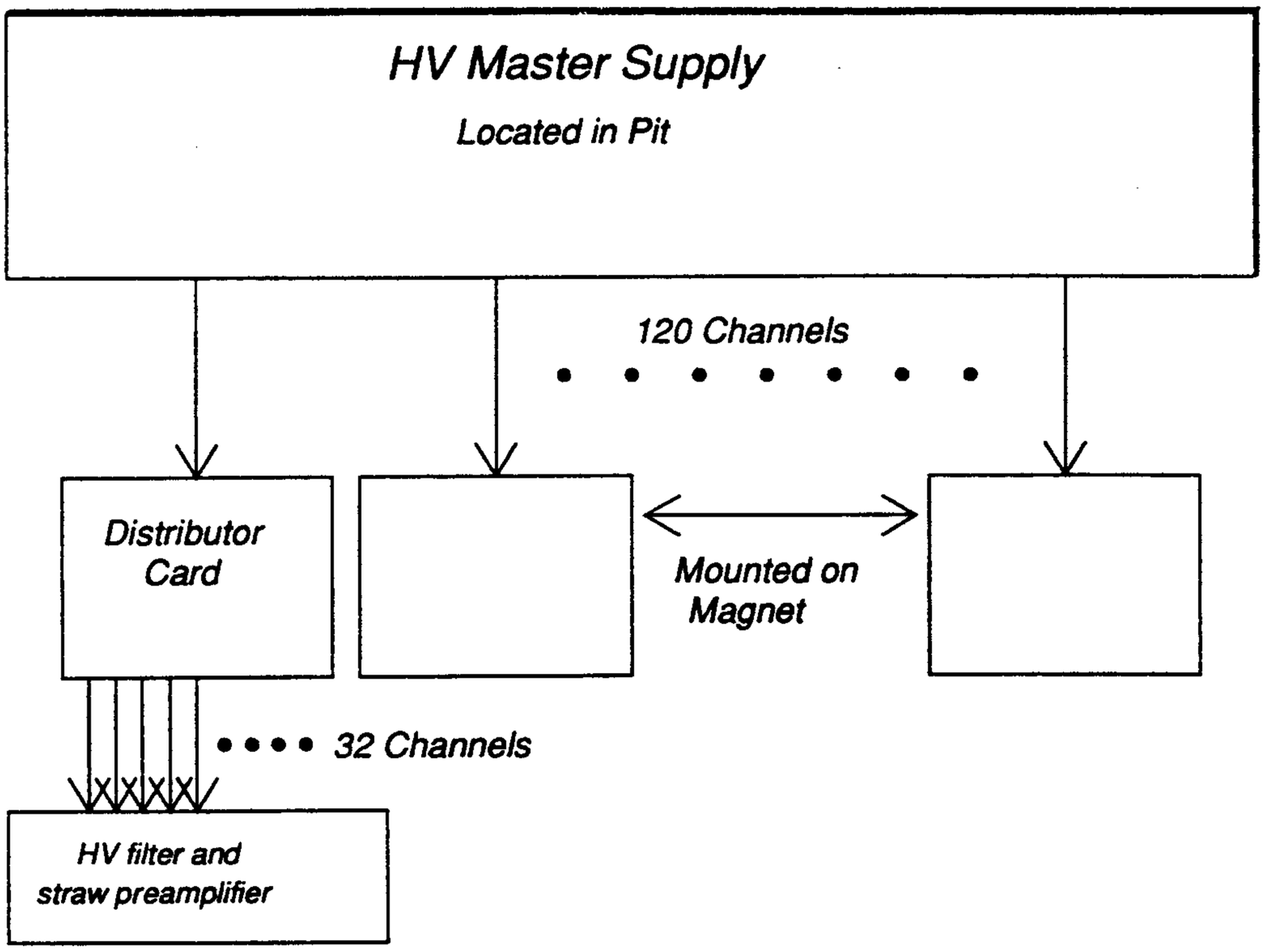

Figure 4.79: High Voltage system.

We can use the $\sim 4 \times 10^6$ K_{μ_2} events per day to monitor the relative position of the various subdetectors. Preliminary Monte Carlo simulations have shown that a longitudinal displacement of 100 μm of a measuring point results in a displacement of $\sim 20 \quad KeV/c$ of the K_{μ_2} peak.

The K_{μ_2} peak, together with the K_{π_2} peak (B.R.= 21 %, p = 205 MeV/c) and the peaks at 261 MeV/c and 273 MeV/c due to the ${}^{12}_{\Lambda}C$ formation will give the absolute calibration of the momentum scale of the spectrometer.

Bibliography

[1] The FINUDA collaboration, FINUDA a Detector for Nuclear Physics at DAΦNE, INFN Report, LNF-93/021, 11 May 1993.

[2] The ALEPH Collaboration, Proposal for a new vertex detector for ALEPH, CERN/LEPC 93-8, 20 May 1993.

[3] R.Turchetta, Nucl. Instr. and Meth. **A335**(1993)44 and V.Radeka and R.A.Boie, Nucl. Instr. and Meth. **178**(1980)543.

[4] F.Sauli, Instrumentation in High Energy Physics, Advanced Series on Directions in High Energy Physics Vol.9, World Scientific.

[5] M.Caccia et al., Nucl. Instr. and Meth. **A260**(1987)124.

[6] E.Nygard et al., Nucl. Instr. and Meth. **A301**(1991)506.

[7] O.Toker et al., Nucl. Instr. and Meth. **A340**(1994)572.

[8] , R. L. Gluckstern NIM **24** (1963) 381-389.

[9] U. Becker in *Instrumentation in High Energy Physics*, ed. Sauli (Word Scientific Publishing Co.), 1992.

[10] M. Basile et al., NIM **A239** (1985), 497-505

[11] G. A. Erskine, NIM **105** (1972), 565

[12] P. R. Burchat et al., NIM **A316** (1992), 217-222

[13] A. Breskin et al., NIM **124** (1975), 189

[14] G. Charpak et al., NIM **108** (1974), 157

[15] D.C. Cheng et al., NIM **117** (1974), 157

[16] R. Bouclier et al., Rep. CERN-PPE/94-111 (10 June 1994)

[17] F. Sauli, Rep. CERN 77-09 (1977)

[18] M. Jibaly et al., NIM **A283** (1989), 692-701

[19] A. Sharma and F. Sauli, Rep. CERN-PPE/93-51 (10 February 1993)

[20] V.M. Aluchenko et. al., *Nucl. Instr. and Meth.* **A283**, (1989) 528.

[21] B. Zhou et. al., *Nucl. Instr. and Meth.* **A287**, (1990) 439.

[22] W.W. Ash et. al., *Nucl. Instr. and Meth.* **A261**, (1987) 399.

[23] W.H. Toki et. al., *SLAC–PUB–5232* March 1990.

[24] R. Cizeron et. al., *Nucl. Instr. and Meth.* **A307**, (1991) 286.

[25] C. Bromberg et. al., *Nucl. Instr. and Meth.* **A307**, (1991) 292.

[26] S.H. Oh et. al., *Nucl. Instr. and Meth.* **A309**, (1991) 368.

[27] Produced by LAMINA Dielectrics England.

[28] L. Benussi et. al., **The First FINUDA Straw Tube Prototype: Construction Details, Signal Characteristics, and Tests with Cosmic Rays,** *FINUDA note ST–01–94* Aprile 94.

[29] L. Benussi et. al., **Test Beam Performance of the First FINUDA Straw Tube Prototype,** *FINUDA note ST–02–94* June 1994

[30] L. Benussi et. al., **Track Fitting with the First FINUDA Straw Tube Prototype,** *FINUDA note ST–03–94* June 1994

[31] L. Benussi et. al., **Electrostatics of straw tubes,** *FINUDA note ST–04–94* July 1994

[32] G. Bari et. al., *Nucl. Instr. and Meth.* **A251**, (1986) 292.

Chapter 5

TOFINO and TOFONE

5.1 Internal scintillator barrel (TOFINO)

5.1.1 General description

TOFINO is the inner scintillator array, the first detector hit by kaons leaving the beam pipe.

TOFINO has two direct and an indirect goals:

- to give a trigger on (K^+, K^-) and (e^+, e^-) pairs,

- to measure the life time of hypernuclei,

- to slow down kaons in order to stop them as close as possible to the external edge of the target.

The third goal fixes the thickness of the scintillators to a value of 2.0 mm, with the consequence of a small light emission.

The TOFINO scintillators will be 14 cm long and 3.1 cm wide, resulting in 12 total strips.

A greater segmentation would produce losses due to the bending of (K^+, K^-) inside the pipe and the dead zone between adjacent strips.

The calculated energy loss in the scintillators for (K^+, K^-), and (π^+, π^-) with momenta foreseen at DAΦNE is shown in Fig. 5.1, taking into account the angular dependence too. As it can be seen, there is a large separation in energy lost by kaons from that lost by pions. The non linear relationship between light output and energy loss introduces a small correction.

5.1.2 TOFINO tests

Different scintillators have been tested with a standard XP2020 PMT. NE104 turned out to exhibit the best performances in light emission (see table 5.1), giving 54 photo-electrons for a minimum ionizing particle with a very short light guide (approx. 10

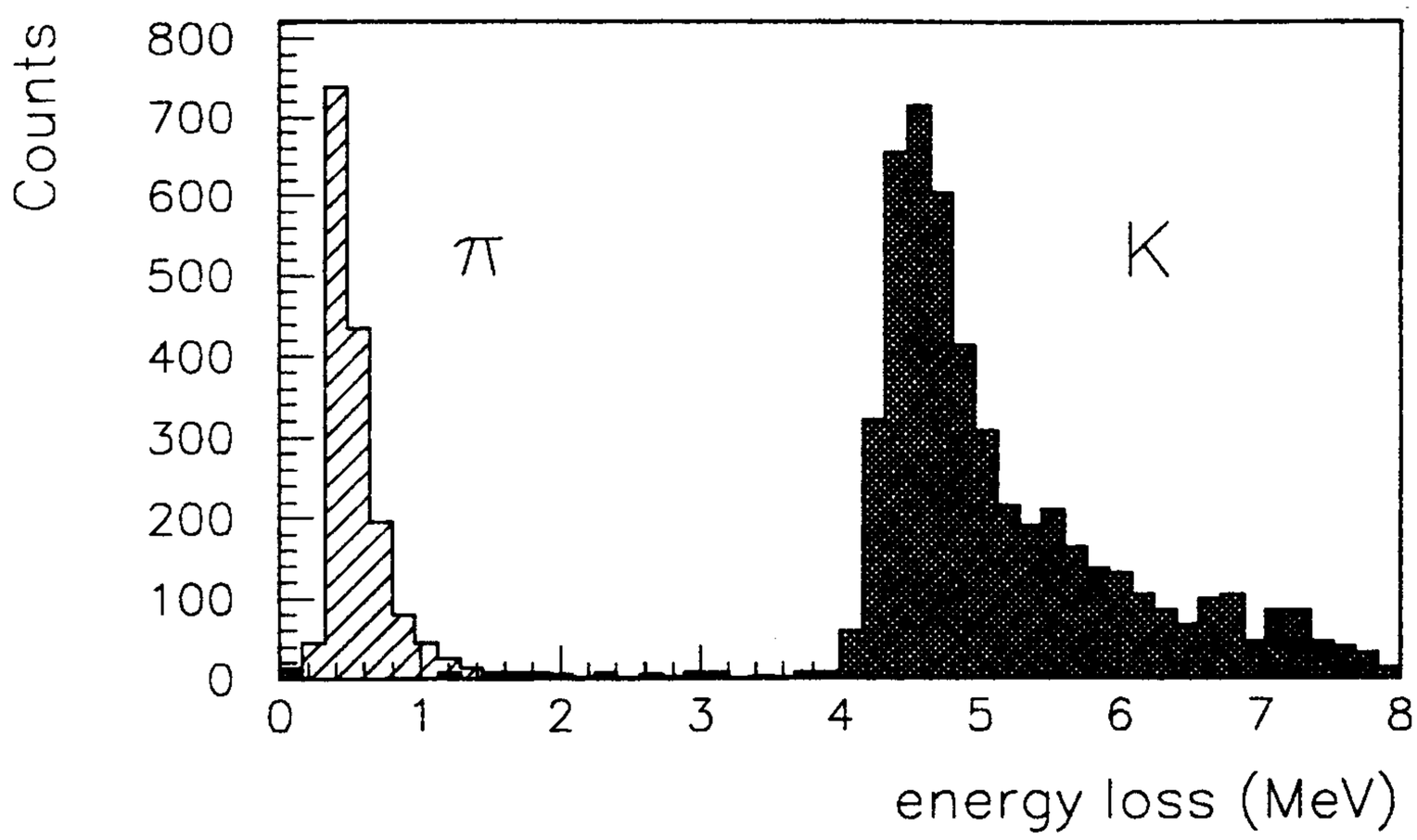

Figure 5.1: Energy loss in the TOFINO scintillators (2.0 mm thick) for kaons and pions.

cm). The use of a longer light guide (2 m) reduces the number of p.e. by a factor 10.

In the meanwhile the mechanical problem of the path that the light guides have to follow to go out from the magnet was studied by the collaboration and no easy solutions have been found.

For these reasons the decision was taken to work inside the magnetic field using, instead of a standard PMT at one side of the scintillator (as foreseen in the proposal), two Hybrid Photo Multiplier Tubes (HPMT) at both sides.

HPMT is a new detector developed by a joint venture between INFN and DEP (Delft Electronische Producten), a factory with experience on image intensifiers based in Roden (The Netherlands).

The HPMT is a proximity focused vacuum tube having a photo-cathode deposited on a glass window or fused silica entrance window and a silicon PIN diode which is biased in reverse as anode. As a function of their energy, which is determined by the high voltage applied to the photo-cathode, a number of electron-hole pairs is generated in the silicon causing a reverse current to flow. The unit can be used in a high magnetic field. The module is mainly made of two stainless steel parts. Experiments with a similar constructed tube have proved that HPMT is insensitive to magnetic fields up to 2 Tesla and that no damage is foreseen at higher magnetic field.

Some tests on a 25 mm HPMT already available by DEP have been performed. The time resolution has been tested versus the number of photo electrons, and the uniformity of the response over the silicon surface, using a conventional trans-impedence pre-amplifier with a gain of 25 mV/μA.

Table 5.1: Characteristic of tested scintillators

Scintillator type	n.ph.el.	light out. (%anthr.)	decay c. (ns)	att.len. (cm)
BC418	30	67	1.4	100
BC420	32	64	1.5	110
BC422	26	55	1.6	8
BC422Q	8	11	0.7	8
NE104	54	68	1.9	120
Pilot U	27	67	1.36	100
NE111A	34	55	1.6	8

The time resolution can be seen in Fig. 5.2,while the uniformity of time response is better than 30 ps, using the last batch of silicon with 20 nm of aluminum deposited on the surface, to obtain a good charge collection.

The gain of the preamplifier is much smaller than the typical gain one can achieve from a PMT, but with a light pulse of 50 p.e. and with a HPMT gain of 3500, one has an output pulse of 28 fC in approx 5 ns. The output current is then about 5 mA, corresponding to 250 mV on 50 ohms.

The difficult point is the noise coming from the diode that reduces the timing performances. Being reverse biased, the diode is fully depleted giving a capacity of 220 pF. The noise in a pre-amp. increases linearly with the capacity at the input, and with this value and 50 p.e. the time resolution cannot be better than 600 ps.

This is the reason why a 25 mm HPMT cannot be used, because the capacity is about 220 pF, a value which is too high to obtain good time resolution.

An HPMT with a silicon diameter of 18 mm, and a distance of 8 mm between the photo-cathode and the diode will be used. This HPMT can work with a high voltage of -15KV giving a current gain of 3500, and has a capacity of only 140 pF. DEP will send the first two prototypes by the half of October.

By the trigger point of view, the use of HPMT gives no special problems. The linearity of these devices is very good (160 db, much better then the linearity of the best pre-amps), and the separation between (K^+, K^-) and the background is easily achieved.

The life time of hypernuclei is a more difficult goal. The birth and death of

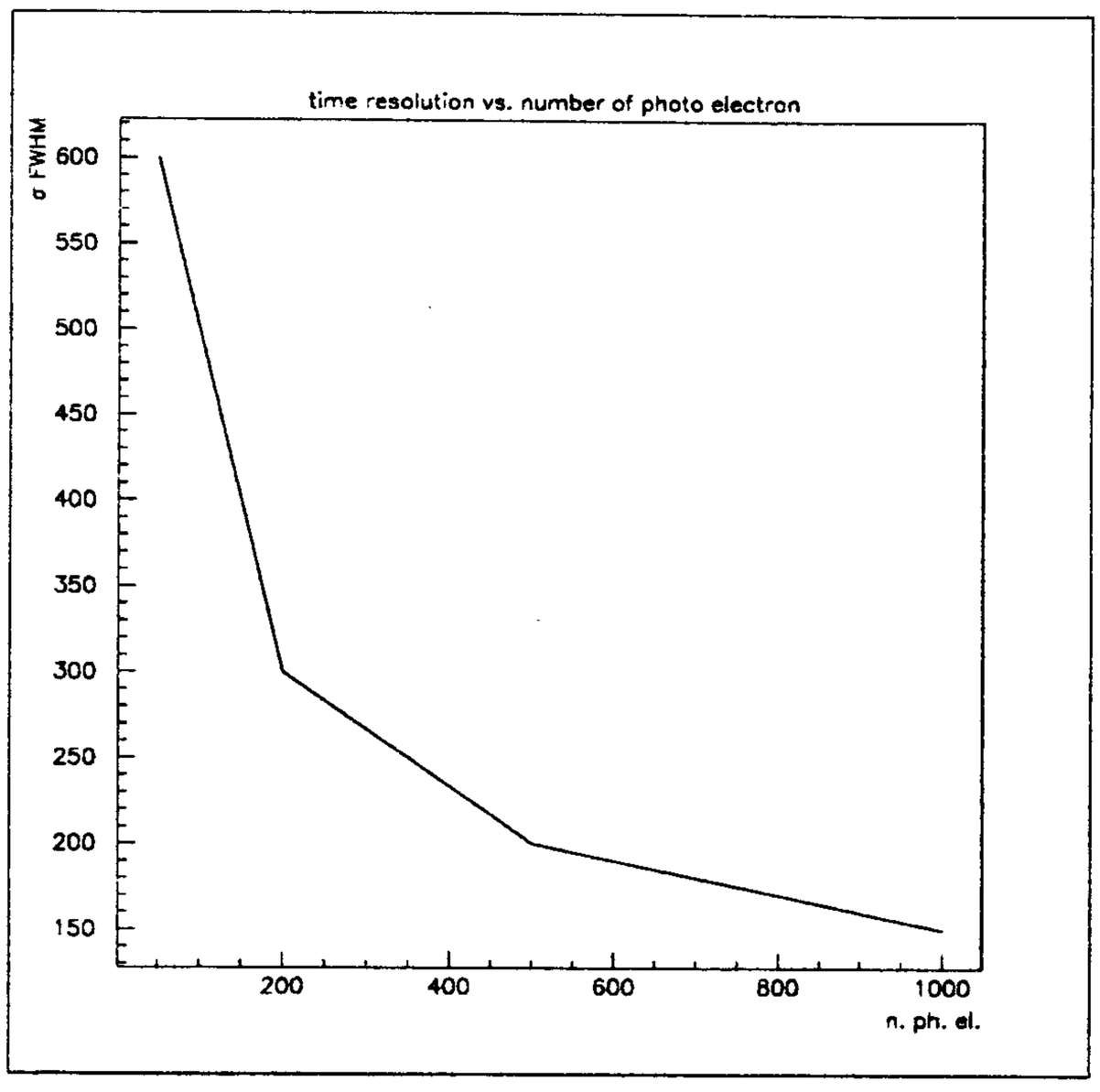

Figure 5.2: Time resolution data for a 25 mm HPMT (experimental data).

an hypernucleus is marked by the K^- stopping into the target, and by the proton coming from a non-mesonic decay. If the proton crosses TOFINO in a slab different from those which detected the K^-K^+ pair, one can use the two signals to measure the life time of hypernuclei, following the technique already used at BNL.

A good timing is then requested only with kaons and protons. As it can be seen from fig. 5.1, a kaon has a ΔE 10 times larger than a pion giving a light output of 500 p.e. and then a time resolution of 200 ps. A proton has an energy loss only 3 times larger than a pion, but in any case can give a time resolution of 300 ps, as it can be seen in fig. 5.2, in which the time resolution foreseen for a 18 mm HPMT is plotted, basing on available data from 25 mm HPMT. If one was able to obtain a time resolution of 250÷300 ps FWHM, it would be possible to measure the asymmetry of the Δt distribution and the life time (τ_Λ) of the hypernucleus. Fig. 5.3 shows a MC simulation of the time distribution of events following an exponential decay with $\tau_\Lambda = 100$ ps and $= 200$ ps respectively. The prompt event distribution ($\tau_\Lambda = 0$) is also shown for comparison. An instrumental time resolution of 300 ps FWHM was assumed. The distributions shown in fig. 5.3 a) are not corrected for different path lengths of the particles. fig 5.3 b) shows the same distributions, corrected for the different path lengths as measured by the tracking devices, under

the same hypotheses. It can be seen that with 10^3 events in the distributions, an error of ± 5 *ps* on τ_Λ is obtained.

5.2 TOFONE mechanical arrangement

In the final mounting TOFONE will be attached to the body of the magnet cryostat, the inner cylindrical surface of which is foreseen to be at a radial position of about 138 cm. Two support rings will be mounted at z-positions approximately 1/3 and 2/3 of the length of the cylinder. They will be manufactured to compensate for the possible 2 - 3 mm radial uncertainty of the inner cryostat surface and to allow for the passage of the optical fibers to inject time and amplitude calibration light pulses into the scintillators. The rings will be screwed to the inner cryostat surface.

Practically all the scintillator slabs will be mounted after the complete pathways of light to the external phototubes will have been tightly glued to them. Only three slabs will be mounted with one of the straight cylindrical bars lacking, to allow preliminary connections of the super-conducting coils for magnetic field tests. The three lacking straight bars will be glued after the final installation in the pit. The last slab to be mounted works as a keystone and therefore it will not be placed with a radial move. It will instead be slided into its position with a move parallel to the z-axis. For this reason, this key-slab will lack of one of the conical connections and attached cylindrical bar during the sliding, but immediately after, the missing light guides will be glued to it.

The dimensions of the slabs allow for tape wrapping aimed at optical thightness. Depending on the real individual depth of these wrappings, the final angular position of each individual slab will require less than 1 mm adjustment. Inserting a limited number of aluminum sheets (a few tenths of mm deep) between the lateral surfaces of the mounted slabs, a self sustained barrel vault will be obtained. For sake of safety, however, we will take advantage of the 1 cm spacing (see fig.5.4) near the ends of each couple of mounted slabs (this was the main goal of the reduction of the transverse dimensions of each slab) to screw on the side flanges of the magnet cryostat metallic bands surrounding the left and right ends of each scintillator.

5.3 TOFONE prototype performance.

Some prototypes of the more common fast plastic scintillators in the shape of long bars have been tested to address our final choice. These have been types NE110 and NE102A manufactured by Nuclear Enterprises and BC408 manufactured by Bicron Corporation. All the bars had a rectangular cross sectional area of 8 cm by 10 cm and a length of 220 cm. Having easily confirmed for all of them the fast response and the amount of prompt luminosity, which resulted comparable, the attention has been focused on their light attenuation length (LAL) which is at a premium value if over 400 cm. While this LAL value is quoted for NE110, the other two scintillators

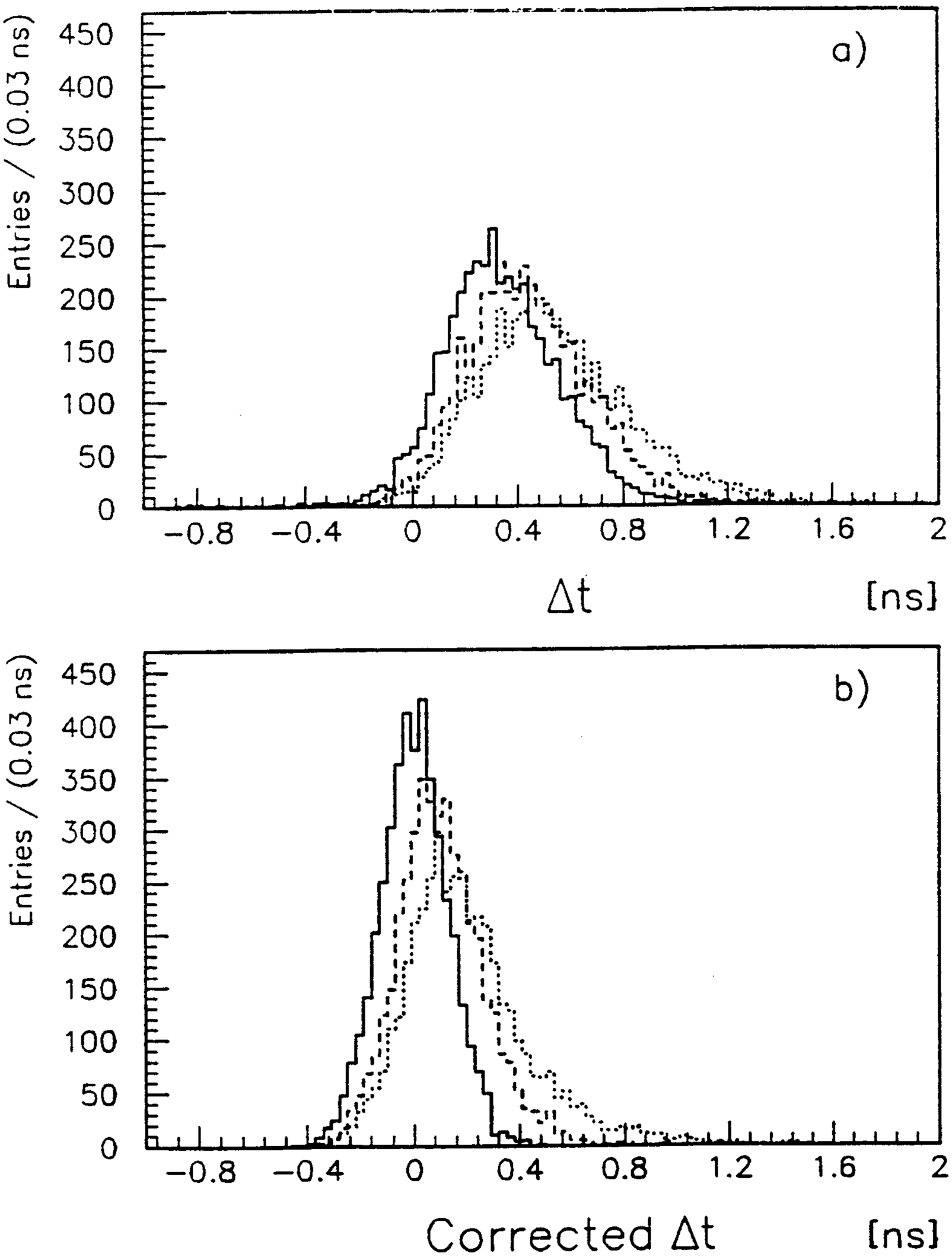

Figure 5.3: Time distribution of events recorded by TOFINO due to proton non-mesonic decays. The dashed and dotted lines refer to $\tau_\Lambda = 100$ and 200 ps respectively. The solid line shows the time distribution for prompt events ($\tau_\Lambda = 0$). The distributions in a) are not corrected for the different path lengths. In b) the correction for the different path lengths is applied.

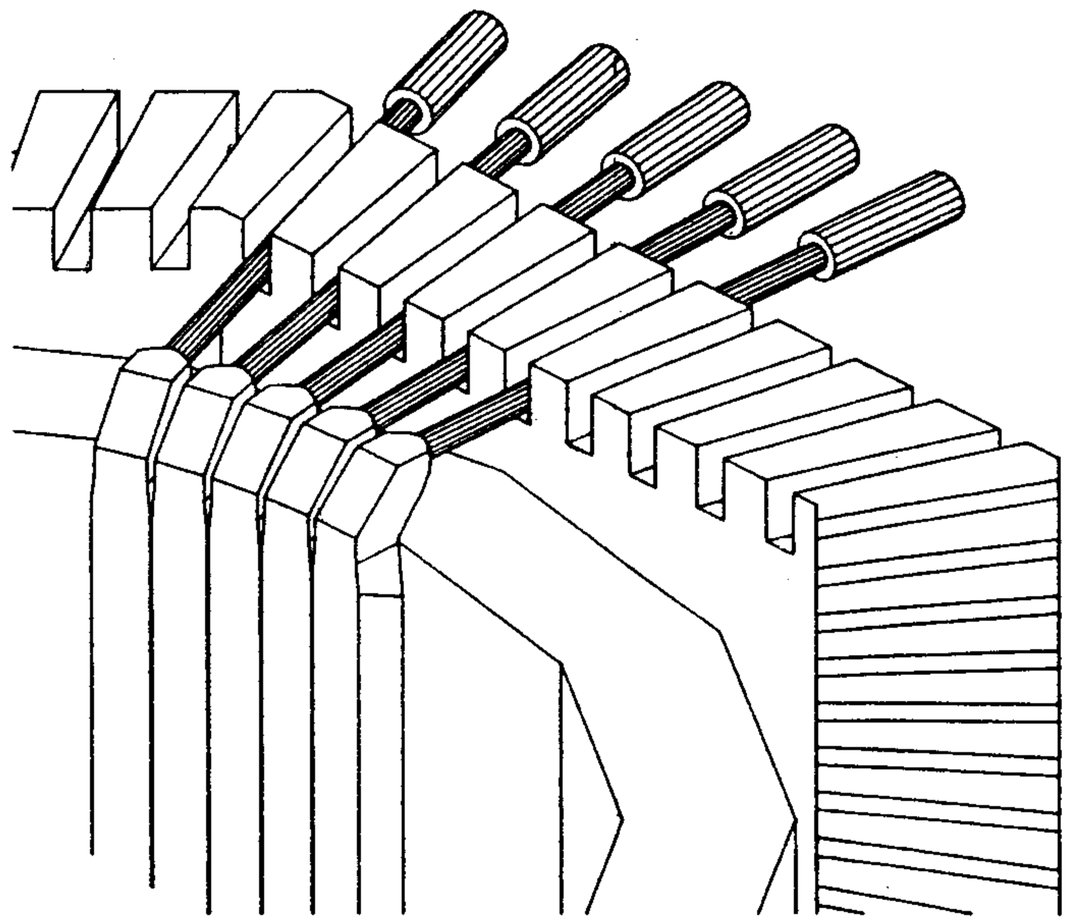

Figure 5.4: Sketch of five TOFONE elements mounted.

do not present such kind of values in their data sheets but the manufacturing firms claim to have achieved optimum results for LAL in the new production of NE102A and BC408.

We therefore attached to the scintillators a conical lucite connection to a Philips XP2020 photomultiplier biased far from saturation and recorded the charge spectrum of the pulses due to cosmic rays crossing the 10 cm dimension, selected in the correct direction with the aid of two small scintillators in coincidence. A typical charge spectrum collected as above is shown in fig.5.5, from which the peak position is easily obtained. Recording and plotting these cosmic ray peak positions versus the distance from the scintillator face connected to the photomultiplier, a typical graph as the one shown in fig.5.6 is obtained from which exponential fit the LAL is obtained as the inverse of the coefficient of the distance.

The results confirm that all the three tested scintillator have a LAL greater than 400 cm. Taking into account the higher density, the conclusion is that NE102A and BC408 are completely equivalent for the purposes of the experiment. In the tender opened to acquire the TOFONE scintillators a value larger than 400 cm has been therefore imposed for LAL. With this particular value, the expected position dependence of the light amplitude pulses collected out of the final 255 cm long TOFONE scintillator bars will be as drawn in fig.5.7, in which one see a left and right dependence going almost to 50%, but a sum (left + right) dependence within 7%.

A second set of measurements has been performed to identify the optimum light guide shape as far as the the transmitted fraction of light is concerned. The shapes taken into account consisted mainly in a lucite conical connector plus cylindrical bars bent at 90 degrees with different bending radii and different ratios of bar diameter to bending radius. During these measurements we did not mount the last straight

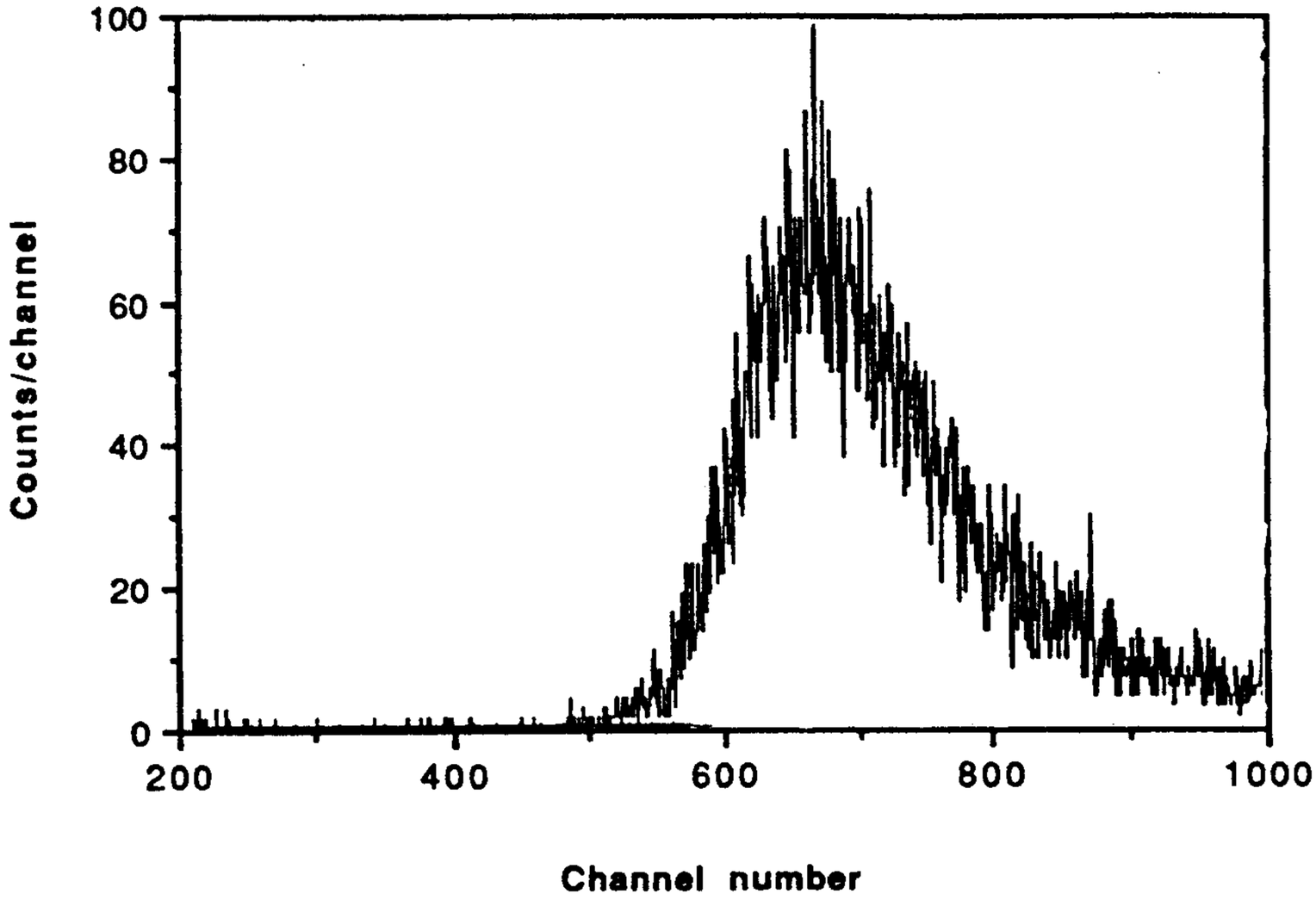

Figure 5.5: Vertically crossing cosmic rays charge amplitude spectrum taken from one side of a prototype scintillator bar.

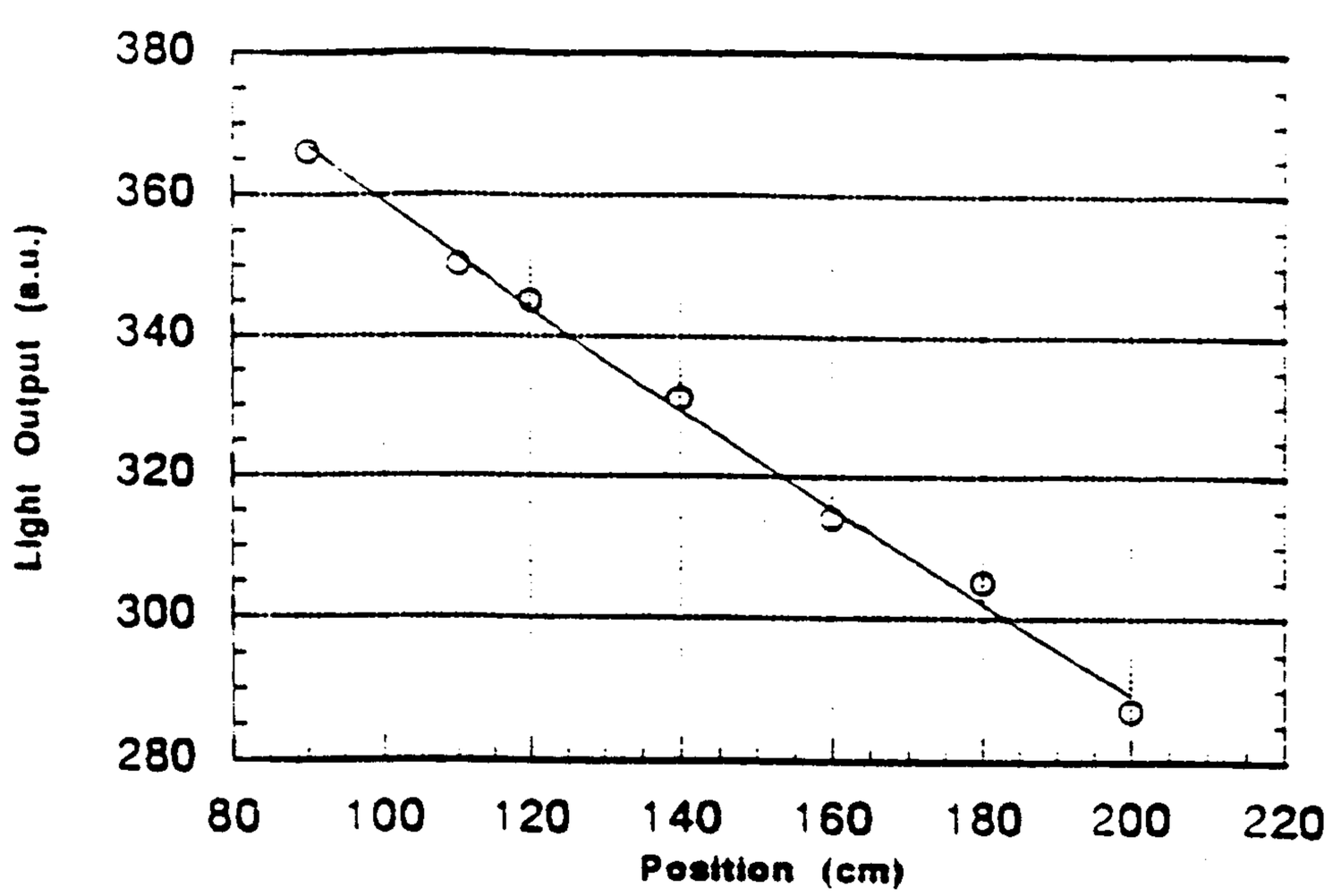

Figure 5.6: Typical plot of the peak positions of vertically crossing cosmic rays taken from one side of a prototype scintillator bar, versus distance from the end of the bar connected to the phototube.

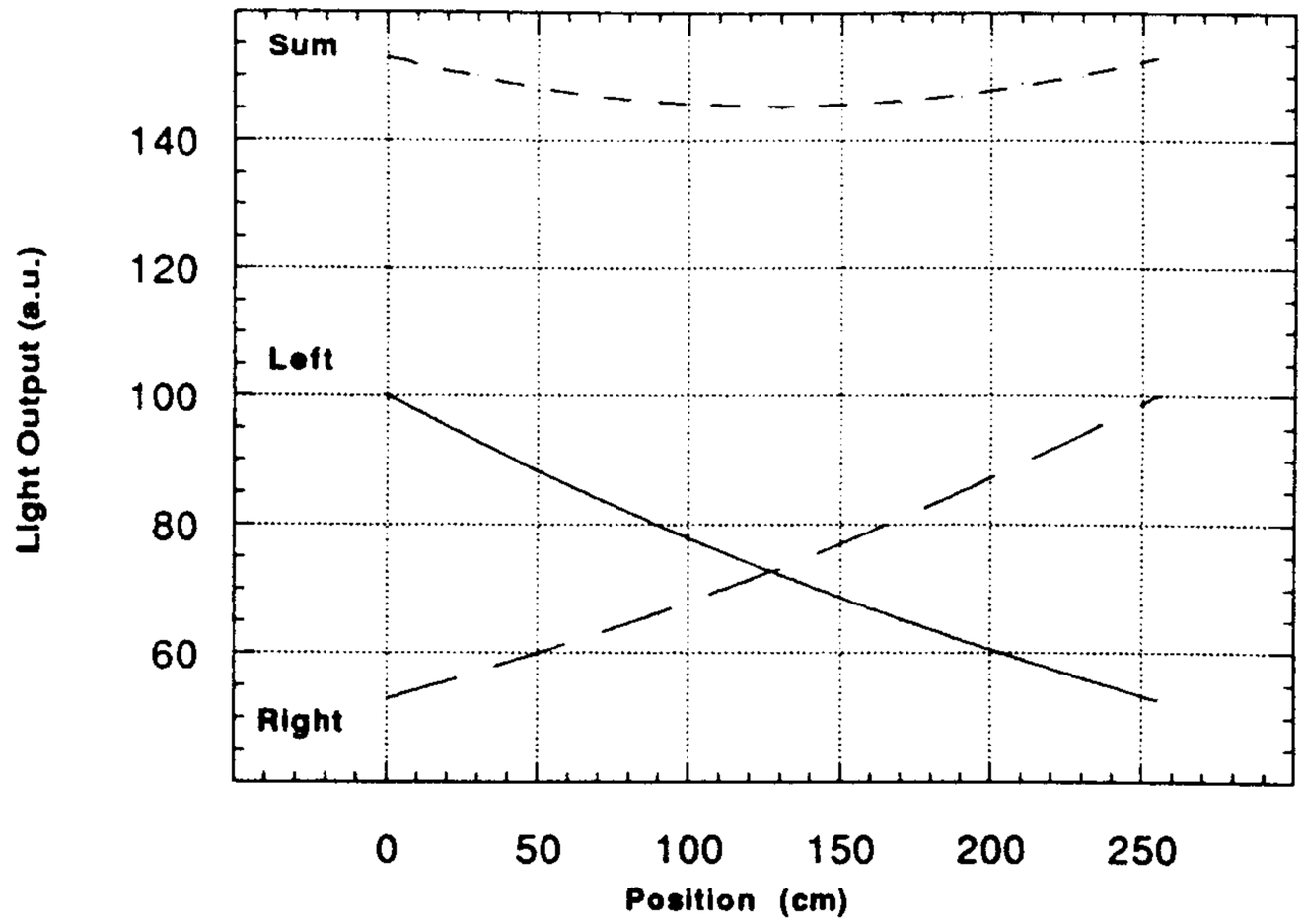

Figure 5.7: Expected light response versus scintillation position in the final TOFONE scintillator slabs with a light attenuation length of 400 cm.

cylindrical guide, considering that it adds the same extra fractional light attenuation in all the cases under test. The amount of the collected light to be compared for the various situations was taken, also for this set of measurements, as the cosmic ray peak position previously described (fig. 5.6). In no case we obtained results better than 60% light transmission with respect to the value taken without any bending. After the bent bar transmission, we tried the 90 degrees deflector prism coupled through a conical connection to the phototube, obtaining 80% light transmission with respect to the same reference as before. We therefore decided to adopt this kind of light deflection, extending the scintillator length slightly out of the magnet cryostat and gaining furthermore in detection solid angle, which is very useful for neutron detection.

A third set of test measurements was undertaken to address our choice of the photomultiplier with the best cost to performance ratio. The tubes taken into account as low cost competitors of the Philips XP2020 one, the latter of already proved quality as far as optimum timing is concerned, have been Philips XP2262B and Hamamatsu R5686. The experimental set up used for these measurements has been the same one allowing the determination of the left side to right side time of arrival difference of the light pulses from the cosmic rays selected as above, having an amplitude dynamic range not greater than 40% as can be argued from fig.5.5. The high voltages used to bias the tubes have been the ones given in their data sheets for best timing results. All the tubes considered have proved to be able to give a left to right TOF with a FWHM smaller than 700 ps. The two low cost tubes considered are therefore equivalent for our goals and their producing firms will compete in the possible tender we are going to open, in case we are not able to recover the needed photomultipliers from other dismounted experiments, in which case the tubes to be employed will be Philips XP2020.

5.4 High voltage and electronics read-out of TOFONE

The high voltages and current requirements for all the photomultiplier tubes of possible interest do not exceed 3000 Volts and 1 - 2 mA per tube. The total number of H.V. channels required is 144. It seems therefore suitable to adopt four crates of the CAEN System SY 127 with 40 H.V. channels/crate given by 10 modules CAEN A333 per crate, controlled via a VME or CAMAC interface. In the last crate the minimum number of A333 modules required is 6, but it is worth to have about 10% extra spare channels for a total of 160 channels.

Constant fraction timing discrimination of anode signals, together with left to right meantiming, will be accomplished employing 16 ch/module/station CAMAC Constant Fraction Discriminators C208 and 16 ch/module/station CAMAC Meantimers C561 manufactured by CAEN, or similar ones, which at the moment have the highest known density of channels per station. With a limited number of spare sub-addresses 10 units of C208 CFTD and 6 units of C561 MT in a CAMAC Crate will be needed. CFTD logic signal from left and right phototubes and MT logic outputs will be conveyed to VME 64 ch/module TDCs VN1488 by CAEN, or similar ones. Four of these units will cover all the required and some useful spare channels.

Analog signals, conveniently delayed by means of specified length transport cables, will be addressed to VME 64 ch/module QDCs VN1465 by CAEN, or similar ones. Three of these units will be sufficient for all the required charge conversion channels and will leave some spare sub-address.

All the VME modules will be hosted in the same VME 9 units extended crate and controlled by the same VME CPU.

5.5 High voltage and controls

As far as the TOFONE scintillator array is concerned the controls will be devoted to timing synchronization and photomultiplier gain, the details of which are reported in next paragraph.

Here it is worth to say that the control procedure will only record pseudo events from which possible small correction of calibrations will be deduced in the off-line analysis. No real time automatic adjustments of high voltage values are foreseen, but only alarm signals when some large variation in gain or in timing happens, after which operator inspection will be worth for troubleshooting. Ordinary sessions of calibration will be scheduled with a loose frequency to avoid possible grow up of one way drifts, in which occasions operator intervention will be possibly required. The just told approach to controls comes from the behavior already observed in scintillator systems like the one of interest here, in which the ordinary small drifts in gain and timing are conveniently taken into account off-line but large variations in timing or in gain are almost always the consequence of a serious failure of some

component from which is not possible to recover with automatic procedures.

5.5.1 Scintillator control: the laser system

Introduction

The first level trigger in the FINUDA experiment is provided by the signals of a complex system of plastic scintillators.

In order to exploit at best the excellent timing resolution of each element of the complex scintillator arrays it is mandatory to have a precise and flexible calibration system allowing to equalize the timing of the different scintillators within 200 ps or better, and to perform periodical controls. Shifts due to the electronics, PMs gain, temperature may be controlled and taken into account.

To this purpose we will realize and test a calibration system based on a laser, whose pulses are transmitted through plexiglass road and optical fibers to each scintillator strip. Some other experiments have used similar arrangements.

As well known, the physical TOF of the particles is obtained from the measurement of the time interval between a START signal given by the PMs coupled to the slabs of TOFINO, and a STOP signal given by the PMs coupled to the slabs of the TOFONE. The time intervals are measured by means of TDCs (Time-to-Digital Converters). In order to obtain the best performances for the whole apparatus, the information from each TDC channel has to be corrected for several effects that introduce time spreads: different cable length, different transit time in the PMs, different propagation time in the cables , different propagation time in the different electronic channels, different thresholds in the discriminators...

The laser based system allows a simple calibration procedure: the same laser pulse, suitably splitted following the optical fibers array, activates all scintillators of the experiment and a good primary timing of the trigger can be given.

The laser-optical fibers system.

The chosen laser is a N2/Dye lasers combination based on a LN203C N2 laser and a LD2S Dye module (supplied by PRA LASER INC., a laser photonics company). The N2 laser provides light of 337.1 nm, with a pulse width of 600 ps FWHM and an energy/pulse of 90 mJ; the frequency is tunable from 10 to 50 Hz. These pulses, can be used directly or to pump a LD2S Dye module containing a Littrow grating dye configuration cavity. In particular the dye absorbs light at 337.1 nm and emits light at a longer wavelength; in our specific case the mean wavelength is 500 nm, with a spectral band width of $\sim$ 3 nm. This choice of 500 nm was the better compromise for minimizing the attenuation along the path of the plexiglass rod and the optical fibers, but still being near the maximum spectral sensitivity characteristic of the PMs.

After the Dye there is a simple optical system feeding a primary optical fiber. It consists of an array of neutral density filters that allow to control the light beam intensity and a biconvex lens for focusing on the primary optical fiber (ϕ =1mm).

We have tested the two different wavelength laser light and we have obtained a better resolution with the 500 mm light.

Then we have performed some tests on two kinds of the optical fibers, silica (ϕ = 1.5 mm) and plastic (ϕ = 1 mm); the better resolution was obtained with the plastic fibers. Also a test of the plexiglass road was performed: in particular we have chosen a plexigalss helix followed by a cylindrical road.

The first is necessary to conform the laser spot to the small diameter of the primary optical fibers (or laser spot, if the laser is directly coupled to the plexiglass rod) to the second rod where the light is diffused to the fibers array.

A good solution will be to embed directly the fibers into scintillators but mechanical problems don't allow this solution.

Probably we will connect the fibers to by means of small, totally reflecting plexiglass prisms glued to the scintillators, at their center. To evaluate the gain stability of the PMs, we need of a reference PM, coupled to a scintillator reached by laser light and irradiated by a radioactive source: the PM pulse analysis give two peaks, the first is the check of the PM gain stability respect to source, the second is the check of the laser light intensity change.

Chapter 6

TRIGGER

The FINUDA apparatus comprises six independently-operated sub-detectors, two of which (TOFINO and TOFONE) generate prompt signals available for triggering at the first level.

The signals coming from TOFINO and TOFONE are centrally combined by the Trigger Source System (TSS), which distributes the basic triggers to the Global Trigger Supervisor (GTS) and to the Local Trigger Supervisor (LTS) of each sub-detector.

This trigger configuration, including two masters, the TSS and the GTS, allows to each sub-detector to perform "stand-alone" runs using TSS and selecting the desired trigger by its own LTS. This feature can be very useful during dedicated adjustment tests and calibrations, in which the Global DAQ is not required. On the other hand, for measurement runs, in which the whole apparatus is required to operate, the GTS can better manage the distribution of the selected trigger and the busy signals coming from each sub-detector.

6.1 Trigger Source System: basic triggers

Trigger data are generated in the TSS which feeds off the prompt signals coming from TOFINO and TOFONE. In the TSS some basic criteria are implemented, e.g. the requirement for particular topologies or for maximum energy deposition.

Several tasks are required in order to satisfy physics measurement runs, tests and calibrations.

During physics measurement runs the goal of the trigger is to distinguish K^+K^- from Bhabha scattering events, other ϕ decays and cosmic rays. On the contrary, during calibrations and tests the sub-detectors can use laser pulses, cosmic rays, Bhabha scattering events or μ^+ and π^+ coming from K^+ decay.

At the luminosity $\mathcal{L} = 10^{32} cm^{-2} s^{-1}$ (we always take into account this $\mathcal{L}$ value in the following considerations), the expected total rate for ϕ production is about 440

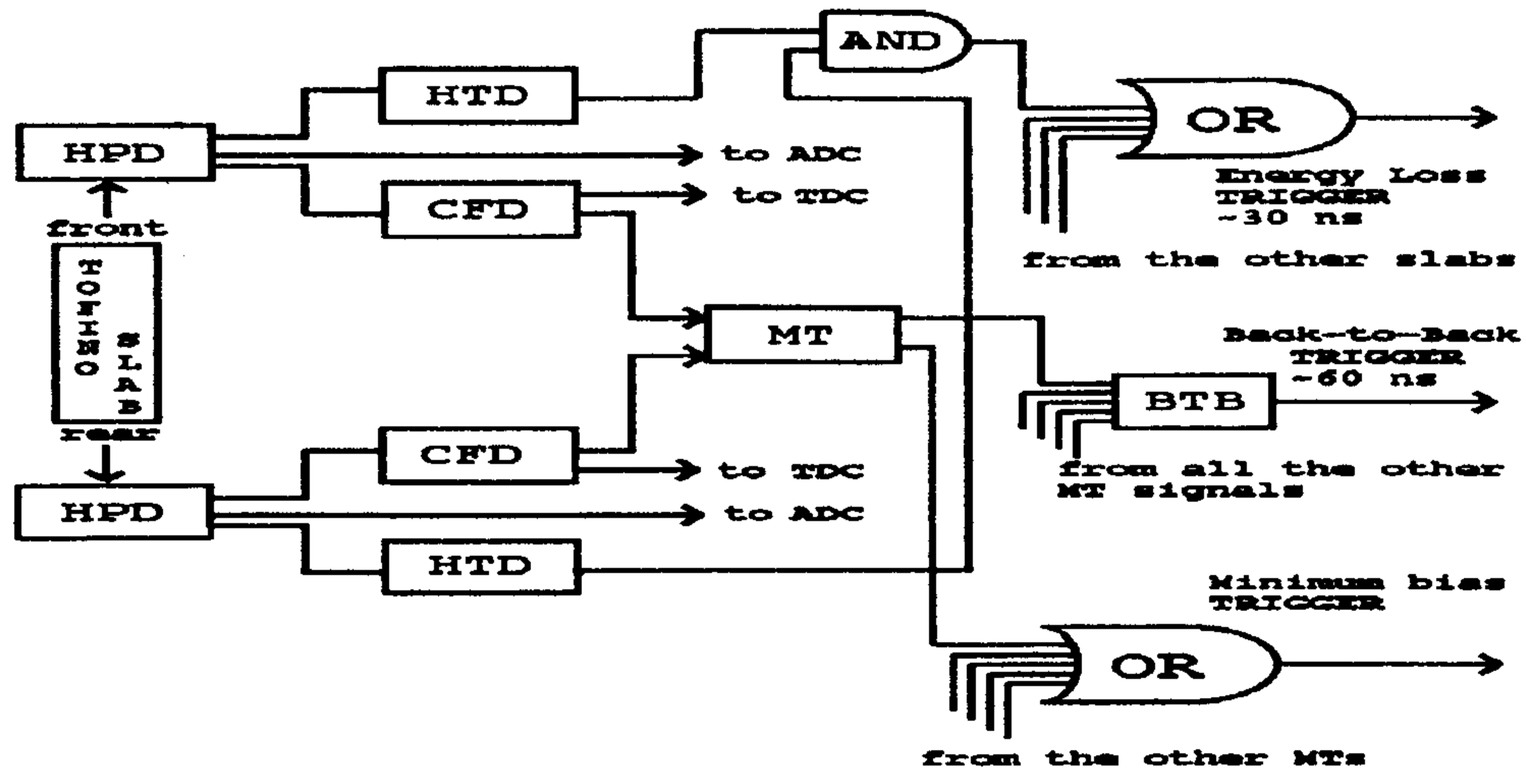

Figure 6.1: Block diagram of the Trigger performed on TOFINO.

Hz. The production rate of ϕ is about $6.2 * 10^{-6}$ per bunch.

In the angular region covered by TOFINO [$35° < \theta < 145°$] the Bhabha scattering cross section is some orders of magnitude lower than in the forward and backward directions. Then rates of K^+K^- and e^+e^- will be of the same orders of magnitude (200 Hz). Rates due to other ϕ decays are smaller and they are considerably reduced by the trigger selection of good events (less than 1 Hz, as shown in tab. 8.2). We can estimate the machine background will be less than 10 Hz (about 100 Hz at the top luminosity $\mathcal{L} = 10^{33} cm^{-2} s^{-1}$) and it will be suppressed by the trigger selection.

Taking advantage of having a fast detector (TOFINO) very close to the interaction region, the trigger is based on the fast identification of good events over background ones, that means we can neglect the RF signal occuring with a very short inter-bunch time ($\sim$ 14 ns at $\mathcal{L} = 10^{32} cm^{-2} s^{-1}$ and $\sim$ 3 ns at $\mathcal{L} = 10^{33} cm^{-2} s^{-1}$) and we can consider to have a continuous source of interactions.

As described in Chap. 5.1 and shown in fig. 6.1, each TOFINO scintillator is viewed by two Hybrid Photomultiplier Tubes (indicated with HPD in the figure) at both ends of the slab and each analog signal feeds two discriminators: a Constant Fraction Discriminator (CFD) and a High Threshold Discriminator (HTD). Then a Mean-Timing (MT) operation is performed between the two signals coming from the left and right CFD*s* in order to correct the crossing point of the particle on the slab.

The MT signal corresponds to a hit slab. The coincidence between two MT signals corresponding to two axially symmetric slabs defines a back-to-back topology. In order to take into account the curvature of kaon trajectory, we can extend the back-to-back configuration requiring the coincidence of one slab with one of the three opposite. The OR of the coincidence signals gives the extended back-to-back topology (BTB) trigger.

The OR of the twelve MT signals can be used as minimum bias (MB) trigger and for providing the best start signal for the Time-of-Flight system and common stop for the ST and the LMDC.

This start signal doesn't give the original time of the event corresponding to the generation of ϕ or e^+e^- scattering, but it gives the time when the products of ϕ decay or Bhabha scattering or LASER pulse or cosmic ray impinge on the TOFINO. If necessary, it's possible to know the original time in the off-line analysis by determining the interaction point by means of information from ISIM.

We can use the information of the energy loss in a scintillator 2 mm thick (see fig. 5.1), in order to discriminate kaons from pions, electrons and cosmic rays.

The OR of the signals coming from the slabs passing HTD*s* gives the Energy Loss (EL) trigger.

Also on TOFONE each slab, at the trigger level, is identified by the MT performed on the signals coming from both sides of the slab.

The hypernuclear events are signaled by at least one fired slab of TOFONE within a narrow timing gate of 10 ns (PC trigger), due to π^- coming from stopped K^- interaction, forming the hypernucleus.

The μ^+ and π^+, coming from the K^+ decay, can be used for momentum calibration of the tracking system (see Chap. 4.4). The μ^+ has an arrival time on TOFONE, due to the K mean life time, which allows to trigger on these events requiring the first hit on TOFONE after 10 ns (SC trigger).

In summary, the TSS performs the following basic triggers:

* **from TOFINO:**

  Minimum Bias trigger (MB);

  Energy Loss trigger (EL);

  Extended Back-to-Back trigger (BTB);

* **from TOFONE:**

  Multiplicity trigger (MUL);

  Prompt Coincidence trigger (PC);

  Slow Coincidence trigger (SC).

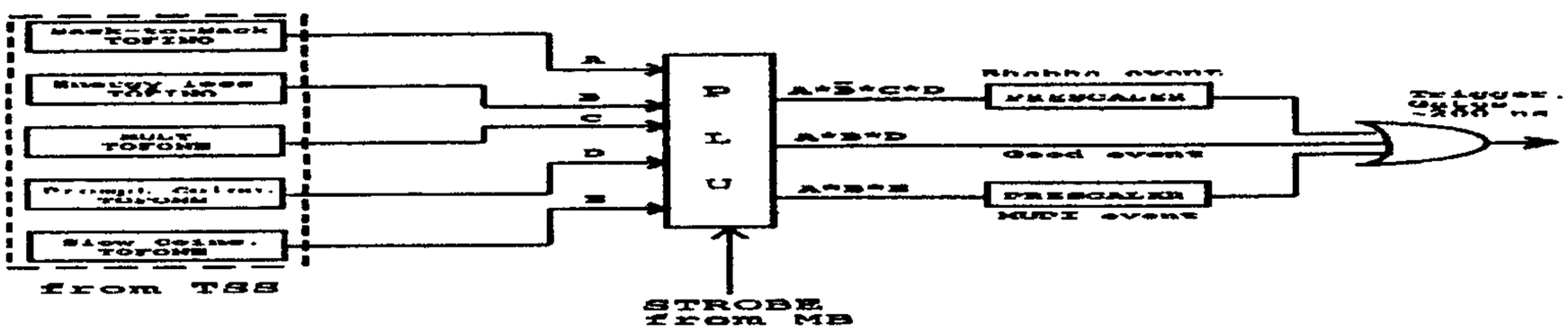

Figure 6.2: Basic Triggers from the Trigger Source System (TSS).

All of them can be performed in less than 150 ns, including the operating time of TOFONE MT signals ($\sim$ 50 ns). In particular triggers from TOFINO can be available in a time of $\sim$ 80 ns.

In order to identify hypernuclear (HYP) events it's necessary to select independently at least one fired slab on TOFINO satisfying the EL condition, an extended BTB configuration and a PC signal on TOFONE, then the following combination of basic triggers is required: HYP = EL*BTB*PC.

The expected rates, calculated by Monte Carlo simulation, for that trigger condition is $\sim$ 1 Hz, which is a factor 10 greater than the hypernuclear production rate, due to the π^- continuous spectrum beyond 200 MeV/c.

For Bhabha scattering (BHA) events the combination is:
BHA = BTB*not(EL)*PC*(MUL=2); corresponding to a BTB configuration, no signal from EL selection, PC signal and multiplicity = 2 on TOFONE.

As far μ^+ and π^+ (MUPI) events they can be selected by the combination:
MUPI = BTB*EL*SC; in fact the BTB*EL asks for K^+K^- on TOFINO and the SC signal correspond to a slow particle hitting TOFONE after 10 ns into a gate of 15 ns. The expected rates of these calibration events selected by that trigger are $\sim$ 50 Hz. Due to the large arrival time distribution of μ^+, some calibration events are expected to pass the HYP trigger. That means we probably don't need to perform a dedicated MUPI trigger with a window on the slow time.

During data taking with e^+e^- beams it can be useful to trigger on a sample of BHA and MUPI events, mixed with the HYP ones, in order to monitor and calibrate continuously the apparatus. For this purpose a combination like the following can be selected on the GTS: HYP + prescaled BHA + prescaled MUPI, as shown in the simple scheme of fig. 6.2.

6.2 The Global Trigger Supervisor and the Local Trigger Supervisor

All the basic triggers are sent to the GTS and to the LTSs from the TSS, which have standard programmable logic units to perform specific trigger combinations. The diagram in fig. 6.3 shows the links among the TSS, GTS and LTS.

In case of "stand-alone" runs each LTS selects the trigger like a combination of the basic ones and it manages the busy signal coming from the corresponding sub-detector during read-out and the supervising action of GTS is excluded.

In case of Global DAQ the GTS plays the major role selecting and distributing the trigger to all LTSs and managing the busy signals from the detectors. The LTSs are just slaves of GTS and they cannot take any action out of the decision of the GTS.

All the synchronization of the trigger system will be supervised by the GTS and will be performed by means of programmable delays connected on key points and by using the pulses coming from LASER firing the scintillator slabs.

The GTS also broadcasts trigger information via a special trigger bus to each LTS.

Processing of the trigger signals proceeds only if the GTS receives a MB strobe from TSS, which is also sent to the Tracking device to give a stop to TDC*s* measuring the drift time, in fact the MB signal correspond to at least one fired slab on TOFINO.

The final trigger decision is available at the first level in $\sim 200\ ns$.

If the trigger decision is negative the GTS broadcasts a reset signal. Sub-detector front-end electronics are then cleared in preparation for another MB signal. If the trigger decision is positive, a trigger signal is broadcast together with a word of trigger signal information.

The LTS*s* then generate local VME interrupts which can start read-out of the sub-detectors and release a busy signal on the trigger bus until their read-out is completed. The GTS inhibits further triggers up to all sub-detectors have removed the busy signal from the trigger bus.

At the moment we don't plan to implement any higher level trigger in the first stage of the experiment, because we foresee good background rejection and high efficiency at the first level, due to the EL trigger (for more details see paragraph 8.3). Then a low rate of $\sim 100\ Hz$, compatible with the read-out capability, is expected.

The GTS also performs the control and monitor of trigger rates, of total dead time, due for each event to the read-out time of the slowest sub-detector. The LTS*s* monitor the individual sub-detector dead times and give the information to GTS.

The LTS*s* reside in the VME crates which house the corresponding Local Event Builder (LEB) and the TSS and GTS are housed in the VME dedicated Trigger System Crate (TSC).

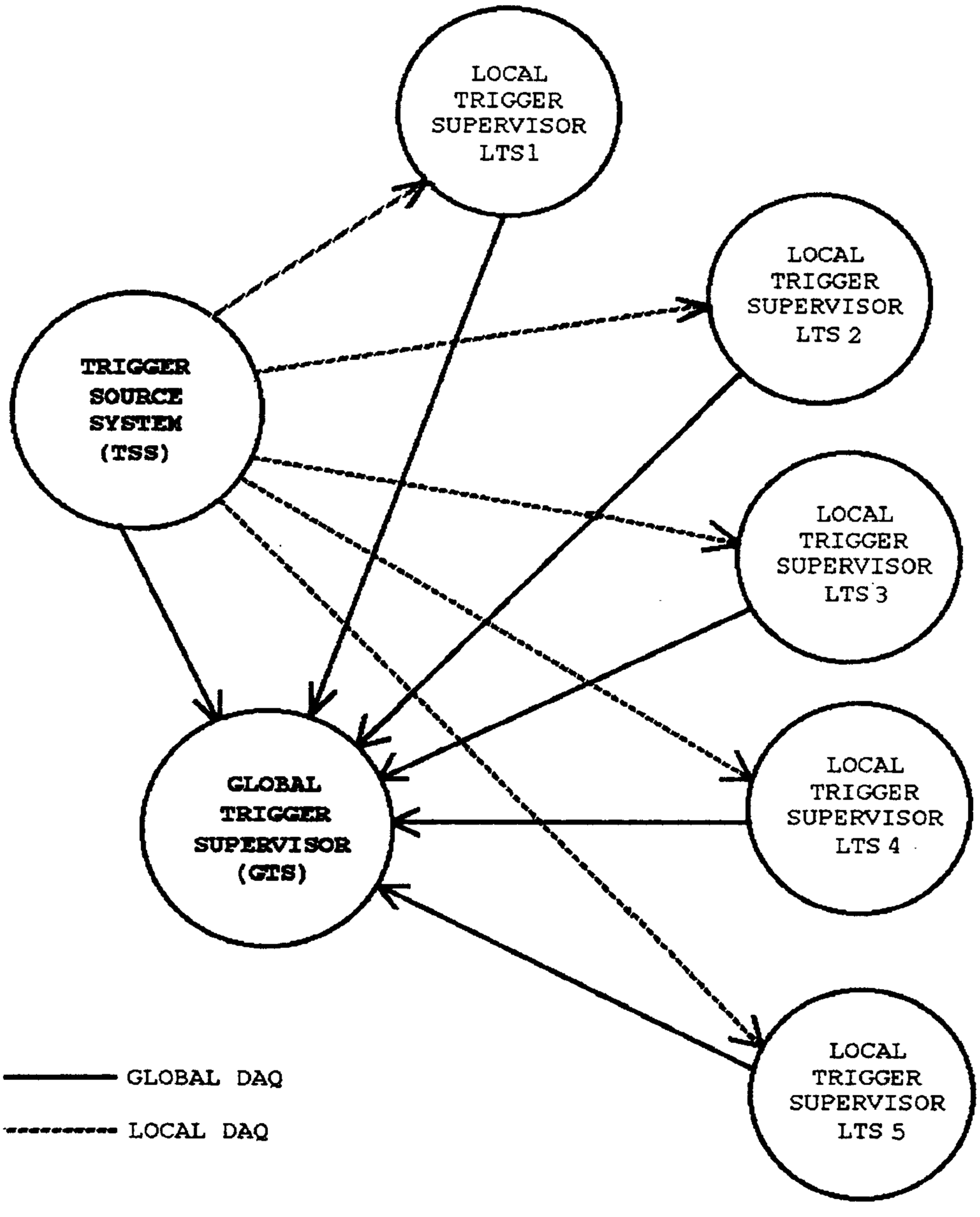

Figure 6.3: Diagram of the links among the Trigger Source System (TSS), the Global Trigger Supervisor (GTS) and the Local Trigger Supervisor (LTS).

Chapter 7

DAQ SYSTEM AND COMPUTER REQUIREMENTS

7.1 Data acquisition (DAQ) architecture

From the DAQ point of view, the experimental setup consists of several sub-detectors, each of them running almost independently.

As far as the number of electronics channel is concerned, the FINUDA detector can be divided in the following parts (from the center to outside):

a) **ISIM and OSIM**
   $\approx$ 40.000 channels;

b) **LMDC*s* and ST**
   $\approx$ 5.000 channels;

c) **TOFINO and TOFONE**
   $\approx$ 200 channels.

The trigger can be considered as a particular sub-detector, since the associated electronics regards essentially the setup procedure. It does not contribute significantly to the event size.

The FINUDA on-line architecture is devised to enable a centralized DAQ, as well as independent data taking for each sub-detector.

The modularity and complexity of the apparatus are taken into account in the DAQ system by a distributed architecture, with a high level of parallelism, adopted in order to cope with the big amount of raw data.

The system requires amplitude and/or time measurements in the channels. It also requires fast logic signals from the scintillators.

The general DAQ scheme is shown in fig. 7.1 and fig. 7.2. In order to allow fast data acquisition and reductions, microprocessors will be used on the various sub-detectors.

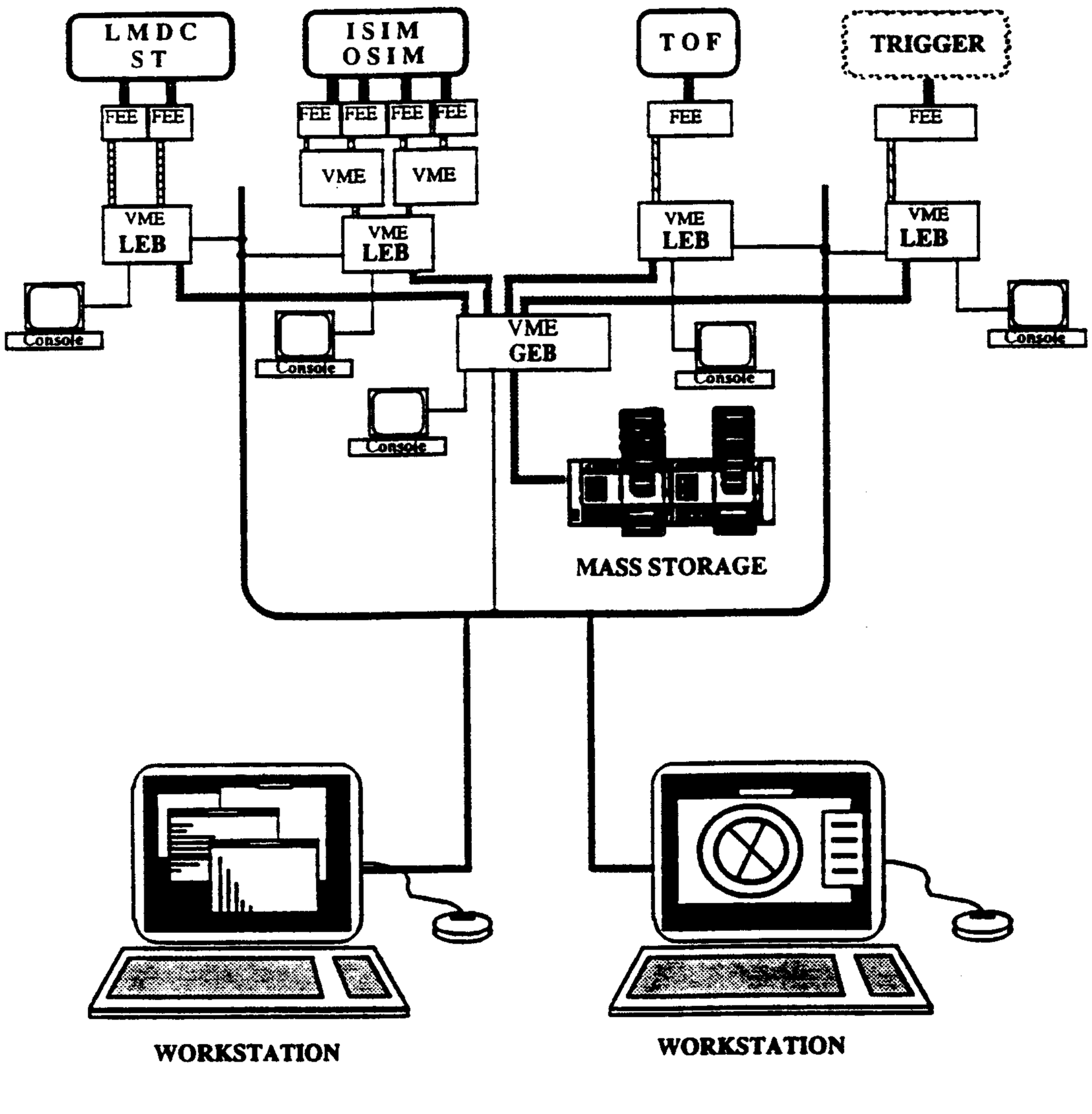

Figure 7.1: General data acquisition scheme.

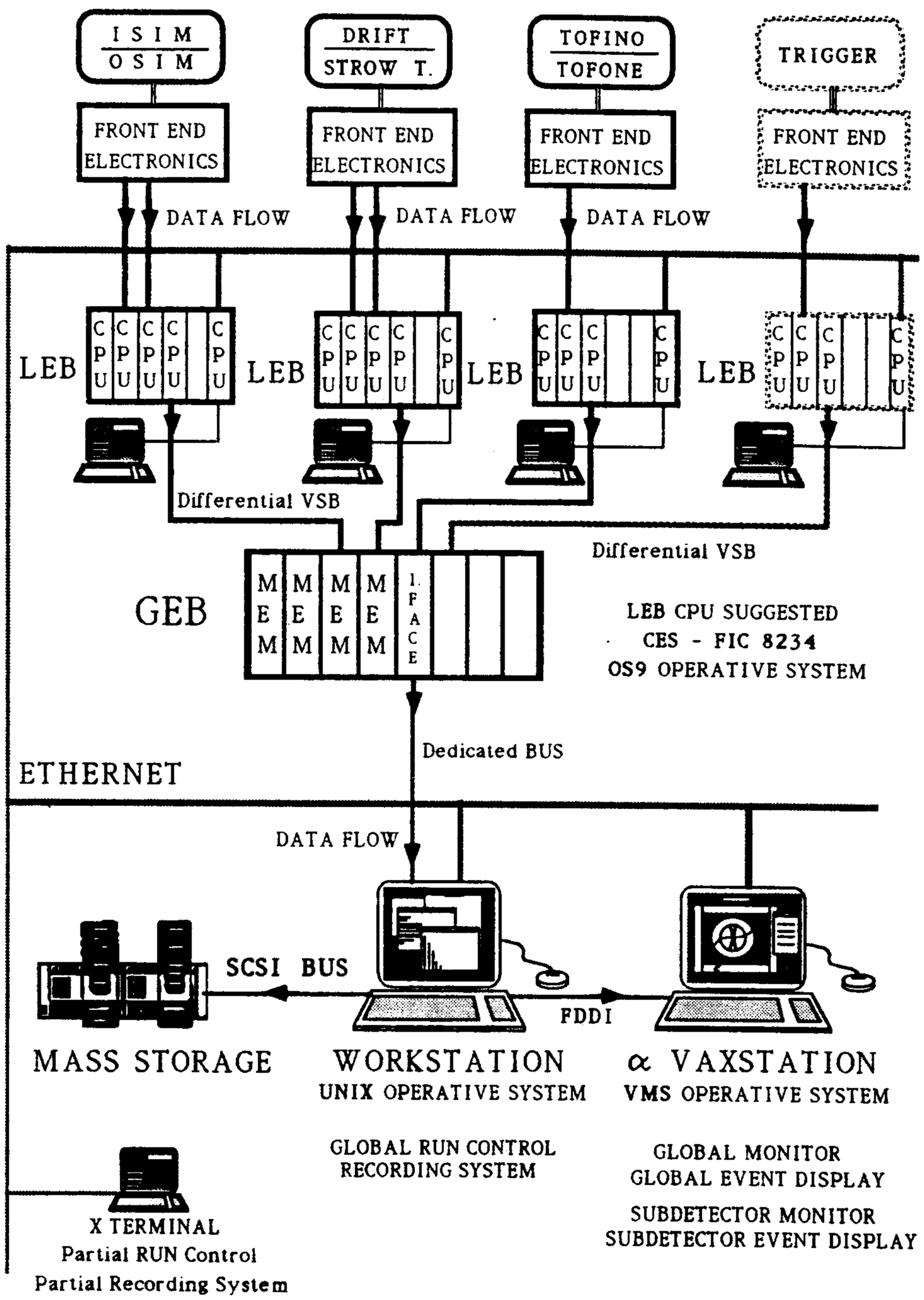

Figure 7.2: Data acquisition architecture.

All the signals coming from the front-end electronics (FEE) of each sub-detector will be read in a parallel mode by one or more VME CPU*s* in order to reduce the overall dead time. Trigger interrupts are seen directly by the microprocessors.

For each sub-detector, one (or more) dedicated VME CPU*s*, called Local Event Builder (LEB), assemble(s) all the information in a sub-event and perform(s) the local monitoring.

The LEB tasks are essentially:

a) sub-event acquisition for each sub-detector;

b) monitoring and calibration of the sub-detector, setup and reset of the associated electronics;

c) status display of the sub-detector components;

d) test and control of the sub-detector.

The LEB computer configuration of each VME crate will be:

a) one MOTOROLA 68040 type CPU for acquisition purposes;

b) one MOTOROLA 68040 type CPU for monitoring purposes;

c) mass storage disks that can be located directly on the VME crate or linked via Ethernet (NFS, Network File System) to the master CPU;

d) Ethernet link.

The sub-events are written, using VSB connections, in memory boards (one for each sub-detector) located in a VME crate, where they are read by a UNIX workstation (IBM PowerPC 601) connected to VME by a special bus adaptor.

The workstation performs the Global Event Building (GEB) task and writes the full event on mass storage devices. At the same time it performs the run control sessions sending and receiving commands via Ethernet.

More than one GEB and run control sessions can run at the same time with different triggers. Let's give an example: let's suppose that it is needed to calibrate TOFINO and TOFONE using laser , while calibrations are needed for the tracking system using cosmic rays. Then two different GEB and run-control sessions can be started at the same time, one from the workstation monitor, the other one from a remote X-terminal. Two different triggers and mass storage devices can be selected.

With this solution the sub-detectors are not requested to have their own private data taking, because they can set up a special GEB and run-control session (when the global acquisition does not run).

The global monitoring and the event display are in charge of one (or more) ALPHA vaxstation running Open-VMS. When the operator wants to see an event, he sends a request to the GEB by the Ethernet link. The GEB sends back the event using an FDDI connection, not to overload Ethernet, what could turn to be a bottleneck.

This structure will allow to use the off-line reconstruction software also at the on-line stage and guarantee an easier maintenance of the programs. The main characteristics of the data flow are:

a) **ISIM and OSIM**
Zero suppression performed by front-end electronics or readout CPU*s*
Sub-event buffer length: $\sim$ 400 *words* (800 *bytes*);

b) **LMDC*s* and ST**
Zero suppression performed by front-end electronics or readout CPU*s*
Sub-event buffer length: $\sim$ 150 *words* (300 *bytes*);

c) **TOFINO, TOFONE and trigger**
Zero suppression performed by front-end electronics
Sub-event buffer length: $\sim$ 100 *words* (200 *bytes*).

The global buffer length should be of the order of 1.5 $Kbytes$.

An estimate of the global event acquisition rate can be obtained taking into account the different steps in the data acquisition: trigger, conversions, interrupts, readout and zero suppression, event building and data storage.

Taking into account the high degree of parallelism of the acquisition, the standard hardware now available ensures at least an acquisition rate of $\sim$ 100 Hz.

This limit is mainly due to the readout and zero suppression of ISIM and OSIM and to the transfer rates of the standard storage media. This rate could be enhanced by a suitable event packing.

Concerning the problem of the data storage, the situation is rapidly evolving. Several new solutions for disk and tape sub-systems have been recently proposed and we are evaluating which could fulfill at best our needs.

7.2 Off-line computing resources

All the off-line programs have been developed in Fortran in VMS environment. Anyway the code has been written keeping in mind the possibility of an easy transportation on UNIX machines.

At present the machine used to develop and to run simulation and reconstruction algorithms is a DEC Vax-station 4000/90, equipped with 64 $Kbytes$ of memory, running VMS. On such a machine $\sim$ 4 s of CPU time are required to simulate the most complex FINUDA event, that is a K^+K^- decay of ϕ, followed by the interactions of the kaon pair inside the target: the first decays according the well known branching ratios, while the second is forced to form an hypernucleus, that afterwards decays in the (n,p) non-mesonic channel. The same event requires $\sim$ 0.1 s to be fully reconstructed.

Even if at present these performances could be considered rather satisfactory, we must consider that such a computer will become rapidly obsolete. So the natural choice for the FINUDA off-line computer seems to be represented by the new DEC ALPHA architecture, but there are no prejudicial reasons against other choices. At the same time we can substitute the Ethernet network with the FDDI one.

Chapter 8

PHYSICS PERFORMANCES

8.1 Apparatus simulation

As mentioned in the proposal of the experiment [1], the simulation of the FINUDA apparatus was performed in the framework provided by the CERN simulation package GEANT3 [2].

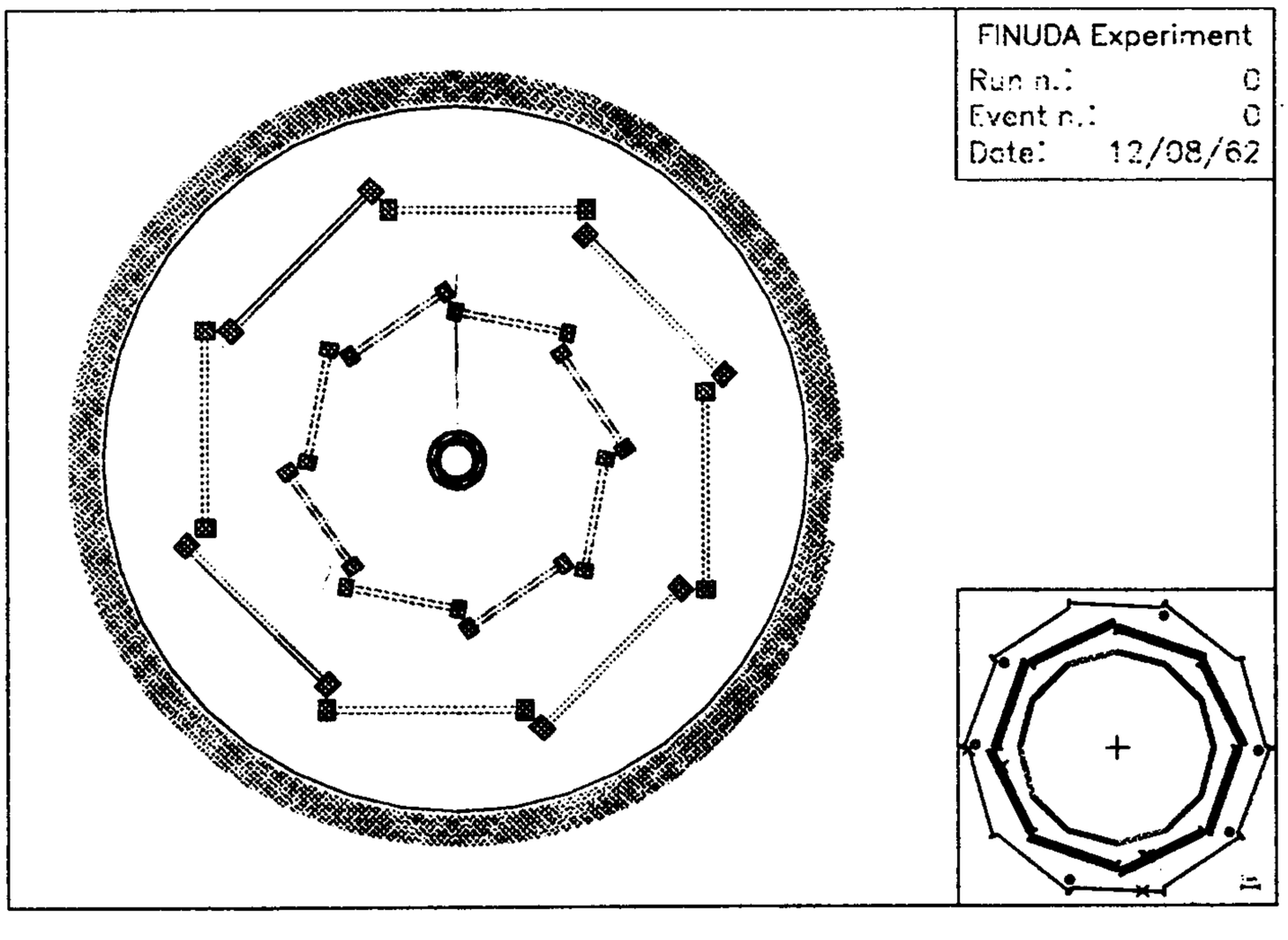

Figure 8.1: Front view of the new configuration of the FINUDA apparatus (only the first straw tubes double-array is drawn for simplicity). The inset shows the interaction region in more detail.

In this design stage the Monte Carlo simulation was mainly finalized to the evaluation, as realistically as possible, of trigger efficiency andrejection, spectrometer

acceptance and resolution and to their optimization. Moreover the simulated events, in terms of hits of the tracks in the sensitive volumes of the detectors, are used as input to the reconstruction and fitting processes which are, at present, under development.

All the relevant physical volumes of the apparatus, detectors structures and sensitive parts, as well as the mechanical supports interposed on the particle paths, were modeled with appropriate level of detail and different geometrical configurations were tested in order to optimize acceptances and resolutions.

The kinematics of the $e^+ + e^- \rightarrow \phi$ formation and the ϕ decay in the different decay channels was simulated using the GEANFI code [3], developed by the KLOE collaboration, whereas the kinematics of the formation and decay of the hypernuclei was generated in a dedicated process.

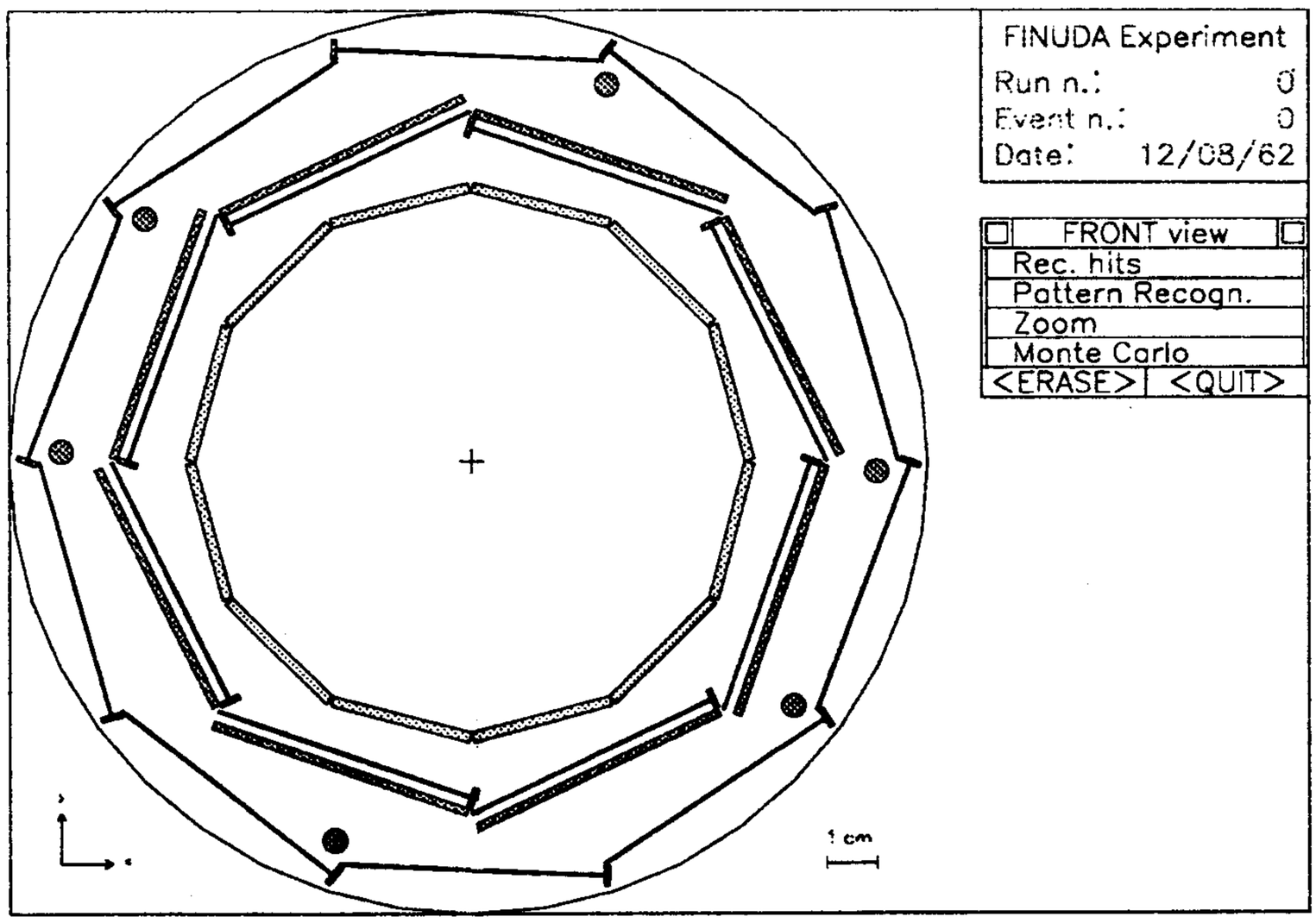

Figure 8.2: Zoomed view of the FINUDA apparatus central region. Note the new design of the target, segmented in 6 slices, placed in contact with the ISIM modules.

The particles produced in the ϕ decay and in the successive interactions are tracked through the various volumes of the apparatus by the GEANT3 tracking package. Energy loss in the different materials with Vavilov and Landau fluctuations, multiple scattering and decay of unstable particles, as well as electromagnetic interaction and showering of light charged particles and photons are taken into account by the tracking package.

In fig. 8.1 and fig. 8.2, respectively, the structure of the full apparatus and the details of the interaction region are shown as they are simulated in the Monte

Carlo program. This final design, which is the result of several tests of different configurations, optimizes the trigger efficiency, the acceptance and the resolution of the apparatus for hypernucleus formation events while keeping, at the same time, easiness of mechanical construction and care.

The simulation of the structure of the apparatus was performed with greater detail for the sensitive parts of the detectors, whereas the mechanical supports and structures are only schematically designed when they are relevant for the acceptance or transparency of the apparatus to the tracked particles.

In previous chapters the detailed description of the structure of the different detectors and their assembly were already given and it will be not reviewed here. We only remark that the main structural modifications relative to the original apparatus design [1] concern the shape of the target (fig. 8.2), whose cylindrical cross section was changed to octogonal in order to position the target material as close as possible to the ISIM microstrips. Moreover, the internal layer of drift chambers was rotated by 11 degrees around the axis of the apparatus. For the calculations presented in this section an octogonal Carbon target of 1.5 mm thickness was assumed.

As it will be better illustrated in the following, the change of the target geometry allows a better accuracy in the determination of the stopping point of the K^- inside the target (vertex position) and makes easier the mechanical construction and assembly of the interaction region. The rotation of the internal layer of drift chambers results in a 30% relative increase in the spectrometer acceptance.

8.2 Detector resolutions and spectrometer momentum resolution and acceptance

The performances of the different detectors in term of time, energy and spatial resolution were measured in tests performed with prototypes, as described in the previous sections, or assumed as a reasonable extrapolation of standard performances of the present technology.

The appropriate resolution functions were inserted in the Monte Carlo simulation of the apparatus as a smearing of the hits of the tracks on the sensitive parts of the detectors.

-) Internal scintillator array (TOFINO) (see Chap. 5.1):

A time resolution of 0.5 ns $FWHM$ is assumed, whereas the resolution on the signal amplitude is evaluated on the estimated gathering of 50 photoelectrons for minimum ionizing particles (pions) and 200 photoelectrons (4 times more) for kaons of 16.1 MeV coming from the ϕ decay.

-) Silicon microstrip detectors (ISIM/OSIM) (see Chap. 4.1):

A spatial resolution and detector granularity with $\sigma = 50$ μm along both the microstrip axes is assumed, whereas the resolution on $\Delta E/\Delta X$ of the kaons

is evaluated at 20% $FWHM$.

-) Low mass drift chambers (LMDC) (see Chap. 4.2):

The spatial resolution is assumed to be 100 μm in the direction octhogonal to the wire (ρ, φ plane), as obtained by the measurement of the drift time. A much coarse resolution ($\sigma \sim 1\%$ of the wire length) is obtained by charge division along the wire direction.

-) External scintillator barrel (TOFONE) (see Chap. 5.2):

The time resolution is assumed 0.5 ns $FWHM$ and within 5 cm $FWHM$ for the zeta coordinate obtained with a suitable treatment of the signals of the two PMs looking at the same scintillator slab.

-) Straw tube array (ST) (see Chap. 4.3):

A spatial resolution $\sigma \sim 100 \mu m$ is assumed in the radial direction (drift line direction) relative to the wire. No measurement of the coordinate along the wire direction by means of charge division is foreseen, since the charge division technique cannot provide the needed spatial resolution. In fact, in order to achieve the desired momentum resolution, at least two zeta coordinates (OSIM and ST) have to be measured with high spatial resolution; the OSIM microstrip provide a resolution of 50 microns while a resolution of the order of the millimeter is requested for the ST array. For this reason the zeta coordinate of the impact of the particle on the Straw Tube array will be determined fitting the particle path through the three straw tube super-layers. One of these layers is longitudinal and fixes the particle trajectory in the (ρ, φ) plane, the other two are tilted by 15 degrees each relative to the longitudinal direction and determine the position of flying path of the particle in the zeta direction. The resolution which can be reached using this technique was evaluated with Monte Carlo events and result of the order of 500 μm.

The momentum resolution of the spectrometer can be evaluated on the basis of well known standard formulae [4], usign the above spatial resolution, an evaluation of the radiation length of the different materials along the particle paths in the spectrometer, assuming the proper average length of the track and a homogeneous magnetic field of 1.1 $Tesla$.

The amount of material along the particle path is kept to the minimum in order to minimize the effect of multiple scattering. For these reasons the windows of the chambers are very thin and the tracking volume is filled with helium. As a result, the radiation length of the complete tracking volume is around 170000 cm to be compared with 570000 cm for pure helium and 30400 cm for air.

In fig. 8.3 a) and b) the $\Delta p/p$ $FWHM$ predicted resolution for pions is plotted versus the pion momentum at polar angles respectively of 90 and 50 $degrees$.

In fig. 8.3 a) the full line represents the total resolution, the dotted line represents the contribution from multiple scattering and the dashed line the contribution from

the helix fit of the track trajectory. The two contributions are summed quadratically. The dashed-dotted lines in fig. 8.3 b) represent the same contributions for the straight line fit in in the (z, s) plane where s is the path length along the track trajectory.

The plots show that for pions of 270 MeV/c the design momentum resolution of $0.2 - 0.3\%$ $FWHM$ is achieved by the present configuration of the apparatus. Besides, it appears that the momentum resolution is dominated by multiple scattering distorting effect and not by the uncertainty in the track fitting. Therefore the momentum resolution of the apparatus will not be critical under possible worsening of the spatial resolutions.

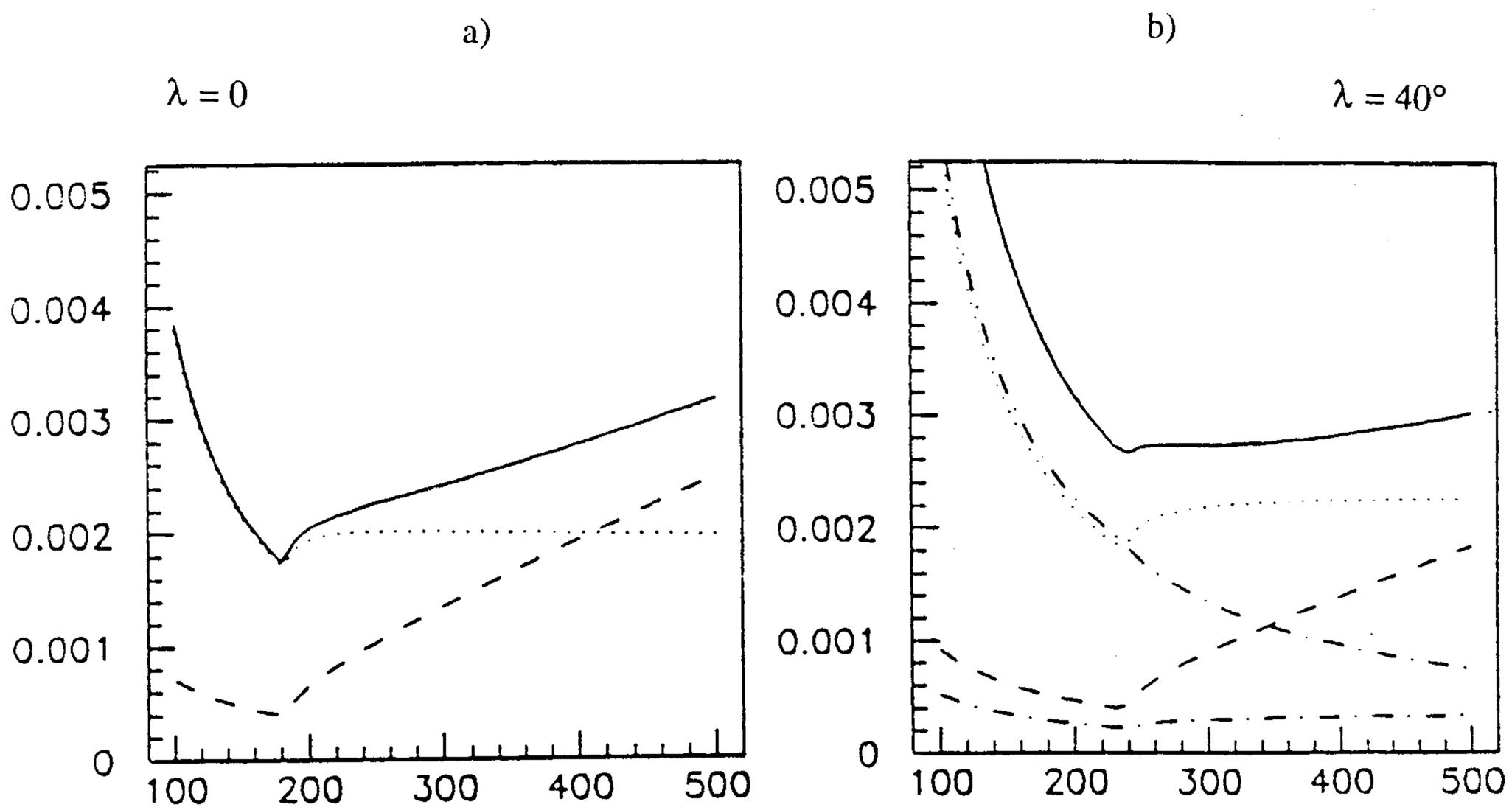

Figure 8.3: Comparison of the various terms that contribute to the spectrometer resolution as a function of the momentum (see text for further details).

The prediction of the standard formula for the momentum resolution was checked by simulating with the FINUDA Monte Carlo program populations of monochromatic pion and proton tracks starting from the external surface of the target and isotropically generated in space. The hits of the tracks with the different detectors are smeared with appropriate resolution functions and used to reconstruct the momentum of the particles by means of a helix fit procedure.

Figs. 8.4 and 8.5 show the reconstructed momentum distributions for pions of 270 MeV/c and protons of 416 MeV/c, respectively. In fig. 8.4 the reconstructed momentum distribution of the pions shows a peak around 270 MeV/c and a broad structure at lower momentum. This latter bump corresponds to the pions that have crossed the structure of the interaction region before entering in the tracking volume

and have lost a part of their energy (backward pions). The peak at 270 MeV/c represents the pions that have entered the spectrometer without crossing the target or the structure of the interaction region (forward pions).

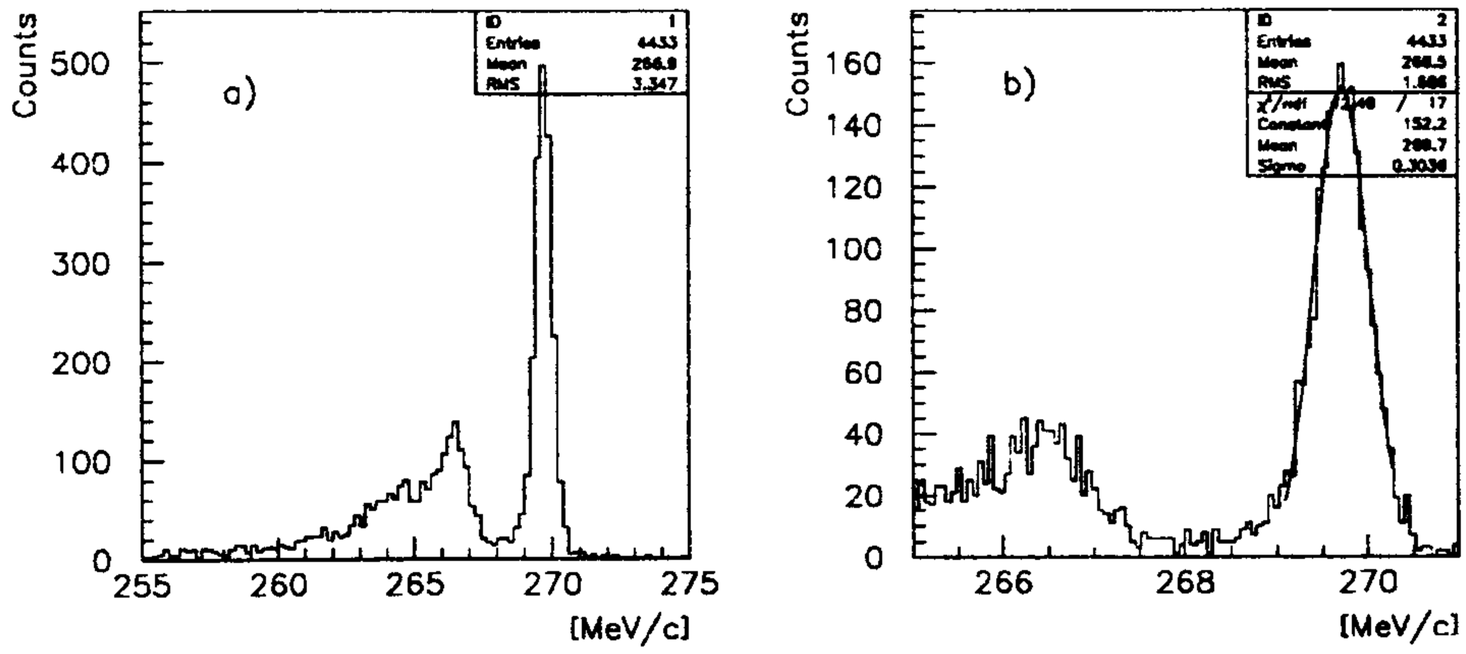

Figure 8.4: a) distribution of reconstructed momentum for pions coming out from the target surface; b) zoomed view of the spectrum beyond $264 MeV/c$. The fit of the peak around 270 MeV/c (the nominal value used in the simulation) allows to estimate the momentum resolution of the spectrometer

The width of this peak gives the momentum resolution of the spectrometer for a monochromatic pion of 270 MeV/c. This resolution is around 0.25% and has to be compared with the curves of fig. 8.3. The agreement is good if one considers that the Monte Carlo tracks are generated over the full solid angle.

Additionally, the number of tracks in the forward pion peak gives the information about the spatial acceptance of the spectrometer for the forward pions which are those useful for high resolution hypernuclear spectroscopy. This number takes into account the geometric acceptance of the spectrometer as well as the reduction in acceptance due to the mechanical structure of the chambers and their dead zones. This overall acceptance for forward pions amounts to 22%, 30% greater than in the previous configuration of the chamber internal layer. It is worth to remark that, in the absence of dead zones and mechanical structures in the two chamber layers the geometrical acceptance of the spectrometer for the forward pions amounts to about 28%.

In fig. 8.5 the same plots for a proton of 416 MeV/c are shown. The resolution for the proton tracks is 0.7%, worse that the for pions, since protons are subjected to more multiple Coulomb scattering deviations.

The present evaluation of the spectrometer resolution was performed with a homogeneous magnetic field and using a helix fit procedure for momentum reconstruction. In fact, the design magnetic field will not be completely homogeneous. However, the deviation from uniformity will be of the order of some percent and localized mainly at the edges or out of the tracking volume. In the final reconstruction

program a track fitting algorithm, which make use of a quintic spline interpolation of the track trajectory [5] and takes into account the non uniformity of the magnetic field, will be used. Several tests with Monte Carlo events and different forms of magnetic fields much more inhomogeneous than the one used by the experiment, demonstrated that the design momentum resolution is preserved when an accurate measurement of the magnetic field components (0.1%) is available.

To give an example, a population of pions of 270 MeV/c was tracked in the apparatus through a rather inhomogeneous magnetic field (up to 10% of the nominal value at the edges of the tracking volume for the three Bx, By, Bz components). In fig. 8.6 a comparison between the distribution of the momentum reconstructed with helix fit (a) and spline (b) algorithm is shown.

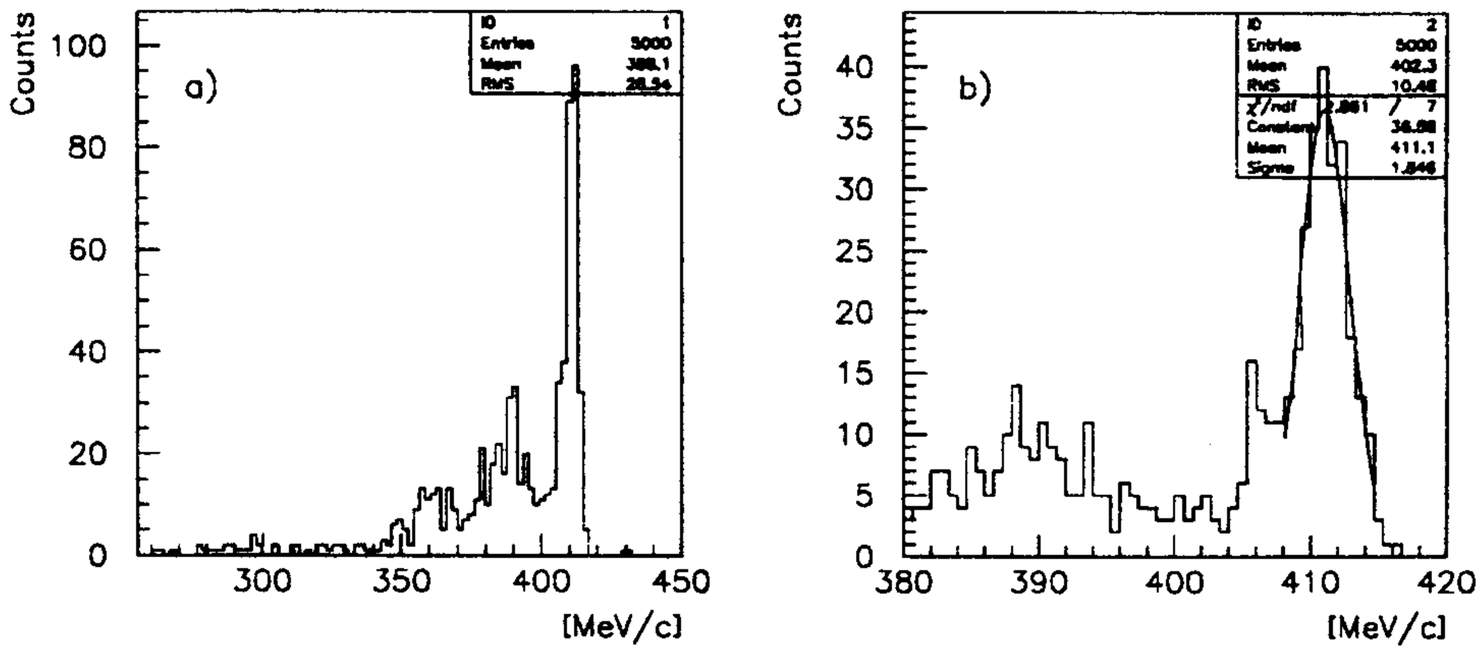

Figure 8.5: a) Distribution of reconstructed momentum for proton coming out from the target surface; b) zoomed view of the spectrum beyond $380 MeV/c$. The fit of the peak around 416 MeV/c (the nominal value used in the simulation) allows to estimate the momentum resolution of the spectrometer.

8.3 Trigger efficiency and background rejection

The goal of the trigger system is to select the $K^+ K^-$ decay of the ϕ formed in the $e^+ e^-$ collision from background events as Bhabha scattering, other ϕ decays and cosmic rays. Furthermore, the trigger system must select hypernuclear events where a prompt pion, coming from the hypernucleus formation, has crossed the tracking volume of the spectrometer.

It is worthwhile to recall that, at the top luminosity $\mathcal{L} = 10^{33}\ cm^{-2}\ s^{-1}$ the expected total rate for ϕ production is about 4.4 kHz and that, in the angular range covered by TOFINO, the Bhabha scattering cross section is some order of magnitudes lower than in the forward and backward directions. Rates of $(K^+ K^-)$ and $(e^+ e^-)$ will be then of the same order of magnitude (few kHz). Rates due to other ϕ decays are considerably smaller.

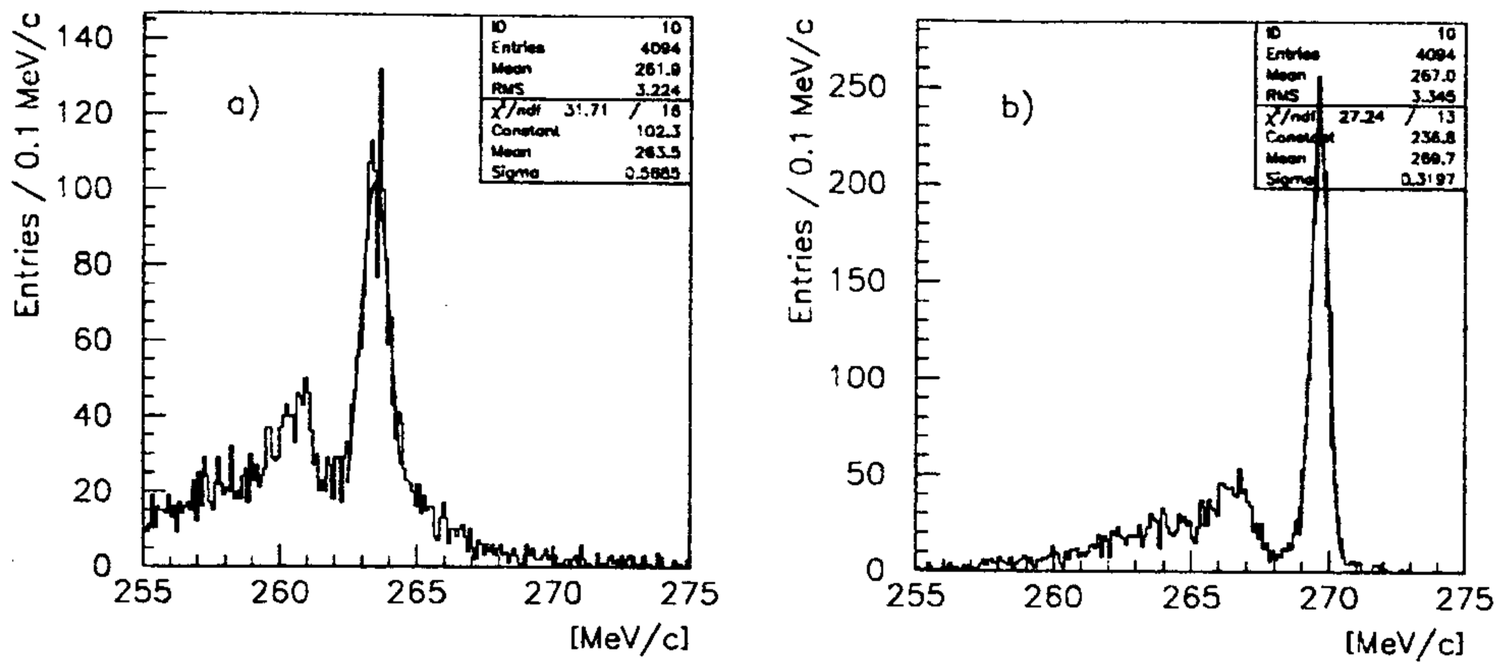

Figure 8.6: Comparison between pion momentum distributions reconstructed using a helix fit (a) and a spline algorithm (b). The particle was tracked in a quite inhomogeneous magnetic field.

For these reasons the simple request of multiplicity two in TOFINO is not enough. However, since there is a large separation between the energy lost by low energy kaons and by minimum ionizing particles (electrons, muons and fast pions) in the 2 mm thick TOFINO slabs, this information can be exploited to select with high efficiency the K^+ K^- from ϕ decay from the background reactions which produce light relativistic particles.

A further constraint can be provided by the request of a "back to back" topology in the interaction region, by simply requiring a coincidence between one TOFINO slab and the axially symmetric one or its two neighboring (extended back to back), in order to account for the curvature of the trajectory of K^+ K^- tracks and the uncertainty of the e^+ e^- interaction point. The latter is characterized in fact by a dispersion with a $\sigma = 2\ mm$ in the horizontal coordinate.

Once the K^+ K^- event has been recognized by means of amplitude discrimination on TOFINO signals and slab topology, the occurrence of a K^- interaction in the target with emission of a prompt pion crossing the tracking volume can be selected by the request of at least one fired slab of TOFONE within a narrow timing gate. It is worth to recall that muons of 236 MeV/c coming from the decay of the K^+ stopped in the target are delayed by the kaon mean life which is of about 12 ns.

In summary, the first level trigger is based on TOFINO and TOFONE and requires the coincidence of the following occurrence :

-) TOFINO

a) "extended" back to back topology (BTB)

b) energy lost above a fixed threshold

-) TOFONE

a) prompt coincidence $\leq$ 10 ns

b) multiplicity $\geq$ 1 (optional)

This trigger strategy has been extensively tested with Monte Carlo simulations. For the timing and amplitude resolutions of the scintillators the values quoted in Chap. 5 were adopted, and furthermore, being the crucial part of the trigger logic based on amplitude threshold discrimination, a possible fluctuation of the electronic threshold of 5% $FWHM$ has been assumed. In terms of energy lost in a single slab by the particles this corresponds to a fluctuation of 0.175 MeV for a threshold of 3.5 MeV.

To evaluate the trigger efficiency a population of hypernuclear formation reactions was simulated, in particular : a ϕ is formed from e^+ e^- collision; it decays in K^+ K^-; when the K^- is emitted into the acceptance volume and stops in the target an hypernucleus is formed and a prompt pion of 270 MeV/c is emitted; after that the hypernucleus decays in non-mesonic mode with a mean life of 0.3 ns emitting a proton and a neutron of 416 MeV/c.

Besides, several background reactions were simulated to evaluate the trigger rejection power.

The results of these calculations are presented in tables 8.1 and 8.2. In table 8.1 the results for the trigger efficiency are shown: the high angular acceptance of the TOFINO barrel and the large energy lost by kaons allows the selection of 75% of the K^+ K^- events which fulfill the topological and threshold conditions. The 25% loss is due to angular acceptance (12%) and decay in flight of the kaons (13%).

The dead zones in the interaction region, the limited solid angle coverage of the spectrometer for particles coming from the interaction region, and the timing gate, reduce the triggered events to 40%.

Table 8.1: Trigger efficiency for $\phi \rightarrow K^+ K^-$ + hypernucleus events

TOFINO $\equiv$ (energy loss * extended BTB)	75%
TRIGGER $\equiv$ TOFINO * TOFONE (prompt coincidence)	40%

It is worthwhile to recall that not all of the triggered events result useful for physics, since the trigger condition can be fulfilled by spurious events too. For instance, the prompt coincidence on one TOFONE slab can be provided by a fast muon from K^+ decay, whereas the pion from hypernucleus decay escapes from the spectrometer acceptance. A detailed analysis of the different classes of events within the triggered ones will be given below.

In table 8.2 the trigger rejection for background events is shown giving the expected rates for some processes; it appears that the trigger strategy allows an efficient background rejection. Within the different conditions imposed by the trigger logic

the most powerful one is, without any doubt, the threshold discrimination on the particle energy loss in TOFINO. In fact it is very unlikely that a couple of minimum ionizing particles coming from the background reactions can release as much energy in the scintillator slabs as a couple of slow kaons coming from the ϕ decay.

Table 8.2: Background events accepted by the trigger

Bhabha scattering	$< 10^{-2} Hz$
$\phi \rightarrow K_S\ K_L$	$< 10^{-1} Hz$
$\phi \rightarrow \rho\ \pi$	$< 10^{-2} Hz$
$\phi \rightarrow \pi^+\ \pi^-\ \pi^0$	$< 10^{-3} Hz$

As noticed above, within the class of triggered events only a subsample corresponds to "useful events", that is events in which the K^- stops in the target, forms the hypernucleus and produces a negative pion which gives the prompt coincidence in TOFONE and deposits hits in the four detectors of the spectrometer (OSIM, two LMDC and ST). Four hits are considered the minimum needed to obtain the best recognition of the track and resolution in momentum. For tracks with 3 hits, recognition and track fitting are possible as well, but with lower quality warrant and worse momentum resolution.

Among the 40% triggered events, 25.5% are useful ones, whereas for 7.5% of them the negative pion gives the prompt coincidence but has less then 4 hits, having hit a structural part. For 7.0% of them the negative pion is out of the acceptance and the prompt coincidence is given by another particle (positive muon, in general).

Finally, half of the 25.5% useful events have forward pions and can be utilized for high resolution hypernuclear spectroscopy.

8.4 Pattern recognition and event reconstruction

The pattern recognition process of the FINUDA apparatus is mainly aimed to the identification, within the events selected by the trigger, of the "useful events" that is the ones in which the stop of a K^- in the target is followed by the emission of a prompt pion crossing the four detector layers of the spectrometer. The measurement of the momentum of the pion emitted from the K^- interaction allows the hypernuclear spectroscopy studies.

Additionally, other charged and neutral products of the interactions or decays such as protons and neutrons from the hypernucleus decay or muons and pions from the K^+ decay, may be recognized in order to perform measurements of the lifetime of the hypernucleus or simply for detector calibration.

The efficiency of this pattern recognition process can greatly affect the capability of the experiment to efficiently separate hypernuclear events from spurious ones and

to utilize at the best the potentiality of the machine and of the apparatus.

The worry is justified, to a greater extent, by the fact that, in order to reduce, as much as possible, the amount of materials along the particle paths, the redundancy of the track position sampling within the spectrometer is reduced to the minimum.

For this reason Monte Carlo simulated events were used to develop and test a number of pattern recognition and event reconstruction procedures designed to fully exploit the information on the event recorded by the FINUDA detectors.

To this aim a first version of the reconstruction program for the apparatus was written, which performs the following tasks:

a) Read in, from the Monte Carlo events, of the description of the hits of the tracks in the different detectors (Raw Data Tape). The hits were smeared by proper resolution functions.

b) Read in, from the Monte Carlo program, of the geometry and material composition of the detectors and structures in the apparatus. Being the reconstruction program based on the GEANT package, the GEANT/GEANE [6] environment can be exploited to perform tracking and back-tracking of particle trajectories through the apparatus volumes, with calculation of energy lost and error matrix transport, with great easiness and accuracy.

c) Management of a data base for the hits in the detectors, reconstructed event structure and calibration data, based on the ZEBRA package.

d) Supply of an user interactive interface, additional to the batch mode, based on the KUIP package [7], as well as of an event display process based on Xwindow/GKS package. The event display is able to show to the user the Monte Carlo generated event, the hits in the detector and the results of the reconstruction process at the same time. The pattern recognition and reconstruction strategies can be tested event by event and adapted to the particular features of the apparatus and to the characteristics of the event topology under study.

e) Connection of the pattern recognition process to the track fitting procedures.

f) Production of a data summary tape containing the results of the reconstruction in terms of recognized topology, interaction and decay point position (K^- and K^+ stopping points in the target) and directions and momenta of the tracks, in the form of ZEBRA banks and PAW n-tuples.

In the following, a short description of the pattern recognition strategy adopted in the first version of the reconstruction program is given, as well as the results concerning its efficiency.

For typical hypernuclear events (useful events) the pattern recognition flow is organized in two successive steps:

a) Identification of the "beam" K^+ K^- couple which crosses the interaction region and deposits hits in two opposite TOFINO slabs and in two correspondent ISIM microstrips. Reconstruction of the "beam" trajectory in the space and extrapolation of the K^- and K^+ tracks inside the target to estimate their stopping points. (Interaction Vertex and K^+ decay point, respectively)

b) Identification, inside the spectrometer, of the helical trajectories which start from one hit in OSIM and cross the other three detector layers of the spectrometer (two LMDC and ST) and possibly TOFONE. These helical trajectories, if they correspond to physical tracks, are connected with the K^- or K^+ stopping points too. For "backward" tracks which cross the interaction region before entering into the spectrometer, the additional hits in the internal detectors (ISIM and TOFINO) are placed near the helical trajectory too. The little amount of material interposed inside the tracking volume and the uniformity of the magnetic field largely allows to approximate the particle trajectories as helices, at least for pattern recognition purposes.

The low level of background and the high rejection power of the trigger allows to expect clean events and promise a high efficiency for the pattern recognition process, in spite of the limited number of hits available.

Tracks with only three points can be identified and reconstructed as well, but with worse recognition quality and momentum resolution. The recognition of the "beam" and, consequently, the reconstruction of the Vertex is considered, on the contrary, essential to validate an useful event and to allow the identification of "backward" and "forward" tracks.

Moreover, the reconstruction of the Interaction Vertex allows the correction of the negative pion momentum, for the energy lost in the already thin target and leads to the best performances the momentum resolution of the apparatus.

8.5 K^+ K^- "beam" identification in the interaction region

The recognition of the K^+ K^- beam in the interaction region starts from the two back to back TOFINO slabs in which the signal amplitude has overcome the requested threshold and triggered the acquisition of the event. Assuming that these two slabs have been fired by kaons from the ϕ decay, the hits of these kaons in the ISIM microstrips in the angular region subtended by the two slabs are searched for.

In fig. 8.7 the interaction region for a typical hypernuclear event is shown; the two TOFINO back to back slabs and the hits of the K^+ K^- beam on ISIM are indicated. They can be distinguished from other hits on ISIM, in the same angular region (see the proton hit near the K^- one), using the information on specific energy loss provided by the Silicon microstrip detector. The $\Delta E/\Delta x$ of the stopping Kaon (average energy at the incident point on ISIM $\sim$ 12 MeV) is $\sim$ 1.5 MeV,

around 4 times the minimum ionizing one. A specific energy loss resolution around 20% $FWHM$, assumed for the Silicon microstrip detectors, results to be largely sufficient to separate the hits produced by slow kaons from those by other particles produced in the interactions.

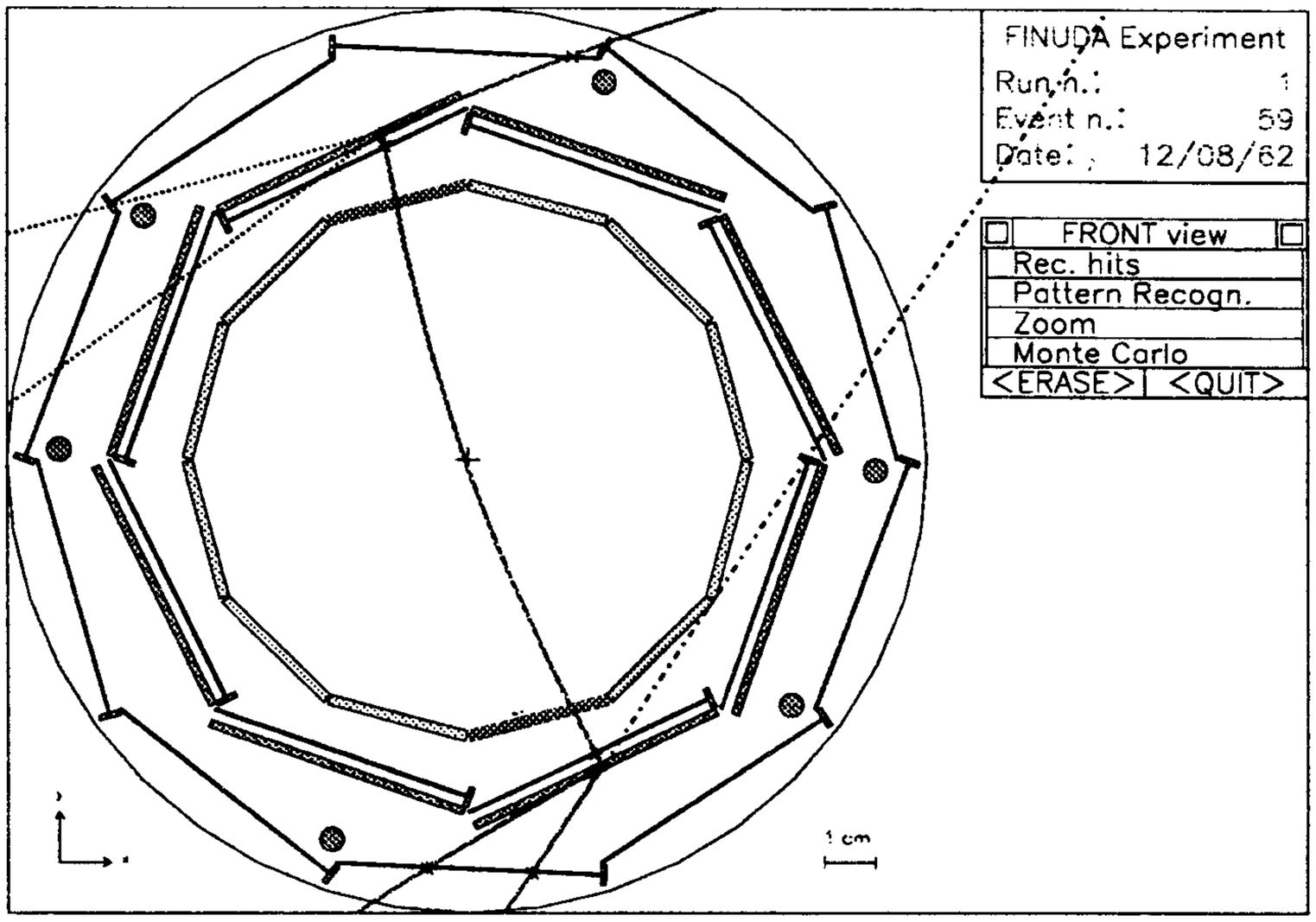

Figure 8.7: A typical FINUDA event: zoomed view of the central part of FINUDA apparatus showing the K^- and K^+ interacting in the target.

Monte Carlo calculations using hypernuclear events with a proton–neutron decay of the hypernucleus, demonstrated that the efficiency for this separation is around 96%.

Once the hits of the beam tracks on ISIM have been recognized, the trajectory of the K^+ K^- couple inside the interaction region can be reconstructed imposing that a helical trajectory corresponding to a nominal momentum of the kaons crosses the two hit points. Having measured, in each point, the three spatial coordinates (x, y, z) with high spatial resolution, this is enough to determine completely the beam trajectory, apart from an ambiguity on the sign of the radius of curvature or, in other words, on the concavity of the curve.

This ambiguity can be easily solved comparing the two alternative trajectories with the e^+ e^- interaction region ($\sigma = 0.2\ cm$ in the horizontal plane and $\sigma = 0.002\ cm$ in the vertical one). The true beam trajectory must cross this region in the e^+ e^- annihilation point. The rare cases for which this ambiguity survives are solved by checking the sign of the particles emitted in the kaon interactions or decay in the target.

The efficiency of this beam identification process was estimated to be $\sim$ 99%

of the K^+ K^- couples which have hit the ISIM microstrip and stopped inside the target.

When the beam trajectory is reconstructed, the stopping position of the K^+ and K^- in the target can be estimated by simple extrapolation of the trajectory to the target, taking into account energy loss in the interposed materials. This task can be easily accomplished by the GEANE tracking package which accounts accurately for the geometry and characteristics of the crossed volumes. The accuracy in the determination of the kaon stopping points with such a method is estimated in some hundreds of microns.

Factors affecting this accuracy are the the fluctuation of the energy loss and the deviations of the kaon trajectory from a helix due to the energy loss and the multiple scattering in TOFINO and ISIM.

To reduce as much as possible this latter effect, which is the most important one, in the new geometrical configuration the target was positioned as close as possible to the ISIM microstrip surface, where the crossing positions of the tracks are measured.

8.6 Track identification inside the spectrometer

The pattern recognition of the tracks produced by the kaon interaction and decay in the target is largely based on the recognition of circular trajectories in the plane orthogonal to the axis of the apparatus, trajectories that start from the target region and cross the sensitive volumes of the different detectors sufficiently close to the projection of the hit points on the same plane. As already mentioned, the uniformity of the magnetic field is sufficient to allow the use of a helix approximation for the track trajectories.

In addition, the simple topology of the searched events and the minimum redundancy of the track position sampling (average number of hits or clusters per event $\sim$ 24) make the use of a simple local pattern recognition method (road method) more appropriate and economic than global pattern recognition methods like the inverse conformal transformation method [8] often used to recognize circular paths with a common origin.

The tracks searched for are supposed to start from one of the two kaon stopping points in the target (vertices) and must cross the sensitive parts of OSIM, internal LMDC, external LMDC, ST (in the order) and possibly ISIM for backward tracks.

Hence the pattern recognition process starts the analysis of the hits considering one hit in OSIM detector. After that it constructs one circle from every possible combination of this hit and two hits in the two LMDC arrays. Since the measurements of the coordinates in the transversal plane is very accurate for the three mentioned detectors, the combination of three hits coming from a true track corresponds to a circular trajectory passing very close to one of the two vertices and close to the hit of the longitudinal straw tubes when they are fired by the track. This first request on the alignment on a circular path of three hits with one of the two vertices and

the ST defines a track candidate to be submitted to further tests.

The OSIM detector provides an accurate determination of the z (longitudinal) coordinate of the hit, while the z coordinate of the vertex is estimated with a good precision by kaon track extrapolation. The two LMDCs provide a coarser accuracy in zeta determination (1% of the wire length). However, the check of the alignment of the z coordinates of these four points along a straight line in the (z, s) plane (s is the path length along the track) is very useful in resolving possible ambiguities and mainly in rejecting spurious candidates.

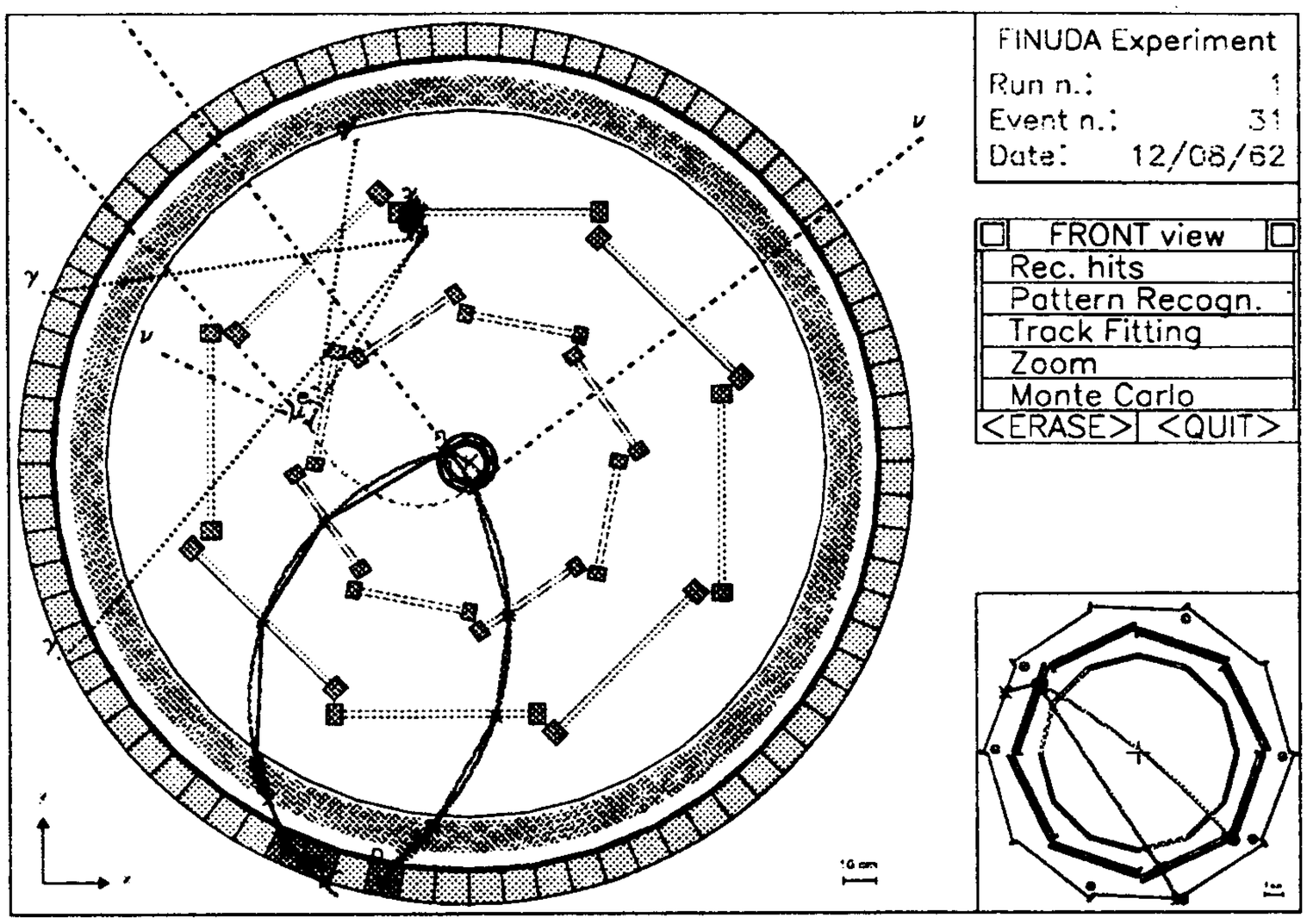

Figure 8.8: A typical FINUDA event: the hypernucleus formation is followed by a n-p non-mesonic decay. The poly-lines superimposed to the Monte Carlo particle trajectories represent the results of the pattern recognition algorithms.

When one track candidate fulfills the requested conditions within tolerances depending on the assumed spatial resolutions, it is validated as a good track and connected in the event structure to the corresponding vertex. The corresponding hits are discarded from the input data structure and no longer considered in the search for track candidates. Additionally the circle parameters provide a first estimation of charge, momentum and direction of the validated track. The process is then repeated for all other hits on OSIM looking for good candidate tracks; residual hits are considered as noise or submitted to search for track candidates of lower quality.

Good candidate tracks may have four measured points (OSIM,LMDCs,ST) if they cross the ST array or three measured points, if not. In the latter case the track may have escaped the tracking volume acceptance or may have such a low

momentum that spiralizes inside the spectrometer; in this case other corresponding hits in the LMDC layers are searched for and connected.

For backward tracks possible hits on ISIM and TOFINO are searched for, as well as hits on TOFONE for both backward and forward tracks. It is worth to remark that once the track has been validated and connected to the corresponding vertex, it becomes possible to distinguish backward from forward tracks.

In fig. 8.8 a hypernuclear event fully recognized by the pattern recognition process is shown; the Monte Carlo tracking is superimposed to the pattern recognition information which is given by poly-lines connecting the hits of each track candidate.

A process of pattern recognition has been developed for the ST array in order to associate longitudinal and tilted (stereo) clusters of ST, fired by the same track and a first version of this process has been tested on Monte Carlo events. The efficiency of the process is rather high, in fact the correct cluster association can be done in about 85% of the cases, without any reference to information from the internal detectors. This is made possible by the simplicity of the triggered events, the expected low level of physical noise and the high granularity of the ST array. The event of Fig. 8.8 shows the great separation of the clusters on the ST array. The worst effect on the ST resolution is given by spiralizing muons or pions coming from K^+ decay or by showering of photons which fire entire sectors of the ST array.

Moreover, the association of longitudinal and tilted straws allows an estimation of the z–coordinate of the hit on the ST array; the accuracy of this estimation is around 1.5 cm. Hence, when the pattern recognition on the ST array has been successfully accomplished before the pattern recognition in the tracking volume, an additional check on the z–coordinate estimated on the ST hit can be performed and provide a better constraint for the validation of the track.

The first version of the pattern recognition process of the FINUDA apparatus was tested on Monte Carlo events and provides an efficiency larger than 95% for tracks crossing the full spectrometer. As expected, the efficiency is very high and the process is not time consuming. Being this the first version of the process, both efficiency and economy can be improved by more clever and refined algorithms.

The reliability of the algorithm in presence of a high level of noise on the detectors is at present under study. First tests show that, owing to the high accuracy of the spatial positions on the detectors, it is unlikely that spurious hits can contaminate a true track or even create a fake track.

8.7 Track fitting and momentum reconstruction

As mentioned before, the track fitting process is accomplished by a helix fit process or by an efficient spline algorithm; OSIM and LMDCs provide measurements of the three spatial coordinates though with less accuracy for the zeta coordinate when the LMDCs are concerned. Besides, reconstructed hit coordinates for the LMDCs in the (ρ, φ) plane depend slightly on the incident angle of the track. This dependence

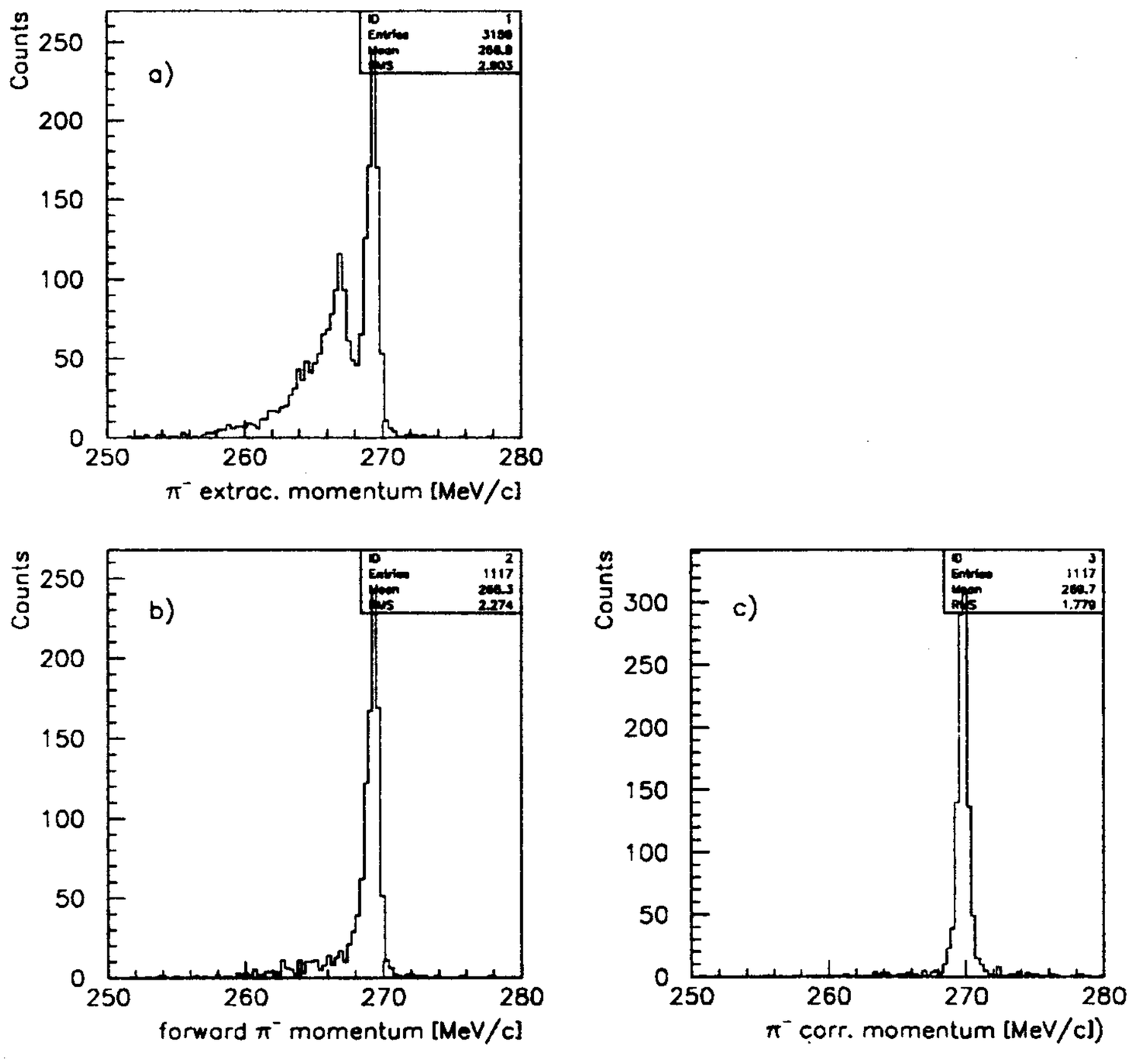

Figure 8.9: The sequences of plots shows the capability of selecting the "useful events" (b) and of correcting the π momentum for the energy lost in the target (c), starting from the global spectrum (a).

will be accurately taken into account in the final fit procedure.

The accurate determination of the longitudinal coordinate for the ST array will be performed by fitting the extrapolation of the track trajectory through the hit stereo tubes; this is done by minimizing the sum of the squares of the differences between :

a) the distance of the trajectory (helix) from the wire of a hit tube;

b) the distance from the same wire corresponding to the product of the drift time and the drift velocity.

First tests of this procedure with Monte Carlo events allow to estimate that the accuracy in the determination of the z coordinate for the ST array is of the order of 500 μm.

In fig. 8.9 a) the reconstructed momentum distribution of a negative pion of 270 MeV/c coming from hypernuclear formation is shown; the spatial resolution of the detectors are those mentioned above. The peaks at lower energy are generated by pions crossing the interaction region structure; they are much more evident that those of fig. 8.4 a) since in that case the pion was generated on the external surface of the target. In the present case, on the contrary, the pion in generate inside the target in the K^- stopping/interaction point, and loses a little but variable part of its energy crossing the target before entering in the spectrometer. The resulting resolution on the peak of forward pions is worsened. In fig. 8.9 b) only the forward pions are selected, cutting on the direction of the pion relative to the position of the vertex; only the forward pion peak survives the cut and show a momentum resolution of 0.3%.

Finally in fig. 8.9 c) the forward pion momenta are corrected as follows. The distance between the reconstructed vertex position and the extrapolation of the pion trajectory on the target is evaluated; this distance estimates the path of the pion in the target material and the evaluation of the energy lost by the pion in the target became possible. This value of the energy lost is used to correct the value of the pion momentum measured by the spectrometer. The resulting distribution is shown in fig. 8.9 c); the peak is now centered around 270 MeV/c and its width correspond to the nominal resolution of 0.25%.

8.8 Hypernuclear spectroscopy resolution

Given the performances illustrated above for the resolution of the different detectors, the pattern recognition and event reconstruction, it is possible to use Monte Carlo simulated events to estimate the resolution and sensitivity of detection of hypernuclear levels in presence of a physical background. As an example, a Monte Carlo calculation was performed in which the K^- originated by the ϕ decay and then stopping in the target, generates a spectrum of negative pions similar to the ones of fig. 1.1, which is a typical spectrum obtained at KEK with a $(CH)_{12}$ target.

The only difference is that the two peaks at 273 and 261 MeV/c were generated as monochromatic lines in the same proportion, relative to the background, as the areas of the two peaks relative to the area of the full spectrum, as seen by fig. 8.10. They correspond to the standard capture rate of 10^{-3}/stopped K^- respectively. Furthermore two additional peaks at 265 MeV/c and 270 MeV/c have been generated corresponding to capture rates of $2 \cdot 10^{-4}$ and 10^{-4} stopped k^- respectively. They would correspond to the excited states at $\sim$ 2.6 MeV and 6.8 MeV in ${}^{12}_{\Lambda}C$, observed with the (π^+, K^+) reaction in flight (see fig. 1.2

The simulated Monte Carlo spectrum was then passed through the full chain of programs described in this Chapter and the final results are shown in fig. 8.11, where the two peaks at 10^{-3} stopped K^- are clearly visible over a flat background, with a resolution and a signal / background ratio as expected and anticipated in Chapter 1 and the peaks at 10^-/ $stoppedk^-$ can still be distinguished from the background. Concerning the expected counting rates, we may finally obtain the following evaluation. At $\mathcal{L} = 10^{32}\ cm^{-2}\ s^{-1}$ we expect $\sim 216\ K^- s^{-1}$; for a production rate of hypernuclei of $10^{-3} K^-_{stopped}$ we expect then 2.16×10^{-1} hypernuclear states s^{-1}. The trigger efficiency is 0.255 and the reconstruction one is 0.95. Furthermore, we have to take into account the circumstance that only the forward pions are useful for fine spectroscopy (a factor ~ 0.5) and that the total transparency of the LMDCs is 0.8. The final rate is then 2.09×10^{-2} hypernuclear states s^{-1}, corresponding to 75 h^{-1}: it means that the spectra shown in fig. 8.11 would be obtained in $\sim 7\ h$ at $\mathcal{L} = 10^{32}\ cm^{-2}\ s^{-1}$, in $\sim 1\ h$ at $\mathcal{L} = 10^{33}\ cm^{-2}\ s^{-1}$, a quite impressive result.

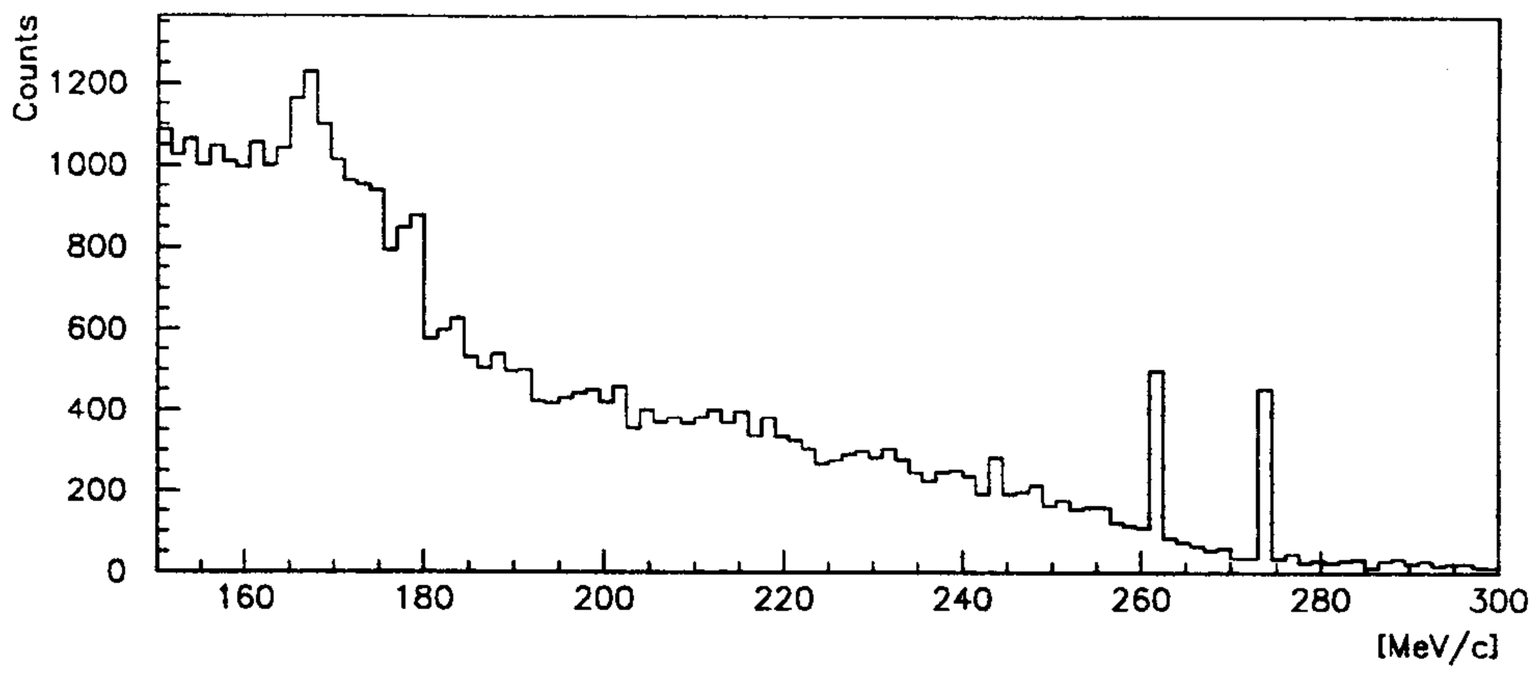

Figure 8.10: Simulated π^- momentum spectrum used as input for the FINUDA Monte Carlo program.

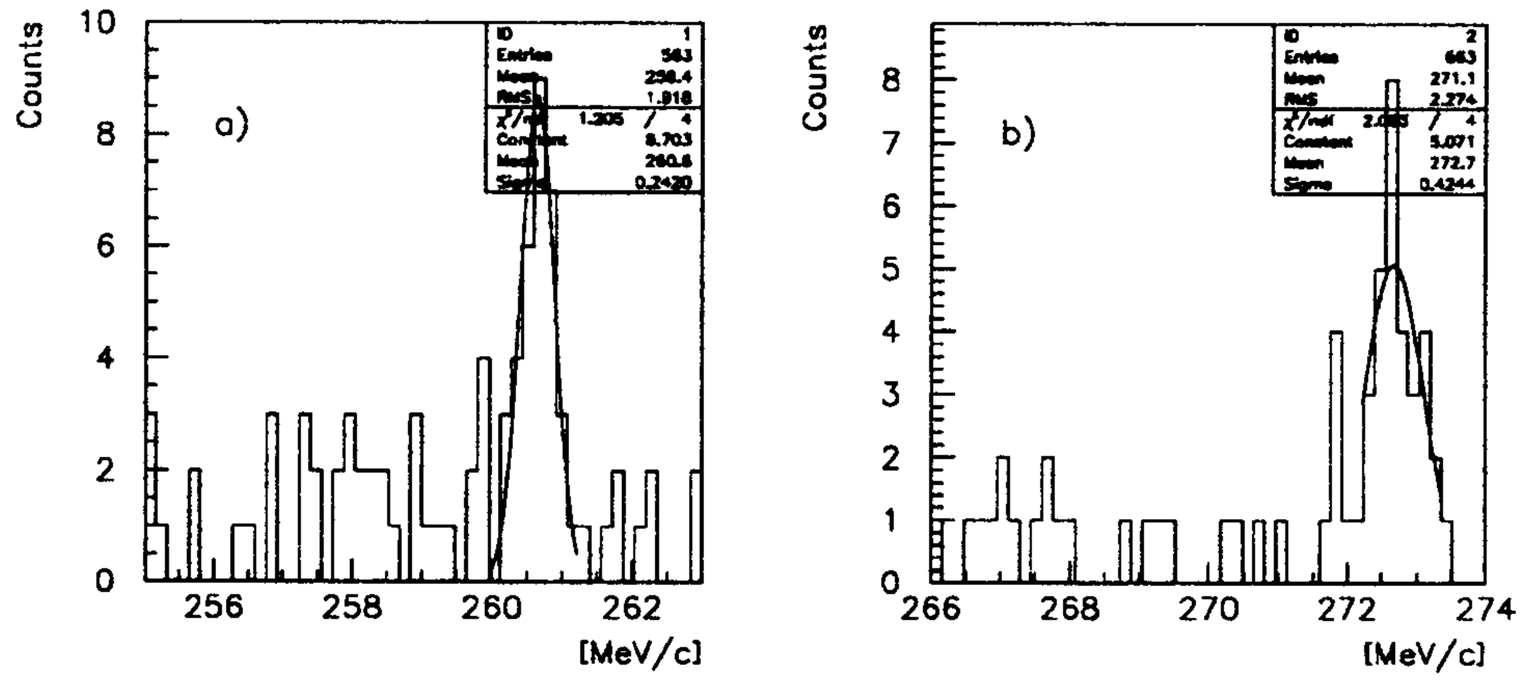

Figure 8.11: The capability of resolving narrow peaks is showed. Note how, despite the not very high statistics, the peaks are clearly emerging from the background.

Bibliography

[1] The FINUDA Collaboration, *FINUDA A detector for nuclear physics at DAΦNE*, Rep. LNF-93/021 (IR), 1993, 1.

[2] R. Brun, F. Bruyant, M. Maire, A.C. McPherson and P. Zanarini, GEANT3, CERN Report DD/EE/84-1 (1987), 1.

[3] A. Antonelli *et al.*, KLOE Note No. 3 (1991), 1;
A. Antonelli *et al.*, KLOE Note No. 23 (1992), 1.

[4] R.L. Gluckstern, NIM 24 (1963) 381.

[5] H. Wind, NIM 115 (1974) 431.

[6] V. Innocente, M. Maire and E. Nagy, GEANE, L3 Report (1988), 1.

[7] R. Brun and P. Zanarini, KUIP – Kit for User Interface Package, CERN Data Handling Division, (1988), 1.

[8] H. Grote, Rep. Prog. Phys. 50 (1987) 473.

Chapter 9

INSTALLATION OF THE EXPERIMENT

9.1 Gas distribution control system

The gas distribution and control system has been designed for the use of different gases and/or mixtures in the drift chambers, straw tubes and in the Helium tank.

The layout of the system consists of the following main sections:

a) distribution;

b) control and blending;

c) detectors;

d) analysis and on line monitoring.

Each of them has specific functions and interacts with the other sections as described in the following.

a) Distribution section

In the flow lines of the gases, between the distribution rack and the control and blending system, a set of valves accomplishes different purposes :

- cut-off valves: they are preset by the Safety Service to automatically stop the gas flows in presence of anomalous concentrations, revealed by gas leakage probes;
- check valves: they avoid fortuitous gas blending in the distribution piping due to erroneous pressure unbalance;
- safety valves: they are preset to safety limits according to our working conditions. On overpressure they release the excess gas towards the exhaust;
- purge valves: they allow purging vent lines and the whole system with an inert gas (Ar).

The piping from distribution rack to experimental racks will be made of stainless steel and polyurethane. To prevent the contamination of He (used as tank gas) with the other gases two separate vent lines are foreseen.

b) Control and blending system

Main components are the thermal mass flow-meters (Brooks model 5850) which measure and control each gas flow according to the preselected values. These values may be set separately for each gas on the control-and-readout equipment, either independently or in servo-mode. In servo-mode, the requested flow-rate of the main blend component (master gas) is set on the controller dial while the flow-rate of the other component (slave gas) is set as a percentage of the master flow. By regulating the master flow, the flow rate of the slave gas will be driven consequently, with no change in the preselected composition of the blend.

On failures or electric power breakdown a bypass emergency line may be activated in order to preserve the gas flow through the detectors. The elements of this line are, in sequence, a manually operated valve, a manometer and a flow-meter with its needle valve. The flow-meters must be adjusted to the same value set on the Brooks valves. The reset of the power supply does not imply the automatic reset of Brooks valves, since a manual restore is requested after blackout: in this way one avoids pressure shocks due to the sudden opening of the valves, especially dangerous for the very thin chamber windows.

c) Detectors

Two control operations are required :

- monitoring of all absolute pressures
- monitoring of all differential pressures

The differential pressure regulation is achieved both by adjustments of gas flow-rates entering the chambers, and proper modification of the oil level in the bubbling devices located between the chambers outlets and the vent lines. Other bubbling devices are inserted before the chambers inlets as additional safety device against pressure raising over preset values.

d) Analysis and online monitoring

It consists of the lines and devices necessary to monitor that the mixture percentages of flowing gases remain constant.

It is possible to test each line of the distribution system and the outlets of each chamber in order to locate easily sources of incidental contaminations or leakages. The test will be performed by a mass spectrometer. Besides local readout, the system is linked with the DAQ in order to allow remote on-line monitoring of the whole set of parameters.

In fig.9.1 an overall scheme of the gas distribution and control system is given.

9.1.1 Drift chambers gas system

The drift chamber gas system is an open-flow circuit supplying an He-Isobutane (70-30) blend, for a total volume of $0.28m^3$. The change rate is 8-10 volumes per day, with a 6-7 l/h leakage rate. The general circulation scheme has been described in Chap. 9.1 .

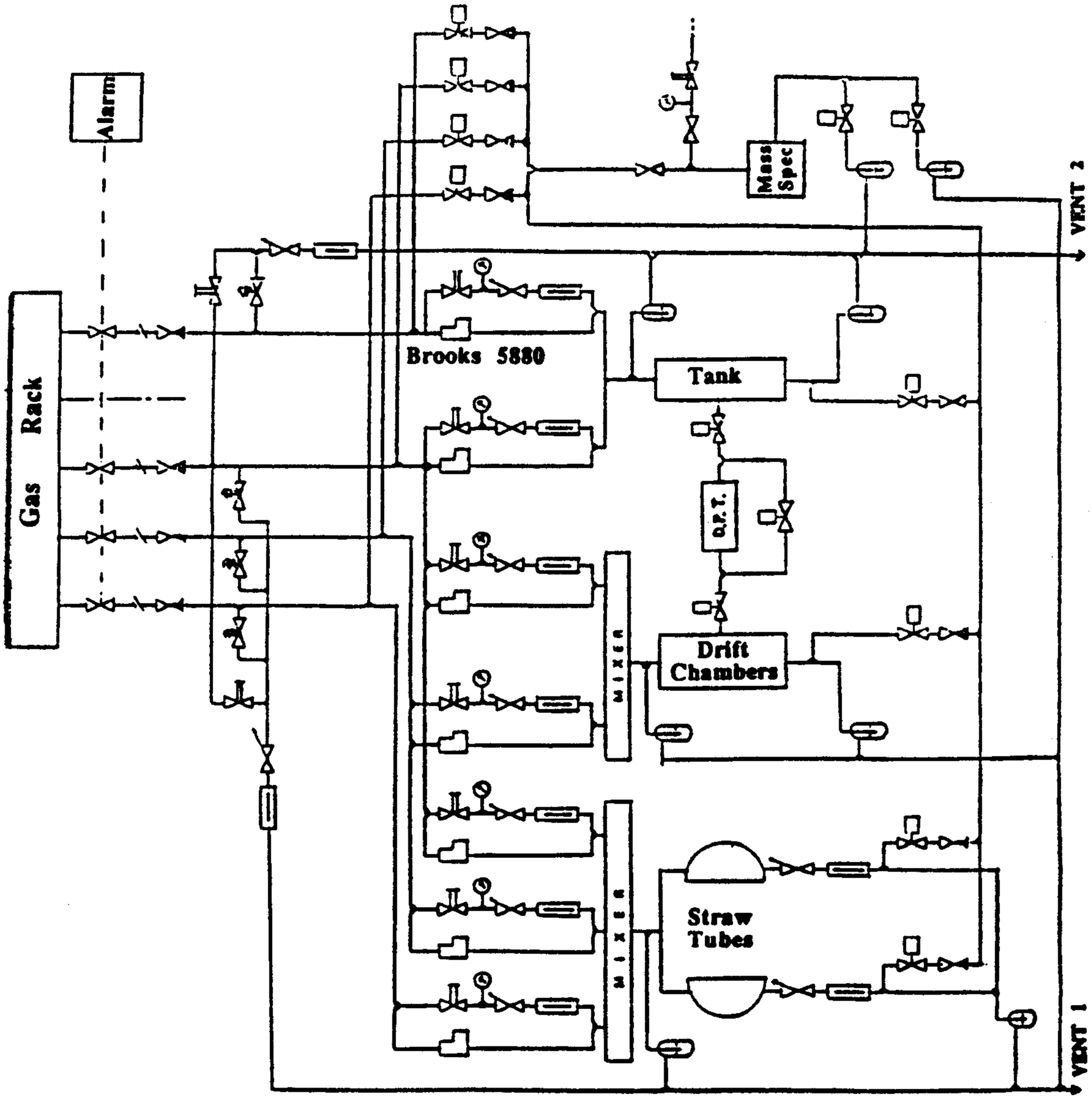

Figure 9.1: Gas distribution and control system.

9.1.2 Straw tube gas system

The straw tube gas system is an open-flow circuit providing 99.99 % pure Dimethyl Ether at a pressure of 1.1 bar. The total gas volume is 1 m^3 and about two volume changes are provided in 24 hours. Therefore the running condition flow rate is a moderate one, $\sim$ 1.4 l/min.

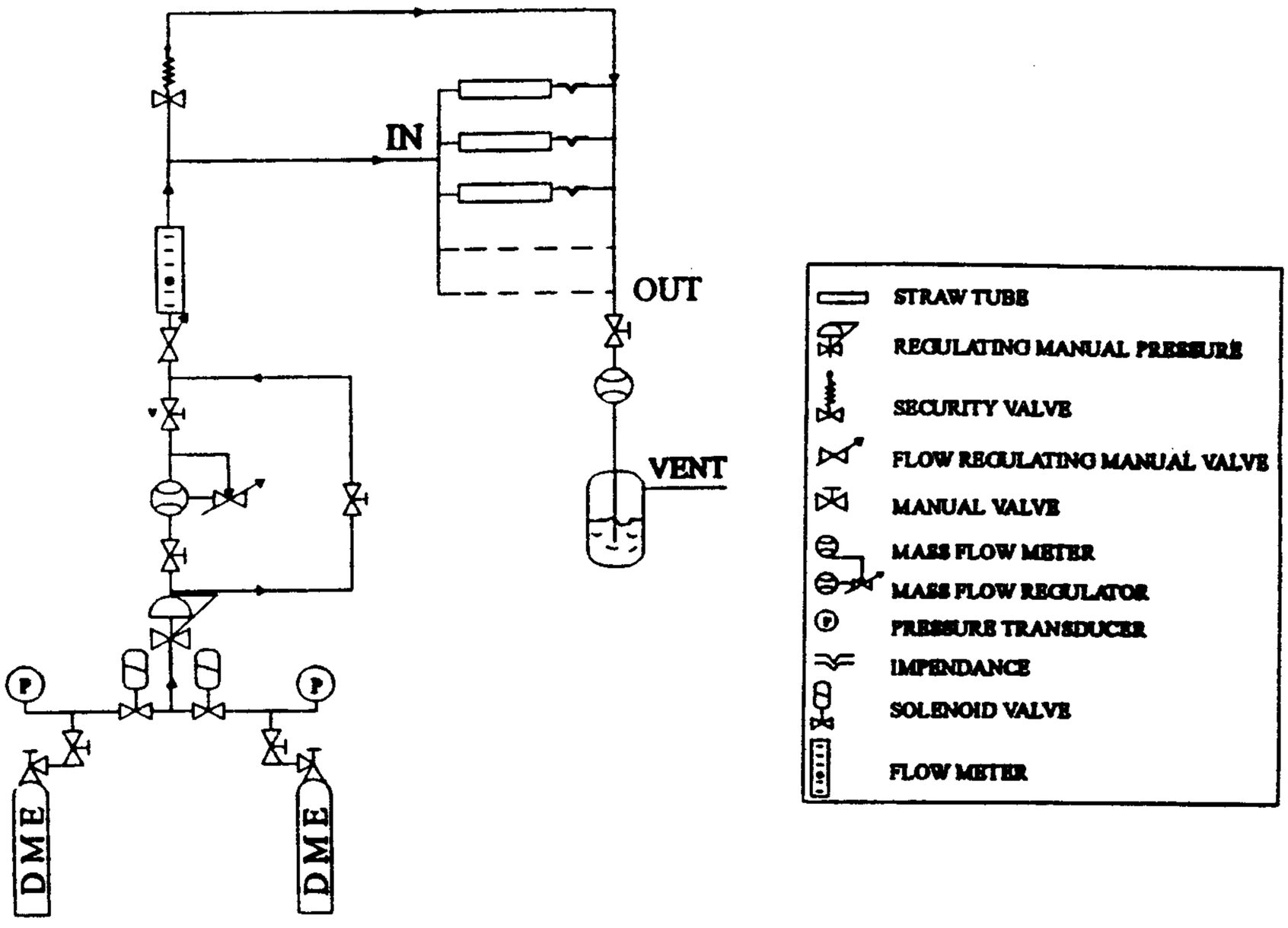

Figure 9.2: Straw tube gas system.

The proposed gas system is shown schematically in fig.9.2. The fact that pure DME is used renders the gas system to be much simpler. The salient features are:

- All tubing from the gas rack to straw tube input distributor and from the outlet to exhaust is made of stainless steel. The connections from the distributor to individual straws are made by polyurethane tubes.

- An automatic switching from an almost empty bottle to a new bottle is provided by a system which is sensitive to the bottle weight. By appropriate setting of the threshold weight, the gas impurities, usually concentrated at the bottom, can therefore be avoided.

- The gas leakage is detected by comparing the incoming and outgoing flow rates and by a set of hydrocarbon sensitive leakage detectors distributed near the straws. In case of any anomalous condition, the gas flow is automatically closed, alarm signals are generated, and a system purge is provided with pure Ar.

- There are provisions to regularly test the gas quality and impurity concentrations by employing a gas chromatograph with samplers inserted near the outlet and inlet distributor.

- Oxysorb filter and Hydrosorb sieve are envisaged to filter out excess oxygen and water vapor from the gas.

- Gas pressure and temperature are monitored and recorded with an accuracy of 1 $mbar$ and 1 ^oC.

- A flow impedance of 0.5 $mbar/(litre/hr)$ is inserted at the exit of each straw providing a flow uniformity through all the straws.

9.2 Detector assembly procedure

The 230 tons magnet, 58 tons-each end-caps, s.c. solenoid, cryostat and carriages will be delivered by Ansaldo to LNF. Subcomponents will be mounted in the Assembly Hall, and magnetic field measured. From the Assembly Hall, the magnet, with part of the TOFONE installed and end-caps, will be transported inside the $DA\Phi NE$ building by means of wheeled-carts, and lowered in the experimental pit. Sub-detectors will be mounted inside the detector frame in the ASTRA Hall. The complete cabled detector will be transported in the experimental pit, hooked-up and turned on for testing electronics, cabling, servicing, etc. Once the magnet is in the pit, the detector will be inserted.

Such a complicated sequence of procedures requires careful planning to cope with unforeseen delays of any subcomponent. The procedure chosen maximizes modularity in order to keep detector assembly independent from magnet assembly and transport.

9.2.1 The Assembly and ASTRA Halls at LNF

The Assembly Hall (formerly MEA Hall) that will be used to assemble the magnet and to perform magnetic field mapping is shown in fig.9.3(top). The Assembly Hall is equipped with a 20t crane, temperature is stabilized within $\pm 2^oC$ (max gradient winter/summer), and floor is rated to sustain a load up to $2kg/cm^2$.

In the ASTRA Hall (fig.9.3 bottom) drift chambers and straw tubes will be installed inside the detector frame, while TOFINO and microstrips will be assembled and installed inside the central tracker support.

The ASTRA Hall is located at the far end of the LNF site (see layout in fig.9.5) and is equipped with two, 0.5t-each column cranes and one 3t one-direction crane. The floor is rated to sustain a $2kg/cm^2$ load. The hall is climatized within $\pm 2^oC$. A class-100, $6m \times 4m$ clean room (fig.9.4) with optical table will be used for precision mounting of the central tracker.

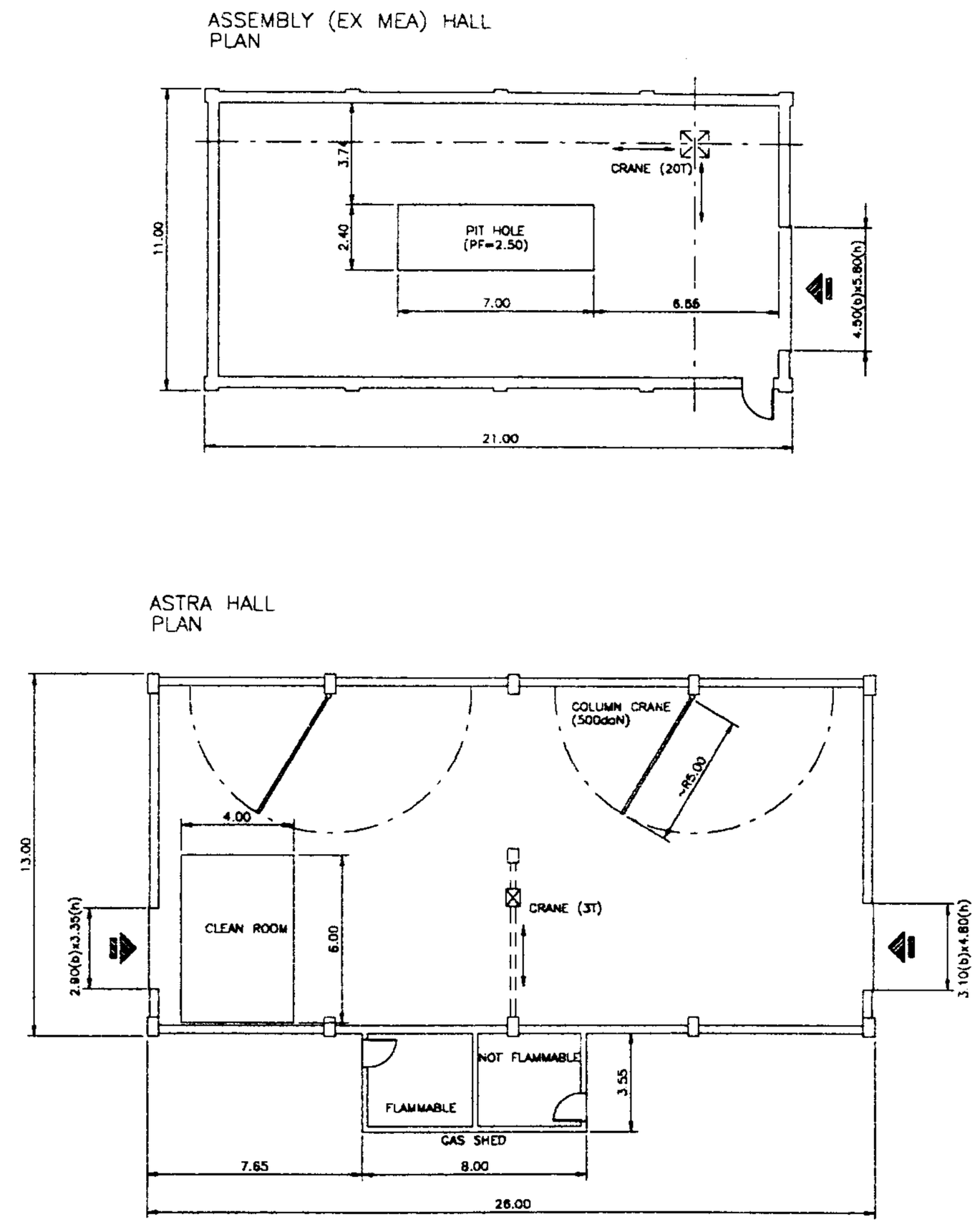

Figure 9.3: Plan of the Assembly (formerly MEA) and ASTRA Halls.

9.2.2 The transport of the solenoid to LNF and the final assembling

Cryostat, s.c. coil and restrain cylinder will be delivered by Ansaldo to LNF. Yoke, cryostat and coil will be assembled by Ansaldo in the Assembly Hall. The half lower part of the octagonal yoke is assembled using the 20 t crane. The cryostat with

coil (about 10t total) is lifted by crane and set on the half lower part of the yoke. The top half of the yoke is assembled, set on top of the lower half, and finally the service chimney is installed and connected (superconducting cable, junctions and connections to the cooling circuit). Alignment of the cryostat into the yoke is done by matching a set of survey marks on both elements.

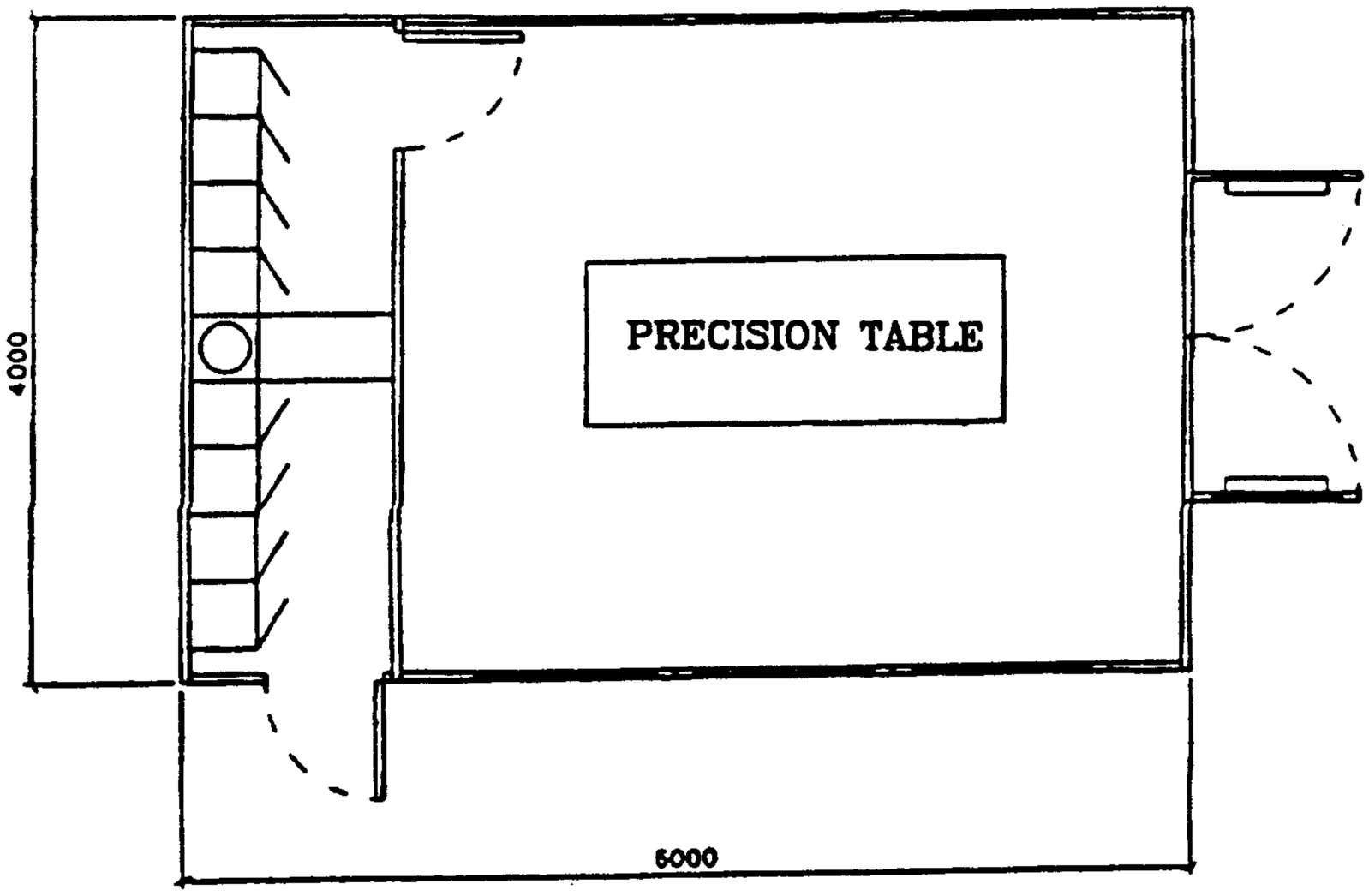

Figure 9.4: Plan of the class-100 clean room located in the ASTRA Hall.

End-caps will be assembled using the hall crane. After the final cryostat vacuum tests, end-caps will be closed using their movement system.

After the vacuum tests, a cooling down to the liquid helium temperature will be necessary in the Assembly Hall. Due to the long distance from the $DA\Phi NE$ liquefaction plant to the Assembly Hall, we do not think that liquid helium will be available easily by a transfer line directly connected with the plant. In order to minimize the helium consumption during the cooling down, it is foreseen the use of liquid nitrogen in the cooling down to 77 K. Also the shields will be cooled using liquid nitrogen. So during this step some liquid nitrogen tanks (2 x 2000 l) have to be installed near the Assembly Hall. This phase, done by Ansaldo personnel, will last about 7 days.

After having reached the liquid nitrogen temperature (80-85 K), one can start using liquid helium. The magnet circuit will be washed by helium gas and the transfer will start from the predisposed dewar. At least 3 x 500 l dewars going back and forward from the liquefaction plant to the Assembly Hall will be necessary to guarantee the supply for all the test (and magnetic measurement) period. A consumption of about 100 l/day is foreseen due to losses of the cryostat, the dewars and the transfer lines. At least a return line to recover the room temperature gas to

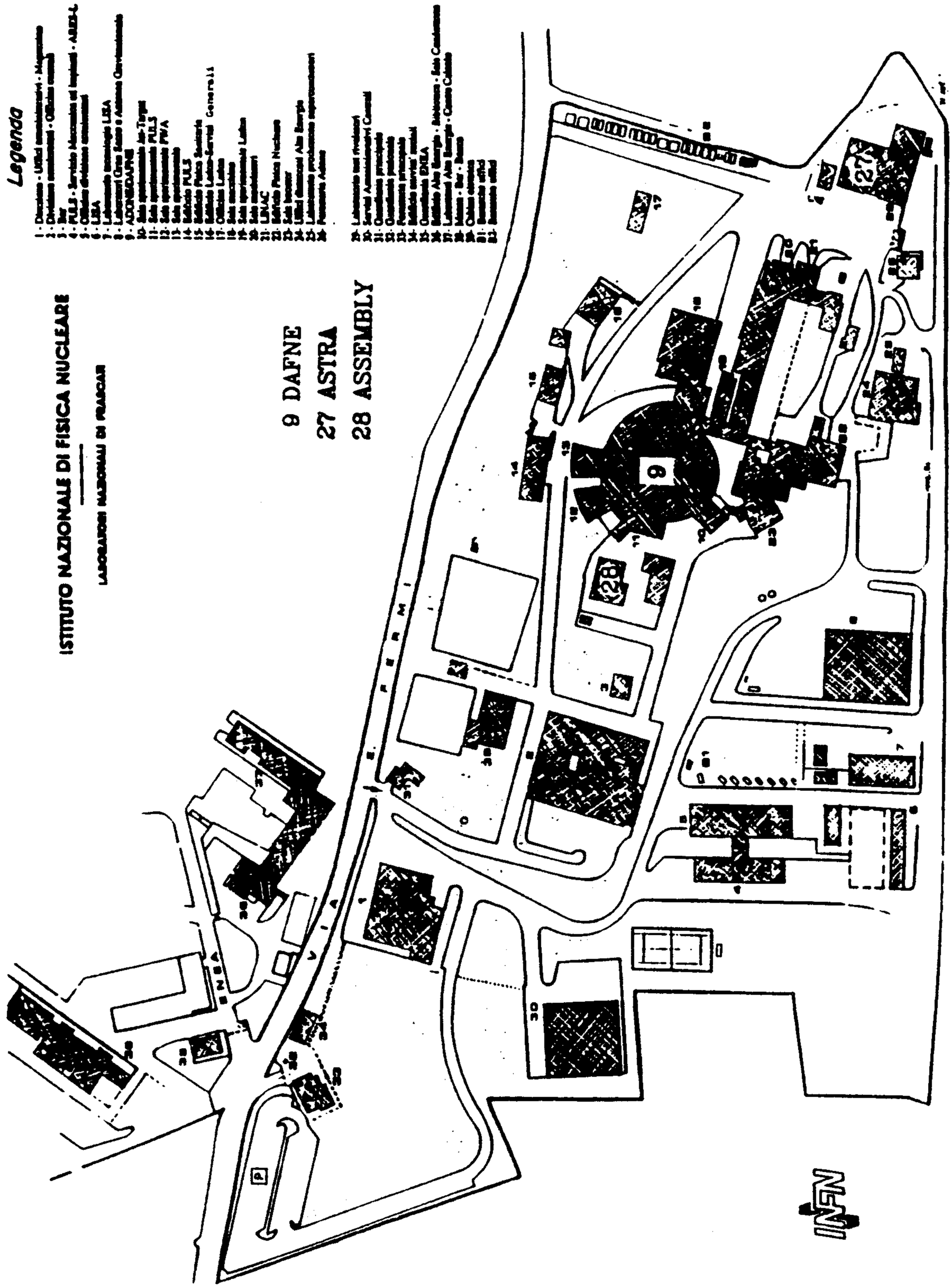

Figure 9.5: The LNF site, showing the Assembly, ASTRA and $DA\Phi NE$ buildings.

the liquefaction plant has to be installed. The Assembly Hall will house the magnetic field measurements described in Chap. 9.3. Taking into account the real difficulty related to perform the cryogenic test in the Assembly Hall, an alternative solution is being studied, where the first cooling down of the FINUDA magnet, complete of iron yoke will be made in the Ansaldo factory using their refrigeration plant. In case the cooling down will be made at Ansaldo, also the magnetic measurement mapping could be performed there. This solution can be even more convenient from the economic point of view.

9.2.3 Transport and installation of the magnet into the pit

The transport of the magnet from the Assembly Hall to the FINUDA pit in DAΦNE building consists of three phases:

1. transport from the Assembly Hall to the entrance of the $DA\Phi NE$ Hall;
2. transport from the entrance of the $DA\Phi NE$ Hall to the pit rim;
3. installation down to the pit.

From the Assembly Hall to the pit rim

The choice of the transport system is conditioned by the dimensions of the $DA\Phi NE$ Hall entrance door.

Door (4.4 m height by 3.8 m width) and magnet (4.2 m height without chimney by 3.80 m width with end-caps, by 2.87m width without end-caps) dimensions force the relocation to be done without end-caps and chimney, and with the magnet axis orthogonal to the access direction.

One of the systems satisfying these constraints is an air cushion. The air cushion will be inserted underneath the magnet and will occupy less than 15 cm vertically. Stability platforms will keep the magnet from toppling over.

The use of an air cushion will require, however, a good quality floor surface: the paved road from the Assembly to the $DA\Phi NE$ Hall will be lined with a cement slab for planarity and metal sheetings for porosity.

In relocating the magnet from the Assembly to the $DA\Phi NE$ Hall entrance, two heavy tractors will be used to drag the magnet towards the access and to compensate the gravitational forces caused by the road being down-hill sloped.

Once at the entrance of the $DA\Phi NE$ hall, one tractor will push the magnet. Thrust will be given by a wheel system assembled in front of the air cushion. Wide steel platforms set on the $DA\Phi NE$ Hall floor will permit to distribute the load uniformly below the limit of $2kg/cm^2$.

Installation in the experimental pit

The magnet on air cushion is now arrived at the pit rim. The magnet carriage is moved on rails towards the pit rim underneath the magnet.

A temporary structure (*carriage plane*) holding a platform whose surface is well-suited to receive the air cushion is assembled on the carriage.

The carriage with the carriage plane is lifted at floor level by hydraulic jacks, concrete blocks and steel spacers.

The magnet on air cushion is moved onto the carriage plane, the air cushion removed by using proper jacks. The carriage is lowered down into the pit. When the carriage reaches the rail, jacks are disassembled from the carriage and connected between floor and magnet. The magnet will be lifted in order to slip out the carriage plane, and to assemble the final supporting structure that connects the magnet to its carriage.

Once the magnet is installed on the carriage, it will be moved to the pit center (fig.9.6.2) and the end-caps will be installed using the crane (fig.9.6.3).

The metal structure with front-end electronics racks will be assembled on both sides of the magnet (fig.9.6.4), and, upon completion, the fully equipped magnet will be moved towards the beam-line, thus allowing space for the detector insertion (fig.9.6.5).

9.2.4 Installation of the detector frame inside the magnet

The detector frame, completed with sub-detector components and fully cabled up to the patch-panels, will be transported from the ASTRA Hall to the $DA\Phi NE$ Hall, lifted by crane and lowered in the pit (pos. A) on a temporary cart(fig.9.6.6). Beam pipe and inner compensating quads will be inserted through the detector frame (fig.9.7.7). After having installed the TOFINO detector and the support structure for the central tracker, the frame will be lifted by crane, the magnet will be moved to pos.A, and the detector frame lowered in pos.B (fig.9.7.8-10). This will allow to completely open both end-caps to roll the detector frame inside the cryostat on support rails (fig.9.7.11), with the beam pipe in place (see sect.3.5.8). One side of the rods supporting the cable patch-panels is retractable, and will be lifted through the notches in the iron yoke after completing the insertion.

9.3 Magnetic measurements

The magnet will be kept cold in its steady state conditions for all the time needed to perform the magnetic field mapping. The tool to perform the field mapping will be provided by ANSALDO according to FINUDA requirements. The basic idea is to use a combination of NMR probes and Hall probes mounted in several rotating arms of 1200 mm radial length. All these arms will have one or two NMR probes

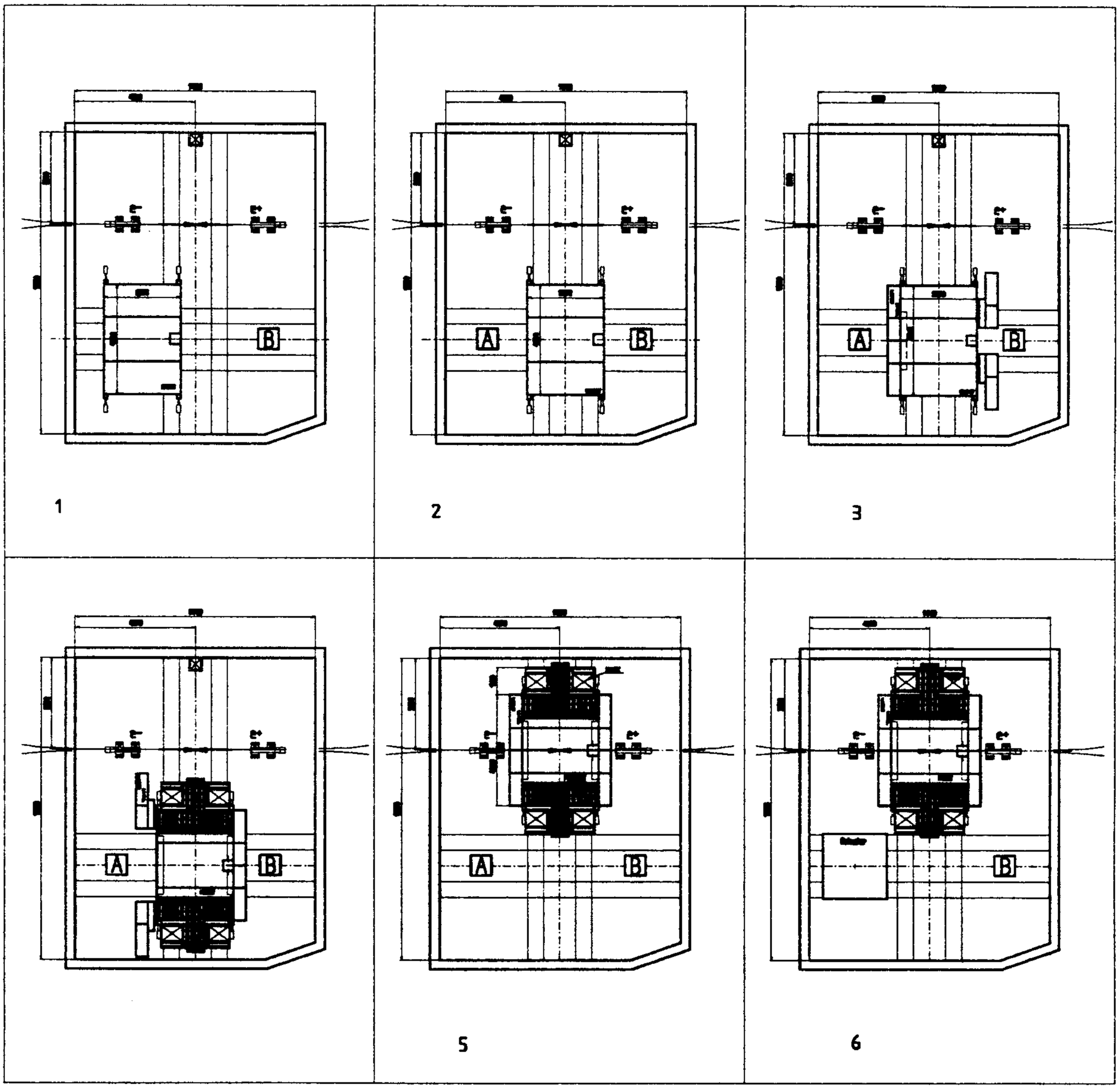

Figure 9.6: Sequence of magnet and detector lowering in the pit and arming: 1) the magnet arrives to the pit with TOFONE installed, and is lowered in pos.A; 2) the magnet is moved to the pit center; 3) the end-caps are mounted; 4) front-end electronics racks are mounted; 5) the magnet is moved on beams; 6) the detector frame is lowered by crane down the experimental pit on a temporary cart located in pos. A. The magnet is complete of front-end electronics racks and TOFONE.

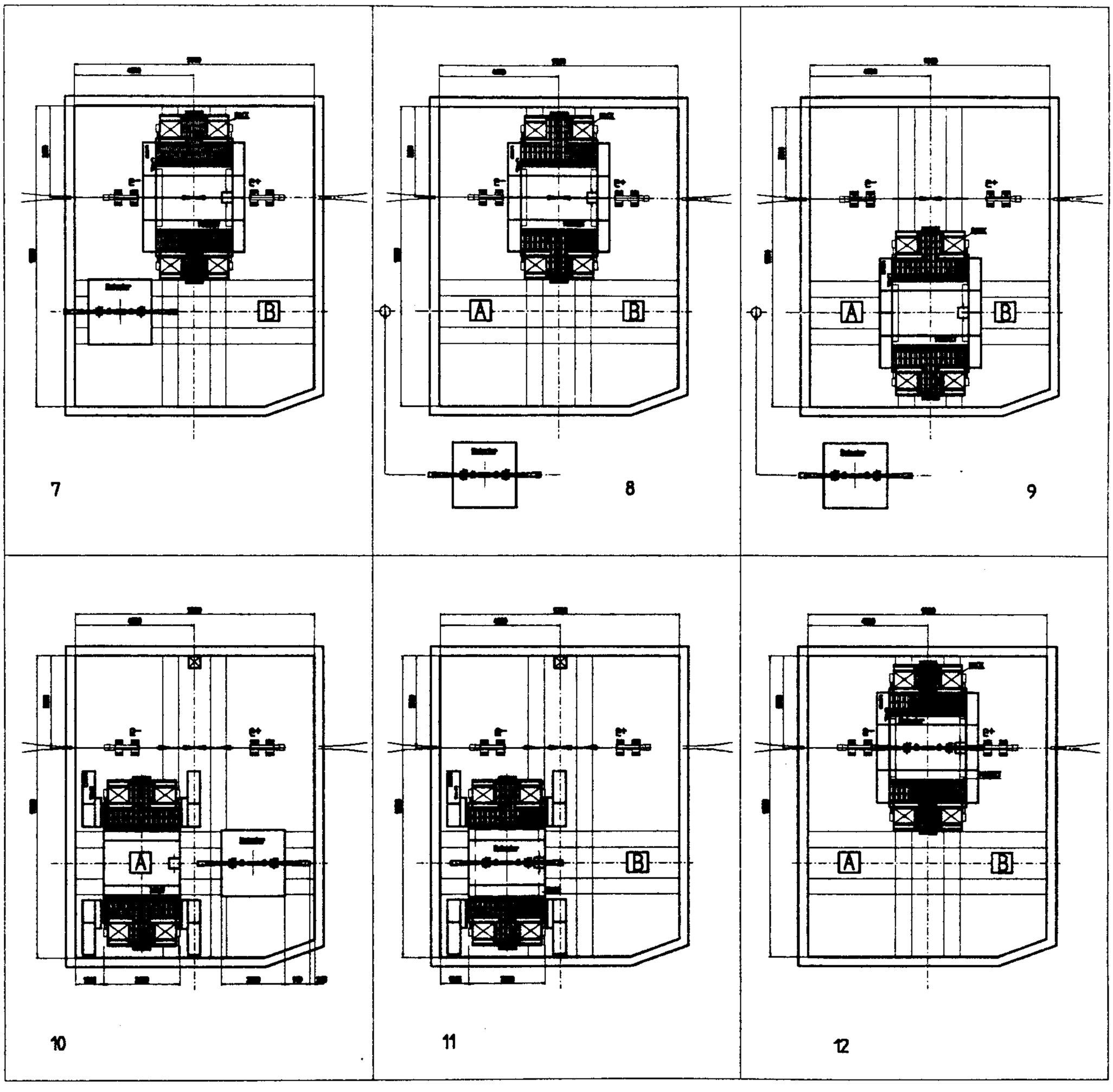

Figure 9.7: Sequence of detector insertion inside the magnet: 7) beam pipe and compensators are inserted through the detector frame. Central tracker and TOFINO are installed, embracing the beam pipe; 8) the detector frame with beam pipe inserted is lifted by crane; 9-10)magnet is moved to pos.A, the detector frame is lowered to pos.B; 11) with the magnet in pos. A, both end-caps can be fully opened and the detector is rolled inside the cryostat; 12) magnet and detector are moved on beams.

and about 10-15 Hall probes for the axial component and the same number for the radial one, mounted at a radial distance decreasing from the center to the periphery, where the change in field values will be greater.

The principal problem of the field mapping is related to the sensor calibration; especially the Hall probes measuring the radial component have to be precisely oriented at 90 degree against the axial field to avoid influence of the larger component. The idea is to correct the error due to the wrong orientation of the Hall probes for the radial component by a measurement of the error in the angle. By radial rotation of the arm, it will be possible to put the Hall probes for the axial component in the position previously occupied by the probes for the radial component; so it will be possible to have the measurement of both the components in the same spatial position. The same will be possible with the NMR probes for some radial position.

The mapping will start putting the tool in the axial (mechanical) center of the magnet where the radial components will be very near to zero and a complete measurement of the plane will be made. The error related to a possible wrong angle between the probe of the radial component and the tool is fixed for any rotation angle of the tool and it will produce a dipole oscillation on the measurement that can be similar to those due to a misplacement of the magnetic axis. By a rotation of 180 degree of the arm on its axis it is possible to eliminate this effect by correlating it to the axial field component measurement. The absolute value of the axial component will be calibrated using the NMR probes. Movement of the tool rotation axis will be made to minimize the dipole variation of the radial component, measured in the external circumference of the volume, in order to find the magnetic axis of the magnet in different axial positions. Using this axis, the complete field mapping at the magnet nominal central field will be made with a lattice in cylindrical coordinate over the field homogeneity volume; the dimensions of the lattice will vary from a maximum of R=z=10 cm, $\Delta\phi$= 5 degree, to a minimum of 1 cm in the three directions, according to the local variation found in the field components: if this variation will be higher than 0.5%, the dimensions of the lattice will be decreased.

Since the necessity to open the end-caps for some reason during the magnetic mapping has to be taken into consideration, to avoid the realignement of the tool, it will be operated from outside the yoke, in such a way the end-caps aperture will not be perturbed. All measurement procedure will be fully automatized, under computer control. The total time needed to perform the magnetic field mapping depends on the number of arms and Hall probes used. For instance, using 2 arms with a total of 50 probes, a schedule of 28 days (24 work for day) is foreseen. Decreasing the number of probes, the number of days needed increases proportionally, together with the cost to keep the magnet cold. The precision of the measurements inside the tracking volume will be of $\pm$ 3 gauss ($\pm$ 0.03%). Measurements with a coarse lattice are foreseen also outside the tracking volume and outside the iron yoke, particularly along the beam axis and near the phototube positions.

9.4 Mechanical alignment

FINUDA is a high-resolution tracking spectrometer which dictates severe requirements on geometrical alignment of all subcomponents, in order to achieve its resolution goals.

The determination of subcomponents spatial coordinates (ultimately: wires, strips, counters) will be performed:

- ⋆ by optical alignment with open end-caps
- ⋆ by optical alignment with closed end-caps
- ⋆ with physical events, performing thus also an absolute calibration of the momentum scale.

The alignment is in fact a two-fold problem: the survey of the relative alignment of the various parts of the apparatus, and the alignment of the whole apparatus on the beam line. Of course, the magnet is the most relevant part of the apparatus.

Considering the whole detector a "matrioska", in which different parts are one inside the other, it is necessary to establish a cascade of spatial relationships between the parts, to allow the subsequent mathematical reconstruction of the complete object from the knowledge of the individual positions.

Four levels of relationships have to be distinguished:

a) Internal geometry: definition of the spatial relationships between the reference system of the whole detector and the reference marks on each individual element of the detector.

b) Detector geometry: spatial description of a modular object (the detector) using its reference marks.

c) Relative geometry: cascade of spatial relationships between adjacent subdetectors.

d) Definite geometry: measurement of the position of the whole detector respect to the beam line from the previous relationships and from direct measurement.

The relationships between the whole apparatus and the beam line will be obtained using accelerator pillars and suitable targets fixed on the wall of the $DA\Phi NE$ building.

To obtain the desired alignment, we will put all reference marks in such a way that they will be always visible with open end caps, while a part of them will be reported on visible marks through the end caps hole. This will give the possibility to re-measure the alignment of all the parts of the whole detector when needed also with magnet on.

In fig. 9.8 an axial view of the FINUDA spectrometer is shown with in evidence the basic parts subjected to survey at opened end-caps. No specific design has been yet developed about how to access to this marks with closed end-caps.

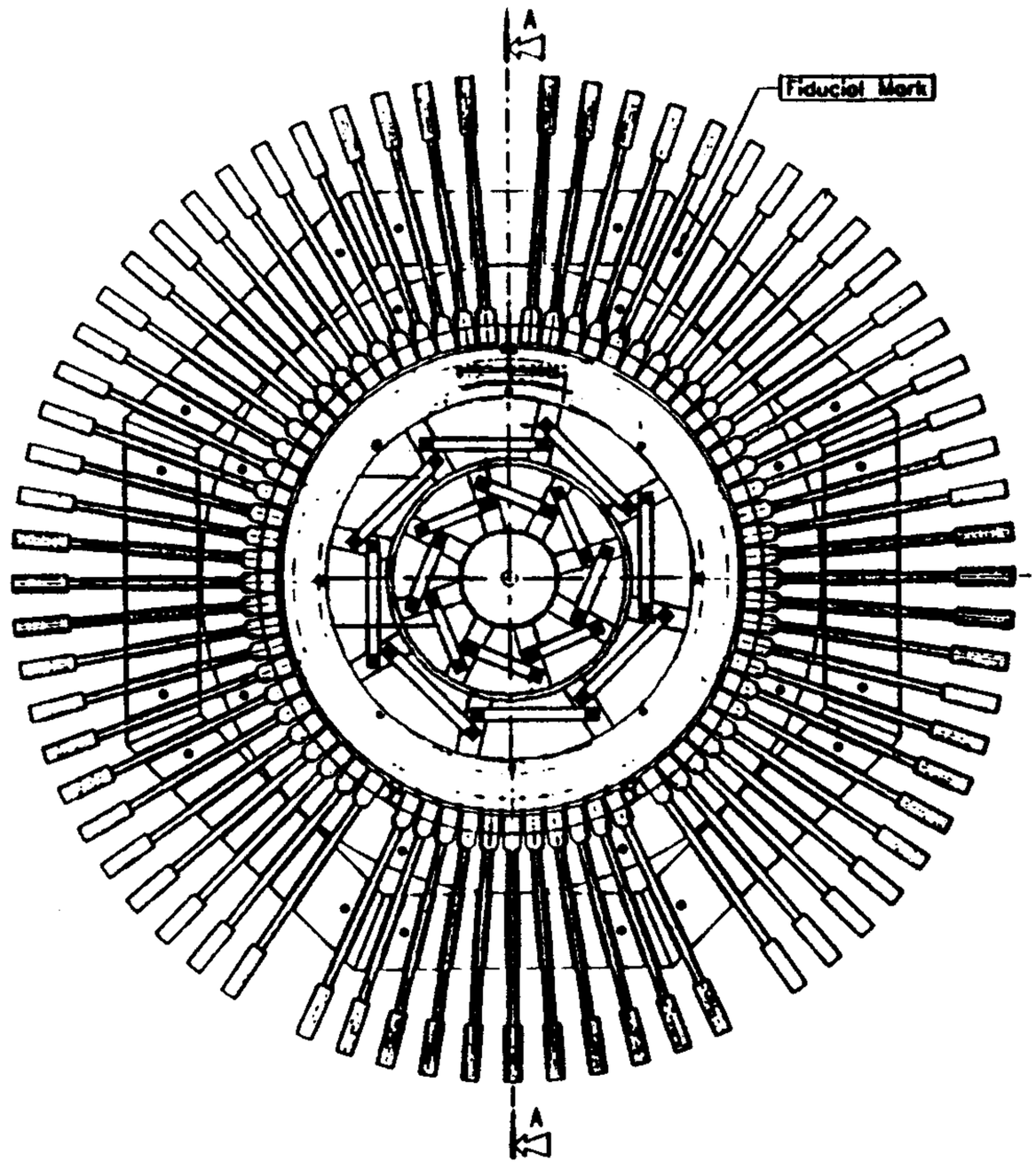

Figure 9.8: Axial view of the FINUDA detectors, with fiducial marks

Table 9.1: Requested precisions of FINUDA magnet and detectors.

FINUDA component	precision
Magnet and cryostat	$\pm 0.5\,mm$ respect to the beam axis
Straw tubes	$\pm 100\,\mu m$ (ρ,ϕ), $\pm 300\,\mu m$ (z)
Drift chambers	$\pm 100\,\mu m$ (ρ,ϕ), $\pm 1\,mm$ (z)
OSIM	$\pm 50\,\mu m$ (ρ,ϕ,z)
ISIM	$\pm 50\,\mu m$ (ρ,ϕ,z)

The relative precision of the alignment of the various detectors regarding the position in space and its reproducibility are shown in table 9.1.

Target, TOFONE and TOFINO have less stringent alignment requirements.

The vertex-target system could be installed and removed as a whole block or individually (without disrupting the $DA\Phi NE$ vacuum), and reproducibility of relative alignment is safeguarded.

Since it is not possible to survey the detection parts (as wires, cells, etc.), the external visible fiducial marks have to be at known position with respect to them.These relationships will be established during the detectors manufacturing process. It is, moreover, foreseen to have suitable holes on each detector extremity (fig. 9.9), allowing the interchangeability of the fiducial marks.

The number of holes for marks on each FINUDA component, their precision in

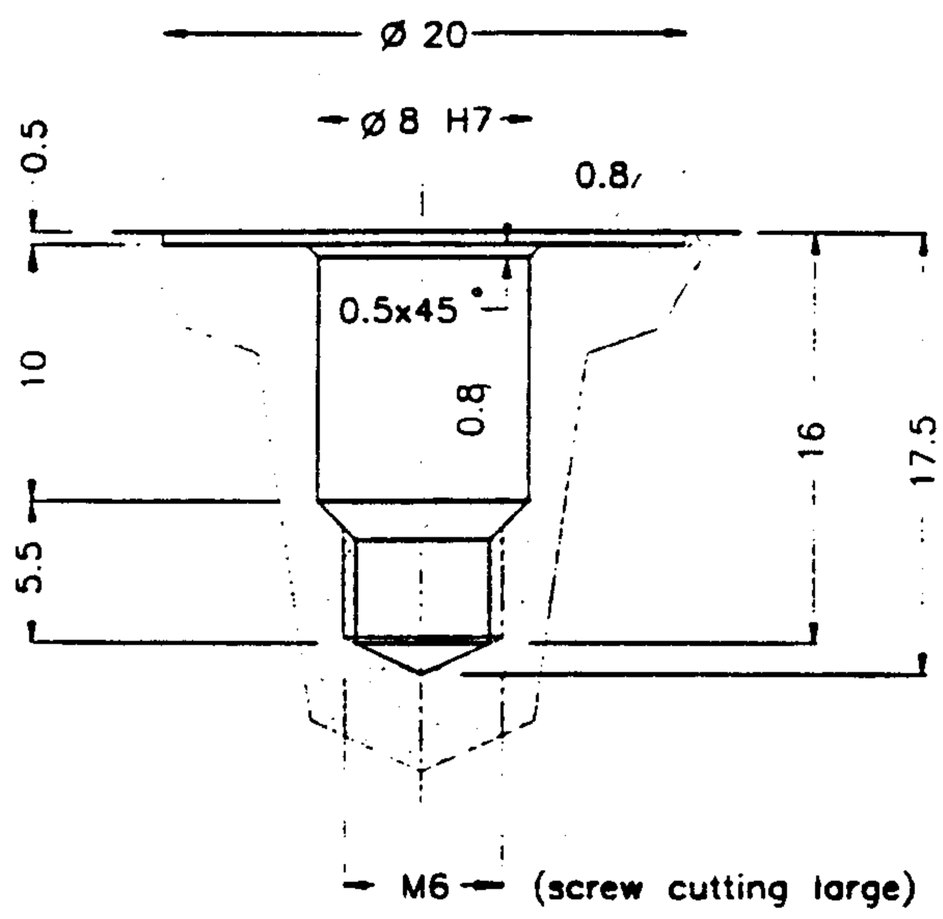

Figure 9.9: Holes for fiducial targets

polar coordinates (ρ, ϕ) are summarized in table9.2.

Regarding the survey techniques, we are taking in consideration the use of the triangulation and photogrammetry ones.

Triangulation is the method of description of an object by coordinated points intersected by two or more electronic theodolites in a common reference system (the accelerator's one). This technique gives versatility, mobility and adaptability. However, the level of precision requested requires much time and the use of high quality equipments (electronic theodolites, portable computers, geodetic levels, digital micrometers, computing effort) and a good expertise team. The accuracy is typically $\pm 100 \mu m$. The cost of the equipment is about 150 Millions of lire. The time spent using this method for each survey is few days.

Photogrammetry offers quite noteworthy benefits as accuracy, in-place measurement in the desired user's position, rapid data acquisition, independence from the number of targets, minimal effects of temperature and loading forces and, finally, turnaround time for measurements as short as a few hours.

With this method, one measures not the object itself but rather negatives of the object taken with one (or more) photogrammetric cameras from two or more locations. Since the photographed object has been viewed from different angles, its spatial coordinates are determined from the two x, y measurements on the film using

Table 9.2: FINUDA reference holes and relative precision

FINUDA component	N. of holes (each side)	precision in ρ $[\mu m]$	precision in ϕ $[mrad]$
Magnet barrel	16	± 50	± 0.03
Cryostat	8	± 50	± 0.03
Straw tubes end-plate	8	± 50	± 0.04
Drift chamber frame	3	± 30	± 0.05
Internal tube cage	8	± 20	± 0.10
Interaction-target block	8	± 10	± 0.10

the fact that the bundles of rays from each photograph intersect each other at the position of the targeted object. Camera's position needs to be known accurately and the full process proves to be very flexible and fast in data taking. Moreover, the existence of a film recorded allows subsequent reanalyses of data.

The accuracy of this method can reach $\pm 50 \mu m$, the cost of the equipment is about 300 Millions of lire, the time spent as short as one day.

9.5 Experimental pit and counting room

The experimental pit is a trapezoidal area sketched in fig. 9.10 and 9.11 with dimensions $\sim 9m \times 11.5m$. The pit floor is composed of a micro-tubing structure to sustain the magnet weight. Displacing the magnet off the $DA\Phi NE$ beam-line is made possible by the rail system shown in fig.9.12.

Once in the pit, the magnet yoke will be equipped with steel platforms holding racks for part of the front-end electronic: preamplifiers, amplifiers and discriminators. Platforms are designed to allow easy access to both front and backplanes of racks (fig.9.14). Each rack in the lower level can be extracted to access the crates' backplane.

The detector frame will be located in the experimental pit fully cabled, up to patch-panels supported by radial rods sticking out of the iron yoke through the notches (fig.9.13). The patch-panels also support HV distributors for drift chambers and straw tubes, allowing simple and safe access to both high- and low-voltage: in case of failure, parts of the detectors can be disconnected without opening the end-caps.

From the patch panels, cables and tubings (gas, etc) are routed to the front-end electronics racks, and from here to the counting room via a telescopic overhead arm (fig.9.15), cable trays on the $DA\Phi NE$ Hall wall, and PVC ducts through the $DA\Phi NE$ outer wall (fig.9.16).

The FINUDA counting room (fig.9.17) is divided in an electronics room, and a terminal room.

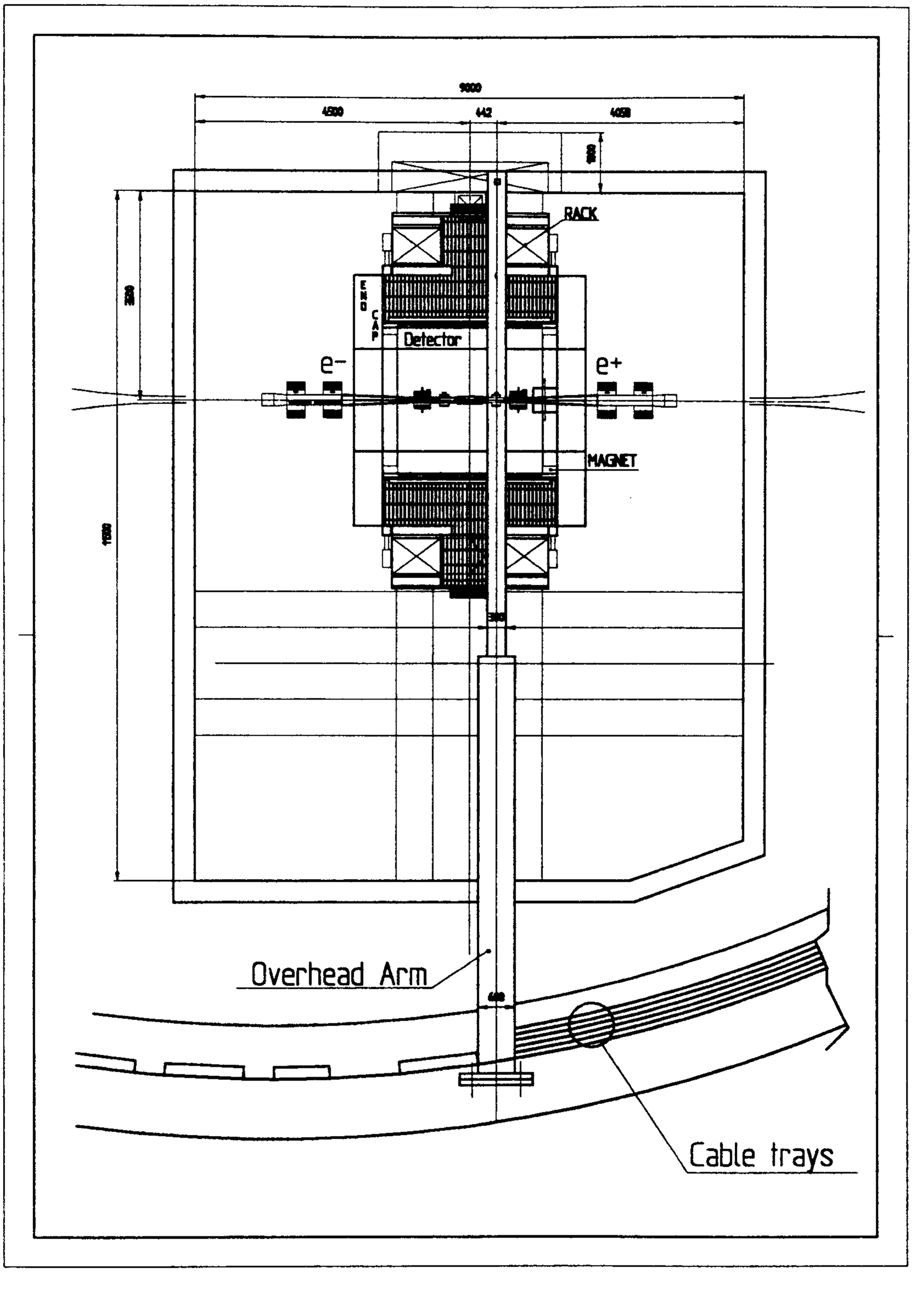

Figure 9.10: The FINUDA experimental pit (detector on beam).

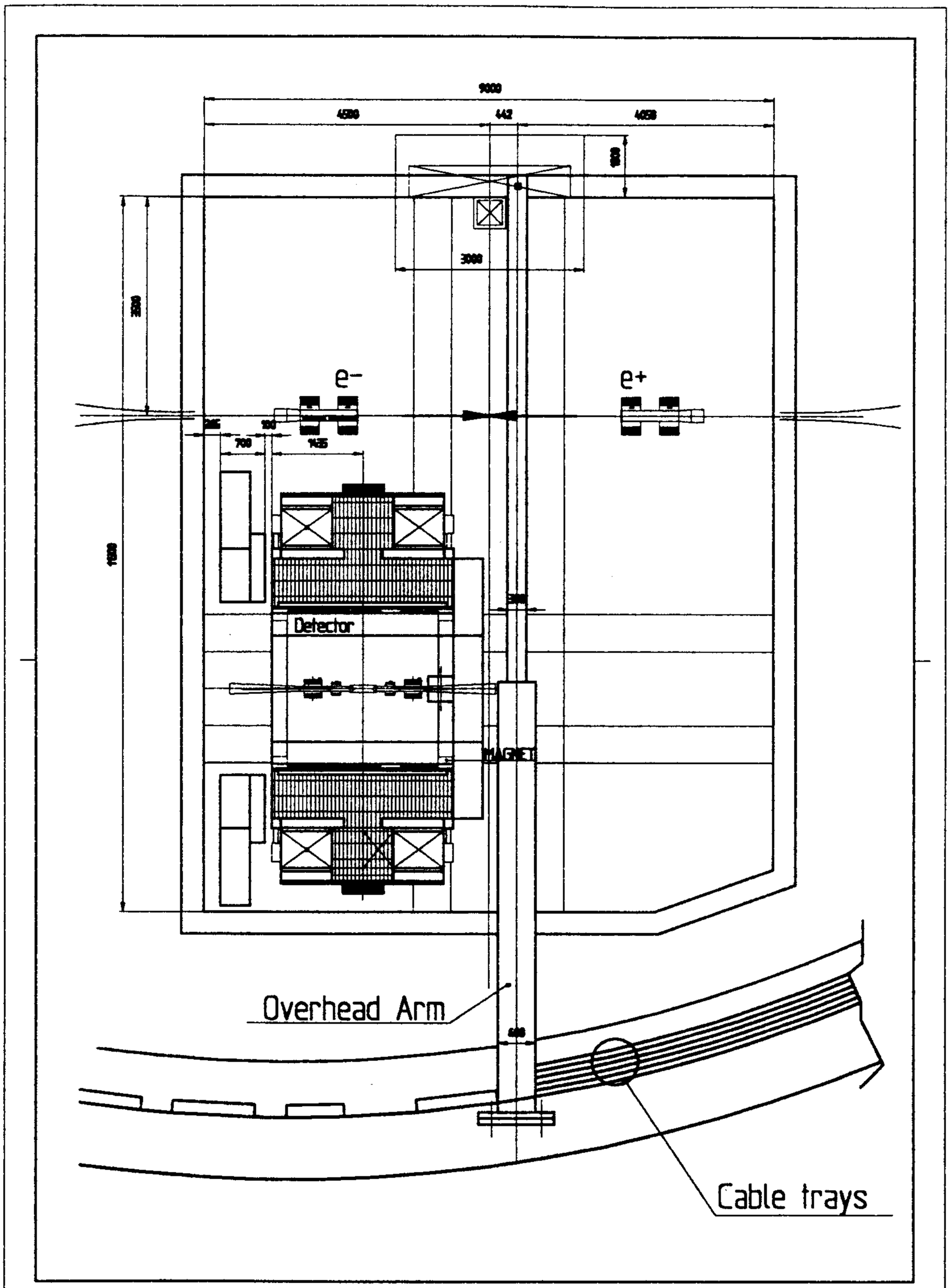

Figure 9.11: The FINUDA experimental pit (detector off-beam with end-caps open on one side).

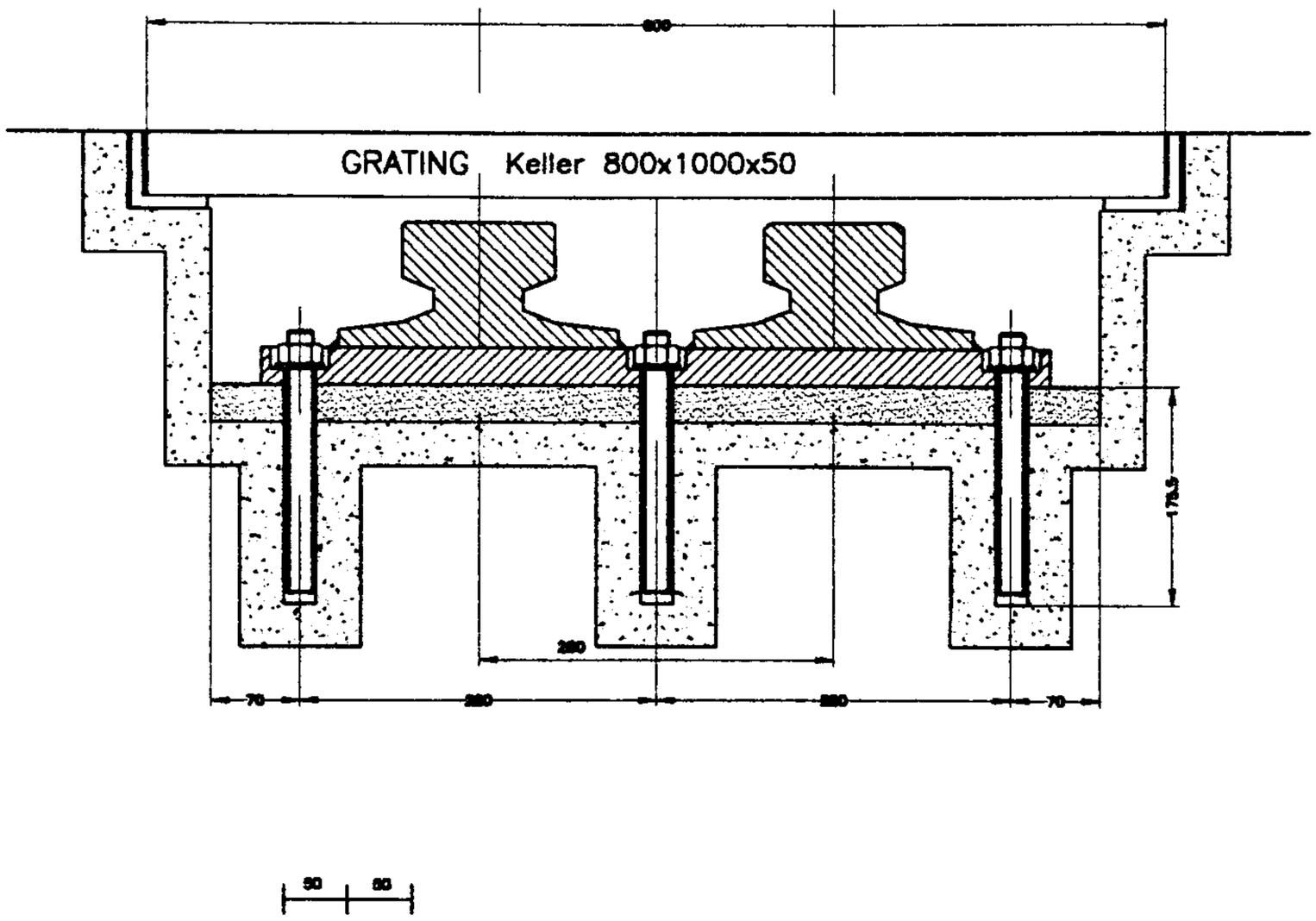

Figure 9.12: Detail of the skating system for magnet movement.

9.6 Operation

All technical solutions selected for the FINUDA detector are aimed to smooth, down-time-free operations for extended periods. This requirement, optional for detectors whose assembly/repair room is adjacent to the experimental pit, is for FINUDA a must.

Power supply distributors are located by the path-panels mounted on rods sticking out the magnet notches, and can be accessed without opening the end-caps: high voltage supplies for drift chambers and straw tubes, low voltages for preamplifiers. In case of trip of one straw tube, for instance, during an access to the $DA\Phi NE$ Hall it will be manually disconnected at the HV distributor level, and voltage will be restored to the tripped HV channel serving the remaining 31 tubes.

Very complex repairs and services can be performed with the magnet in place and open end-caps. All sub-detectors can be fully accessed. Drift chambers can be extracted from the detector frame. The central tracker can also be moved out during repairs, or routine target change. The beam pipe enclosure will stay in place, thus leaving the $DA\Phi NE$ vacuum undisturbed. Even in the unlikely event of a massive fault of the straw tube system, they will be replaced and re-strung to tension in place.

Only in case of severe faults, or in case of major upgrades and changes in the detector configurations, sectioning the $DA\Phi NE$ vacuum will be required, moving the magnet out of the beam, opening the end-caps and extracting the detector frame.

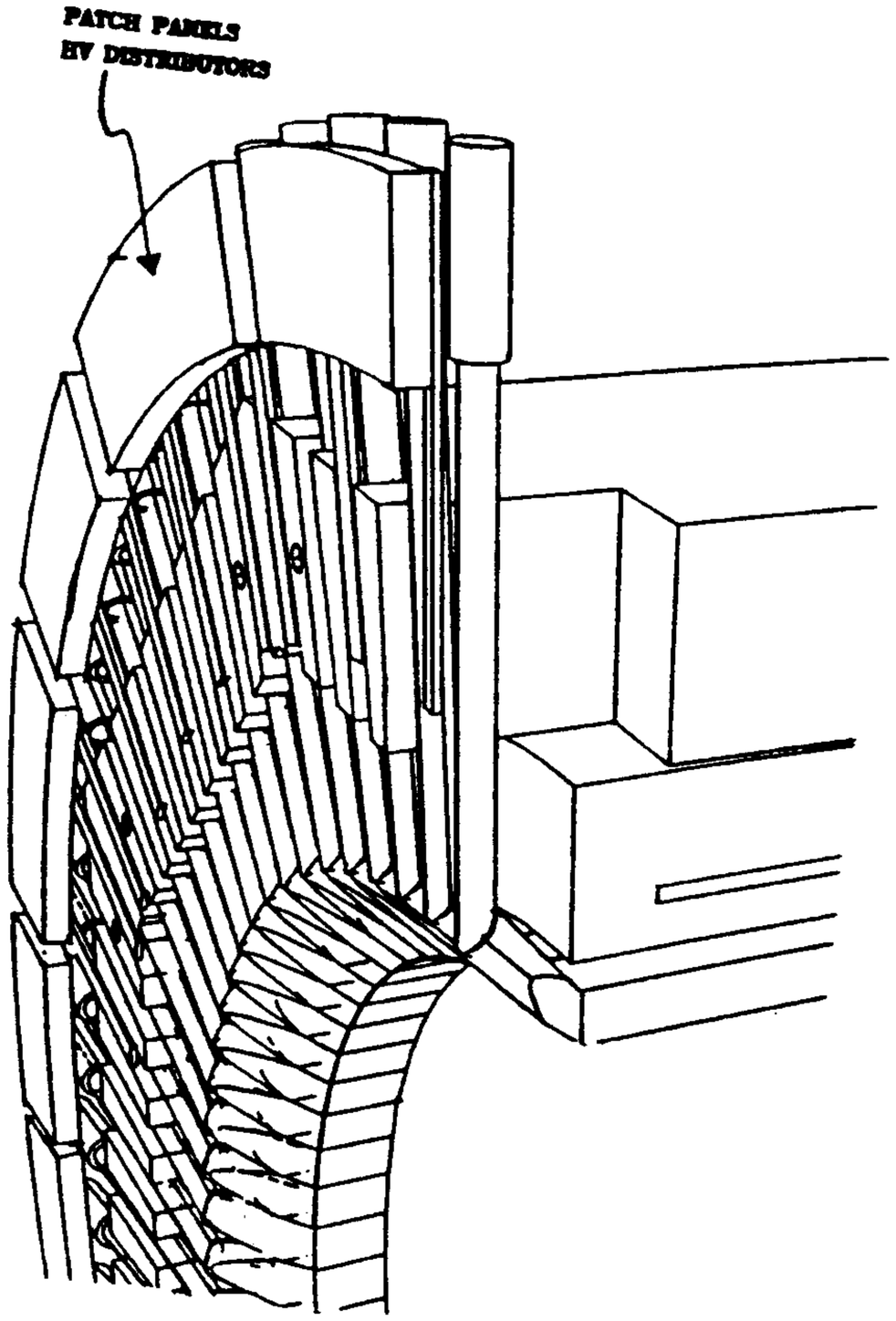

Figure 9.13: Sketch of patch-panels and voltage supplies distributors.

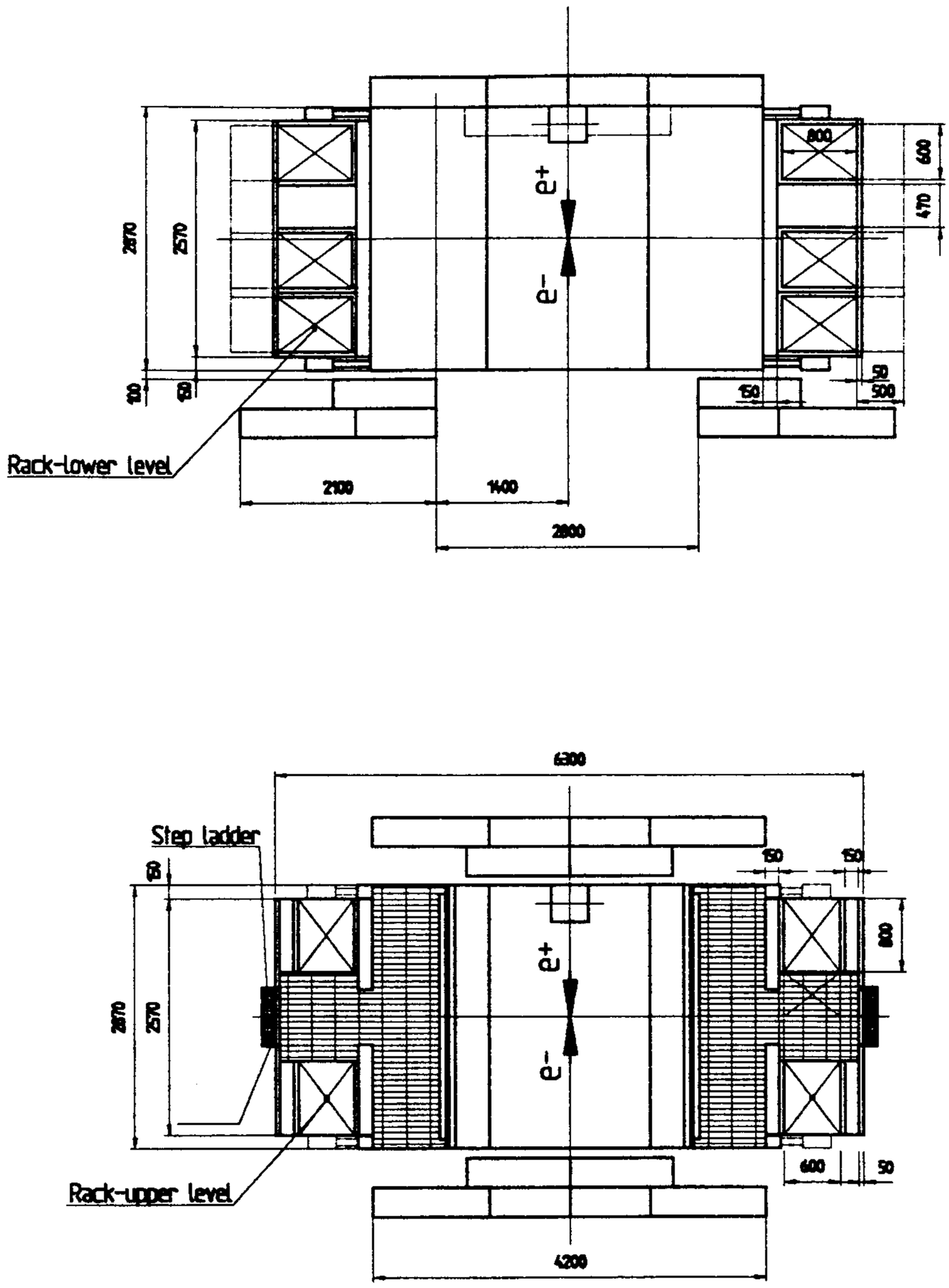

Figure 9.14: Front-end electronics installed on both sides of the magnet.

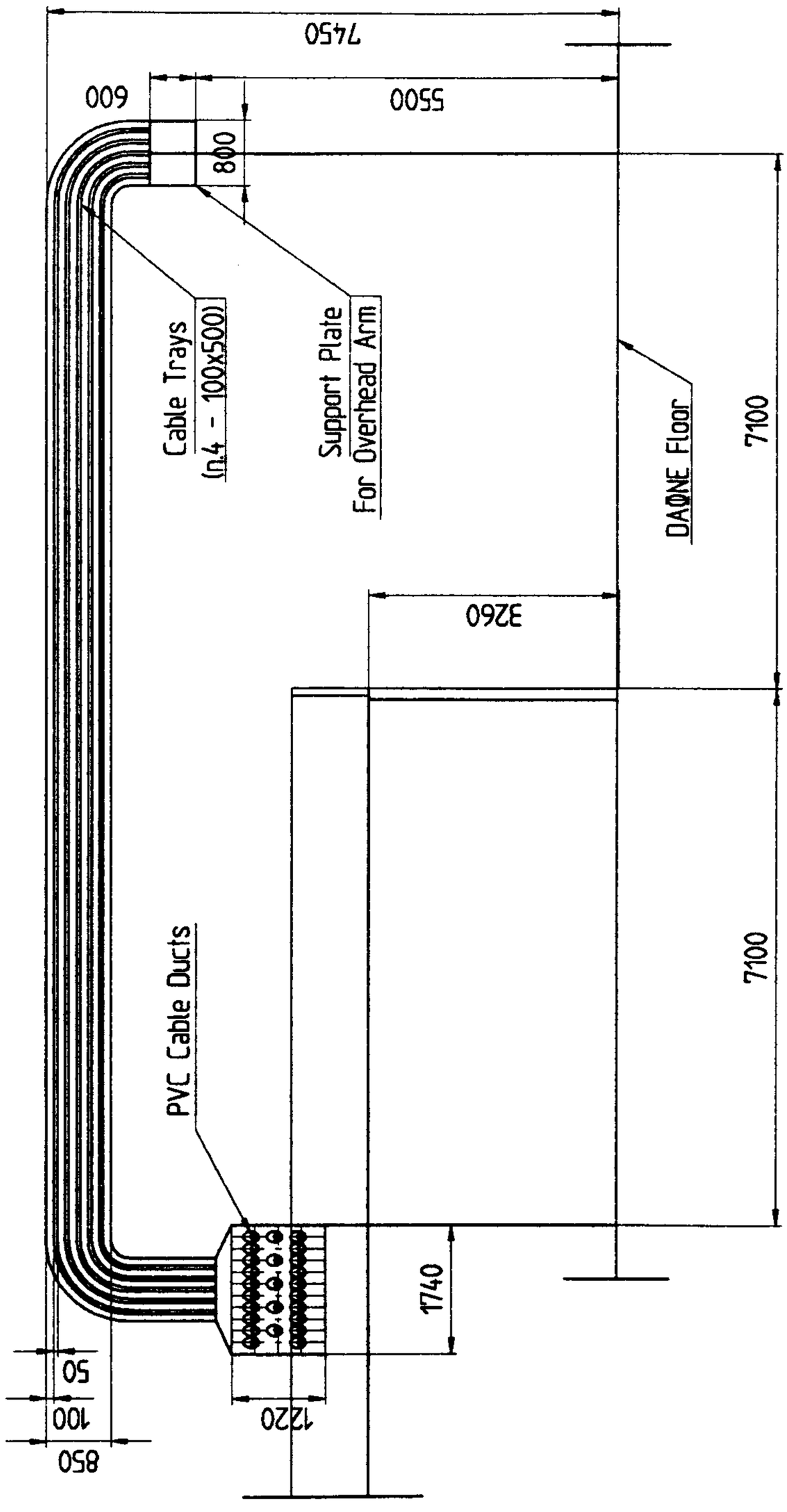

Figure 9.16: Routing of cables from overhead arm to PVC ducts.

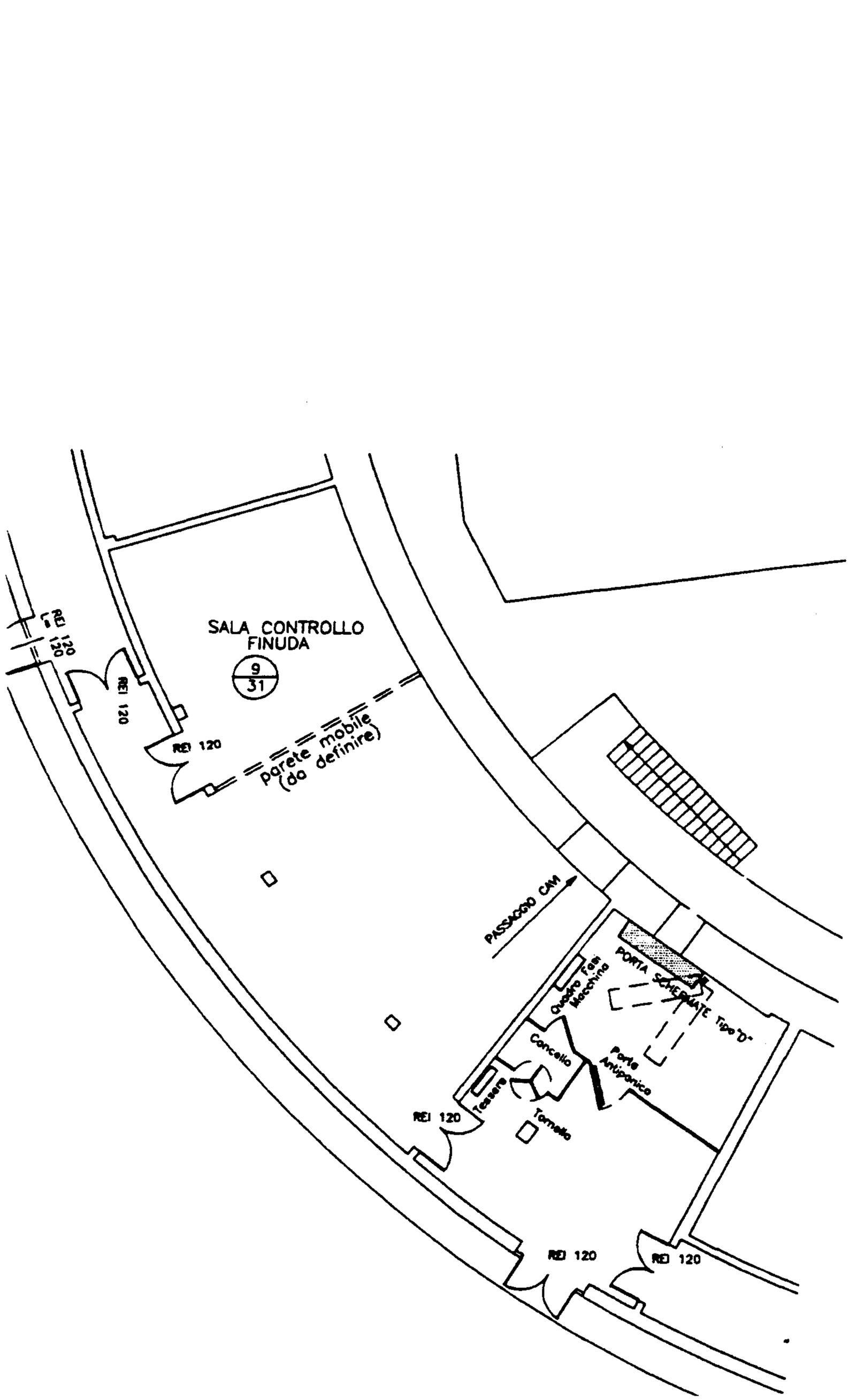

Figure 9.17: The FINUDA counting room.

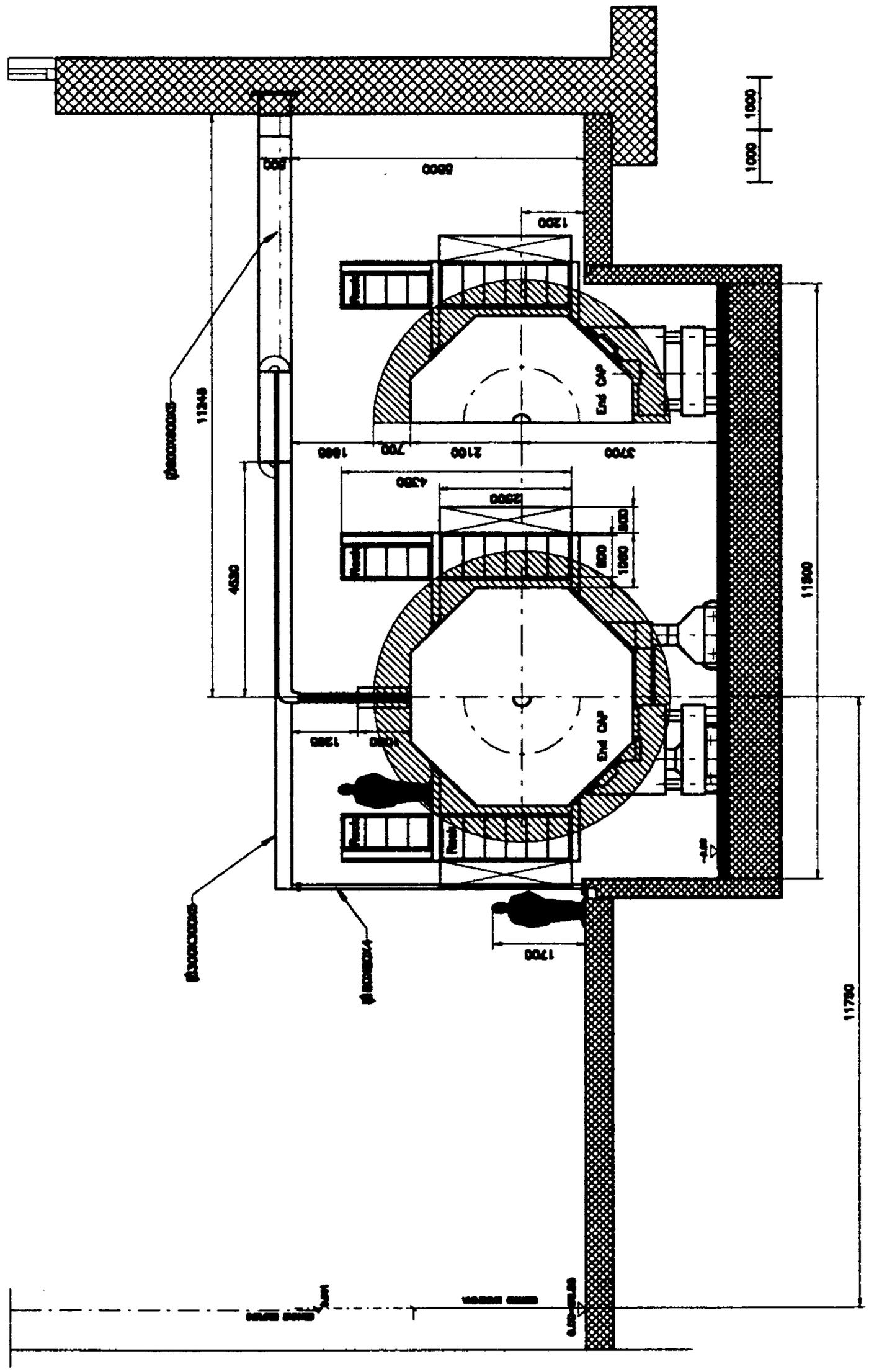

Figure 9.15: FINUDA cable and servicing overhead transport system.

Chapter 10

RESPONSIBILITIES AND TIME SCHEDULE

The responsibility of the design, test on prototypes and final delivery of the different parts of the apparatus is shared among the different Institutions participating to the experiment as illustrated in Table 10.1. The off-line programs are developed by members of all the above Institutions.

The budget for FINUDA has been approved by the Nuclear Physics Committee of INFN (Gruppo III) following a schedule that foresees the installation of the full experiment by mid 1996. With the budget of the years 1993-1994 the following items has been already tendered or will be tendered in the forth-coming month:

- The magnet
- A great part of the components of TOFONE
- TOFINO
- Materials for LMDC's and Mechanics
- A great part of the components of μ-strip Detectors
- Some parts of the front End Electronics
- Some parts of the DAQ system

The remaining main parts that have to be purchased by the budget of the years 1994-1995 are:

- The straw tubes array
- The electronics for LMDC's, Straw Tubes and for the Trigger
- The DAQ
- The gas control system
- Remaining minor items for the completion of the experiment.

Table 10.1: Sharing of responsibilities: five • mean full responsibility.

	Magnet	Mechanics	Detectors & related elect.	DAQ & Trigger	Monte Carlo	Installation facilities	Test Beam facilities
Bari			(TOFONE) ••••• (I&O) ••	•			
Brescia		•••	(LMDC) •		••		
Frascati	••••	••	(STRAW) •••••	•		•••••	
Torino	•		(LMDC) •••	••	••		
Trieste			I&O •••				
Pavia			(TOFINO) •••••	•	•		
TRIUMF			(LMDC) •				•••••

10.1 Construction schedule

The construction schedule for FINUDA experiment is summarized in Table 10.2

Table 10.2: Construction schedule

Year	Magnet	Tofino Tofone	Straw Tubes	LMDC	Vertex Detector	Mechanics	DAQ Trigger	On-line Off-line Monte Carlo
1994	↑ design +	tests on prototypes tenders	final tests tenders for electronics and materials	final tests start construction tenders for electronics	tender for Si detector tender for electronics	↑ design ↓	architecture + tests	Monte Carlo tracking and fitting pattern recognition
1995	construction	delivery machining test of efficiency	delivery + construction	delivery + construction	delivery + Si mounting	↑ construction ↓	delivery electronics	event display on-line procedures off-line procedures
1996	delivery magnetic measur. installation	assembly installation	assembly installation	assembly installation	assembly installation	assembly installation	installation	tests

Acknowledgments

We have to thank F. Sauli for his continuous suggestions during the developing of the drift chambers. This report includes parts that received major contributions from B.Dulach and E. Pace to whom goes our appreciation for their friendly help. A. Cecchetti, D.Orecchini, A. Ceccarelli with skill, dedication and patience achieved mechanical solution to most of our "crazy" conceptual ideas. C. Corradi, A. Balla, M. Santroni, had a relevant role in realizing preamplifiers and discriminators prototypes for the straw tubes. D. Pierluigi made possible the editing of this Technical Report fulfilling our pressing needs with enormous patience and solving them with ability. Finally, we acknowledge the support of the Centro di Calcolo, SPECAS Officina, SIS and Divisione Macchina of the Laboratori Nazionali di Frascati.